

**An apparatus for measuring the electron's electric dipole  
moment in trapped  $\text{ThF}^+$**

by

**Noah Schlossberger**

B.S., Indiana University Bloomington, 2018

M.S., University of Colorado Boulder, 2021

A thesis submitted to the  
Faculty of the Graduate School of the  
University of Colorado in partial fulfillment  
of the requirements for the degree of  
Doctor of Philosophy  
Department of Physics  
2023

Committee Members:

Eric A. Cornell, Chair

Jun Ye

John Bohn

Adam Kaufman

Joshua Combes

Schlossberger, Noah (Ph.D., Physics)

An apparatus for measuring the electron's electric dipole moment in trapped  $\text{ThF}^+$

Thesis directed by Prof. Eric A. Cornell

Unresolved questions in the universe, such as the matter-antimatter asymmetry, challenge the limitations of the Standard Model. As searches for beyond-the-Standard-Model physics face escalating energy scale requirements in particle accelerator experiments, low energy investigations targeting symmetry-breaking properties, like the electron's electric dipole moment (eEDM), have become a key tool in probing these theories. Recently, our group at JILA set a world-record limit on the eEDM, providing a new constraint on the masses of supersymmetric particles.

In order to achieve any more sensitivity in such a measurement, the next iteration of the experiment must grow dramatically in complexity. The new generation of JILA eEDM experiment is different in three main ways. First, a new molecular ion species,  $\text{ThF}^+$ , gives inherently longer coherence times because the experiment can be performed in the ground electronic, vibrational, and rotational state of the molecule. In order to gain access to this long coherence time, we must introduce cryogenics to the ion trap so as to reduce ambient black-body radiation that can incoherently excite the relevant quantum states. Finally, in order to access long coherence times without sacrificing count rate, the experiment is designed to eventually be multiplexed.

The resulting experiment will take of order one decade from conception to result. This thesis will cover the design and construction of the third generation eEDM experiment, as well as demonstrate preliminary measurements of the eEDM-sensitive states of  $\text{ThF}^+$ .

## Acknowledgements

I would like to express my sincere gratitude to Prof. Eric Cornell for his invaluable guidance and patience throughout my journey. His ability to intuitively frame complex problems has played a vital role in shaping me into the researcher I am today. I am also deeply thankful to Prof. Jun Ye, whose technical expertise has consistently pulled me out of challenging situations.

I am indebted to my mentor, Kia Boon Ng, for his invaluable teachings and guidance. Additionally, I extend my thanks to my labmates Sun Yool Park, Anzhou Wang, Yuval Shagam, Tanya Roussy, Trevor Wright, and Luke Caldwell, who have made the lab a friendly and enjoyable space.

I cannot give enough gratitude to the technical staff at JILA, particularly J. R. Raith, Hans Green, and James Urich, who have not only taught me invaluable skills but have also offered rewarding friendships.

Furthermore, I am grateful to my close friends who have provided unwavering emotional support throughout this journey, including Sinéad Ryan, Drew Morrill, Anya Grafov, Hope Whitelock, and my loving family, without whom this accomplishment would not have been possible.

# Contents

Chapter	
<b>1</b>	<b>Introduction</b> <span style="float: right;"><b>1</b></span>
1.1	Symmetry and the electron electric dipole moment . . . . . 1
1.2	Thesis layout . . . . . 5
<b>2</b>	<b>Experiment Overview</b> <span style="float: right;"><b>6</b></span>
2.1	Measurement concept . . . . . 6
2.1.1	Molecular structure and the eEDM . . . . . 8
2.1.2	Laboratory fields . . . . . 13
2.1.3	Measuring energy levels in a molecule . . . . . 15
2.1.4	Sensitivity . . . . . 18
2.2	Experimental realization . . . . . 19
<b>3</b>	<b>State preparation</b> <span style="float: right;"><b>24</b></span>
3.1	Ionization . . . . . 24
3.2	Optical pumping . . . . . 25
3.2.1	Continuous wave laser overview . . . . . 28
3.2.2	Rb reference . . . . . 30
3.2.3	Microwaves . . . . . 36
3.2.4	Spectroscopy . . . . . 46

<b>4</b>	<b>Electric Fields</b>	<b>50</b>
4.1	Electrode design . . . . .	50
4.1.1	Overview . . . . .	52
4.1.2	Ponderomotive potential . . . . .	52
4.1.3	Paul trap . . . . .	55
4.1.4	Rotating polarizing field . . . . .	60
4.2	Electronics . . . . .	61
4.2.1	Amplitude and timing requirements . . . . .	61
4.2.2	DDS boards . . . . .	63
4.2.3	Resonant transformers . . . . .	66
4.2.4	Transformer theory . . . . .	70
4.2.5	Coupling between rods . . . . .	75
4.2.6	Control matrix . . . . .	82
<b>5</b>	<b>Magnetic Fields</b>	<b>88</b>
5.1	Effect of magnetic fields in the Hamiltonian . . . . .	88
5.2	$f_0$ from anti-Helmholtz coils . . . . .	89
5.3	Characterization of homogeneity . . . . .	90
5.3.1	Multipole expansion . . . . .	91
5.3.2	Sources of decoherence . . . . .	94
5.3.3	Magnetic field measurement scheme . . . . .	96
5.4	Background fields from the optical table . . . . .	98
5.5	Field-distorting effects of the optical table . . . . .	99
5.6	Homogeneity of anti-Helmholtz fields . . . . .	100
5.7	Shim coils for $B_{4,0}$ and $B_{4,2}$ . . . . .	103
<b>6</b>	<b>Detection</b>	<b>106</b>
6.1	Dissociation . . . . .	106

6.1.1	Optics . . . . .	106
6.1.2	Spectroscopy . . . . .	109
6.1.3	Hyperfine selectivity . . . . .	112
6.2	Ion imaging . . . . .	112
6.2.1	Electronics . . . . .	114
6.2.2	Mesh gating . . . . .	116
6.2.3	Phosphor screen gating . . . . .	117
6.2.4	Capacitive readout interpretation . . . . .	120
6.2.5	Ion counting . . . . .	125
6.3	Simultaneous doublet readout . . . . .	126
<b>7</b>	<b>Preliminary Results and Conclusion</b>	<b>130</b>
7.1	Rabi oscillations . . . . .	130
7.2	Ramsey oscillations . . . . .	132
7.3	Concluding remarks . . . . .	132
	<b>Bibliography</b>	<b>135</b>
	<b>Appendix</b>	
<b>A</b>	<b>Biot-Savart Integrals</b>	<b>140</b>
A.1	Square current loop . . . . .	140
A.2	Circular current loop . . . . .	142
<b>B</b>	<b>A modified chain rule for vector fields</b>	<b>143</b>

# Chapter 1

## Introduction

### 1.1 Symmetry and the electron electric dipole moment

The prevalence of matter over antimatter is one of the most important outstanding problems in physics. Before the big bang, the universe had no matter, meaning the universe started with a symmetric amount of matter and antimatter. The asymmetry must have arisen due to the matter-forming interactions in the first few moments of the universe. The current most accepted description for the formation of this asymmetry is called Baryogenesis, and it requires three elements<sup>1</sup> [1]:

- interactions that violate baryon number symmetry, meaning they can create more matter than antimatter or vice-versa
- interactions that violate charge-parity (CP) symmetry, meaning that they don't work the same way if you swap all charge in the universe with negative charge and flip all spatial coordinates ( $\vec{r} \rightarrow -\vec{r}$ )
- the universe to be out of thermal equilibrium, meaning that energy can be unequally distributed in the universe.

To see why we both baryon number symmetry violating and CP symmetry violating interactions to end up with more matter than antimatter, first consider why we need both baryon number symmetry violation and charge (C) violation. Charge symmetry implies that matter and antimatter should behave the same, meaning that for every baryon number symmetry violating interaction that

---

<sup>1</sup> These requirements are known in the field of cosmology as the “Sakharov conditions.”

produces more matter than antimatter there is an equivalent interaction that produces equally more antimatter than matter, so the total amount of each would still be symmetric if C symmetry is preserved. By extension, CP symmetry would also not allow for Baryogenesis, since it would imply equal amounts of matter of one parity and antimatter of the other. Since it would do so for both parities, this would still overall lead to equal amounts of matter and antimatter.

The existence of the amount of CP violation that would allow for Baryogenesis is inconsistent with our understanding of the universe. The current best understanding of the structure of matter, known as the Standard Model of particle physics, does not contain enough CP symmetry violation to give rise to Baryogenesis [2], meaning that the Standard Model cannot adequately explain our existence. Several extensions to the Standard Model have been proposed to fix this [3, 4]. However, these models require experimental verification. This can be done by measuring the CP-violating properties of the universe and comparing them to the predicted values from these theories. One such property is an electric dipole moment (EDM) of any fundamental particle with spin.

To understand why an EDM of a fundamental particle with spin is fundamentally CP violating, consider the relative orientations of the particle's electric dipole moment and magnetic dipole moment (arising from the particle's spin). A diagram of the orientation of these properties under charge and parity inversion are shown in Figure 1.1.

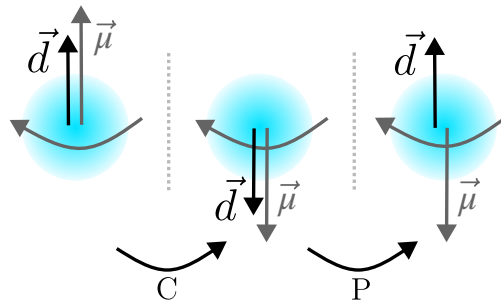


Figure 1.1: Transformations of a particle's magnetic dipole moment  $\vec{\mu}$  and electric dipole moment  $\vec{d}$  under a charge (C) and parity (P) symmetry transformation. The rotation arrow indicates the direction of classical rotation of the negative charge that would give rise to the particle's magnetic moment.

In order to visualize how spin changes under various inversions, it is helpful to think of the



particle's spin as arising from a charge distribution rotating classically. Under charge inversion, the electric dipole moment flips, and the sign of the classically rotating charge distribution flips meaning the magnetic moment flips as well. Next, under parity inversion, the electric dipole moment flips, but the spin does not (rotation direction does not flip under  $\vec{r} \rightarrow -\vec{r}$ ). This means that under CP inversion, the relative orientation of the electric dipole moment and the magnetic dipole moment of the particle is reversed. Therefore a particle having both an electric dipole moment and a spin is inherently CP violating.

Efforts to constrain particle physics include measuring the electric dipole moment of the muon, neutron, and proton. So far the measurement of these quantities is consistent with zero, so the results are expressed as a bound on the magnitude of the dipole moments. A history of these measurements is shown in Figure 1.2.

Any dipole moment measured above the Standard Model prediction would be a clear signature of beyond-the-Standard-Model physics. Electron EDM measurements are particularly exciting because they have been able to reach much greater sensitivity than neutron EDM measurements, and the gap between the current experimental bounds and the Standard Model background is shrinking.

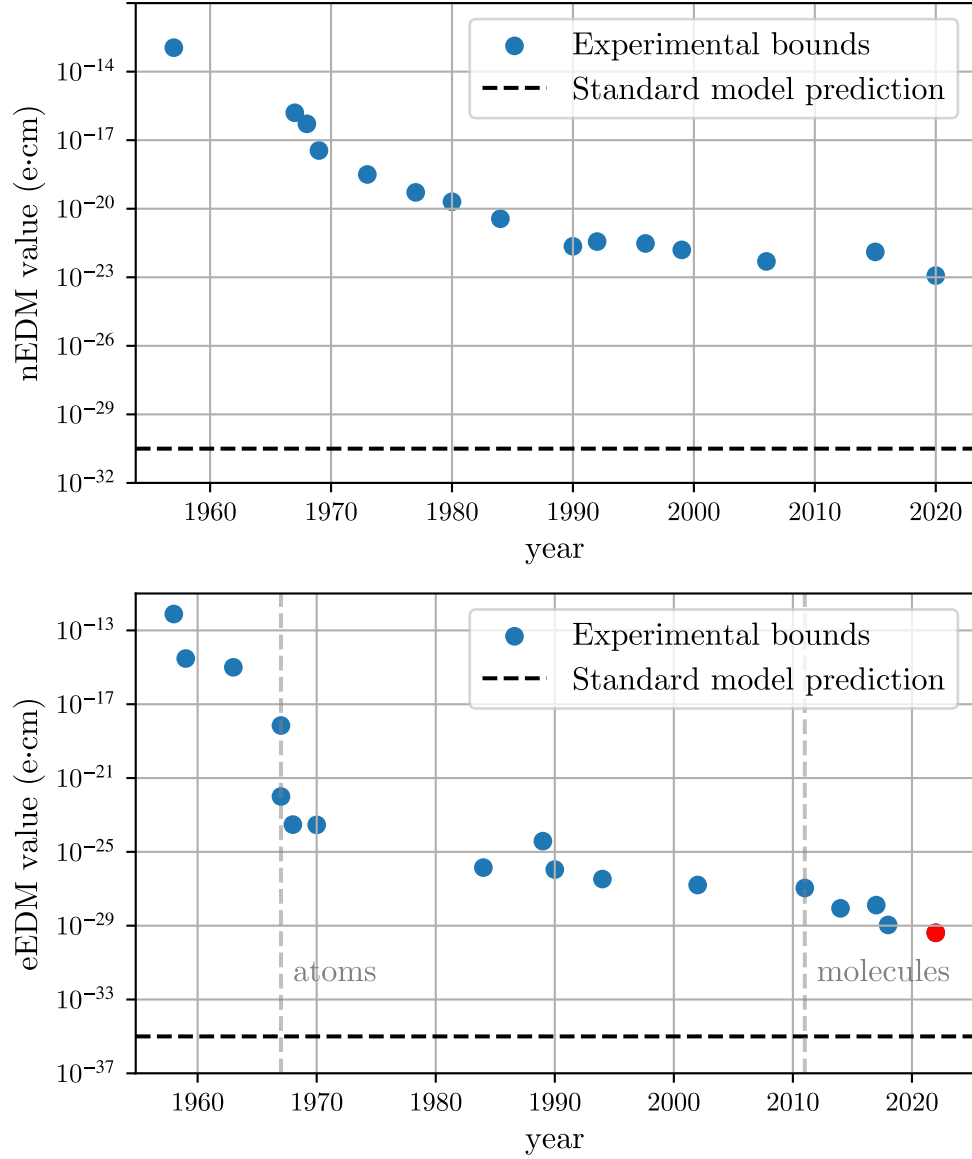


Figure 1.2: Historical and theoretical context for EDM searches.

**Top:** Experimental upper bounds [5, 6, 7, 8, 9, 10, 11, 12, 13, 14, 15, 16, 17, 18, 19] on the neutron’s electric dipole moment (nEDM) compared to the Standard Model prediction [20]. Experimental upper bounds represent the 90 percent confidence interval for the magnitude of the EDM.

**Bottom:** Experimental upper bounds [21, 22, 23, 24, 25, 26, 27, 28, 29, 30, 31, 32, 33, 34, 35, 36] on the electron’s electric dipole moment (eEDM) compared to the Standard Model prediction [37]. Highlighted in red is our 2023 JILA result [38]. Vertical gray dashed lines indicate the paradigm shifts of the best bounds being placed by eEDM searches in heavy atoms in 1967 and in polar molecules in 2011.

## 1.2 Thesis layout

This thesis was written at a similar time to that of Kia Boon Ng [39], another graduate student working on the third generation of JILA eEDM measurements. This thesis delves more into the technological efforts towards the eEDM measurement while Ng's focuses more on the physics of the experiment. The two function well as companion references to a complete understanding of the experiment.

The thesis is organized as follows: first Chapter 2 will describe in overview the details of measuring the eEDM in  $\text{ThF}^+$ , providing both an abstract explanation of the measurement concept and a complete view of the actual experiment. Subsequent chapters will describe the technical details of the instrumentation developed to do this, highlighting the technical requirements, the solution, and any data taken. Specifically, Chapter 3 will cover preparation of the ions from their atomic sources into the relevant quantum states, Chapter 4 will cover the electric fields needed to trap and polarize the ions, and Chapter 5 the magnetic fields needed to generate the base frequency  $f_0$  and possible sources of decoherence. Next, Chapter 6 will cover the way that the population in the states of interest is read out, and finally Chapter 7 will present preliminary data and make concluding remarks.

## Chapter 2

### Experiment Overview

#### 2.1 Measurement concept

An electric dipole moment has an energy associated with it when placed in an external electric field. An intuitive explanation of this is shown in Figure 2.1.

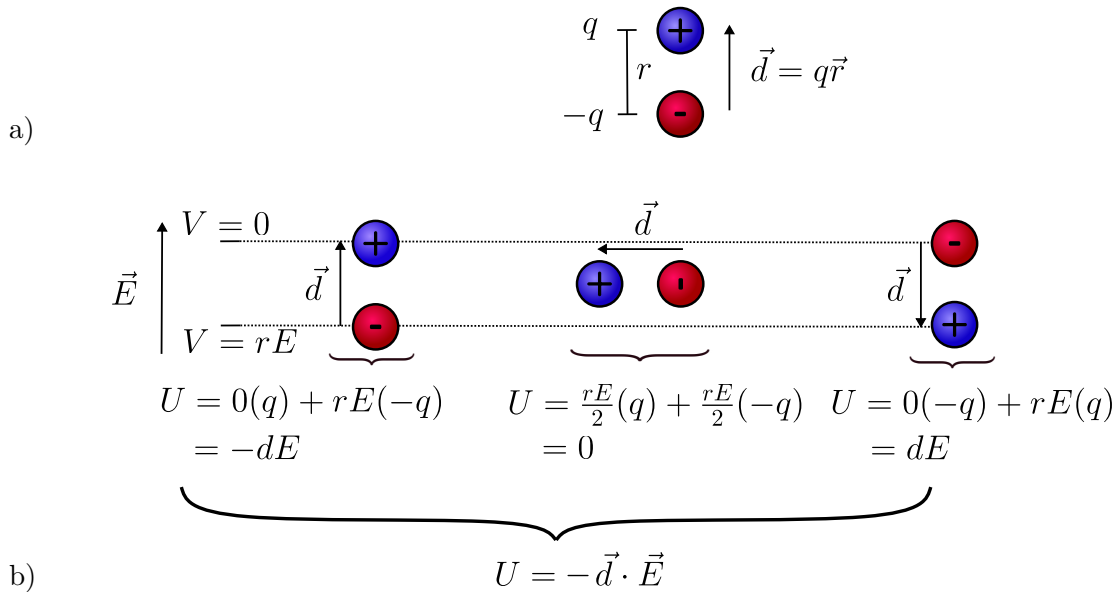


Figure 2.1: Intuitive picture of the DC Stark effect.

a) An ideal dipole consisting of two opposite charges of charge magnitude  $q$  separated by an infinitesimal distance  $r$ , resulting in a dipole moment  $|\vec{d}| = qr$

b) The ideal dipole in an external electric field. The electric potential difference between two points a distance  $r$  away is given by  $\Delta V = \frac{dV}{dr}r = -Er$ . We can then calculate the energy of each configuration as the sum of the Coulomb potentials of each charge  $U = \sum_i V(\vec{r}_i)q_i$ . The energies are shown for several orientations, and it follows that the energy is exactly the projection of the dipole moment onto the external electric field  $U = -\vec{d} \cdot \vec{E}$ .

This energy, known as the DC Stark shift, allows us to measure the dipole moment of the electron  $d_e$ . The difficulty comes from the extremely small size of  $\vec{d}_e$ . Even if one were to place 10 kV across electrodes 1 mm apart, the resulting field would produce a Stark shift of less than 1 nHz<sup>1</sup> (using the current bound on the magnitude of  $\vec{d}_e$  [38]).

The solution is to measure the DC Stark shift in the valence electrons of a heavy polar molecule, as in Figure 2.2

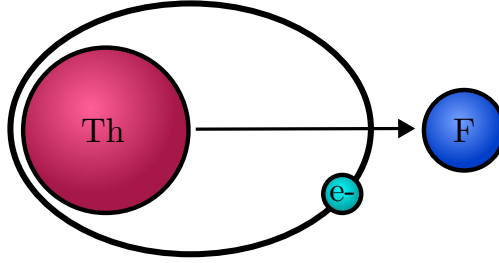


Figure 2.2: A valence electron in a  $\text{ThF}^+$  molecule. The internal electric field arising from the polar nature of the molecule as well as a classical trajectory of the the eEDM-sensitive valence electron is illustrated. While this classical trajectory is not particularly physical, it demonstrates the key feature of an eccentric orbit, meaning that the electron experiences vastly different “velocities” at different spatial locations in the molecule.

The electric fields inside the polar molecule are significantly larger than any electric field that one can create in a lab. However, the time-averaged electric field experienced by the electron  $\langle E \rangle_t$  must be zero for the electron to be bound. Even so, the time averaged Stark shift  $\langle -\vec{d}_e \cdot \vec{E} \rangle_t$  can be nonzero due to the eccentric orbit of the electron.<sup>2</sup> As the electron zips by the heavier atom in the polar molecule, the length contraction of the electron in the laboratory frame means that  $\vec{d}_e$  shrinks in magnitude. This gives rise to a nonzero time average Stark shift in the laboratory frame, with the complexity of this effect absorbed into an “effective” electric field  $\vec{E}_{\text{eff}}$

$$\langle \vec{d}_e \cdot \vec{E} \rangle_t \equiv \vec{d}_e \cdot \vec{E}_{\text{eff}}. \quad (2.1)$$

Table 2.1 lists the relativistic effective electric field experienced by a valence electron each polar

<sup>1</sup> Here the energy is given as a frequency via implicit division by Planck’s constant  $h$ . Frequencies and energies will be used interchangeably throughout this thesis.

<sup>2</sup> Of the two valence electrons in  $\text{ThF}^+$ , only the  $\sigma$  electron exhibits this property.

molecule in the world’s leading eEDM measurements<sup>3</sup>.

Molecule	$E_{\text{eff}}$ (GV/cm)	Experiment
ThO	$78 \pm 2$ [40, 41]	ACME II [42]
HfF <sup>+</sup>	$21 \pm 2$ [43, 44, 45]	JILA Gen. I [46] and II [38]
ThF <sup>+</sup>	$36 \pm 1$ [47, 48]	JILA Gen. III (this work)

Table 2.1: Effective electric fields of the polar molecules used in leading eEDM experiments. The error bars presented are the standard deviation of the theory predictions over the square root of the number of predictions.

These effective electric fields in the tens of GV/cm are much greater than one could create with electrodes, and bring the frequency of the Stark shift at the current eEDM bounds up to the  $\mu\text{Hz}$  scale, which can be measured in a Ramsey-type experiment.

### 2.1.1 Molecular structure and the eEDM

The eEDM-sensitive Stark shift described in the previous section manifests as a shift in the quantized energy levels of the polar molecule which can be measured. First, we must understand the structure of the molecule to see where the shift shows up.

The quantum state of a molecule is described by quantization of all possible degrees of freedom, including the configuration of electrons within the molecule, inter-atomic vibration of the molecule, and rotation of the molecule.

The electron configuration is described by the electronic state, denoted by the molecular term symbol

$$^{2S+1}\Lambda_{\Omega} \quad (2.2)$$

where  $S$  is the total spin of the unpaired electrons,  $\Lambda$  is the projection of the orbital angular momentum onto the internuclear axis (expressed as Greek letters where  $\Sigma = 0$ ,  $\Pi = 1$ ,  $\Delta = 2$ , ...), and  $\Omega$  is the projection of the total angular momentum onto the internuclear axis. The ground electronic state of ThF<sup>+</sup> is  $^3\Delta_1$ , meaning the two valence electrons give a spin of  $S = 1$ , with orbital

<sup>3</sup> While ThO boasts a higher  $E_{\text{eff}}$  than the JILA molecular ion species, the increased interrogation time offered by using trapped ions leads to an overall increased sensitivity.

angular momentum along the internuclear axis of  $\Lambda = 2$ , and with these two adding in opposite directions to give a total angular momentum of  $\Omega = 1$  along the internuclear axis.

In addition, the vibrational mode of the two constituent atoms is quantized into the vibrational quantum number  $v$ . The bottom of the potential as a function of inter-atomic distance looks roughly harmonic, so the vibrational levels have harmonic-oscillator-like behavior, starting at  $v = 0$  and having roughly equal energy spacing. This is illustrated in Figure 2.3

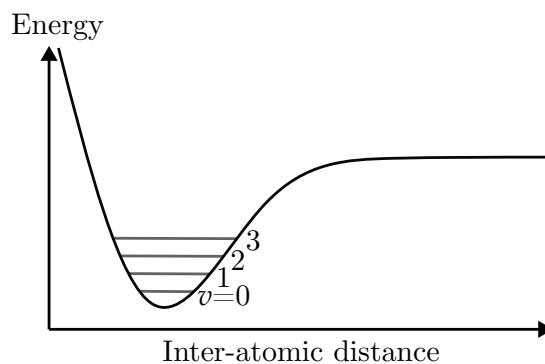


Figure 2.3: Illustration of the quantization of the vibrations of a molecule.

Finally, the rigid-body rotation of the molecule is quantized. Since this is an angular momentum, it can add with the angular momentum of the electronic wavefunction. The rotational quantum number  $J$  is actually the projection of the total angular momentum (including  $\Omega$  and molecular rotation) onto the internuclear axis. For this reason,  $J$  must be at least  $\Omega$ , so the ground rotational state of  ${}^3\Delta_1$ ,  $v = 0$  is  $J = 1$ .

Finer structure arises from the nuclear spins of the constituent atoms. The hyperfine states are depicted in Figure 2.4.  ${}^{232}\text{Th}$  has a nuclear spin of 0, while  ${}^{19}\text{F}$  has a nuclear spin of  $1/2$  [49]. Therefore the total angular momentum quantum number  $F$  of  $({}^3\Delta_1, v = 0, J = 1)$  comes from the addition of one unit of angular momentum from the angular momentum of the electronic state ( $\Omega = 1$ ) and  $1/2$  unit of angular momentum from the nuclear spin of fluorine, with allowed values of either  $1/2$  or  $3/2$ . Within each  $F$ , there can be a projection of the total angular momentum  $m_F \in [-F, F]$ . Finally, each  $m_F$  level has two nearly degenerate states corresponding to the parity of the wavefunction, with the degeneracy lifted by a higher order coupling known as  $\Omega$ -doubling.

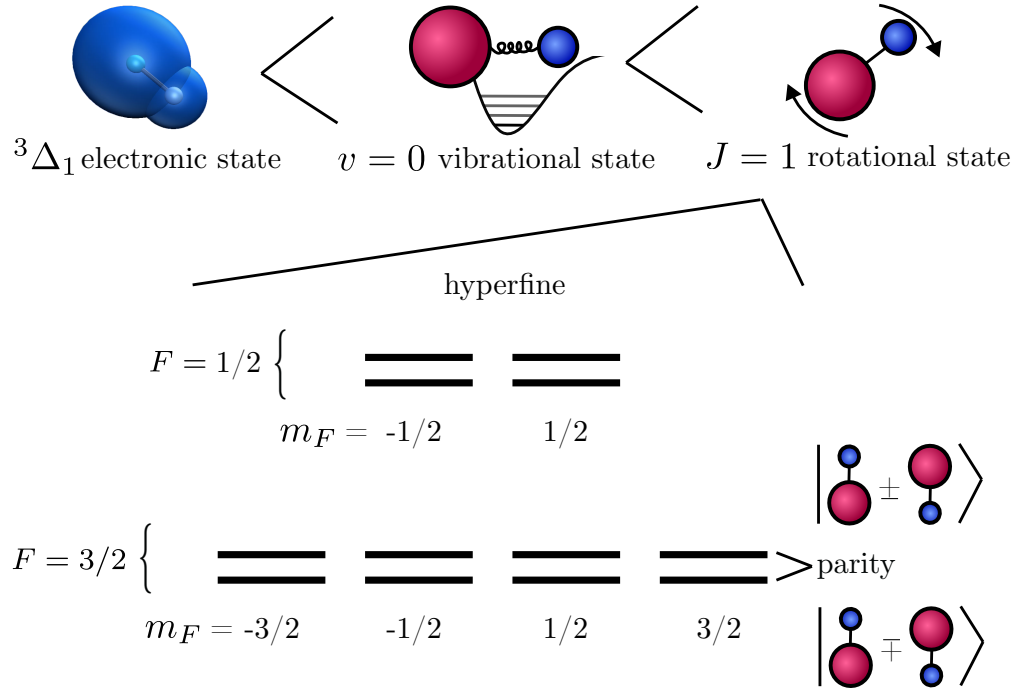


Figure 2.4: Structure of the hyperfine states within  ${}^3\Delta_1$ ,  $v = 0$ ,  $J = 1$ . Without any external fields, nothing sets the quantization axis. In this case, parity is a good quantum number, with degeneracy of the parities lifted by  $\Omega$ -doubling. The parity states are illustrated with a  $\pm$  or  $\mp$  sign because it is not clear which parity has higher energy, and this was never experimentally determined.

We are interested in the  $F = 3/2$  hyperfine manifold, particularly when we apply an external electric field  $\vec{E}_{\text{app}}$ . The effect of applying such a field on the quantum states is shown in Figure 2.5.

With an external electric field, spatial symmetry is broken and the molecules become polarized. Without spatial symmetry, parity is no longer a good quantum number, and each  $m_F$  level becomes split instead into two orientation states (aligned or anti-aligned) of the molecule. Because the molecule is polar it has its own molecular-frame electric dipole moment,

$$d_{\text{mf}} = 3.37(9) \text{ Debye [50]}, \quad (2.3)$$

the energy shift of the orientation states is then set by the DC Stark shifts from the molecule's electric dipole moment  $-\vec{d}_{\text{mf}} \cdot \vec{E}_{\text{app}}$ . In addition, because there is a well defined orientation of



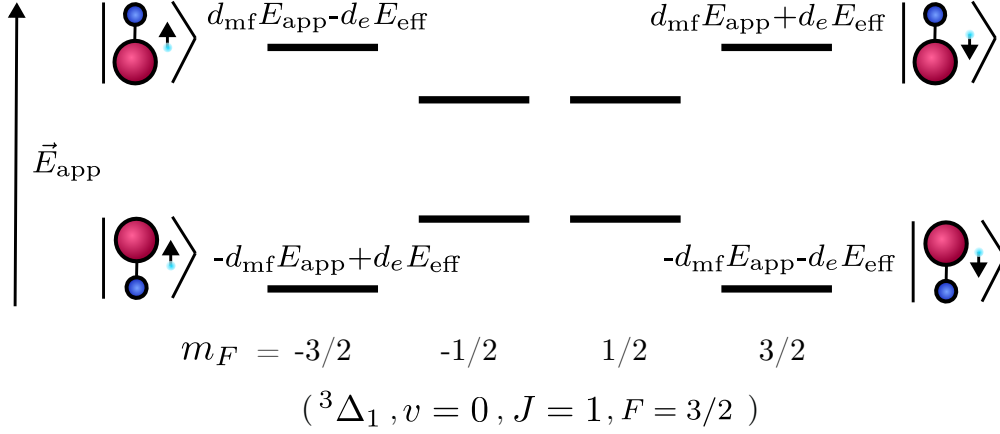


Figure 2.5: Energy level diagram of the  $^3\Delta_1, v=0, J=1, F=3/2$  manifold of  $\text{ThF}^+$  in the presence of an external electric field. For each  $m_F = \pm 3/2$  state, the energy of the state (relative to the baseline  $F=3/2$  center energy) are labeled and the quantum state depicting the orientation of the molecule and the pointing of the eEDM-sensitive valence electron's spin (and therefore also its  $\vec{d}_e$ ) are illustrated.

the molecule and therefore its internal electric field relative to the spin<sup>4</sup> of the eEDM-sensitive electron, these states become modified by the eEDM sensitive Stark splitting<sup>5</sup>  $-\vec{d}_e \cdot \vec{E}_{\text{eff}}$ , with the sign of the dot product determined by the relative orientation of the molecule and the electron.

Finally, one more modification to the states is useful. In practice, energy levels of a molecule are measured as the *difference* between two energy levels as a frequency. If we want to measure the energy difference between the opposite sign  $m_F = \pm 3/2$  states for a given orientation, it is useful to create an intentional energy difference between these states so that the frequency can be tuned to an experimentally convenient timescale. We can do this by introducing a magnetic field  $\vec{B}_{\text{app}}$ . The modification of the states in the presence of this field is shown in Figure 2.6.

The magnetic field  $\vec{B}_{\text{app}}$  couples to the projection of the angular momentum onto the quantization axis  $m_F$  through the Zeeman effect:

$$\Delta U_{\text{Zeeman}} = -\vec{\mu}_{\text{total}} \cdot \vec{B}_{\text{app}} = \pm m_F g \mu_B B_{\text{app}} \quad (2.4)$$

where  $g$  is the g-factor and  $\mu_B$  is the Bohr magneton. Note that the g-factor is slightly different

<sup>4</sup> The electric dipole moment of the electron is defined to point the same direction of the spin, so the orientation of the spin is the same as the orientation of  $\vec{d}_e$ .

<sup>5</sup> Here we can neglect the  $-\vec{d}_e \cdot \vec{E}_{\text{app}}$  coupling since  $E_{\text{app}} \ll E_{\text{eff}}$  by nine orders of magnitude.

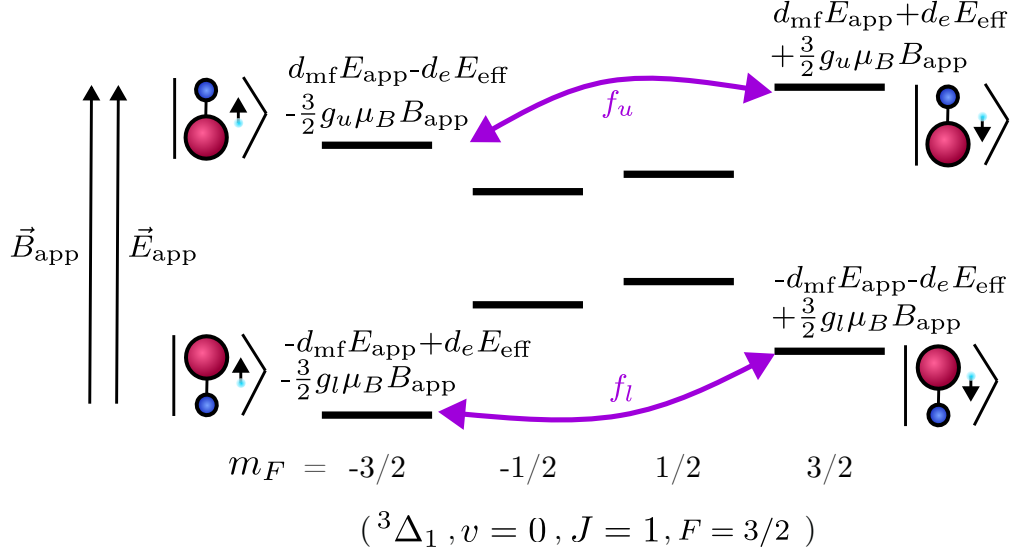


Figure 2.6: Energy level diagram of the  $^3\Delta_1, v=0, J=1, F=3/2$  manifold of  $\text{ThF}^+$  in the presence of an external electric and magnetic field.

for the two orientations, so we label the g-factor as  $g_u$  and  $g_l$  for the upper and lower pair of states respectively, which we measured to be

$$\begin{cases} g_u = 0.1475(30) [50] \\ g_l = 0.1505(30) [50]. \end{cases} \quad (2.5)$$

We call the upper pair of states the “upper doublet” and the lower pair of states the “lower doublet.”

The electric dipole moment of the electron can be measured by measuring the energy differences of each doublet  $f_u$  and  $f_l$  (violet in Figure 2.6), whose energies are

$$\begin{cases} f_u = 3g_u\mu_B B_{\text{app}} + 2d_e E_{\text{eff}} \\ f_l = 3g_l\mu_B B_{\text{app}} - 2d_e E_{\text{eff}}. \end{cases} \quad (2.6)$$

Note that by measuring energy differences between states of the same molecular orientation, the  $d_{\text{mf}}$ -dependent term drops out. The magnetic field component gives a background energy  $f_0 = 3g\mu_B B_{\text{app}}$  designed to turn the eEDM-sensitive energy from nominally zero frequency to one that can be easily measured (with our  $f_0$  on the order of 50Hz), turning the eEDM signal into a small frequency modification that turns into a phase offset at late time.

Flipping the orientation of different fields and taking a linear combination of the measured energies can then isolate the contribution from the electron's electric dipole moment  $d_e E_{\text{eff}}$ .

This encapsulates the essence of the eEDM measurement: measure the energy shift due to the Stark energy of the electron inside of a polar molecule with large internal effective electric field, realized by measuring the energy difference between two internal quantum states of the molecule in the presence of known applied laboratory fields.

### 2.1.2 Laboratory fields

In the above scheme, we apply an external electric field  $\vec{E}_{\text{app}}$  in order to polarize the molecules. However, since the molecules are ions, the resulting Coulomb force must have a nonzero time average in order for the molecules to remain trapped, i.e.

$$\langle q\vec{E}_{\text{app}}(t) \rangle_t = 0. \quad (2.7)$$

To get around this, we apply a rotating electric field polarize the molecules, rotating at a frequency  $\omega_{\text{rot}}$

$$\vec{\mathcal{E}}_{\text{rot}} = \mathcal{E}_{\text{rot}}(\cos(\omega_{\text{rot}}t)\hat{x} + \sin(\omega_{\text{rot}}t)\hat{y}). \quad (2.8)$$

Then the coulomb force on the ions becomes a centripetal force, and the ions move in a circular trajectory with radius  $r_{\text{rot}}$ . This is shown in Figure 2.7.

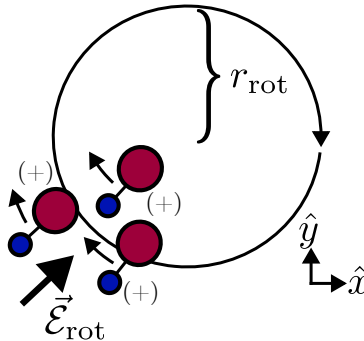


Figure 2.7: The rotating polarizing field  $\vec{\mathcal{E}}_{\text{rot}}$  giving rise to circular motion of the molecular ions with a trajectory radius of  $r_{\text{rot}}$ .

The radius of the trajectory can be calculated by setting the magnitude of the coulomb force  $F = qE$  equal to the centripetal force in angular form  $F = m\omega^2 r$  and solving for the radius, yielding

$$r_{\text{rot}} = \frac{q\mathcal{E}_{\text{rot}}}{m\omega_{\text{rot}}^2} \quad (2.9)$$

where  $m$  is the mass of the ion =  $(\underbrace{232}_{\text{Th}} + \underbrace{19}_{\text{F}})$  atomic mass units and  $q$  is the charge of the ion = 1 electron charge. For the typical values used in the experiment ( $\omega_{\text{rot}} = 2\pi \cdot 150$  kHz,  $\mathcal{E}_{\text{rot}} = 60$  V/cm), the molecules move in a circle of radius  $r_{\text{rot}} = 2.6$  mm.

Since the polarizing field and thus the quantization axis is now rotating, naively one might think that the magnetic field we apply to generate  $f_0$  must also rotate so that there is a well defined magnetic field along the quantization axis. However, we can instead apply a static magnetic field that diverges in the plane of rotation. This is demonstrated in Figure 2.8.

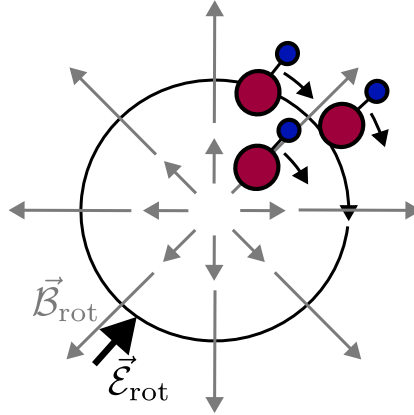


Figure 2.8: The diverging (in the  $x - y$  plane) magnetic field that gives rise to a non-zero  $\langle \vec{B} \cdot \hat{\mathcal{E}}_{\text{rot}} \rangle_t$ .

At each point in the trajectory, the magnetic field is exactly anti-aligned with  $\vec{\mathcal{E}}_{\text{rot}}$  and therefore the quantization axis. We can generate such a field by applying a field with an axial gradient (a field with a gradient in  $z$  along  $\hat{z}$ ):

$$\vec{B} = B_{\text{axgrad}}(x\hat{x} + y\hat{y} - 2z\hat{z}). \quad (2.10)$$

Then  $\mathcal{B}_{\text{rot}}$ , the value of the magnetic field along the quantization axis, is simply given by

$$\mathcal{B}_{\text{rot}} = B_{\text{axgrad}}r_{\text{rot}}. \quad (2.11)$$

From the illustration, it may seem as though this method requires that the center of the path traced out by the ions be exactly at the center of the divergence of the magnetic field. However, an offset  $(x_0, y_0)$  in the position of the field just looks like a uniform background field,

$$B_{\text{axgrad}}((x - x_0)\hat{x} + (y - y_0)\hat{y} - 2z\hat{z}) = \underbrace{B_{\text{axgrad}}(x\hat{x} + y\hat{y} - 2z\hat{z})}_{\text{intended field}} + \underbrace{B_{\text{axgrad}}(-x_0\hat{x} - y_0\hat{y})}_{\text{uniform background}}, \quad (2.12)$$

and the contribution from this background field will cancel out as the quantization axis rotates one cycle (this is shown analytically in Section 5.1). This means that the ions can trace a circular trajectory of radius  $r_{\text{rot}}$  around any point in the  $x - y$  plane and experience the same time-averaged field into the quantization axis:

$$\langle \vec{B} \cdot \hat{\mathcal{E}}_{\text{rot}} \rangle_t = \mathcal{B}_{\text{rot}}. \quad (2.13)$$

### 2.1.3 Measuring energy levels in a molecule

The method we use to measure the energy difference between states in a molecule relies on the fact for an eigenstate of the molecule's Hamiltonian ( $\hat{H}\Psi = E_{\Psi}\Psi$ ), the solution to the Schrödinger equation has a solution of a complex exponential,

$$i\hbar \frac{d}{dt}\Psi = \hat{H}\Psi = E_{\Psi}\Psi \rightarrow \Psi(t) = \Psi(t=0) e^{-i\frac{E_{\Psi}}{\hbar}t}, \quad (2.14)$$

which means the phase of the state  $\Psi$  accrues at a frequency equal to its energy divided by Planck's constant:

$$\omega_{\Psi} = \frac{E_{\Psi}}{\hbar}. \quad (2.15)$$

The phase *difference* between two states then accrues at a frequency proportional to the energy difference between the states. We can measure this phase using a technique called Ramsey interferometry.

To understand how Ramsey interferometry works, it's useful to parameterize a superposition of the two states  $|g\rangle, |e\rangle$  in terms of two angles

$$|\psi\rangle = \cos(\theta) |g\rangle + e^{i\phi} \sin(\theta) |e\rangle. \quad (2.16)$$

We can then represent any such state as a unit vector on a sphere with coordinates dictated by the polar angle  $\theta$  and azimuthal angle  $\phi$  (known as the “Bloch sphere”). The space of this representation is illustrated in Figure 2.9

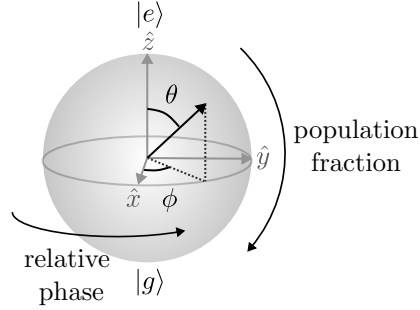


Figure 2.9: The Bloch sphere representation of a superposition of two quantum states.

There are important two properties of the state in this formalism. First, if we measure a state many times to extract the probability of it being in either eigenstate, we have essentially measured the angle  $\theta$ :

$$\begin{cases} P_{|g\rangle} = |\langle g|\psi\rangle|^2 = \cos^2(\theta) \\ P_{|e\rangle} = |\langle e|\psi\rangle|^2 = \sin^2(\theta). \end{cases} \quad (2.17)$$

Second,  $\phi$  is the relative phase between the two states, so time evolution of the state looks like rotation about  $\phi$  at a rate of  $\frac{\Delta E}{\hbar}t$ . where  $\Delta E$  is the energy difference between the states  $\Delta E = E_e - E_g$ .

With these two properties, we can understand the Ramsey-type measurement scheme, which is as follows:

- prepare a pure state, represented by  $\theta = 0$  or  $\hat{z}$
- rotate<sup>6</sup> about  $\hat{x}$  by  $\pi/2$
- wait some time  $t$  for  $\phi$  to evolve by  $\frac{\Delta E}{\hbar}t$  (a rotation about  $\hat{z}$ )
- rotate about  $\hat{x}$  by  $\pi/2$ .

<sup>6</sup> The rotation can be in any direction (other than  $\hat{z}$ ) as long as both  $\pi/2$  rotations are along the same axis, with a rotation axis in the  $x$ - $y$  plane giving the most contrast.

A representation of this scheme on the Bloch sphere is illustrated in Figure 2.10.

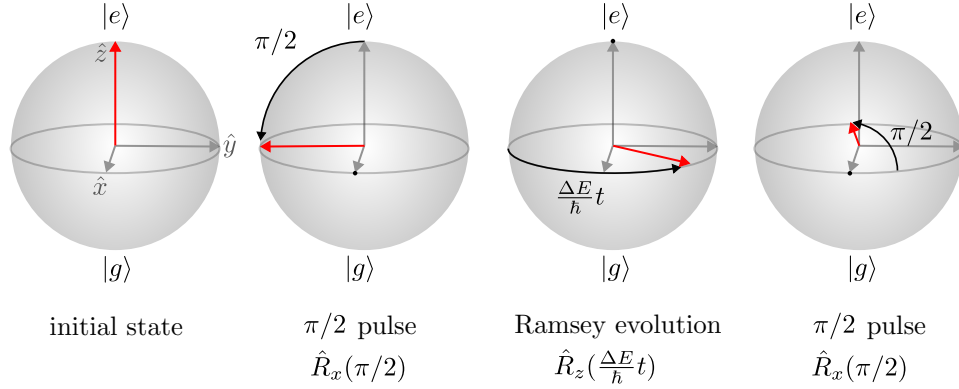


Figure 2.10: Bloch sphere representation of the three operators that make up a Ramsey interferometry measurement.

This scheme works by encoding the phase evolution of  $\phi$  (a quantum phase) onto  $\theta$  (a measurable probability), which happens because rotations along different axes do not commute. Mathematically we can represent this scheme as an operator  $\hat{O}$  operating on our initial state  $\hat{z}$  via 3D rotation operators:

$$\hat{O} \hat{z} = \hat{R}_x(\pi/2) \hat{R}_z\left(\frac{\Delta E}{\hbar} t\right) \hat{R}_x(\pi/2) \hat{z}. \quad (2.18)$$

If we write out these rotation operators as matrices and perform the operation, we can see how this encodes the phase accrued onto  $\theta$ :

$$\hat{O} \hat{z} = \begin{bmatrix} 1 & 0 & 0 \\ 0 & \cos(\pi/2) & -\sin(\pi/2) \\ 0 & \sin(\pi/2) & \cos(\pi/2) \end{bmatrix} \begin{bmatrix} \cos(\frac{\Delta E}{\hbar} t) & -\sin(\frac{\Delta E}{\hbar} t) & 0 \\ \sin(\frac{\Delta E}{\hbar} t) & \cos(\frac{\Delta E}{\hbar} t) & 0 \\ 0 & 0 & 1 \end{bmatrix} \begin{bmatrix} 1 & 0 & 0 \\ 0 & \cos(\pi/2) & -\sin(\pi/2) \\ 0 & \sin(\pi/2) & \cos(\pi/2) \end{bmatrix} \hat{z} \quad (2.19)$$

$$= \begin{bmatrix} \sin(\frac{\Delta E}{\hbar} t) \\ 0 \\ -\cos(\frac{\Delta E}{\hbar} t) \end{bmatrix}. \quad (2.20)$$

If we convert this back to spherical coordinates to find  $\theta$ , we get

$$\theta = \tan^{-1} \left( \frac{\sqrt{x^2 + y^2}}{z} \right) = \tan^{-1} \left( \frac{\sqrt{\sin^2(\frac{\Delta E}{\hbar} t)}}{-\cos(\frac{\Delta E}{\hbar} t)} \right) = -\frac{\Delta E}{\hbar} t, \quad (2.21)$$

so the probability of measuring the either eigenstate after the Ramsey sequence becomes

$$\begin{cases} P_{|g\rangle} = \cos^2(\frac{\Delta E}{\hbar}t) \\ P_{|e\rangle} = \sin^2(\frac{\Delta E}{\hbar}t). \end{cases} \quad (2.22)$$

We can then simply vary the evolution time  $t$  and count the number of cycles in order to measure the energy difference  $\Delta E$  between the states.

With this technique, we can measure the eEDM-sensitive frequencies  $f_u$  and  $f_l$  introduced in Equation 2.6.

#### 2.1.4 Sensitivity

In our experiment, the sensitivity  $\delta d_e$  to the eEDM scales as

$$\delta d_e \propto \frac{1}{E_{\text{eff}}\tau\sqrt{N}}, \quad (2.23)$$

where  $\tau$  is the Ramsey evolution time of the measurement (limited by the coherence time) and  $N$  is the total number of ions measured. Several key innovations in our new experiment maximize these parameters. By moving from HfF<sup>+</sup> (the species used in our current best bound [38]) to ThF<sup>+</sup>, the sensitivity increases in several ways. The coherence time in HfF<sup>+</sup> is limited by spontaneous decay of the eEDM-sensitive states ( $\sim 2$  s), while the eEDM-sensitive states in ThF<sup>+</sup> are in the ground electronic, vibrational, and rotational state, meaning that they do not spontaneously decay. Instead, the coherence time is limited by excitation from blackbody radiation (with cryogenic cooling of the experiment, coherence times of 20 s are theoretically possible, with more information in Ng's thesis [39]). Furthermore, ThF<sup>+</sup> has a slightly higher  $E_{\text{eff}}$  than HfF<sup>+</sup>, as mentioned previously.

Measuring the ions for a Ramsey time of 20 s would severely limit the rate at which the measurements could be done. Therefore, to fully leverage the long coherence time, we design the experiment to be multiplexed, i.e. ions will be continually loaded and prepared, then shuttled down the length of the trap as their Ramsey phase evolves, then read out on the other side of the trap. We can then make a measurement once per ion loading time ( $\sim .5$  s) rather than once per Ramsey time ( $\sim 20$  s).



The current iteration of the experiment as was developed in this thesis is not fully multiplexed, but tests some of the key technology required by shuttling the Ramsey evolving ions down to a cold region, then back to the original position for detection, demonstrating both the shuttling capabilities of the electrodes and the coherence time available via cryogenic cooling.

With all the planned improvements, we can make a rough estimate of the statistical sensitivity we expect to reach with this experiment, which is done in Table 2.2.

Experiment	Gen II	Gen III
$E_{\text{eff}}$	$21 \pm 2$ GV/cm [43, 44, 45]	$36 \pm 1$ GV/cm [40, 41]
$\tau$	$\sim 2$ s	$\sim 20$ s
$N/t_{\text{meas}}$	$\sim 120/(2 \text{ s})$	$\sim 20/(.5 \text{ s})$
$t_{\text{meas}}$	$\sim 500$ hr	$\sim 500$ hr
$\delta d_e$	$2.1 \times 10^{-30} e \cdot \text{cm}$ [38]	$\sim 1 \times 10^{-31} e \cdot \text{cm}$ (projected)

Table 2.2: Projected sensitivity for the third generation of eEDM experiment at JILA compared to the second generation. The projected sensitivity is calculated by scaling the Gen II sensitivity by the factor prescribed in Equation 2.23.

This projected sensitivity hinges on the success of long coherence times and multiplexing, and it only represents the possible statistical uncertainty of the experiment. Systematic sources of uncertainty can limit the sensitivity of the experiment as well (see [51] for an example of a study of systematic uncertainty).

## 2.2 Experimental realization

Now that we have seen how to measure the eEDM in an abstract sense and what makes such a measurement sensitive, this section will describe how such an experiment is actually realized.

The first step of the experiment is to create  $\text{ThF}^+$  out of sulfur hexafluoride gas and solid thorium. The technique for doing this is shown in Figure 2.11 A pulsed Nd:YAG laser ablates a pellet of thorium, vaporising a small amount of the metal. At the same time, a gas valve pulses some  $\text{SF}_6$  gas, which reacts with the Th vapor to create a beam of neutral ThF in a supersonic expansion.

The pellet is on a rotation and translation stage that rotates after each ablation such that

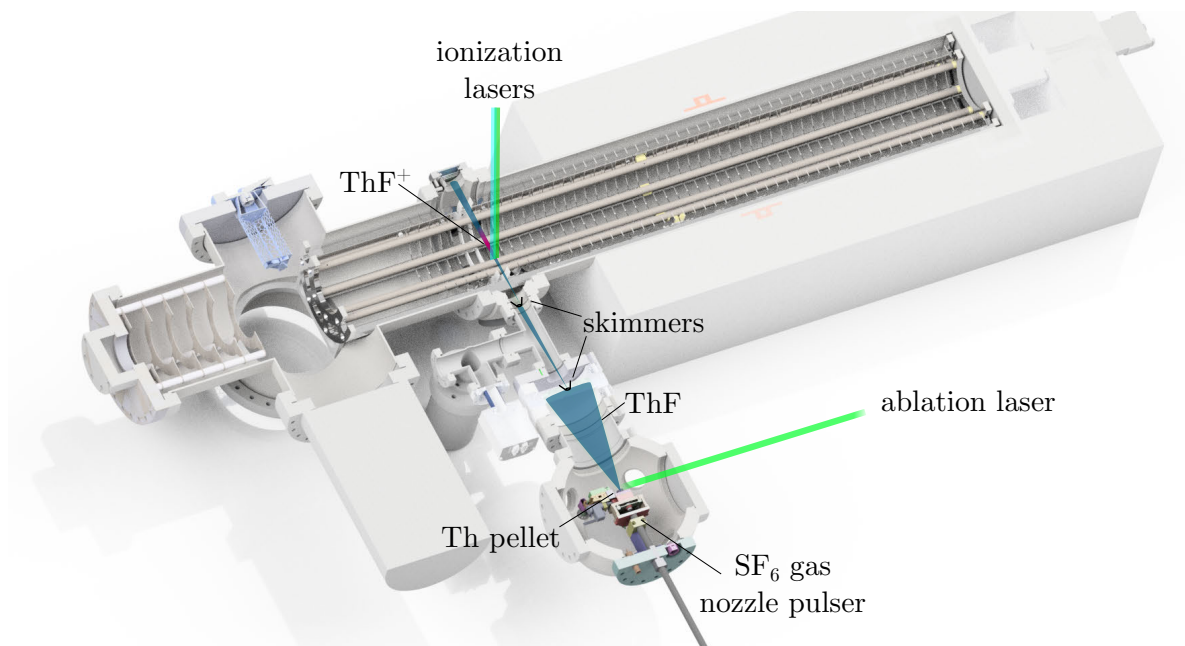


Figure 2.11: Setup for creation of  $\text{ThF}^+$  ions in the experiment.

each laser pulse hits a fresh polished surface of Th metal. The Th must be periodically polished as laser ablates away the clean surface in order to maintain production efficiency. The  $\text{SF}_6$  gas is pressurized to 80 pounds per square inch on the other end of the nozzle.

The ThF beam then passes through two skimmers, which are mm-scale pinholes with a conical shape. The skimmers reduce the angle of the beam such that when it reaches the trap it is about 1cm in size. The first skimmer is held at 30V to reject any ionized species in the beam.

Between the skimmers is an intermediate vacuum, with a pressure between that of the vacuum where the molecules are created ( $\sim 10^{-8}$  Torr, limited by consistent vacuum breaks to polish Th and consistent leaking of pressurized gas) and the vacuum in the trapping region ( $< 10^{-9}$  Torr, which must be low to allow for long coherence time). The small aperture of the skimmers allow for such a pressure gradient.<sup>7</sup>

Finally, the neutral beam of ThF is photo-ionized to create a packet of  $\text{ThF}^+$  ions. The photoionization process is covered in Section 3.1.

<sup>7</sup> At these pressures, intuition for vacuum behavior is governed by random scattering of individual atoms rather than traditional properties of fluid mechanics.

The next steps are illustrated in Figure 2.12.

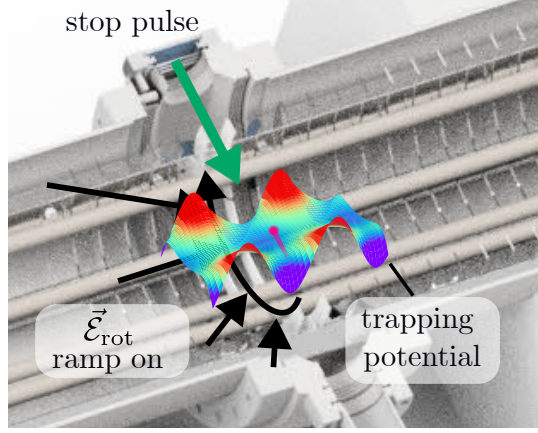


Figure 2.12: Illustration of the experimental procedure for stopping and trapping the ions.

Immediately after ionization, a large electric field is applied in the direction in which the ions are coming from, which slows the ions to a velocity distribution that can be trapped. The pulse is roughly 5.3 V/cm for 4.1  $\mu\text{s}$  (though the actual energy delivered to the ions is obscured by inhomogeneity of the field and rise time of the electrode drivers).

At the same time, the trapping potentials are turned on so that once the ions are slowed they are immediately trapped. The trapping potentials are discussed in Section 4.1.3

Finally, the rotating polarizing field  $\mathcal{E}_{\text{rot}}$  is ramped up over 1.2 ms, a time such that the ramp is adiabatic with respect to the rotation of the field ( $\frac{1}{\omega_{\text{rot}}} = \frac{1}{150 \text{ kHz}} \approx 7 \mu\text{s} \ll 1.2 \text{ ms}$ ). The details on generating the polarizing field are covered in Section 4.1.4.

Once the molecules are polarized, they can be pumped into the eEDM-sensitive states with lasers and microwaves through four of the viewports of the vacuum chamber, as shown in Figure 2.13. The details of optical pumping are described in Section 3.2.

With the proper initial quantum state prepared, we can execute the Ramsey sequence. This is shown in Figure 2.14. First, we apply the  $\pi/2$  pulse by momentarily ramping down the polarizing field such that the hyperfine states become degenerate. Next, during the Ramsey evolution, the trapping potentials are modulated to translate the ions down the trap into a region where the trap is cryogenically cooled and the ions are shielded from room-temperature blackbody radiation. At

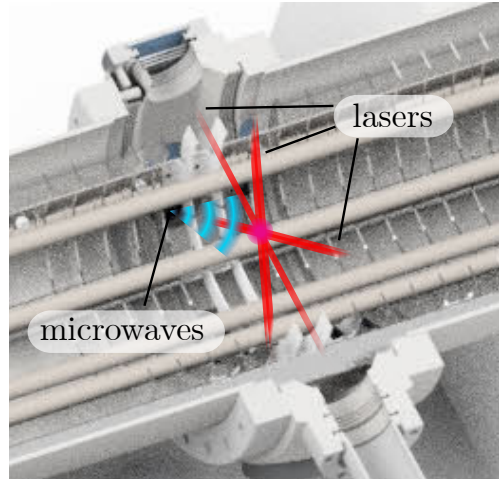


Figure 2.13: Illustration of the experimental procedure for optically pumping them into the eEDM-sensitive states.

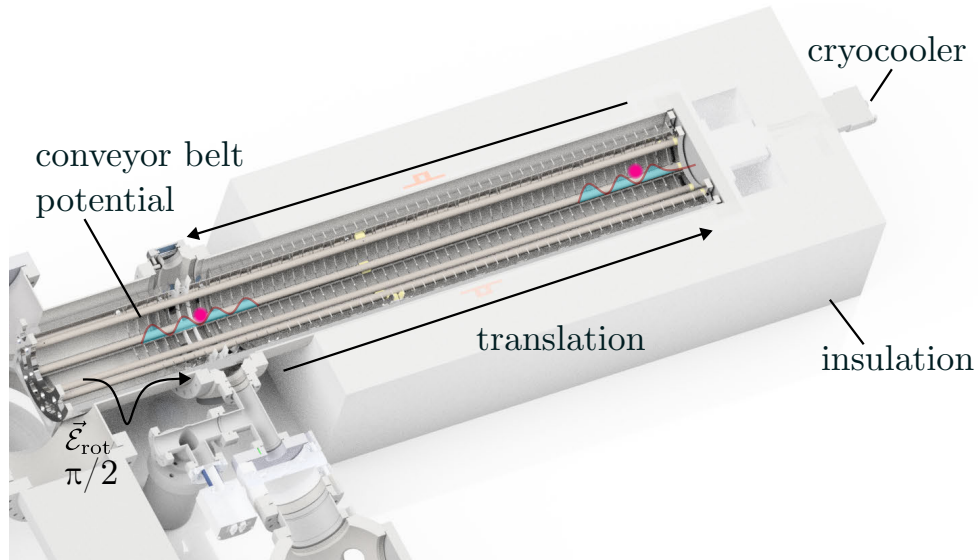


Figure 2.14: Illustration of the Ramsey evolution period of the experiment.

the end of the Ramsey evolution time, the ions are shuttled back and given another  $\pi/2$  pulse. More details on the  $\pi/2$  pulse and blackbody radiation can be found in Ng's thesis [39].

Finally, the state can be read out, as shown in Figure 2.15. The ions are state-selectively photo-dissociated (details in Section 6.1), while the trapping fields are turned off and  $\mathcal{E}_{\text{rot}}$  is ramped down to zero. A strong electric field in the direction of the detector (4.9 V/cm for 20  $\mu\text{s}$ ) is then pulsed in order to kick the ions onto the detector. The dissociated  $\text{Th}^+$  ions as well as the

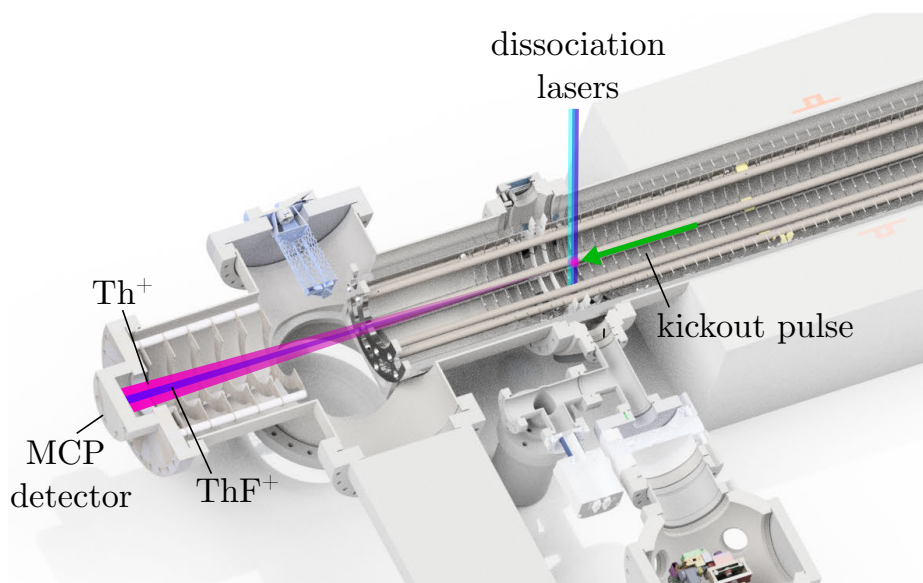


Figure 2.15: Illustration of the state detection sequence of the experiment.

undissociated  $\text{ThF}^+$  ions then arrive on the detector where they are imaged. Details of the detection scheme are provided in Section 6.2.

The chapters that follow will describe the details of each of these steps as well as the instrumentation that was designed and built to actualize each step.

## Chapter 3

### State preparation

#### 3.1 Ionization

The neutral ThF atoms are ionized in a process called resonance-enhanced multi-photon ionization (REMPI). An energy level diagram for this process is shown in Figure 3.1.

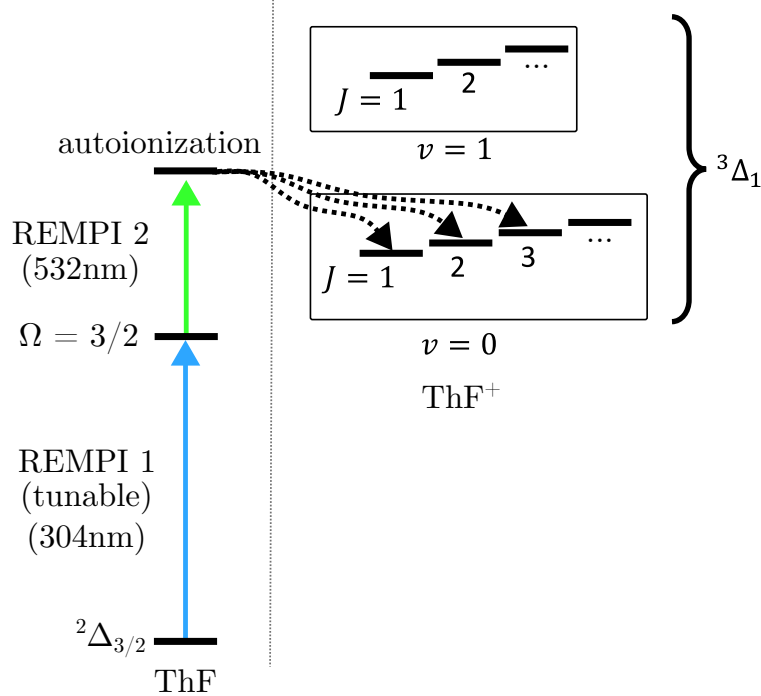


Figure 3.1: Diagram of the two photon ionization process

The first laser, denoted REMPI 1, pumps the neutral ThF into an intermediate state, then a second laser labeled REMPI 2 excites the atoms above the ionization threshold. Ionizing through an intermediate state of ThF allows the ionization to be state-selective, only ionizing the ground

state atoms of ThF and leaving the atoms with a well-defined energy, which is just barely above the ground state of ThF<sup>+</sup>. This means that when we ionize, we only populate the ground electronic (<sup>3</sup>Δ<sub>1</sub>) and vibrational ( $v = 0$ ) state. The energy resolution is not fine enough to select the ground rotational or hyperfine states, so we populate a mixture of  $m_F$  and  $J$  levels within <sup>3</sup>Δ<sub>1</sub>,  $v = 0$ .

The REMPI1 photon is provided by a Lioptec LiopStar dye laser, while the REMPI2 photon is provided by a Quanta-Ray INDI-40-10 pulsed Nd:YAG laser (the 532 nm light from the Quanta-Ray also pumps the Lioptec dye laser).

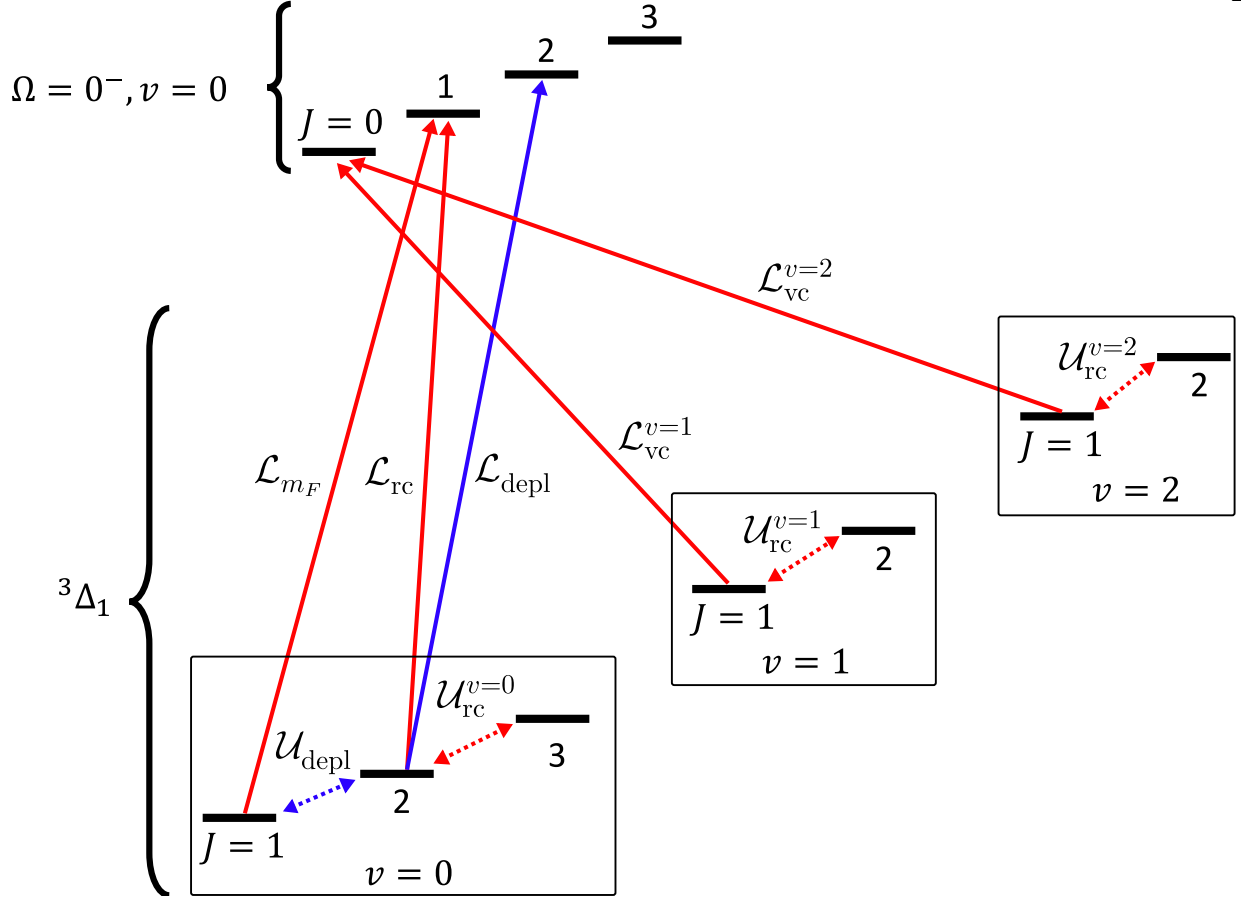
### 3.2 Optical pumping

After the ThF<sup>+</sup> ions are prepared into the <sup>3</sup>Δ<sub>1</sub>,  $v = 0$  manifold, we then optically pump them into the  $J = 0$ ,  $m_F = \pm 3/2$  states. The lasers used to do this are shown in Figure 3.2.

Each higher vibrational state is optically pumped with lasers labeled “vibrational cleanup” to a higher  $\Omega = 0$ ,  $v = 0$  state, which then decays among the vibrational levels of <sup>3</sup>Δ<sub>1</sub>. Higher rotational states within these vibrational states are coupled to the  $J = 1$  state that the respective laser talks to using microwaves, labeled “rotational cleanup.” These frequency of these microwaves are swept to address all the hyperfine transitions in the vibrational manifold. Together these lasers and microwaves close all the transitions to the next two higher vibrational states of <sup>3</sup>Δ<sub>1</sub> (the Honl-London factors are such that the  $v = 3$  and above levels are not populated).

Similarly, the higher rotational states of  $v = 0$  are closed with  $\mathcal{L}_{rc}$  and  $\mathcal{U}_{rc}^{v=0}$ .

The two remaining sets of photons are meant to move population within the  $v = 0$ ,  $J = 1$  state. In order to deplete one of the two doublets,  $\mathcal{U}_{depl}$  couples the upper or lower doublet to  $v = 0$ ,  $J = 2$ , where  $\mathcal{L}_{depl}$  then shelves it to a higher rotational state. After some time this moves the population from the doublet of interest into higher rotational levels of <sup>3</sup>Δ<sub>1</sub> which cannot decay back into  $v = 0$ ,  $J = 1$ . This way a single doublet within  $J = 1$  has been moved to other metastable states, and the population of the remaining doublet can be read out directly by reading out population in  $J = 1$ . Finally,  $\mathcal{L}_{m_F}$  is designed to move population into either  $m_F = 3/2$  or  $m_F = -3/2$ . A diagram of how this works is shown in Figure 3.3.



Label	Description	Wavelength/Frequency	Polarization	Power	See Fig.
$\mathcal{L}_{m_F}$	$m_F$ pumping	685.4436371(43) nm	circular	3 mW*	3.8
$\mathcal{L}_{rc}$	rotational cleanup	685.489059(1) nm	linear (z)	80 mW	
$\mathcal{U}_{rc}^{v=0}$	rotational cleanup	43.627-43.667 GHz swept	linear (z)	-10 dBm	
$\mathcal{L}_{vc}^{v=1}$	vibrational cleanup	717.591265(27) nm	linear (z)	15 mW	3.9
$\mathcal{U}_{rc}^{v=1}$	rotational cleanup	28.81-28.90 GHz swept	linear (z)	-10 dBm	3.17
$\mathcal{L}_{vc}^{v=2}$	vibrational cleanup	752.658792(10) nm	linear (z)	30 mW	3.10
$\mathcal{U}_{rc}^{v=2}$	rotational cleanup	28.94-28.98 GHz swept	linear (z)	-10 dBm	3.19
$\mathcal{U}_{depl}$	depletion	$\begin{cases} 29.115642(57) & \text{lower} \\ 29.082823(29) & \text{upper} \end{cases}$	linear (z)	-21 dBm	3.16
$\mathcal{L}_{depl}$	depletion	685.38160(1) nm	linear (z)	25 mW	

Figure 3.2: Lasers and microwaves for state manipulation. Red indicates photons for optical pumping, while blue indicates photons for depletion, with solid lines representing optical transitions and dashed lines representing microwave transitions. The powers are given as light going into the chamber for optical transitions, and power going into the microwave horn for microwave transitions (the power inside the chamber has never been empirically measured and relies on the calculations in Section 3.2.3.2). Each laser is shaped to have a Gaussian beam width ( $1\sigma$ ) of roughly 2.5 mm to match the spatial extent of the ion cloud.

\*  $\mathcal{L}_{m_F}$  is strobed, so the typical power given here corresponds to a duty cycle of 0.5%, i.e. the peak power of the laser is  $\sim 600$  mW.



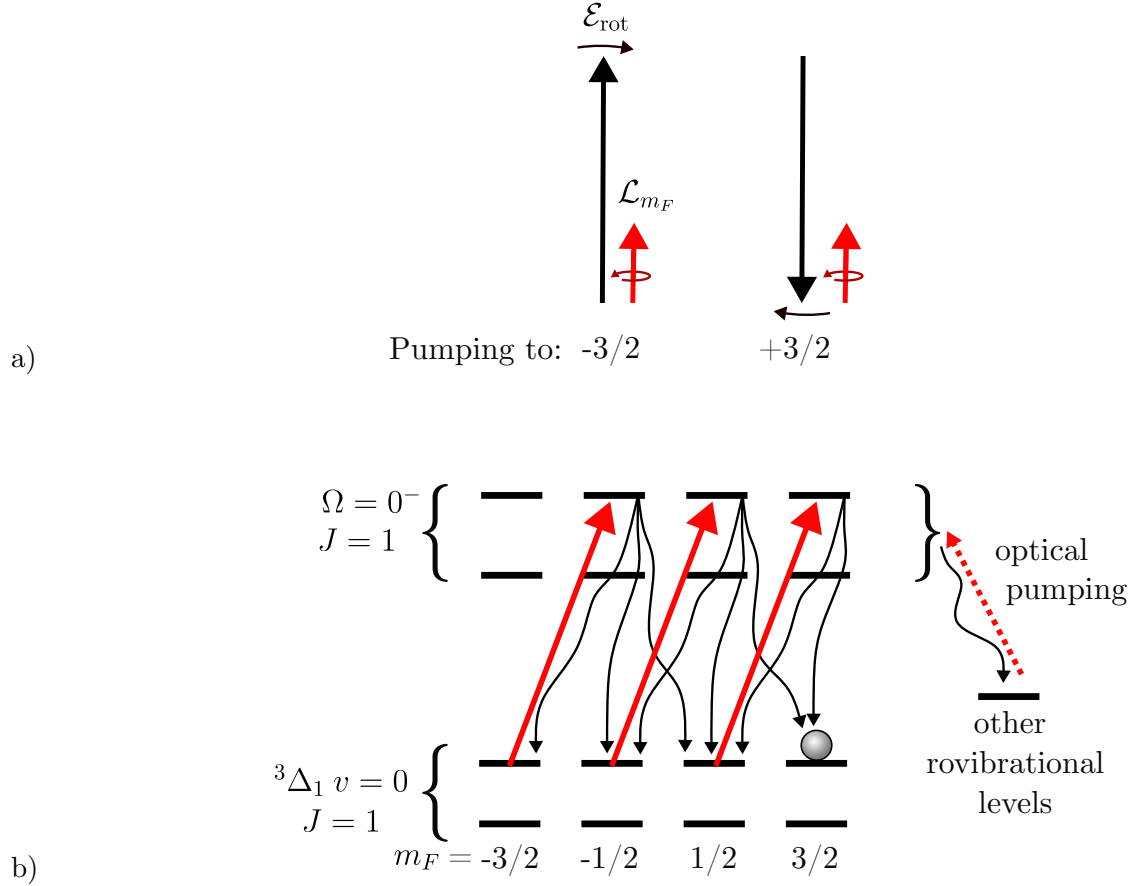


Figure 3.3: The  $m_F$  pumping scheme using  $\mathcal{L}_{m_F}$ .

**a)**  $\mathcal{L}_{m_F}$  is circularly polarized, and is strobed so that it is only on when it is either aligned (left) or anti-aligned (right) to the quantization axis defined by  $\mathcal{E}_{\text{rot}}$  (each pulse of light is only 0.5% of one cycle of  $\mathcal{E}_{\text{rot}}$ ). This way each photon absorbed gives a well defined quanta of angular momentum along the quantization axis. The pulsing of  $\mathcal{L}_{m_F}$  is done by sending the laser tightly focused through an acousto-optic modulator (AOM), so the laser can be turned on and off on a  $\sim 10$  ns timescale with an RF switch on the input signal to the AOM. The pulse is then aligned to the correct phase of  $\mathcal{E}_{\text{rot}}$  empirically by scanning the timing and looking at population distributions. Note that the chirality of  $\mathcal{L}_{m_F}$  was never actually measured, so an ambiguity exists with respect to which side we pump to for a given alignment, i.e. the labels for this depiction could be reversed.

**b)** Energy level diagram of how pumping to  $m_F = +3/2$  works. Because each photon absorbed increases the angular momentum by 1, absorbing a photon moves to the right. Even though each intermediate state can decay with  $\Delta m_F = \{-1, 0, +1\}$ , the total angular momentum change from absorption and spontaneous emission is between 0 and +2, so they cannot move to the left and on average they move to the right. While these states can also fall to other rotational and vibrational levels, these are closed with the optical pumping photons discussed above. Thus if  $\mathcal{L}_{m_F}$  and optical pumping photons are on for long enough, population will eventually land in  $m_F = +3/2$ . Pumping to  $m_F = -3/2$  works exactly the same way, but with each photon taking away one angular momentum.

### 3.2.1 Continuous wave laser overview

Optical pumping is done with low power (tens of mW) continuous wave lasers in the red part of the visible spectrum. Historically these lasers have been external cavity diode lasers (ECDLs) fabricated by the JILA instrument shop, however many have been switched to fiber lasers or commercial ECDLs in order to achieve higher power and stability. The currently used optical pumping lasers are listed in Table 3.1.

Photon	Description	Manufacturer	Model
$\mathcal{L}_{m_F}$	Fiber laser	Precilaser	PL202106532
$\mathcal{L}_{rc}$	Fiber laser	Precilaser	PL202106533
$\mathcal{L}_{depl}$	JILA ECDL Diode	Thorlabs	HL6750MG
$\mathcal{L}_{depl}$	JILA TA	Toptica Eagleyard	RLS/680NM-TA-250MW
$\mathcal{L}_{vc}^{v=1}$	JILA ECDL Diode	Toptica	LD-0725-0040-AR-1
$\mathcal{L}_{vc}^{v=2}$	Commercial ECDL	Toptica	DL-pro

Table 3.1: Model numbers for each component of the optical pumping laser system

The complete optical pumping system, highlighting the layout of the JILA ECDLs, is shown in Figure 3.4. The physical layout of one such JILA ECDL is shown in Figure 3.5. It functions as follows: The cavity is defined between the back of the diode and the first order diffraction off the grating. The supported wavelength of the cavity can be tuned by adjusting the angle of the grating. The grating is mounted on a kinematic mount with a piezoelectric crystal in the horizontal axis, allowing fine control of the wavelength to be done electronically. To prevent parasitic lasing modes, the diodes are anti-reflection coated to prevent a cavity from forming between the two surfaces of the diode. For stability purposes, the temperature of both the diode and the cavity are fixed using a thermoelectric cooler (TEC) and a thermistor. TEC 1 controls the temperature of the laser diode, whereas TEC 2 stabilizes the temperature of the aluminum enclosure on which the diode and grating are mounted, preventing cavity length drifts due to thermal expansion. The whole system is mounted on a large block of aluminum which stabilizes the temperature and acts as a thermal reservoir for the temperature feedback system.

The light then leaves the ECDL enclosure and passes through an optical isolator to prevent

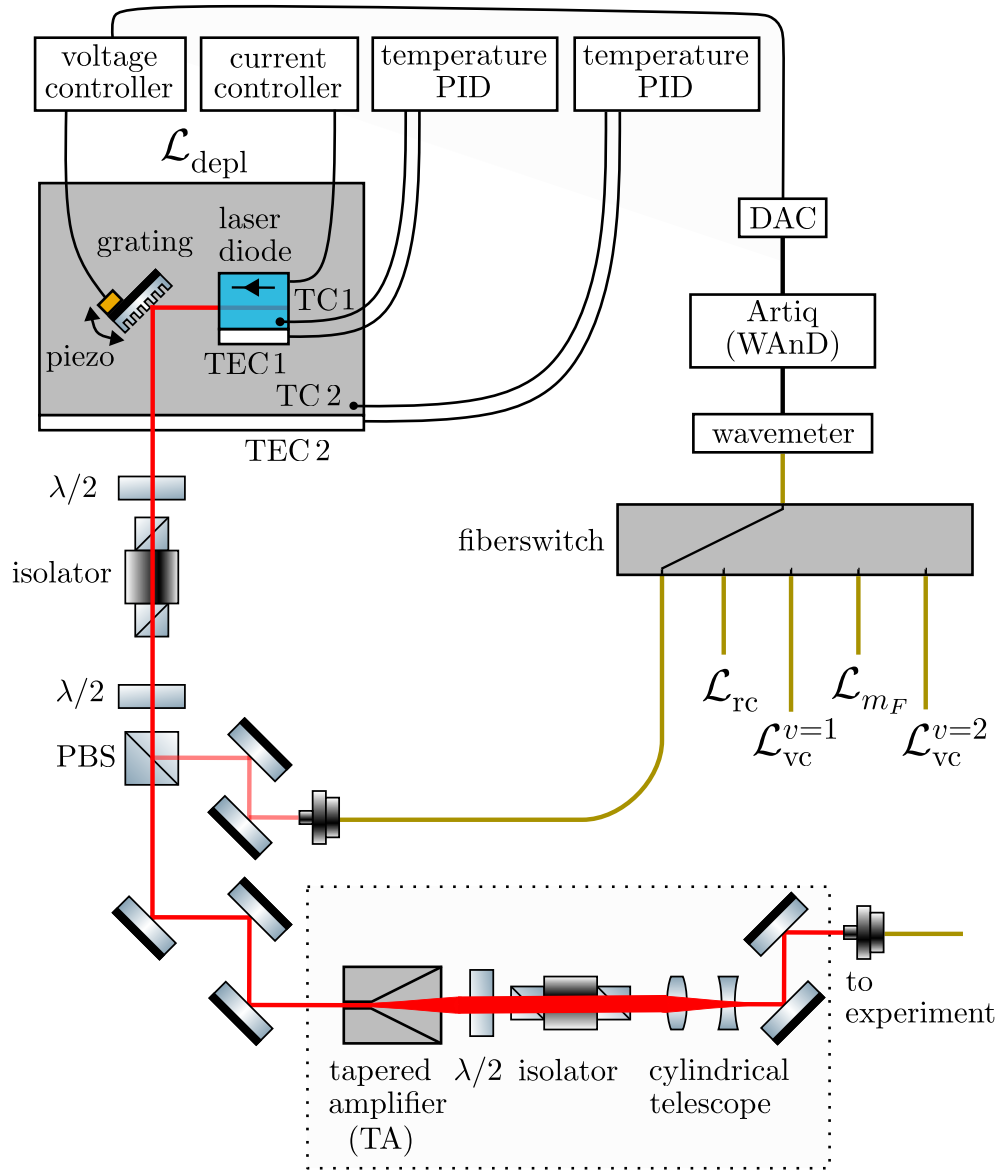


Figure 3.4: Optical pumping laser system configuration. Shown is a JILA ECDL and TA pair, as well as the frequency locking configuration. The fiber switch is a DiCon MEMS 1xN switch and the wavemeter is a HighFinesse WS-7.

reflections from damaging the laser diode. Some light is then picked off and sent to a fiber switch, which forwards it to a wavemeter for spectral measurement. When the laser is locked, python will extract the frequency from the wavemeter, and feed back the difference from the desired frequency to a voltage on the piezo.

The rate at which the frequency is sampled and the feedback signal is updated is limited by

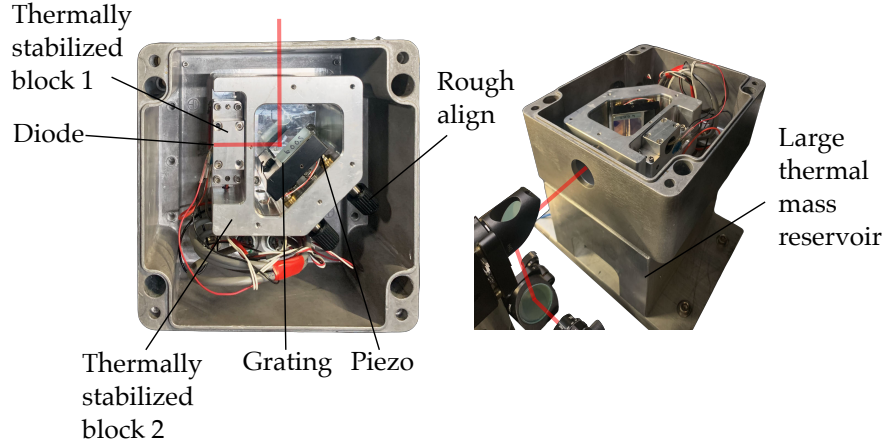


Figure 3.5: Photos of the JILA ECDL assembly with the lids removed.

the speed of the fiber switch. While all continuous wave lasers are being locked at once, each laser is sampled approximately once per second, which is sufficient to compensate for slow thermo/mechanical fluctuations. With this system each laser is stable to within  $\sim 5$  MHz.

### 3.2.2 Rb reference

In order to reference the lasers to an absolute frequency standard, we lock a laser to an atomic transition in Rubidium in a vapor cell. Then the wavemeter can be calibrated to the known energy of this transition, thereby calibrating the wavemeter’s measurements of all other lasers. A diagram of the setup is shown in Figure 3.6.

This technique, known as “saturated absorption spectroscopy” or “Doppler-free spectroscopy” makes use of two counter-propagating laser beams such that the signal corresponds to light that is resonant in both directions, allowing us to resolve beyond the Doppler width. This is necessary because the one-sigma Doppler width of the transition, given by

$$\Delta f = \sqrt{\frac{kT}{mc^2}} f_0, \quad (3.1)$$

is  $\sim 200$  MHz for red light on room temperature rubidium atoms, and we want to lock the lasers to the  $\sim 1$  MHz level.

The technique works as follows: a high-power pump beam is sent one way through the Rb

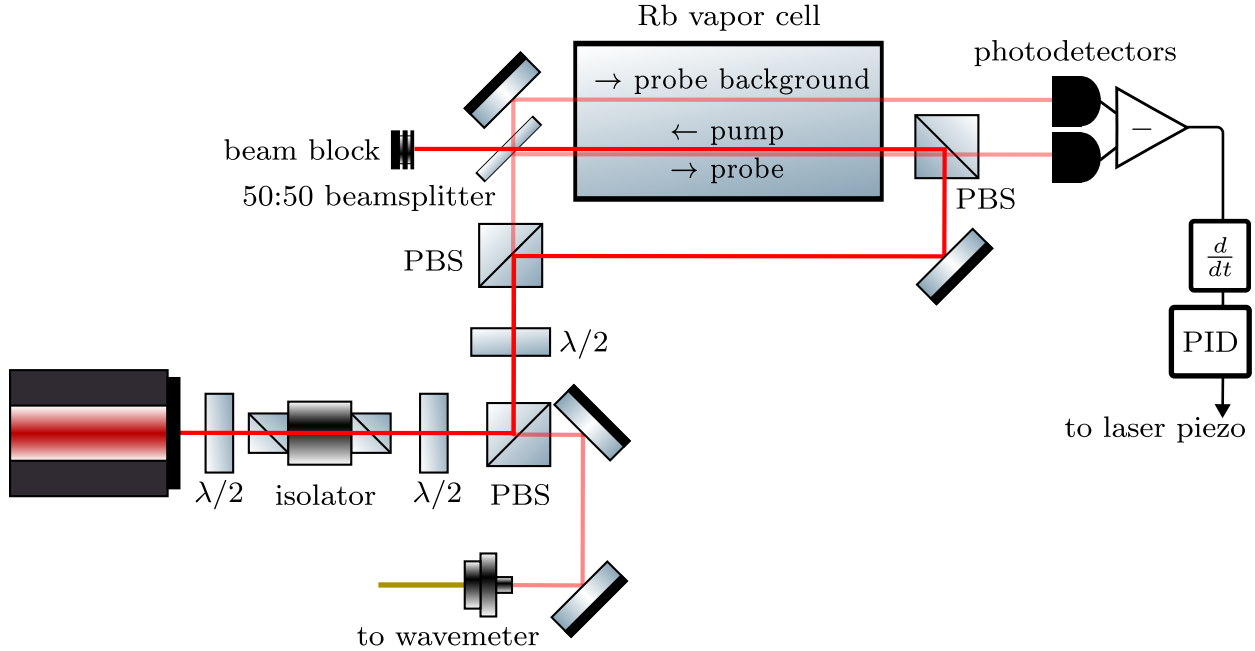


Figure 3.6: Optical setup for locking the reference laser to the Rb line.

vapor cell, and a weak probe beam is sent collinearly the other direction and onto a photodetector. When the pump beam is on resonance for a transition in the Rb, it saturates the transition, so the probe beam is not absorbed, leading to a spike in the transmission of the pump beam.

When we scan the laser frequency (by scanning the voltage on the piezo controlling the grating of the ECDL), the resulting signal looks like a broad Doppler absorption dip with local saturation-induced transparencies at each individual transition. A copy of the probe beam with no pump is also sent through the vapor cell, which captures only the broad Doppler absorption dip. The two signal can then be subtracted, leaving only the Doppler-free peaks. The results are shown in Figure 3.7.

The laser is locked to the ( $5^2S_{1/2} \rightarrow 5^2P_{3/2}$ ) transition of  $^{87}\text{Rb}$ , from  $F=2$  to halfway between  $F'=2$  and  $F'=3$  in a so called “crossover transition”. This transition has an energy of  $384.2279818773(55)$  THz [52]. Crossover transitions occur when the atoms are moving at a velocity such that the Doppler shift is exactly half the spacing between two atom-frame transitions. This way the atom sees each beam as addressing one of the two separate transitions, which still results

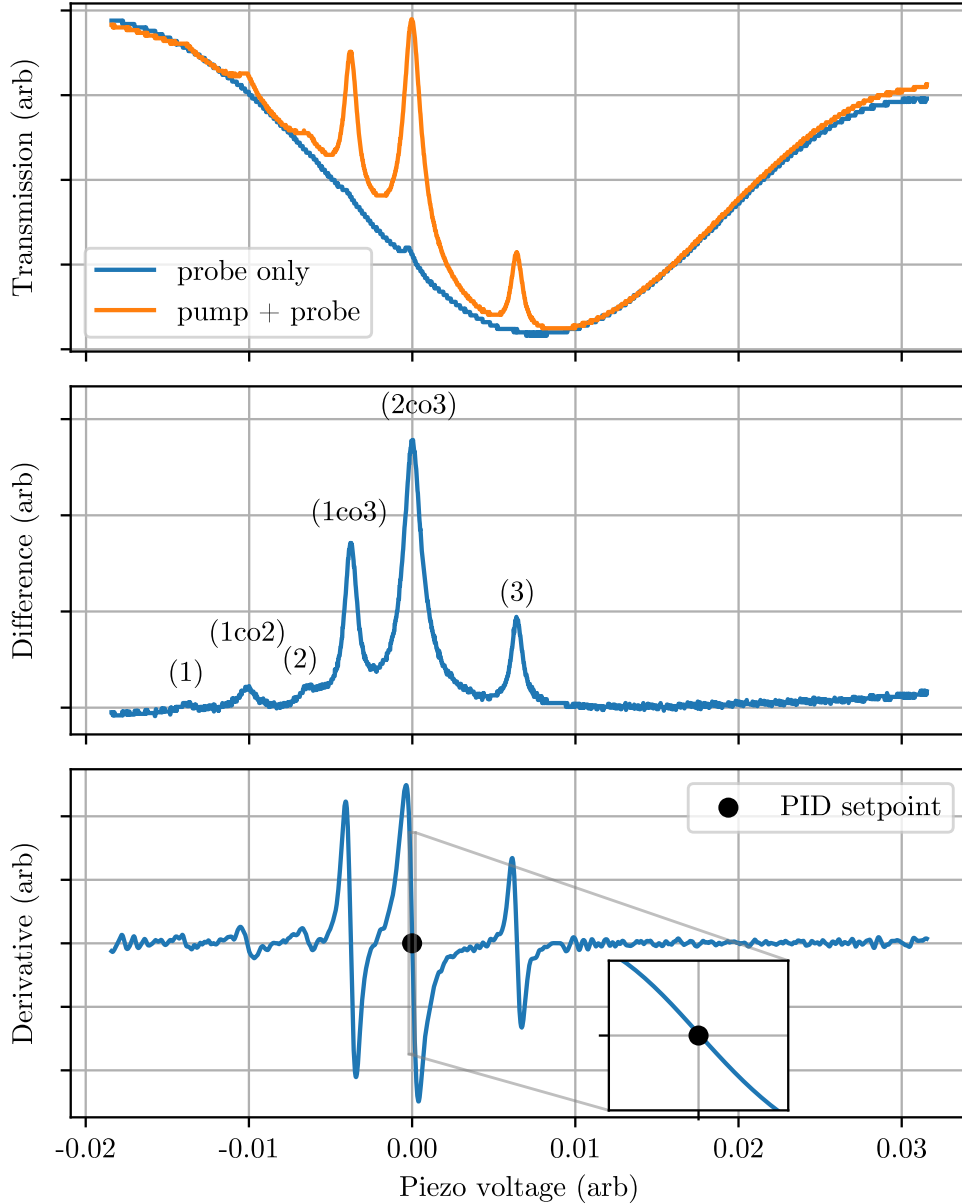


Figure 3.7: Spectroscopy of the  $\text{Rb}^{87}$   $F=2$  line used to calibrate the wavemeter. Top: the raw photodiode signals of the two beam paths. Middle: the difference of the two photodiode signals. Each peak is labeled with the  $F$  to which the transition goes, with ‘co’ indicating a crossover between two transitions. Bottom: the derivative of the difference signal, which is used to lock the laser. The zero crossing corresponding to the peak of the  $(2\text{co}3)$  line is used, with the derivative providing a signed linear feedback signal which can be used to lock the frequency of the laser.

in transparency of the atoms to the probe beam as the atoms are pumped out of  $F = 2$ . Generally, these crossover transitions are stronger than the Doppler free transitions because of the thermal

distribution of atoms in the vapor cell (there are more atoms with the crossover-inducing velocity in the axis of the beams than atoms with no velocity in the axis of the beams).

Because the crossover transition between  $F' = 2$  and  $F' = 3$  is the most predominant feature, it is the most stable feature to lock to so we lock the laser to this transition. The lock is done with electronics that produce a small dither on the piezo voltage, and takes the time derivative of the Doppler-free signal. Because the derivative should go to zero at the peak, the derivative can be used as a signed feedback, which goes into a PID to control the central piezo voltage. In this way, the laser can be locked to within  $\sim 1$  MHz, providing a stable absolute frequency reference to which we can calibrate the wavemeter.

### 3.2.2.1 Spectroscopy of optical pumping transitions

We can measure the energy of the optical transitions by reading off the population in the states that each laser addresses using techniques described in Chapter 6. We can then scan the frequency of the laser, with the population of the state decreasing when the laser is on resonance.

First we measure the frequency of the  $\mathcal{L}_{m_F}$  transition. If we were to measure the frequency of the transition with the polarizing field  $\mathcal{E}_{\text{rot}}$ , the large Doppler shift caused by the rotation of the ions would significantly broaden the transition (to beyond the free spectral range of the ECDL, meaning it couldn't be measured in a single scan), as well as shift the center frequency if the timing of the pulse is off. For this reason we measure the frequency of this transition in the absence of  $\mathcal{E}_{\text{rot}}$ . We can then simply look at the dip in population in  $v = 0$ ,  $J = 1$  when the laser is turned on. This is done in Figure 3.8.

The width of the Gaussian fits to 106.8(3.4) MHz. This apparent linewidth is predominantly due to the Doppler shift from the micromotion of the ions, rather than from a Doppler width corresponding to the temperature of the secular motion, a natural linewidth of the transition, or the width corresponding to the stability of the laser ( $\sim 5$  MHz).

We repeat this measurement for  $\mathcal{L}_{\text{vc}}^{v=1}$  and  $\mathcal{L}_{\text{vc}}^{v=2}$  in Figures 3.9 and 3.10 respectively.

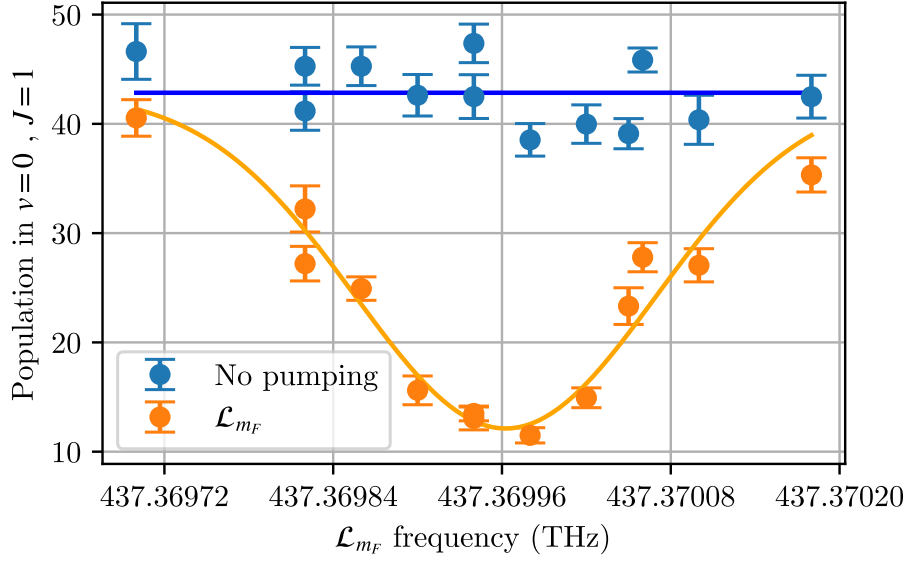


Figure 3.8: Frequency scan of the  $\mathcal{L}_{m_F}$  laser with no  $\mathcal{E}_{\text{rot}}$ . Population in  $v = 0, J = 1$  is read out by dissociating from the  $(^3\Delta_1, v = 0, J = 1) \rightarrow (\Omega = 0, J = 2)$  transition measured in Figure 6.3. The dip in population is fit to a Gaussian, which yields a center frequency of 437.3699627(27) THz or a vacuum wavelength of 685.4436371(43) nm.

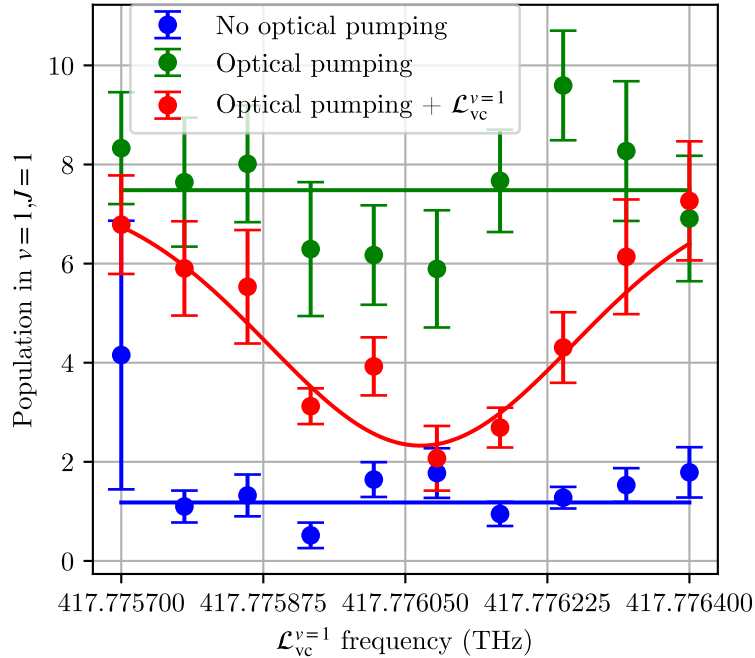


Figure 3.9: Frequency scan of the  $\mathcal{L}_{\text{vc}}^{v=1}$  laser with no  $\mathcal{E}_{\text{rot}}$ . Population in  $v = 1, J = 1$  is read out by dissociating via the  $(^3\Delta_1, v = 1, J = 1) \rightarrow (\Omega = 0, J = 2)$  transition measured in Figure 6.4. The Gaussian dip fits to a frequency of 417.776069(16) THz or a vacuum wavelength of 717.591265(27) nm.



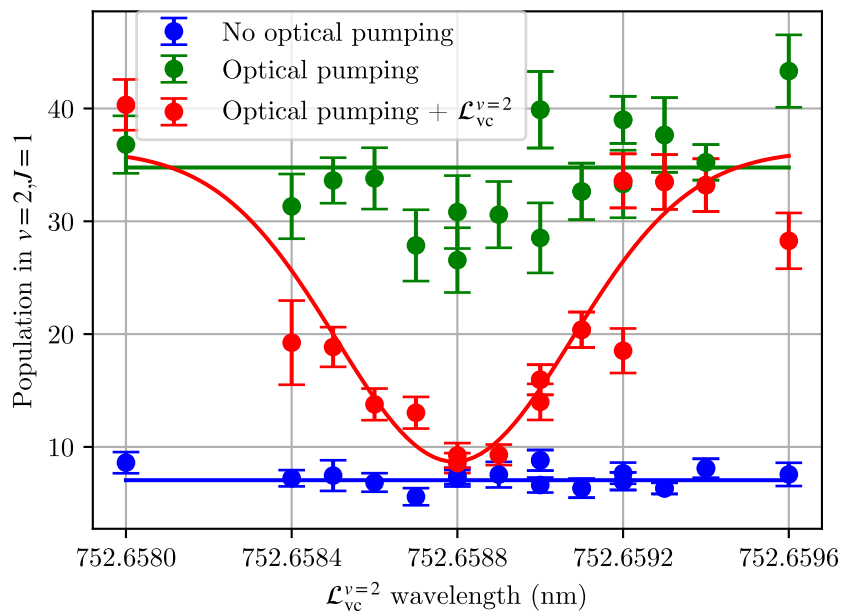


Figure 3.10: Frequency scan of the  $\mathcal{L}_{vc}^{v=2}$  laser with no  $\mathcal{E}_{rot}$ . Population in  $v = 2, J = 1$  is read out by dissociating from the  $(^3\Delta_1, v = 2, J = 1) \rightarrow (\Omega = 2, J = 2)$  transition measured in Figure 6.5. The Gaussian dip fits to a frequency of 398.311241(05) THz or a vacuum wavelength of 752.658792(10) nm.

### 3.2.3 Microwaves

#### 3.2.3.1 Theory

To predict the microwave transition rates, we begin with a model of the microwave-molecule interactions. We can use a Jaynes-Cummings model Hamiltonian, which is nice because it is physically intuitive and time-independent, meaning that it's mathematically simple to work with and we don't have to do any work doing a rotating wave approximation to get out the dynamics of the system (since this approximation is already built in to the Jaynes-Cummings model).

The Jaynes-Cummings Hamiltonian for the molecule and light field are given by

$$H = H_{\text{molecule}} + H_{\text{light}} + H_{\text{interaction}} \quad (3.2)$$

$$= \frac{1}{2}\hbar\omega_0\hat{\sigma}_z + \hbar\omega(\hat{a}^\dagger\hat{a} + \frac{1}{2}) + \hbar g(\hat{\sigma}_+\hat{a} + \hat{a}^\dagger\hat{\sigma}_-). \quad (3.3)$$

In the first term,  $\hbar\omega_0$  is the energy spacing between the two unperturbed molecular states. This represents the energy of the molecule with an offset to symmetrize the matrix. In the second term,  $\omega$  is the frequency of the applied light and  $\hat{a}^\dagger$  and  $\hat{a}$  are the photon creation and annihilation operators. This term represents the energy of all the photons =  $\hbar\omega(n + 1/2)$ . The third term represents the interaction whereby a photon can be annihilated and the molecule excited or a photon can be created and the molecule de-excited. The coupling strength of the interaction is characterized by  $g$ , the vacuum Rabi rate given by

$$g = \frac{\vec{d} \cdot \hat{E}}{\hbar} \sqrt{\frac{\hbar\omega}{2\epsilon_0 V}} = \frac{q \langle g | \vec{r} | e \rangle \cdot \hat{E}}{\hbar} \sqrt{\frac{\hbar\omega}{2\epsilon_0 V}}, \quad (3.4)$$

where  $V$  is the volume of the cavity mode,  $q$  is the electron charge,  $\hat{E}$  is the unit vector indicating the polarization of the light, and  $\vec{d}$  is the dipole transition matrix element of the molecular transition, with  $|g\rangle$  and  $|e\rangle$  being the lower and excited states of the molecular transition. Since the microwaves are not actually in a cavity, it's more instructive to write the interaction part of the Hamiltonian semi-classically.

First, recognize that the only two relevant combined photon-molecule states are  $|n, e\rangle$  and  $|n + 1, g\rangle$ , where  $n$  is the number of microwave photons which is arbitrarily large, and  $e$  and  $g$

reference the excited and ground states of the molecule. In this basis, we can write the interaction Hamiltonian as

$$H_{\text{interaction}} = \hbar g \begin{bmatrix} 0 & \sqrt{n} \\ \sqrt{n} & 0 \end{bmatrix}. \quad (3.5)$$

In this basis, the whole Hamiltonian is then

$$H = \frac{1}{2} \hbar \omega_0 \begin{bmatrix} 1 & 0 \\ 0 & -1 \end{bmatrix} + \hbar \omega \left( \begin{bmatrix} n & 0 \\ 0 & n+1 \end{bmatrix} + \frac{1}{2} \right) + \hbar g \begin{bmatrix} 0 & \sqrt{n} \\ \sqrt{n} & 0 \end{bmatrix}. \quad (3.6)$$

To get from terms that depend on the cavity properties and the number of photons to terms that depend only on the classical field strength, we can treat the microwave field in some finite volume  $V$  as light in a cavity. We can then calculate the energy in this volume due to the classical field and compare this to the photon energy in order to solve for the number of photons  $n$ :

$$n \hbar \omega = \int_V \frac{1}{2} \epsilon_0 |E|^2 d^3 r = \frac{1}{2} \epsilon_0 |E_0|^2 V. \quad (3.7)$$

Then we can write

$$g \sqrt{n} = g \sqrt{\frac{1}{2 \hbar \omega} \epsilon_0 |E|^2 V} = \frac{q \langle g | \vec{r} | e \rangle \cdot \hat{E}}{\hbar} \sqrt{\frac{\hbar \omega}{2 \epsilon_0 V}} \sqrt{\frac{1}{2 \hbar \omega} \epsilon_0 |E_0|^2 V} = \frac{1}{2} \frac{q \langle g | \vec{r} | e \rangle \cdot \vec{E}}{\hbar}, \quad (3.8)$$

and we have recovered the classical Rabi rate

$$\Omega \equiv \frac{q \langle g | \vec{r} | e \rangle \cdot \vec{E}}{\hbar}. \quad (3.9)$$

Knowing that  $g \sqrt{n} = \Omega/2$ , we can write the Hamiltonian as

$$H = \frac{1}{2} \hbar \omega_0 \begin{bmatrix} 1 & 0 \\ 0 & -1 \end{bmatrix} + \hbar \omega \left( \begin{bmatrix} n & 0 \\ 0 & n+1 \end{bmatrix} + \frac{1}{2} \right) + \hbar \Omega \begin{bmatrix} 0 & \frac{1}{2} \\ \frac{1}{2} & 0 \end{bmatrix}. \quad (3.10)$$

We now have a Hamiltonian in which the diagonal components describe the combined energies of the molecule and a photon that would be absorbed or emitted to transfer molecular states in a second quantization framework, and the off-diagonal components are semi-classical field couplings. This representation allows both physical intuition of all parts as well as mathematical simplicity.

Since the dynamics of the system are invariant to overall energy shifts, we can add a constant to the Hamiltonian. If we add  $-\hbar\omega(n + \frac{1}{2})$ , the light field energy term simplifies to a symmetric energy difference of the two states. With this the Hamiltonian becomes fully symmetrized.

$$H = \frac{1}{2}\hbar\omega_0 \begin{bmatrix} 1 & 0 \\ 0 & -1 \end{bmatrix} + \hbar\omega \begin{bmatrix} -\frac{1}{2} & 0 \\ 0 & \frac{1}{2} \end{bmatrix} + \hbar\Omega \begin{bmatrix} 0 & \frac{1}{2} \\ \frac{1}{2} & 0 \end{bmatrix} \quad (3.11)$$

$$= \hbar \begin{bmatrix} -\frac{1}{2}(\omega - \omega_0) & \frac{\Omega}{2} \\ \frac{\Omega}{2} & \frac{1}{2}(\omega - \omega_0) \end{bmatrix} \quad (3.12)$$

$$= \hbar \begin{bmatrix} -\frac{\Delta}{2} & \frac{\Omega}{2} \\ \frac{\Omega}{2} & \frac{\Delta}{2} \end{bmatrix}, \quad (3.13)$$

where  $\Delta$  is the detuning of the light from the resonance  $\Delta \equiv (\omega - \omega_0)$ . If we plot the eigenenergies of this Hamiltonian as a function of the detuning, we observe an avoided crossing, as shown in Figure 3.11.

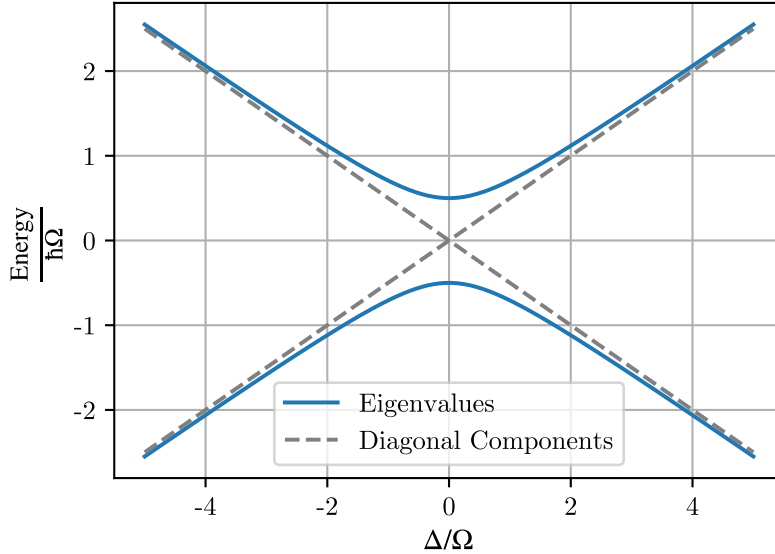


Figure 3.11: Energies of the dressed state Hamiltonian as a function of the detuning  $\Delta$ .

If the microwaves are swept, then the dynamics of the dressed states can be described using the Landau-Zener formulation. The goal of the microwaves is to de-excite the molecule, i.e. population

starting in  $|n, e\rangle$  transfers to  $|n + 1, g\rangle$ . If the microwaves are swept adiabatically, the system will follow the avoided crossings and all population will be transferred. However, if the sweeping of the microwave frequency is diabatic, some population will remain in the molecular excited state. In the Landau-Zener formulation, the probability of not transferring (staying in  $|n, e\rangle$ ) after a single sweep through the resonance is given by [53]

$$P_{e \rightarrow e} = e^{-2\pi \frac{|H_{12}|^2/\hbar}{|\frac{d}{dt}(H_{22}-H_{11})|}}. \quad (3.14)$$

The denominator is simply the sweep rate  $|\frac{d}{dt}\hbar\Delta| = \hbar|\frac{d}{dt}(\omega - \omega_0)| = \hbar|\frac{d\omega}{dt}|$ . The probability of transferring in a single sweep is then given by

$$P_{e \rightarrow g} = 1 - P_{e \rightarrow e} = 1 - e^{-\frac{\pi}{2} \frac{\Omega^2}{|\frac{d\omega}{dt}|}}. \quad (3.15)$$

If the sweep occurs periodically with a period  $T_s$  and sweeps over a frequency range  $\Delta\omega$ , then we can turn this probability into a transition rate (assuming a small portion transferred each sweep and that transferred population is then coupled out of the new state by a laser):

$$\Gamma_\mu = P_{e \rightarrow g}/T_s = \frac{1 - e^{-\frac{\pi}{2} \frac{\Omega^2}{|\Delta\omega/T_s|}}}{T_s}. \quad (3.16)$$

If we plug in the expression for  $\Omega$  from Equation 3.9 and solve for the electric field, we can get the field strength we need to get a desired rate

$$|\vec{E}| = \frac{1}{\left(\langle g | \vec{r} | e \rangle \cdot \hat{E} \right) q} \frac{\hbar}{q} \sqrt{\frac{2 \ln\left(\frac{1}{1 - T_s \Gamma_\mu}\right) \Delta\omega}{\pi T_s}}. \quad (3.17)$$

Calculating the dipole matrix elements  $\langle g | \vec{r} | e \rangle \cdot \hat{E}$  is highly nontrivial and requires some advanced angular momentum algebra, but we can say that it will be of the form

$$|\langle g | \vec{r} | e \rangle| = \frac{1}{q} \vec{d}_{\text{mf}} A_{g,e}, \quad (3.18)$$

where  $q$  is the charge of the electron,  $\vec{d}_{\text{mf}}$  is the molecular frame dipole moment (coming from the electronic configuration  $\langle \psi_{\text{electronic}} | r | \psi_{\text{electronic}} \rangle = d_{\text{mf}}/q$ ), and  $A_{g,e}$  is a dimensionless constant of order unity. We can then write

$$|\vec{E}| = \frac{\hbar}{d_{\text{MF}} A_{g,e}} \sqrt{\frac{2 \ln\left(\frac{1}{1 - T_s \Gamma_\mu}\right) \Delta\omega}{\pi T_s}}. \quad (3.19)$$

### 3.2.3.2 Power requirements

To calculate the required microwave power, we need to know the strength of the microwave field at the ion location for a given power we apply. The microwaves are radiated with a horn through a window in the vacuum chamber. It then passes through the trap electrodes and hits the ion cloud.

A naive calculation of the field strength can be performed using the directivity  $D_{\text{dBi}}$  of the microwave horn measured by the manufacturer. Given that the horn is pointed directly at the ion cloud and is located a distance  $r_{\text{horn}}$  away, the intensity of the electric field seen at the ions is then

$$I = \frac{P_{\text{horn}}}{4\pi r_{\text{horn}}^2} \left(10^{D_{\text{dBi}}/10}\right). \quad (3.20)$$

For our setup, the distance from the horn to the ions when placed against a window of the octagon is  $r_{\text{horn}} = 15\text{cm}$ , and the directivity of the horn is 17.9 dBi. The electric field magnitude is then

$$E_0 = \sqrt{\frac{2I}{c\epsilon_0}} = \sqrt{\frac{P_{\text{horn}}}{2\pi r_{\text{horn}}^2 c\epsilon_0} \left(10^{D_{\text{dBi}}/10}\right)} = \sqrt{\frac{P_{\text{horn}}}{1 \text{ W}}} \cdot 4.05 \text{ V/cm}. \quad (3.21)$$

Because the electrodes are spaced apart by a distance of similar magnitude to the wavelength of the radiation, they can significantly alter the field. For a more accurate calculation the electric field incident on the ions, we can run a finite element model of the geometry of the horn and electrodes. The COMSOL model simulation results are shown in Figure 3.12.

The result of the simulation is that for a power of 1 W into the horn, the electric field amplitude at the ion location is 6 V/cm. The electric field seen at the ions as a function of the power into the horn is thus:

$$E_0 = \sqrt{\frac{P_{\text{horn}}}{1 \text{ W}}} \cdot 6 \text{ V/cm}. \quad (3.22)$$

The result is actually a slight enhancement over the naïve calculation (Equation 3.21) due to the focusing of the field by the rod electrodes.

Another consideration is the loss due to reflection of the microwaves off of the UHV window. We can treat the free space before and after the glass as well as the propagation in the glass itself

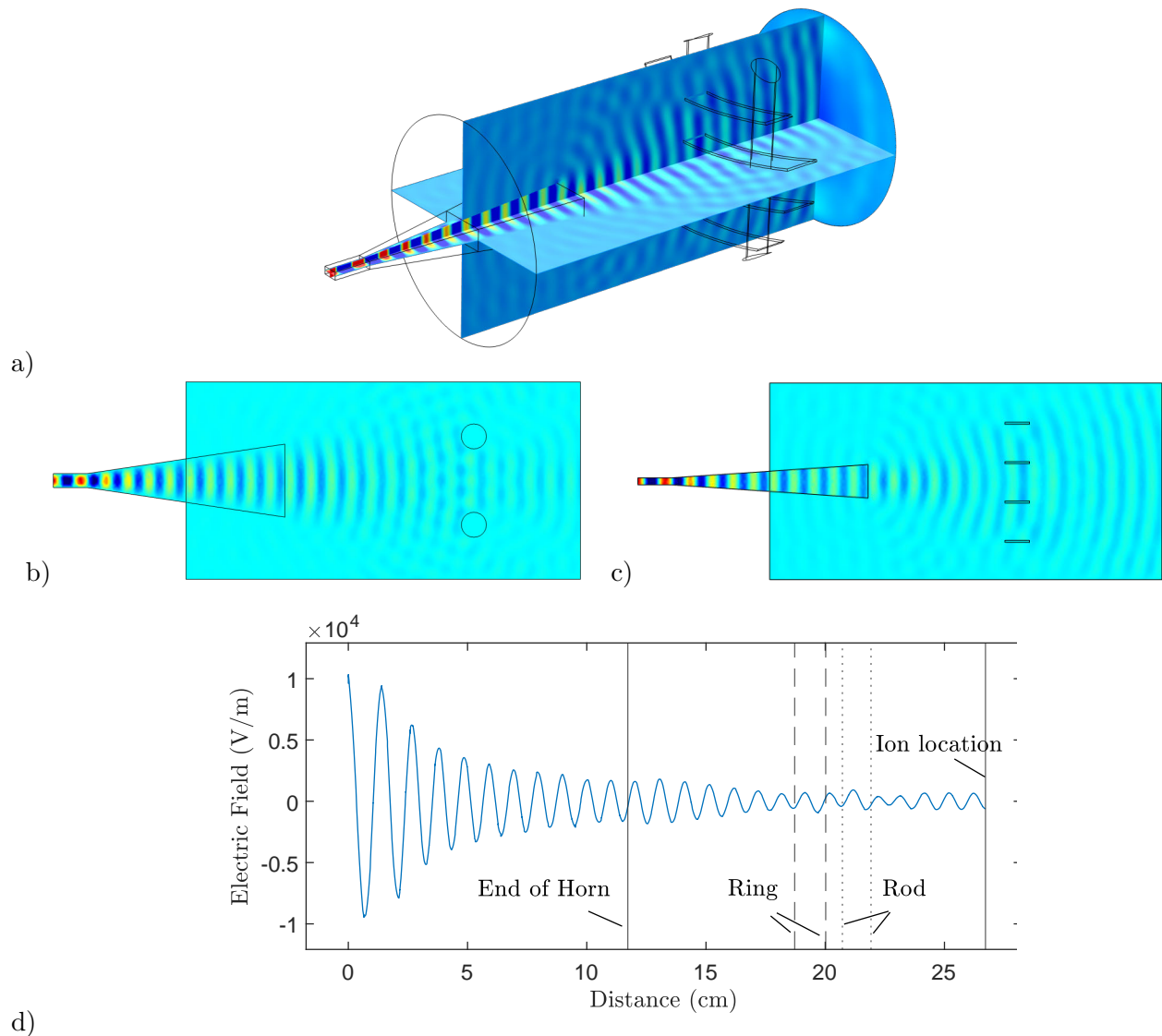


Figure 3.12: Finite element simulations of 30 GHz microwaves exiting the horn and passing through the electrodes

a) 3D view of the COMSOL model.

b) The microwave field in the plane of the rod electrodes. The field is polarized into the page, parallel to the rod electrodes. This means that the field must go to zero near the rod electrodes to satisfy boundary conditions. The result is an interference pattern where the rods cast a "shadow".

c) The microwave field in the plane of the ring electrodes. Since the field is polarized up and down, perpendicular to the ring electrodes, the boundary conditions do not require that the electric field go to zero near these electrodes. As such, the ring electrodes have little effect on the microwave field. However, the boundary conditions do forbid curvature of the field near them since the tangential field must be zero, so we observe a "flattening" of the wavefront near these electrodes.

d) The electric field on the axis of the microwave horn. The origin is the injection port of the horn where the field originates from.

as propagation along a transmission line. The characteristic impedance of the air before and after the glass is given by the free space impedance:

$$Z_0 \equiv \sqrt{\frac{\mu_0}{\epsilon_0}}. \quad (3.23)$$

If the glass has a relative permeability  $\epsilon_r$  at the microwave frequency, the glass has a characteristic impedance

$$Z_{\text{window}} = \sqrt{\frac{\mu_0}{\epsilon_0 \epsilon_r}} = \frac{1}{\sqrt{\epsilon_r}} Z_0. \quad (3.24)$$

The effective impedance of propagation through the glass of thickness  $l$  and then into free space is then given by [54]

$$Z_{\text{prop, interface}} = Z_{\text{window}} \left( \frac{Z_0 + i Z_{\text{window}} \tan(\beta l)}{Z_{\text{window}} + i Z_0 \tan(\beta l)} \right), \quad (3.25)$$

where  $\beta$  is the propagation constant in the glass  $\beta = 2\pi \frac{\sqrt{\epsilon_r} f}{c}$  where  $c$  is the speed of light. Then the reflection coefficient of the light incident on the glass is given by

$$\Gamma = \frac{Z_{\text{prop, interface}} - Z_0}{Z_{\text{prop, interface}} + Z_0}. \quad (3.26)$$

The total power reflected is then

$$P_r = P_0 |\Gamma|^2 = P_0 \frac{(1 - \epsilon_r)^2}{(1 + \epsilon_r)^2 + 4\epsilon_r \cot^2(\beta l)}. \quad (3.27)$$

The vacuum windows are made from fused silica (quartz), which has a relative permittivity of about 3.8 in the Ka band [55]. Using this value we can calculate the power reflected off the glass for varying thicknesses, as shown in Figure 3.13.

Applying this 20% reduction to our COMSOL result of Equation 3.22, we have a prediction for the field seen by the ions as

$$E_0 \approx \sqrt{\frac{P_{\text{horn}}}{1 \text{ W}}} \cdot 5 \text{ V/cm}. \quad (3.28)$$

We can now use Equation 3.19 to calculate the power we need to apply. A good approximation for the coupling constant  $A_{g,e}$  is a Clebsch Gordan coefficient associated with projecting the angular momentum of the initial state and the photon absorbed into the angular momentum of the final state. Since each hyperfine state in the higher rotational state is swept over a transition to all other



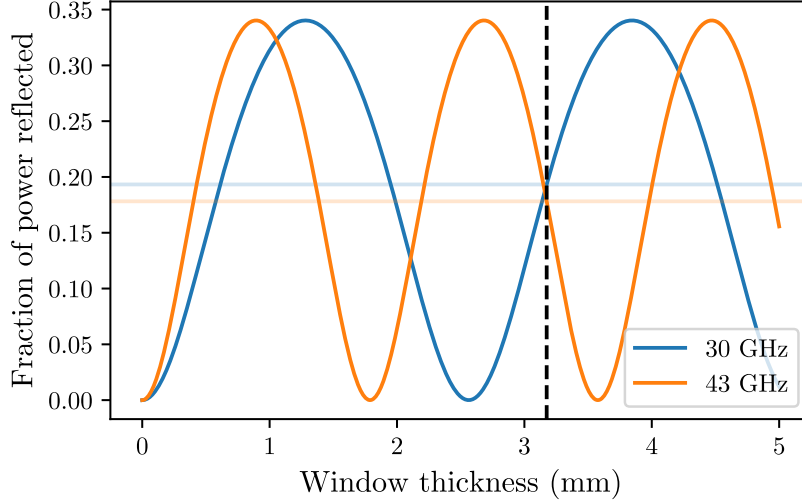


Figure 3.13: The fraction of power reflected off of a glass window of a given thickness, using a relative permittivity of 3.8. The dashed line represents the thickness of the windows used in the experiment.

hyperfine states in the lower rotational stage, the transfer rate out of a specific hyperfine state is at least the rate given by the transition with the highest Clebsch-Gordan coefficient. The total transfer out of the higher rotational state is then limited by the slowest of these maximum rates. Thus taking the minimum over the hyperfine initial states of the maximum over each state it goes to, we can establish a lower bound on the total population transfer rate.

The required microwave powers are shown in Table 3.2.

	Lower doublet	Upper doublet	J = 3 → 2	J = 2 → 1
Frequency (GHz)	29.1038	29.0942	43.6450 (swept)	28.9828 (swept)
Directivity (dBi)	17.92	17.92	21.41	17.90
Limiting CG coefficient	1	1	$\sqrt{10/21}$	$\sqrt{1/2}$
Required electric field (V/cm)	.0075	.0075	.01094	.011
Required $P_{\text{out}}$ (dBm)	-26	-26	-24	-23

Table 3.2: The power required to achieve a microwave coupling rate of  $\Gamma_{\mu} = 200 \text{ s}^{-1}$ , calculated using Equation 3.19 for the electric field, with powers calculated using Equation 3.28 for 30 GHz and a 20% reduced Equation 3.21 for 43 GHz with the relevant directivity.

A microwave coupling rate of  $\Gamma_{\mu} = 200 \text{ s}^{-1}$  is chosen to be fast compared to the fastest relevant spontaneous decay rate ( $\sim 20 \text{ s}^{-1}$ ).

### 3.2.3.3 Microwave sources

A photograph of the setup for generating the microwaves is shown in Figure 3.14.

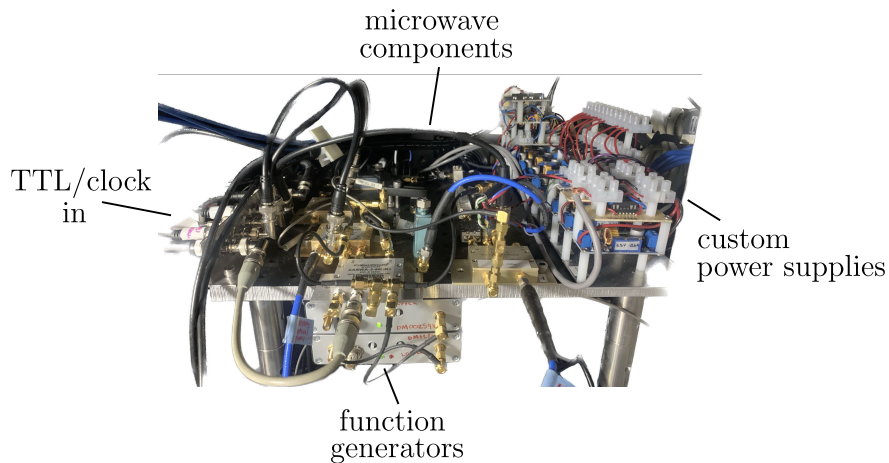
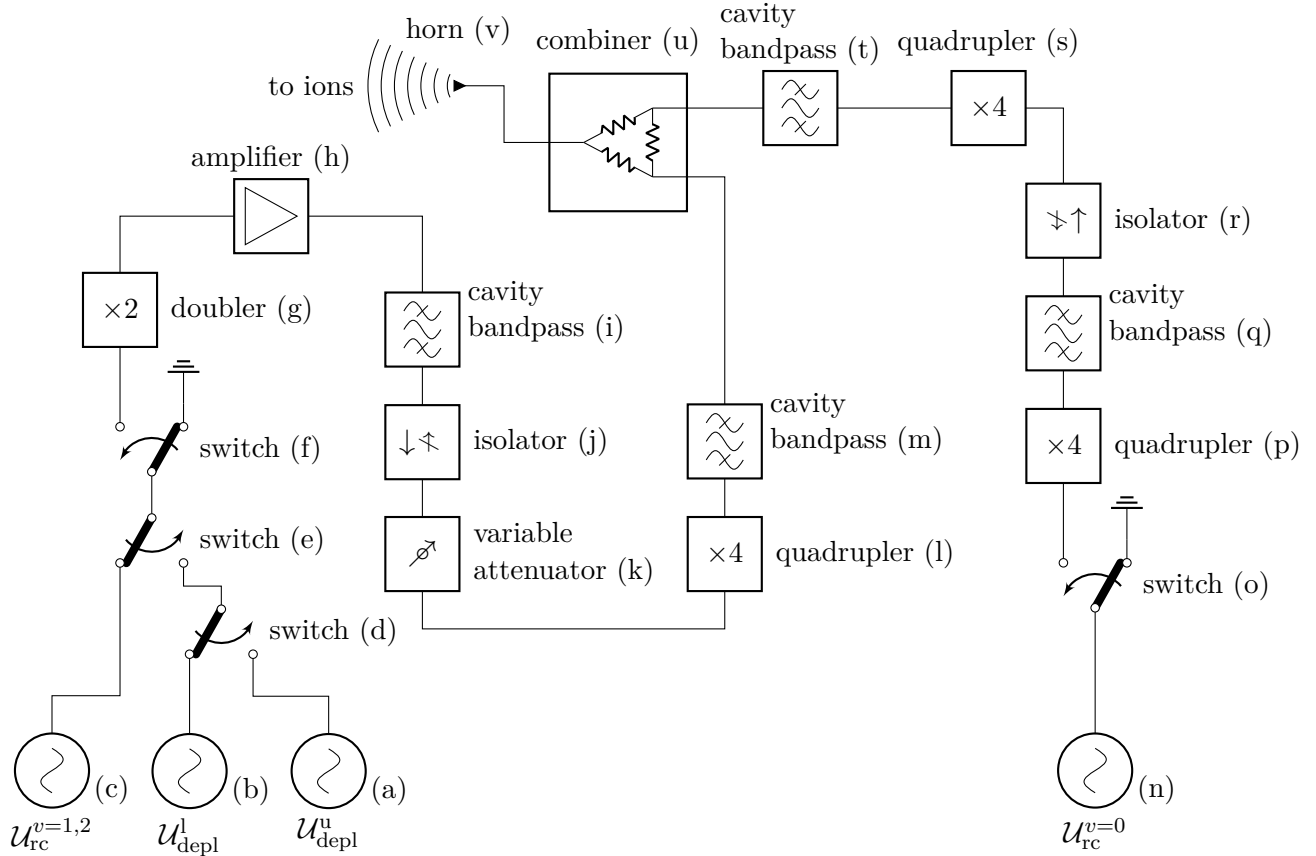


Figure 3.14: Photo of the microwave generating setup.

The system consists of many discrete microwave components assembled together. Each microwave component gets its own power supply that current limits to the appropriate value for each component. Furthermore, the transistor-based microwave components will suffer damage if the positive supply rail is applied before the negative supply rail. In this case the positive rail is supplied through a relay which is only open if the negative rail is active. Furthermore, the negative rail is given a much larger parallel capacitance so that if the negative rail is interrupted the voltage slowly returns to zero giving the relay time to disengage. Each custom power supply runs on the same  $\pm 15$  V supply so that the whole system can be easily powered off or on.

A schematic of the setup is shown in Figure 3.15.

The system consists of two branches, one at 30 GHz to address  $J = 1 \leftrightarrow J = 2$  transitions and one at 43 GHz to address  $J = 2 \leftrightarrow J = 3$  transitions. The signals then get combined and applied to the ions with a custom broadband microwave horn.



label	description	manufacturer	part no.
a	1/8(29.082941 GHz) source	RF-Consultant	TPI-1001-B
b	1/8(29.115175 GHz) source	RF-Consultant	TPI-1001-B
c	1/8(28.81-28.98 GHz) swept source	Agilent	E8251A
d	switch, doublet select	Mini-Circuits	ZYSWA-2-50DR+
e	switch, pumping/depletion	Mini-Circuits	ZYSWA-2-50DR+
f	switch, 30 GHz on/off	Mini-Circuits	ZYSWA-2-50DR+
g	passive frequency doubler	Marki	D97281
h	amplifier, 20 dB	Avantek	APT-18646
i	cavity bandpass 7.25 to 7.75 GHz	Pasternack	PE8741
j	isolator	$\mu$ -wave Associates	MA7L604
k	variable attenuator	narda	4798
l	active frequency quadrupler	Marki	AQA-2156
m	cavity bandpass 27.5 to 31 GHz	Pasternack	PE8747
n	1/16(43.63-43.67 GHz) swept source	Agilent	N5181A
o	switch, 43 GHz on/off	Mini-Circuits	ZYSWA-2-50DR+
p	active frequency quadrupler	Marki	AQA-1933K
q	cavity bandpass 10.55 to 11.8 GHz	Pasternack	PE87FL1001
r	isolator	Ditom	D3I8012
s	active frequency quadrupler	Marki	AQA-2156
t	cavity bandpass 39 to 45 GHz	RF-Lambda	RBPF39G45G
u	broadband splitter/combiner	Mini-Circuits	ZC2PD-V18443+
v	microwave horn, broadband (28.0 to 45.0 GHz)	Dolph	DH-320WDBLP122PA

Figure 3.15: The circuit for generating microwave signals

### 3.2.4 Spectroscopy

Once again we can measure the exact energy for each transition by using them to deplete the relevant states and looking for a dip in the population. The two  $\mathcal{U}_{\text{depl}}$  transitions are measured in Figure 3.16.

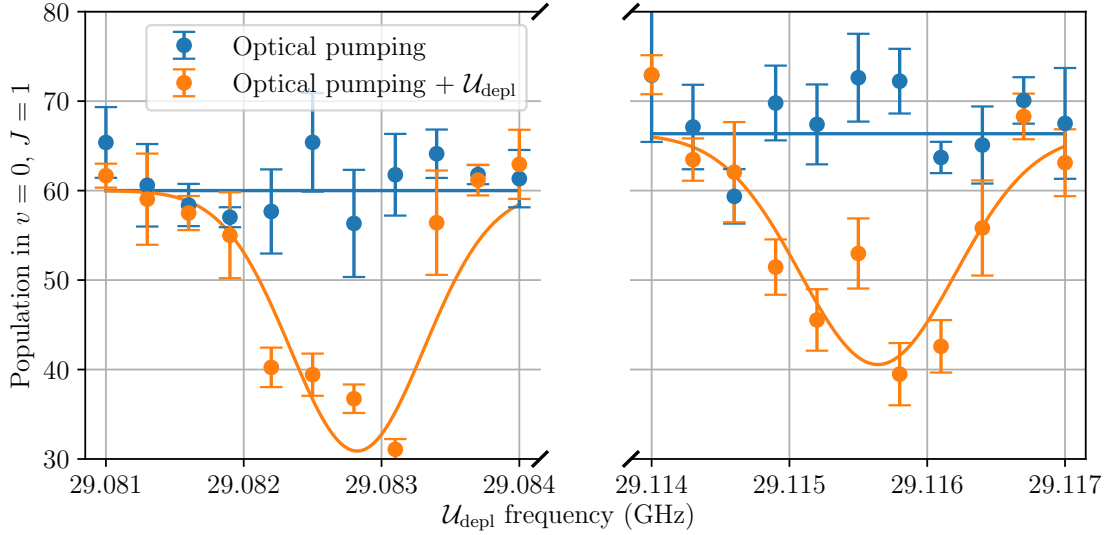


Figure 3.16: Frequency scan of  $\mathcal{U}_{\text{depl}}$  at an  $\mathcal{E}_{\text{rot}}$  of 60 V/cm. The lower frequency dip corresponds to optically pumping into the upper doublet then depleting the upper doublet, while the higher frequency dip corresponds to optically pumping into the lower doublet, then depleting the lower doublet. The lower doublet transition  $\mathcal{U}_{\text{depl}}^{\text{l}}$  fits to a frequency of 29.115642(57) GHz, while the upper doublet transition  $\mathcal{U}_{\text{depl}}^{\text{u}}$  fits to a frequency of 29.082823(29) GHz.

The swept microwaves can be measured in a similar manner.  $\mathcal{U}_{\text{rc}}^{v=1}$  is measured by pumping up to  $v = 1, J = 2$  and then watching population fall back down to  $v = 0, J = 1$  as the microwave and laser pair couple ions out of this state. The results are shown in Figure 3.17.

An important note is that at 60 V/cm, sweeping over this whole range will also address the  $m_f = \pm \frac{3}{2}$  transition in  $v = 0$ , thus depleting some of the states of scientific interest. This is shown in Figure 3.18. To avoid this, we only sweep  $\mathcal{U}_{\text{rc}}^{v=1}$  to a maximum of 28.995 GHz to maintain a safe distance from these transitions.

Finally  $\mathcal{U}_{\text{rc}}^{v=2}$  is measured in Figure 3.19.

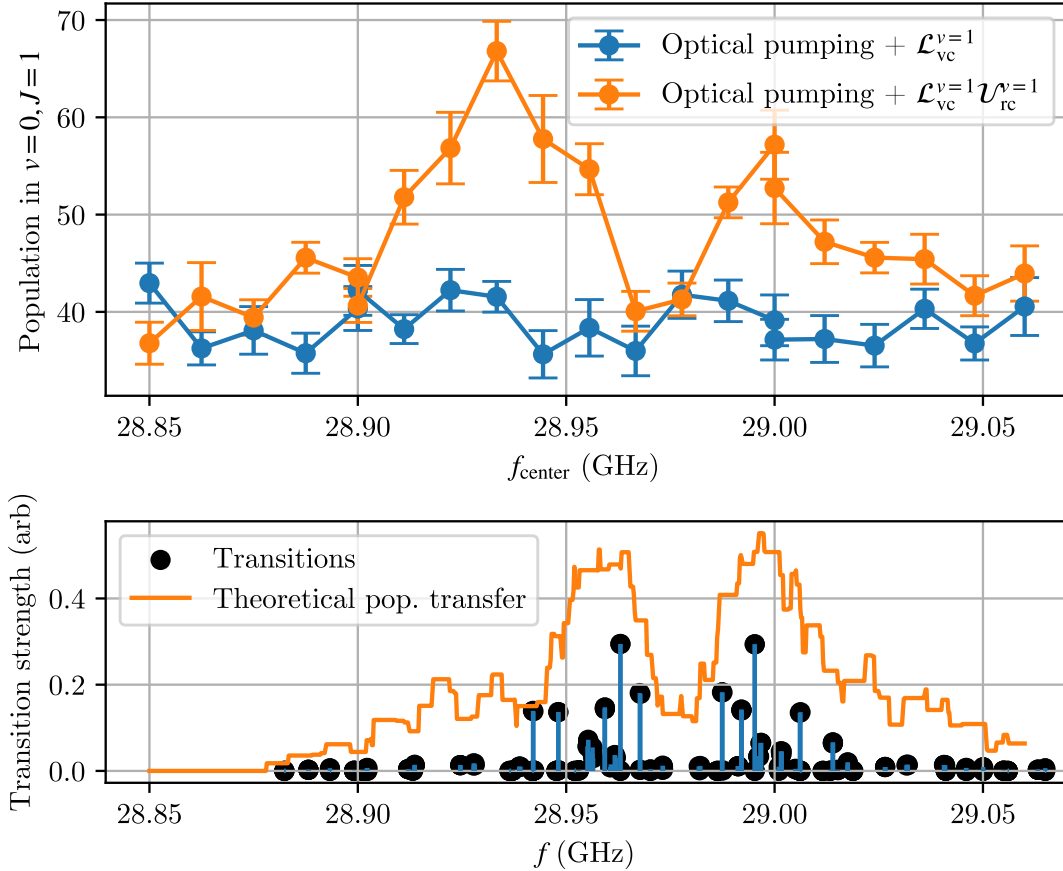


Figure 3.17: Microwave scan of the  $\mathcal{U}_{rc}^{v=1}$ .

Top: Spectroscopy of the transition. The ions are first optically pumped into  $v = 1$ , then either only  $\mathcal{L}_{vc}^{v=1}$  is turned on to pump out  $v = 1, J = 2$  which falls back down to  $v = 0, J = 1$  or  $\mathcal{U}_{rc}^{v=1}$  is also turned on, resulting in additional population from  $v = 1, J = 2$ . The microwaves are swept only 5 MHz around the frequency on the axis.

Bottom: Theoretical location and relative strengths of transitions based off of a 32-level Hamiltonian as calculated by Kia Boon Ng [39]. The theoretical population transfer is found by modeling a fixed time of sweeping the frequency over each transition using the calculated transition rates.

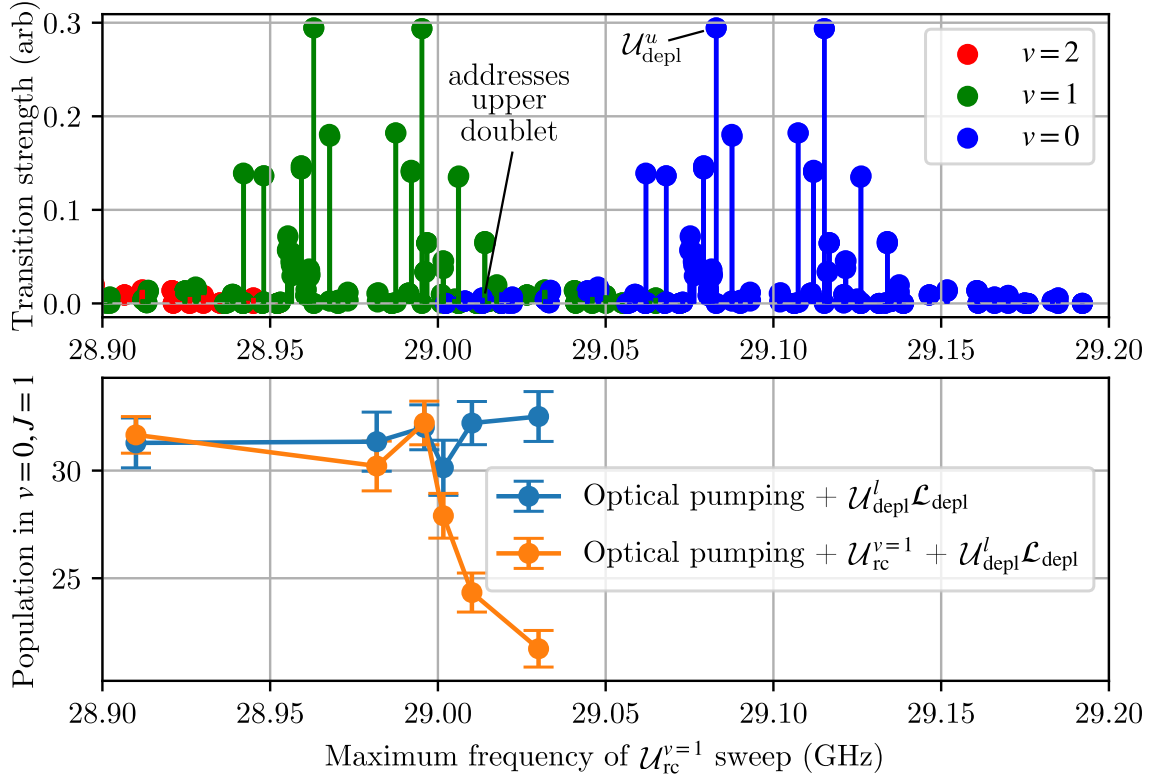


Figure 3.18: Demonstration of  $\mathcal{U}_{rc}^{v=1}$  depleting the upper doublet if the frequency is swept too high. Top: calculated rotational microwave transitions for each vibrational manifold at  $\mathcal{E}_{rot} = 60$  V/cm. Labeled are the lowest  $v = 0$  transition that addresses the upper doublet as well as the transition  $\mathcal{U}_{depl}^u$  that we use to intentionally deplete the upper doublet.

Bottom: measured population in the ro-vibrational manifold containing the states of interest. The populations are measured after optically pumping, then either doing nothing or applying the swept  $\mathcal{U}_{rc}^{v=1}$ , then depleting the lower doublet. This process leaves only population in the upper doublet, thus a dip in population indicates a transfer of population from the upper doublet.

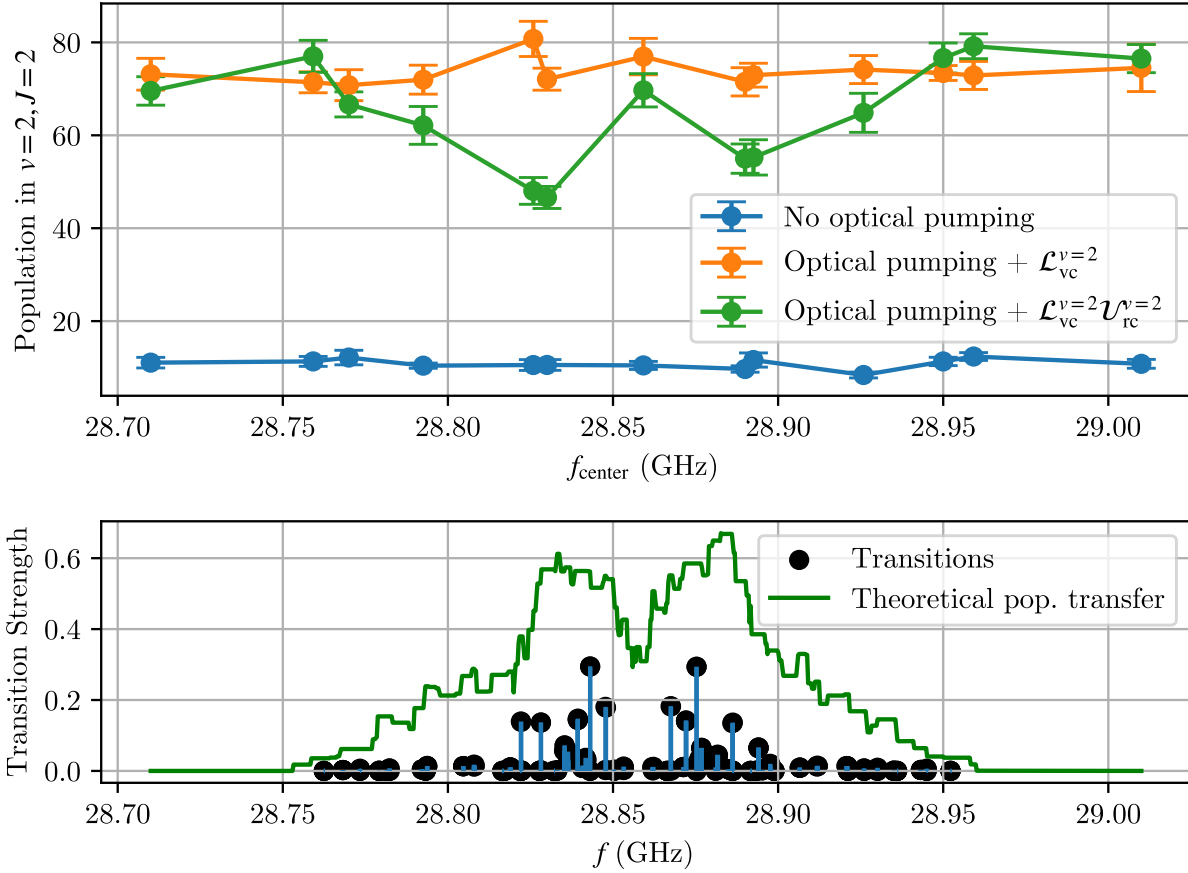


Figure 3.19: Microwave scan  $\mathcal{U}_{rc}^{v=2}$ .

Top: Spectroscopy of the transition. First the ions are optically pumped up to  $v = 2$ , then the population there is depleted using the microwaves, and measured directly. The population in  $v = 2, J = 2$  is measured by dissociating from the  $(^3\Delta_1, v = 2, J = 2) \rightarrow (\Omega = 2, J = 3)$  transition measured in Figure 6.5. The microwaves are swept only 5MHz around the frequency on the axis. Bottom: Theoretical location and relative strengths of transitions based off of a 32-level Hamiltonian as calculated by Kia Boon Ng [39]. The theoretical population transfer is found by modeling a fixed time of sweeping the frequency over each transition using the calculated transition rates.

## Chapter 4

### Electric Fields

#### 4.1 Electrode design

The electrodes used to apply fields to the ions are made up of 8 long "rod" electrodes running the length of the trap to apply fields in the  $x$ - $y$  plane and many small uniformly spaced "ring" electrodes along the axial direction to apply fields along the  $z$ -axis. The electrodes were designed in collaboration with and fabricated by Calvin Schwadron of the JILA instrument shop. The electrode configuration is displayed in Figure 4.1.

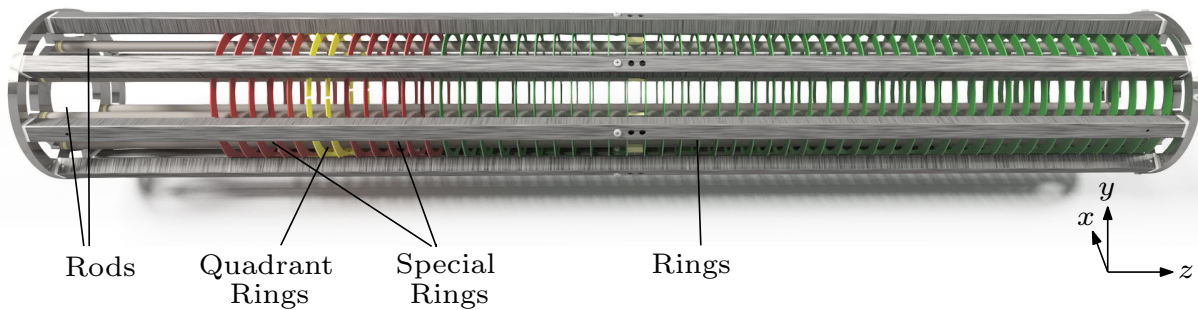


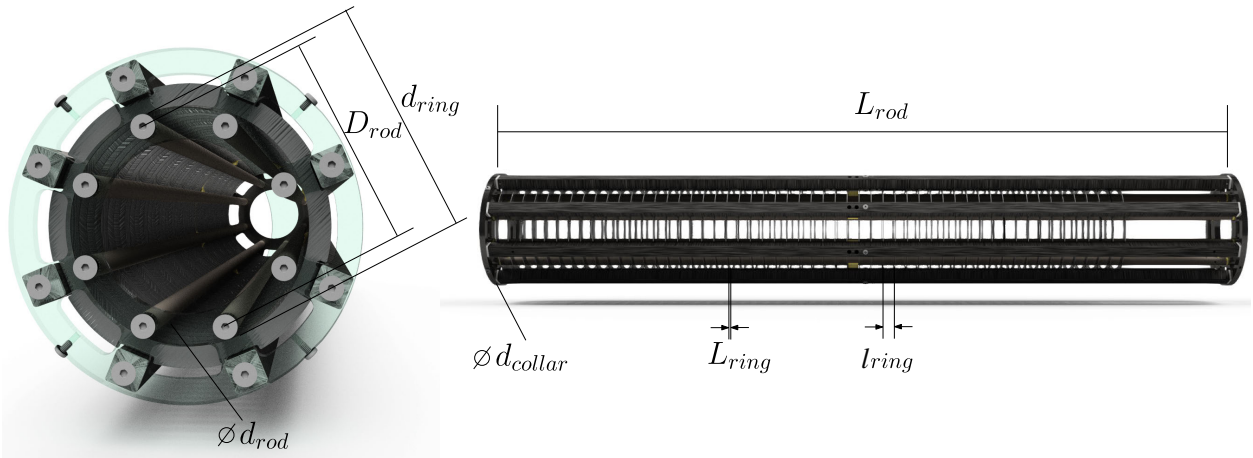
Figure 4.1: CAD rendering of the finalized electrode design.

The ions enter the electrode assembly out of the page between the quadrant ring electrodes (yellow). Both of these electrodes are divided into four regions with individual control, so they can apply localized fields in the  $x$ - $y$  plane as well as along the  $z$  axis. They can then be used to pulse an electric field along  $+x$  right after ionization in order to stop the ions. In addition, individual



control of the special ring electrodes (red) allows us to pulse a high voltage electric field along  $-z$  to kick the ions to the left onto the detector. Finally, the rest of the ring electrodes (green) are wired with every fourth electrode held at the same potential. We can then use these rings to translate the ions forward and backward along the  $z$ -axis.

The dimensions of the electrode assembly are given in Figure 4.2.



Dimension	Value	Description
$d_{rod}$	12.7 mm	Diameter of rod electrodes
$D_{rod}$	11.7 cm	Distance between opposite pairs of rod electrodes
$L_{rod}$	123.2 cm	Length of rod electrodes
$d_{ring}$	13.5 cm	Inner diameter of the ring electrodes
$l_{ring}$	2 cm	Axial spacing of ring electrodes
$L_{ring}$	1 mm	Thickness of ring electrodes
$d_{collar}$	19.3 cm	Outer diameter of the support collars

Figure 4.2: Relevant dimensions of the electrodes

The choice to have the rod electrodes inside of the ring electrodes is made because the electric fields that need to be generated in  $\hat{x}$  and  $\hat{y}$  are much stronger than the fields that need to be generated along  $\hat{z}$ , and having another set of electrodes between the other electrodes and the ions shields the ions from the electric fields generated by the outer electrodes.

The dimensions are selected with several considerations in mind. First, the whole assembly must fit inside the vacuum chamber. The vacuum tube is a 10" outer diameter flange nipple, which

is the largest diameter of the standard ultra-high-vacuum components and has an inner diameter of 19.7 cm, inside of which  $d_{collar}$  must fit. The rod electrodes are then placed as far apart as possible in the interest of making the fields near the center of the trap as homogeneous as possible.

#### 4.1.1 Overview

There are three main electric fields the electrodes must generate (in addition to the pulses to stop the initial velocity of the ions and to kick them out onto the detector). These fields are demonstrated in Figure 4.3. First, the electrodes must apply a strong electric field to polarize the molecules (Figure 4.3.a). For this field not to apply a time-averaged force on the ions, the field must rotate. This way there is no net force on the ions over one rotation cycle, and the instantaneous force acts as a centripetal force as the ions move in a circular trajectory. This field will be further explained in Section 4.1.4.

Next, the electrodes must generate fields to trap the ions, and translate them along the axial dimension of the trap. This is done with an oscillating quadrupole field (Figure 4.3.b) applied by the rod electrodes and a sinusoidal potential along the axial direction (Figure 4.3.c) applied with the ring electrodes. The mechanism for which these two fields lead to trapping of the ions is explained in Section 4.1.3

#### 4.1.2 Ponderomotive potential

Before discussing the fields generated by the electrodes, we need to discuss the ponderomotive effect, by which sinusoidally oscillating inhomogeneous fields impart a time-average force on the ions. An argument for this force is as follows:

If there is a periodic electric field

$$\vec{E}(\vec{r}, t) = \vec{E}_0(\vec{r}) \cos(\omega t), \quad (4.1)$$

then the equation of motion for a charged particle of charge  $q$  and mass  $m$  is

$$m \frac{d^2 \vec{r}}{dt^2} = q \vec{E}_0(\vec{r}) \cos(\omega t). \quad (4.2)$$

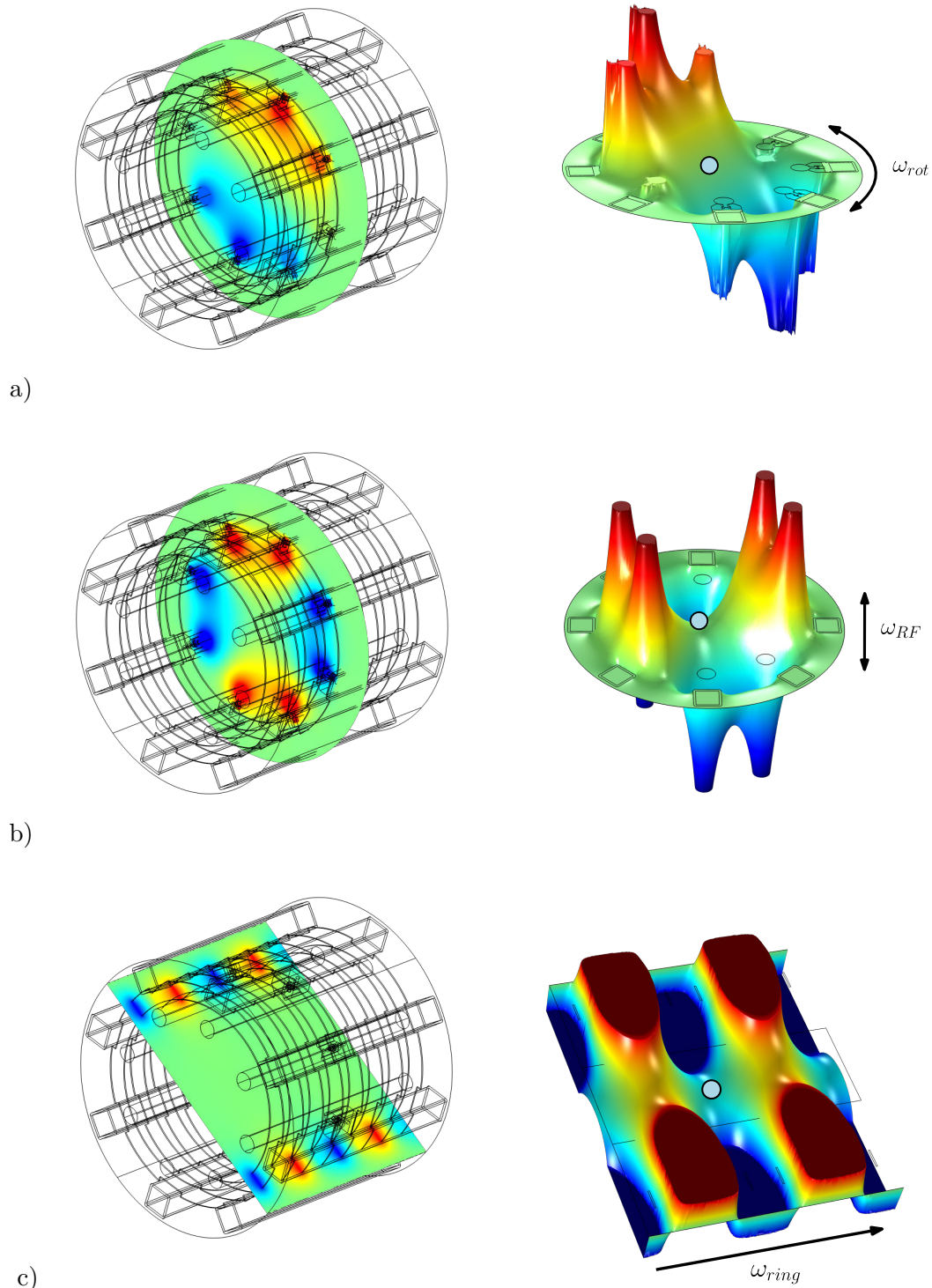


Figure 4.3: Electric potentials generated with the rod and ring electrodes. Left: slice of the electric potential for the respective type of potential applied. Potentials are generated using COMSOL Multiphysics finite element analysis software. Red represents positive potential while blue represents negative potential. Right: Electric potential surfaces for each of the fields. The two horizontal axes represent physical dimensions while the vertical axis represents potential depth.

a)  $V_{rot}$  polarizing field

b)  $V_{RF}$ , oscillating saddle point potential that provides radial confinement

c)  $V_{axial}$ , sinusoidal potential that provides axial confinement at each valley of the sinusoid

We then assume the solution looks like an small oscillation (micromotion) at the driven frequency  $\omega$  with amplitude  $\vec{r}_\mu$ , plus a slow spatially larger secular motion  $\vec{r}_{sec}(t)$ :

$$\vec{r}(t) = \vec{r}_\mu \cos(\omega t) + \vec{r}_{sec}(t). \quad (4.3)$$

If the micromotion is small compared to the secular motion  $\vec{r}_\mu \ll \vec{r}_{sec}$ , then we can expand the electric field about  $\vec{r}_{sec}$ :

$$\vec{E}_0(\vec{r}) \approx \vec{E}_0(\vec{r}_{sec}) + \vec{\nabla} \vec{E}_0(\vec{r}_{sec}) \cdot \vec{r}_\mu \cos(\omega t), \quad (4.4)$$

where  $\vec{\nabla} \vec{E}_0$  is the gradient of the vector field, yielding a tensor

$$\vec{\nabla} \vec{E}_0 \equiv \begin{bmatrix} \frac{\partial}{\partial x} \vec{E}_0 \\ \frac{\partial}{\partial y} \vec{E}_0 \\ \frac{\partial}{\partial z} \vec{E}_0 \end{bmatrix}. \quad (4.5)$$

To find the amplitude of the micromotion, we can plug Equations 4.3 and 4.4 into Equation 4.2:

$$m \left( -\omega^2 \vec{r}_\mu \cos(\omega t) + \frac{d^2 \vec{r}_{sec}}{dt^2} \right) = q \cos(\omega t) \left( \vec{E}_0(\vec{r}_{sec}) + \vec{\nabla} \vec{E}_0(\vec{r}_{sec}) \cdot \vec{r}_\mu \cos(\omega t) \right). \quad (4.6)$$

Grouping terms by timescale,

$$\left( m\omega^2 \vec{r}_\mu + q \vec{E}_0(\vec{r}_{sec}) \right) \cos(\omega t) + \left( q \vec{\nabla} \vec{E}_0(\vec{r}_{sec}) \cdot \vec{r}_\mu \right) \cos^2(\omega t) - m \frac{d^2 \vec{r}_{sec}}{dt^2} = 0. \quad (4.7)$$

Note that the second two terms are small in magnitude compared to the first term, and they change on different timescales. Therefore, we can extract the micromotion amplitude by setting the first term equal to zero, giving

$$\vec{r}_\mu \approx -\frac{q \vec{E}_0(\vec{r}_{sec})}{m\omega^2}. \quad (4.8)$$

We can then write Equation 4.2 as

$$m \left( \omega^2 \frac{q \vec{E}_0(\vec{r}_{sec})}{\omega^2 m} \cos(\omega t) + \frac{d^2 \vec{r}_{sec}}{dt^2} \right) \approx q \vec{E}_0(\vec{r}) \cos(\omega t) \quad (4.9)$$

$$q \vec{E}_0(\vec{r}_{sec}) \cos(\omega t) + m \frac{d^2 \vec{r}_{sec}}{dt^2} \approx q \left( \vec{E}_0(\vec{r}_{sec}) + \vec{\nabla} \vec{E}_0(\vec{r}_{sec}) \cdot \vec{r}_\mu \cos(\omega t) \right) \cos(\omega t) \quad (4.10)$$

$$m \frac{d^2 \vec{r}_{sec}}{dt^2} \approx q \vec{\nabla} \vec{E}_0(\vec{r}_{sec}) \cdot \vec{r}_\mu \cos^2(\omega t). \quad (4.11)$$

Finally, we can plug Equation 4.8 into this and average over a cycle of  $\omega$  to get

$$m \frac{d^2 \vec{r}_{sec}}{dt^2} = - \frac{q^2 \vec{\nabla} \vec{E}_0(\vec{r}_{sec}) \cdot \vec{E}_0(\vec{r}_{sec})}{2m\omega^2}. \quad (4.12)$$

We can use a modified version of a chain rule (proven in Appendix B),

$$(\vec{\nabla} \vec{E}) \cdot \vec{E} = \frac{1}{2} \vec{\nabla} |E|^2 - \vec{E} \times (\vec{\nabla} \times \vec{E}) \quad \overset{0}{}, \quad (4.13)$$

where we have ignored the cross term since electrostatic fields that obey Maxwell's equations must have  $\vec{\nabla} \times \vec{E} = 0$ . With this, we arrive at

$$m \frac{d^2 \vec{r}_{sec}}{dt^2} = - \vec{\nabla} \frac{q^2 |E_0(\vec{r}_{sec})|^2}{4m\omega^2}, \quad (4.14)$$

and thus the secular motion is described by an effective potential

$$U = \frac{q^2 |E_0|^2}{4m\omega^2}. \quad (4.15)$$

This effective potential is known as the ponderomotive potential. This potential can be thought of as the classical harmonic oscillator energy of the micromotion.

$$U = \frac{1}{2} m \omega^2 \langle r_{\text{micromotion}}^2 \rangle_t = \frac{1}{2} m \omega^2 \langle (r_\mu \cos(\omega t))^2 \rangle_t = \frac{1}{4} m \omega^2 r_\mu^2, \quad (4.16)$$

yielding the same result if we use the expression for  $r_\mu$  from Equation 4.8.

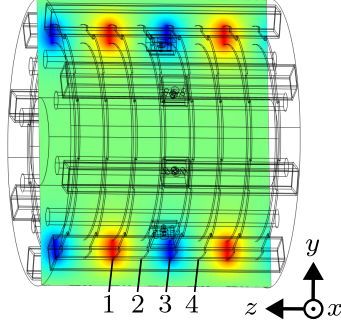
### 4.1.3 Paul trap

The ions are trapped axially with the ring electrodes producing a sinusoid. The voltages applied to the rings are shown in Figure 4.4.

By modulating  $\phi_{\text{translate}}$ , the minima of the sinusoid are spatially translated along  $z$ . Thus by changing the phase of the ring electrodes, the ions can be translated. The relationship between spatial translation and phase applied to the electrodes is given by

$$z_{\text{translated}} = \phi_{\text{translate}} \frac{4l_{\text{ring}}}{2\pi}. \quad (4.17)$$

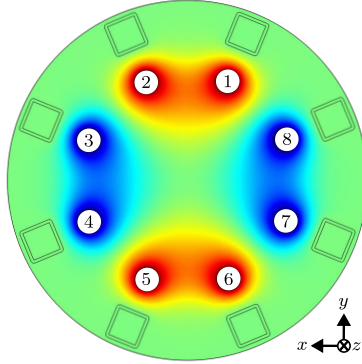
While this potential is confining along  $z$ , it is anti-confining along  $x$  and  $y$  (see Figure 4.3.c). In general, any static electric potential we can apply with the electrodes can only be confining in up



Ring	Potential applied
1	$V_{\text{ring},pk} \cos(\frac{0\pi}{2} + \phi_{\text{translate}}(t))$
2	$V_{\text{ring},pk} \cos(\frac{1\pi}{2} + \phi_{\text{translate}}(t))$
3	$V_{\text{ring},pk} \cos(\frac{2\pi}{2} + \phi_{\text{translate}}(t))$
4	$V_{\text{ring},pk} \cos(\frac{3\pi}{2} + \phi_{\text{translate}}(t))$

Figure 4.4: Voltages applied to the ring electrodes to trap the ions axially and to translate them. The potentials are periodic every fourth ring, e.g. the voltage on the 5th ring is the same as the voltage on the 1st ring.

to two dimensions since there are no sources ( $\vec{\nabla} \cdot \vec{E} = 0$ ). In order to overcome this anti-confining potential and confine the ions along  $x$  and  $y$ , we apply a pseudopotential that is constant along  $z$  and confining along  $x$  and  $y$ . This is done by applying a quadrupole potential with the rod electrodes that oscillates at  $\omega_{\text{RF}} = 2\pi \times 50$  kHz. The voltages applied are shown in Figure 4.5.



Rod	Potential applied
1	$V_{\text{RF},pk} \cos(\omega_{\text{RF}} t)$
2	$V_{\text{RF},pk} \cos(\omega_{\text{RF}} t)$
3	$V_{\text{RF},pk} \cos(\omega_{\text{RF}} t + \pi)$
4	$V_{\text{RF},pk} \cos(\omega_{\text{RF}} t + \pi)$
5	$V_{\text{RF},pk} \cos(\omega_{\text{RF}} t)$
6	$V_{\text{RF},pk} \cos(\omega_{\text{RF}} t)$
7	$V_{\text{RF},pk} \cos(\omega_{\text{RF}} t + \pi)$
8	$V_{\text{RF},pk} \cos(\omega_{\text{RF}} t + \pi)$

Figure 4.5: The voltages applied to the rods in order to generate the RF quadrupole potential

Even though the resulting potential is a saddle point instantaneously, the oscillations of the field give rise to a ponderomotive potential that is proportional to  $|E|^2$ , which is radially confining. This is displayed in Figure 4.6. The saddle point potential near the center of the trap looks like

$$V_{\text{RF}} \approx \alpha_{\text{RF}} V_{\text{RF},pk} (x^2 - y^2), \quad (4.18)$$

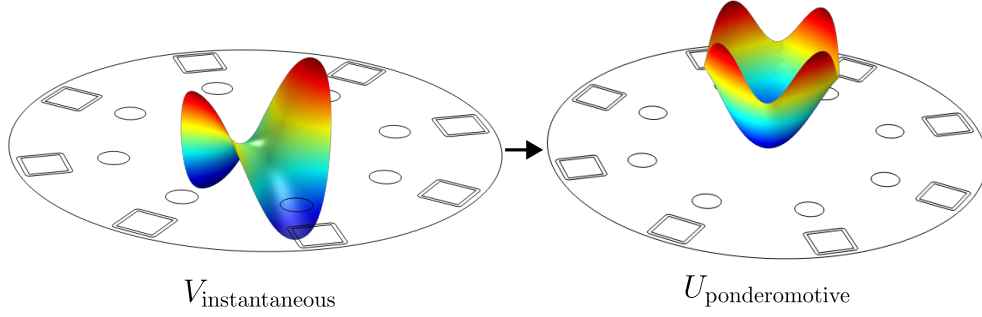


Figure 4.6: The transformation of the RF saddle point potential to its confining effective ponderomotive potential near the center of the trap.

where  $\alpha_{\text{RF}}$  is a scaling factor based on the geometry of the electrodes. Then the electric field is

$$\vec{E}_{\text{RF}} = -\vec{\nabla}V_{\text{RF}} \approx \alpha_{\text{RF}}V_{\text{RF,pk}}(-2x\hat{x} + 2y\hat{y}). \quad (4.19)$$

This gives rise to a ponderomotive potential of

$$U_{\text{RF}} = \frac{e^2|E_{\text{RF}}|^2}{4m\omega_{\text{RF}}^2} = \frac{e^2(\alpha_{\text{RF}}V_{\text{RF,pk}})^2(x^2 + y^2)}{m\omega_{\text{RF}}^2} = \frac{e^2\alpha_{\text{RF}}^2V_{\text{RF,pk}}^2\rho^2}{m\omega_{\text{RF}}^2}, \quad (4.20)$$

where  $e$  is the electron charge and  $\rho$  is the cylindrical radial coordinate  $\rho = \sqrt{x^2 + y^2}$ . The potential from the axial field looks like (up to a constant which can be neglected)

$$U_{\text{ring}} = eV_{\text{ring}} \approx e\alpha_{\text{ring}}V_{\text{ring,pk}}(2z^2 - \rho^2), \quad (4.21)$$

where  $\alpha_{\text{ring}}$  is once again a scaling factor due to electrode geometry. Thus the full trapping potential experienced by the ions is given by

$$U_{\text{trap}} = U_{\text{RF}} + U_{\text{ring}} = \frac{1}{2} \underbrace{\left( \frac{2e^2\alpha_{\text{RF}}^2V_{\text{RF,pk}}^2}{m\omega_{\text{RF}}^2} - 2e\alpha_{\text{ring}}V_{\text{ring,pk}} \right)}_{k_\rho} \rho^2 + \frac{1}{2} \underbrace{(4e\alpha_{\text{ring}}V_{\text{ring,pk}})}_{k_z} z^2. \quad (4.22)$$

The effective potential has the form of a harmonic oscillator potential. In this form it is easy to see that the secular motion of the ions in the trap will undergo oscillations at frequencies in  $\rho$  and  $z$  respectively:

$$\omega_\rho = \sqrt{\frac{k_\rho}{m}} = \sqrt{\frac{2e^2\alpha_{\text{RF}}^2V_{\text{RF,pk}}^2}{m^2\omega_{\text{RF}}^2} - \frac{2e\alpha_{\text{ring}}V_{\text{ring,pk}}}{m}} \quad (4.23)$$

$$\omega_z = \sqrt{\frac{k_z}{m}} = \sqrt{\frac{4e\alpha_{\text{ring}}V_{\text{ring,pk}}}{m}}. \quad (4.24)$$

We can invert these equations to find the required voltages to apply to the electrodes in order to get the desired secular frequencies:

$$V_{\text{RF,pk}} = \frac{m\omega_{\text{RF}}\sqrt{2\omega_{\rho}^2 + \omega_z^2}}{2\alpha_{\text{RF}}e} \quad (4.25)$$

$$V_{\text{ring,pk}} = \frac{m\omega_z^2}{4\alpha_{\text{ring}}e}. \quad (4.26)$$

The value of the scaling constants can be found by fitting the potentials from the COMSOL simulations, yielding

$$\begin{cases} \alpha_{\text{RF}} = 348 \text{ m}^{-2} \\ \alpha_{\text{ring}} = 8.73 \text{ m}^{-2}. \end{cases} \quad (4.27)$$

With this we can calculate the parameters of the trap. For example, to get a secular frequency of  $2\pi \times 2$  kHz in each dimension, the voltages are  $V_{\text{RF,pk}} = 25.6$  V and  $V_{\text{ring,pk}} = 11.8$  V. The digital to analog converters (DACs) driving the ring electrodes can only go up to 10 V, so we instead apply a  $V_{\text{ring,pk}}$  of 9.95 V to stay within the limit, giving us an theoretical  $\omega_z$  of 1.84 kHz and  $\omega_{\rho}$  of 2.08 kHz.

Far enough away from the center of the trap, the harmonic approximation of the potentials break down. Furthermore, the radial anti-confining of the ring potential grows faster than the radial confining of the RF potential, leading to a point at which the total effective potential curls over and is no longer confining. This is shown in Figure 4.7.

The RF confining potential is stronger along the diagonal axes such as (b) than the axes of the saddle point such as (a), and are thus more tightly radially confined. We can assign each of the local maxima where the potential curls over an effective trap depth  $\Delta U$ , equal to the difference between the minimum of the trap and the local maximum. These values are calculated to be

$$\begin{cases} \Delta U_{\text{axial}} = 1330 \text{ K} \\ \Delta U_{\text{radial,a}} = 894 \text{ K} \\ \Delta U_{\text{radial,b}} = 5070 \text{ K}. \end{cases} \quad (4.28)$$



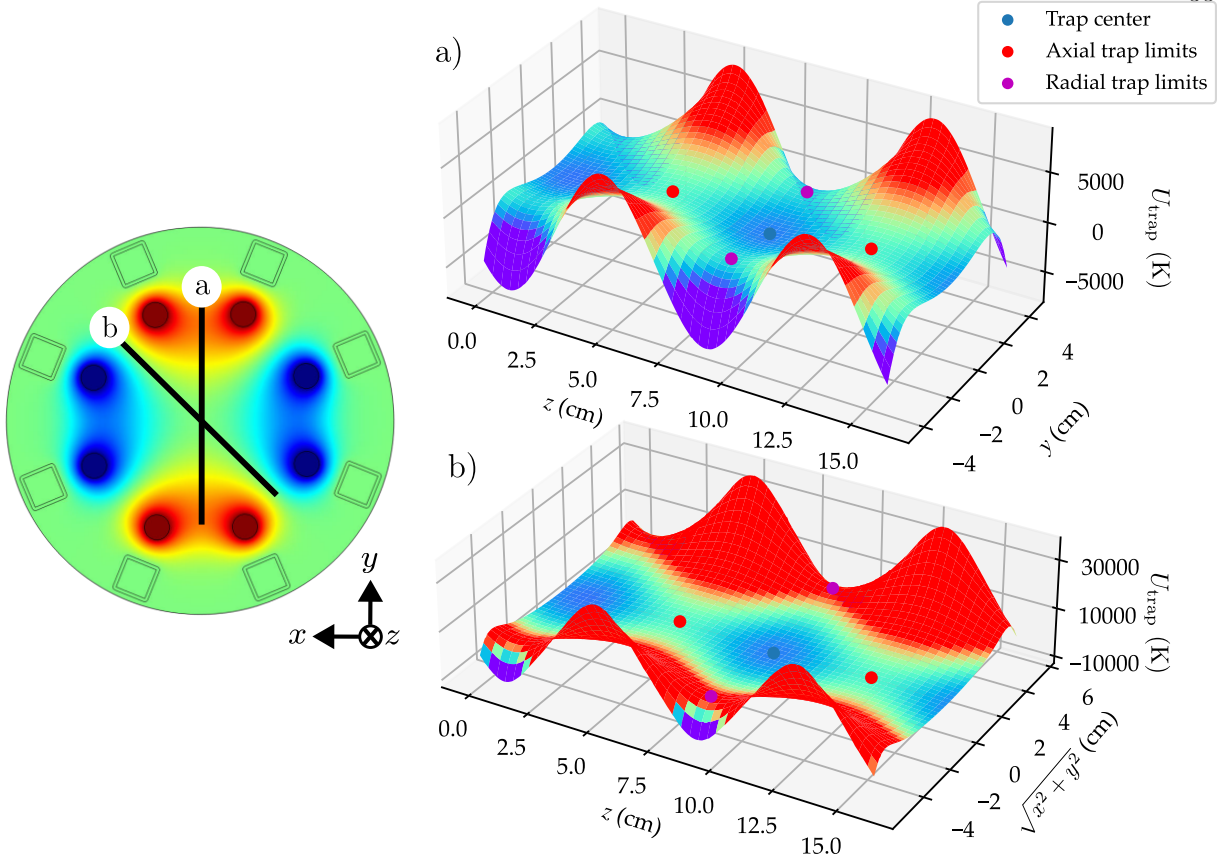


Figure 4.7: The total effective trap potentials experienced by the ions with  $V_{\text{RF,pk}} = 25.6\text{V}$  and  $V_{\text{ring,pk}} = 9.95\text{V}$  using  $|E_{\text{RF}}|^2$  and  $V_{\text{ring}}$  fields generated in COMSOL. Left: a diagram of the RF potentials showing the two slices over which the total effective potentials are plotted. Right: Surface plots of the total effective potentials in Kelvin (related to the potential energy by the Boltzmann constant). Then highlighted are the potential minimum at which the ions sit and the four points in which the potential is no longer confining, indicating the boundary of the trap.

In addition, the distance  $\Delta r$  from the bottom of the trap to each of these local maxima is also a useful criteria:

$$\begin{cases} \Delta r_{\text{axial}} = 4.0 \text{ cm} \\ \Delta r_{\text{radial,a}} = 2.7 \text{ cm} \\ \Delta r_{\text{radial,b}} = 4.4 \text{ cm}. \end{cases} \quad (4.29)$$

With cross-dimensional thermalization, the trap depth is limited by the weakest radial trap depth, so only ions cooler than 900 K will be trapped. A final useful quantity is the maximum slope of the ponderomotive potential before the local maximum, which tells us how much we can tilt the

potential before it no longer has any minimum. By dividing by the charge  $q$  of the ion, this then represents the maximum electric field we can apply in that direction before there is no trap:

$$\begin{cases} \frac{1}{q} \frac{\partial U}{\partial z}_{\text{axial}} = 0.049 \text{ V/cm} \\ \frac{1}{q} \frac{\partial U}{\partial \rho}_{\text{radial,a}} = 0.047 \text{ V/cm} \\ \frac{1}{q} \frac{\partial U}{\partial \rho}_{\text{radial,b}} = 0.228 \text{ V/cm.} \end{cases} \quad (4.30)$$

#### 4.1.4 Rotating polarizing field

The voltages applied to the electrodes in order to generate the rotating polarizing field  $\vec{\mathcal{E}}_{\text{rot}}$  are shown in Figure 4.8.

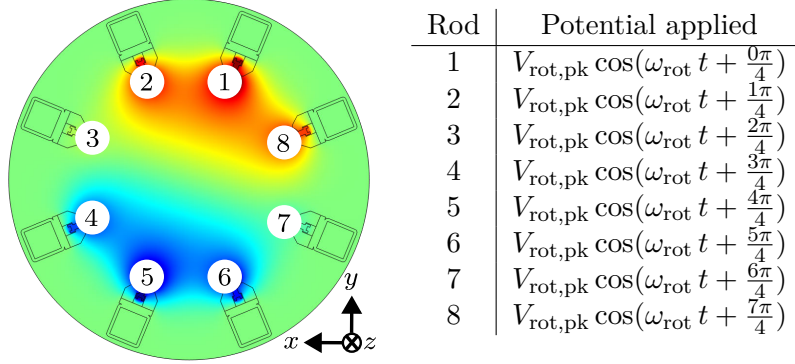


Figure 4.8: Voltages applied to the rod electrodes to apply the rotating polarizing field

The homogeneity of the field applied is very important for several reasons. Firstly, the magnitude of the field goes directly into the Ramsey frequency  $f_0$  (see Section 5.1), since

$$f_0 \propto \mathcal{B}_{\text{rot}} \propto r_{\text{rot}} \propto \mathcal{E}_{\text{rot}}. \quad (4.31)$$

This means that the homogeneity requirement of  $\frac{\Delta f}{f} < 10^{-4}$  from Section 5.3.2 requires that in the region in which the ions are trapped,  $\frac{\Delta \mathcal{E}_{\text{rot}}}{\mathcal{E}_{\text{rot}}} < 10^{-4}$ .

Secondly, any gradients in the strength of the field applied generates a ponderomotive potential that could disrupt the ions and cause them to fall out of the trap (while the field is rotating

rather than oscillating meaning that it can't be written in the form of Equation 4.1, the ponderomotive force argument can be made separately in each dimension, where the projection of the field onto that dimension can be written in this form).

If the electric field oscillating at  $\omega_{\text{rot}}$  applied is composed of the intended uniform-magnitude  $\vec{\mathcal{E}}_{\text{rot}}$  and a small spatially-varying perturbation  $\vec{E}_{\text{dev}}$ , then the ponderomotive potential is

$$U_{\text{pond,rot}} = \frac{e^2}{4m\omega_{\text{rot}}^2} \left| \vec{\mathcal{E}}_{\text{rot}} + \vec{E}_{\text{dev}} \right|^2 = \frac{e^2}{4m\omega_{\text{rot}}^2} \left( |\mathcal{E}_{\text{rot}}|^2 + \underbrace{2\vec{\mathcal{E}}_{\text{rot}} \cdot \vec{E}_{\text{dev}}}_{\text{cross term}} + |E_{\text{dev}}|^2 \right). \quad (4.32)$$

Since  $|\mathcal{E}_{\text{rot}}|^2$  is a constant (not spatially varying), it can be neglected from the potential. Further, since  $|E_{\text{dev}}| \ll |\mathcal{E}_{\text{rot}}|$ , the ponderomotive potential comes mainly from the cross term

$$U_{\text{pond,rot}} \approx \frac{e^2}{2m\omega_{\text{rot}}^2} \vec{\mathcal{E}}_{\text{rot}} \cdot \vec{E}_{\text{dev}}. \quad (4.33)$$

This places a constraint on how big the deviation can be before the ions can be lost from the trap

$$\Delta|\vec{E}_{\text{dev}}| < \frac{2m\omega_{\text{rot}}^2}{e^2|\vec{\mathcal{E}}_{\text{rot}}|} U_{\text{trap depth}} = 0.6 \text{ V/cm}. \quad (4.34)$$

given a  $U_{\text{trap depth}}$  of 900 K, an  $\mathcal{E}_{\text{rot}}$  of 60 V/cm, and an  $\omega_{\text{rot}}$  of  $2\pi \times 150$  kHz.

Studies of the electrode geometry to meet these requirements is detailed in Kia Boon Ng's thesis [39].

## 4.2 Electronics

### 4.2.1 Amplitude and timing requirements

The electric fields described in the previous section must have their amplitudes modulated during the experiment, as well as have well defined phases with respect to laser pulses and other trap potentials. A typical experimental sequence is shown in Figure 4.9 that demonstrates the specific requirements of these signals.

At the beginning of stage 1, our pulsed lasers ionize the beam of neutral ThF molecules, and special ring electrodes apply a pulsed potential gradient to slow them. At the same time, the RF confining potentials are diabatically turned on. The initial phase of  $V_{\text{RF}}$  is defined such that at the

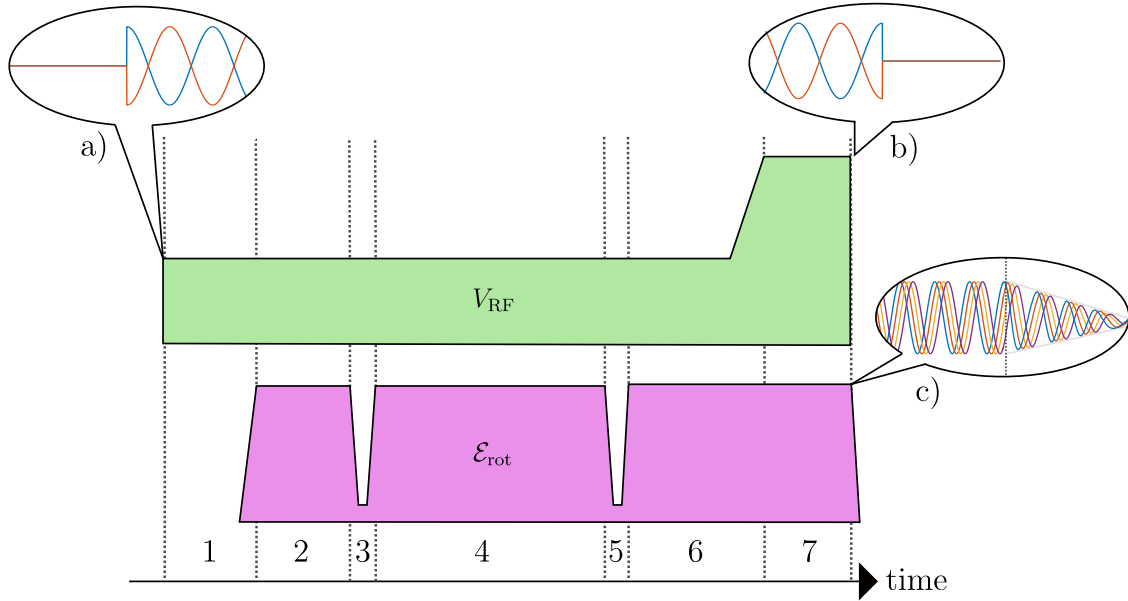


Figure 4.9: AC trap electrode envelope profiles for a typical experiment. The experiment is broken into different functional periods indicated with numerals, with three phase matching conditions indicated with letters.

- 1) Catching the ions
- 2) State preparation
- 3)  $\pi/2$  pulse
- 4) Ramsey evolution time
- 5)  $\pi/2$  pulse
- 6) Depletion
- 7) Dissociation and kickout

a) and b): The trap must be turned on and off when its amplitude is at a maximum. This corresponds to the point in the ions' micromotional trajectories where velocity is minimized, meaning they will not be heated when caught and the cloud will not undergo excess expansion when dissociated and kicked out.

c): In order to align the axis of the molecules with the polarization of the dissociation pulse,  $\mathcal{E}_{\text{rot}}$  must have a well defined phase at the time of dissociation/kickout. It must then be ramped down so that it does not affect the trajectories of the dissociated ions as they travel to the detector.

catch time, the RF potentials are at a maximum, as shown in phase criteria a). This minimizes possible heating of the ion cloud from the applied potentials. The ions are then held for some time so they can thermalize and reach equilibrium mean trajectories.  $\mathcal{E}_{\text{rot}}$  is then adiabatically ramped up to lift the degeneracy of the hyperfine states, thus beginning stage 2. In this stage, the ions are optically pumped into the  $J = 1$ ,  $m_F = \pm 3/2$  states. Then in stage 3,  $\mathcal{E}_{\text{rot}}$  is ramped down to allow for mixing of the  $m_F$  states, then ramped back up. This results in an effective  $\pi/2$  pulse for

each doublet. In stage 4, the ions are allowed to freely Ramsey evolve, before undergoing another  $\pi/2$  pulse in stage 5. Finally, we optically deplete the states in stage 6, before ramping up the trap depth and performing dissociation in step 7. At the end of step 7, the dissociated ions are then kicked out and more special ring electrodes accelerate them towards an imaging MCP.

Once again, the kickout must be done at a place in the micromotion where velocity is minimized to avoid additional expansion of the cloud after the trap is turned off (see phase requirement c). To achieve this, the kickout time is chosen to be an integer multiple of RF cycles from the catch time. Finally, the polarization of the dissociation photons with respect to the quantization axis is critical in achieving high dissociation efficiency, so the phase of  $\mathcal{E}_{\text{rot}}$  during dissociation and kickout must also be well-defined. This is done by setting the initial phase of  $\mathcal{E}_{\text{rot}}$  at the start of the experiment such that it will match up at the dissociation time.

#### 4.2.2 DDS boards

In order to generate these waveforms, a multiplexed system of field programmable gate arrays (FPGAs) and direct digital synthesis (DDS) signal generator chips are used. The system was designed by Felix Vietmeyer of the JILA electronics. Each board, which outputs a single waveform, contains its own FPGA and DDS. A schematic is shown in Figure 4.10.

Each DDS has four channels of output which can each be programmed with their own phase and amplitude. These channels then each pass through their own multiplying digital to analog converters (DACs) and switches which can ramp the amplitudes and turn the signal on and off in real time. They then pass through a summing amplifier to combine the signals into a single channel.

The system also has two standalone DACs which can also be controlled in real time, but these are not used in the current configuration (the signals are AC coupled to the electrodes so DC components cannot be applied with these boards).

The computer programs the system via a USB serial decoder which talks to the FPGA. The FPGA logic can be divided into two devices, one labeled “A1” which forwards the serial commands

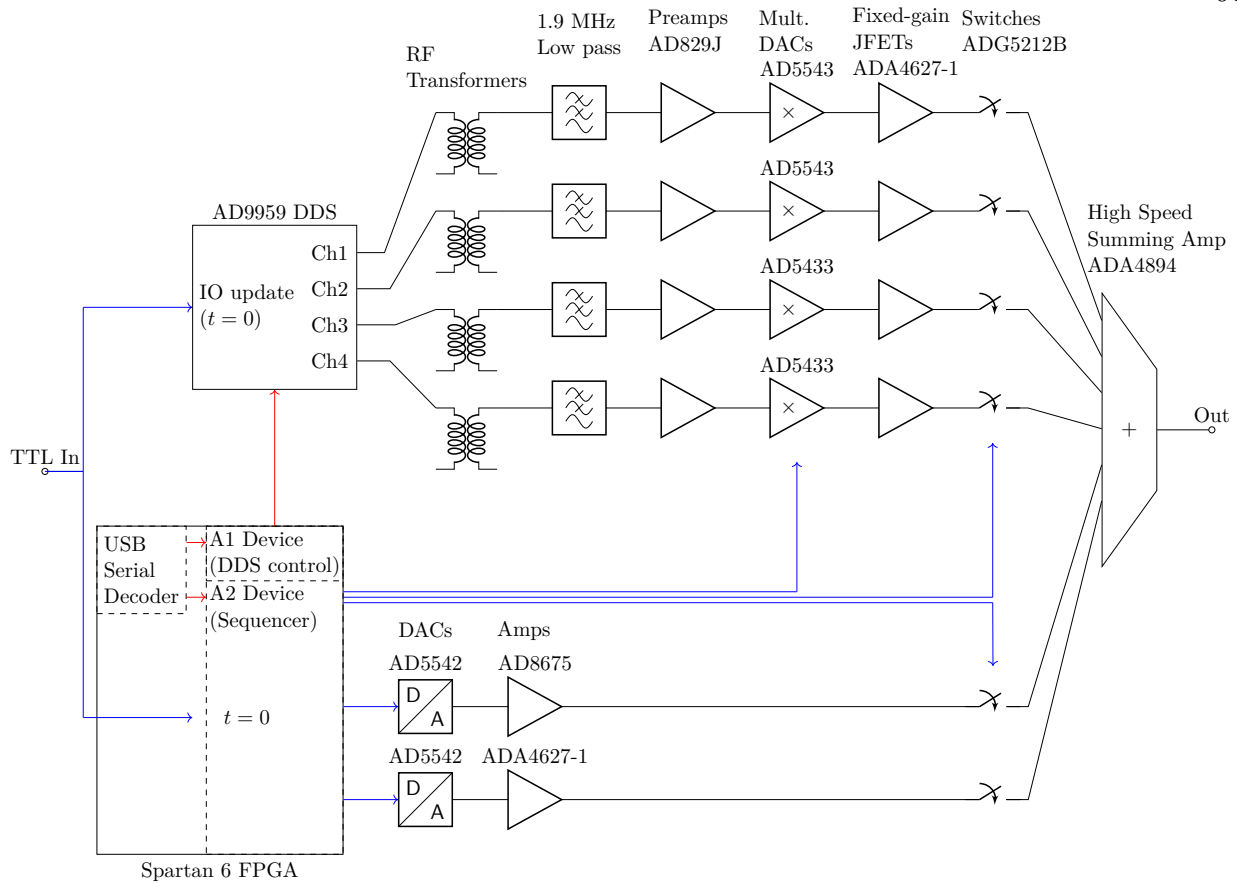


Figure 4.10: A schematic of the JILA-designed DDS boards. Blue wires represent synchronous, real-time digital control while red wires represent asynchronous programming done between shots of the experiment. Black wires represent analog signal channels.

to the DDS chip with the appropriate formatting, and another labeled “A2” which programs a sequencer. The sequencer stores a list of times (as number of clock cycles) and values of multiplying DACs, switches, and DACs. Once the system receives a TTL pulse indicating the experiment has begun, it then executes this table synchronously.

Each channel of the DDS can be programmed asynchronously with its own amplitude and phase. Generally only relative amplitudes that remain fixed (such as the voltages prescribed in Figure 4.22) are written to the DDS, and then their amplitudes are ramped synchronously during the experiment using the multiplying DACs. The only synchronous component of the DDS is that the TTL input is tied to the DDS’s ‘IO update’ pin, which resets the phase to the programmed

phase at the next logical clock rising edge, thus synchronizing the phases of each channel to the  $t = 0$  of the system.

Synchronizing the  $t = 0$  of the DDS and the sequencer to each other and also to the  $t = 0$  of the system supplying the TTL pulse requires some care. Generally these systems are operating at different logical clock rates, which can lead to timing jitter if the timings are not synchronized to the least common denominator of these clock periods. A diagram of the clock distribution setup is shown in Figure 4.11.

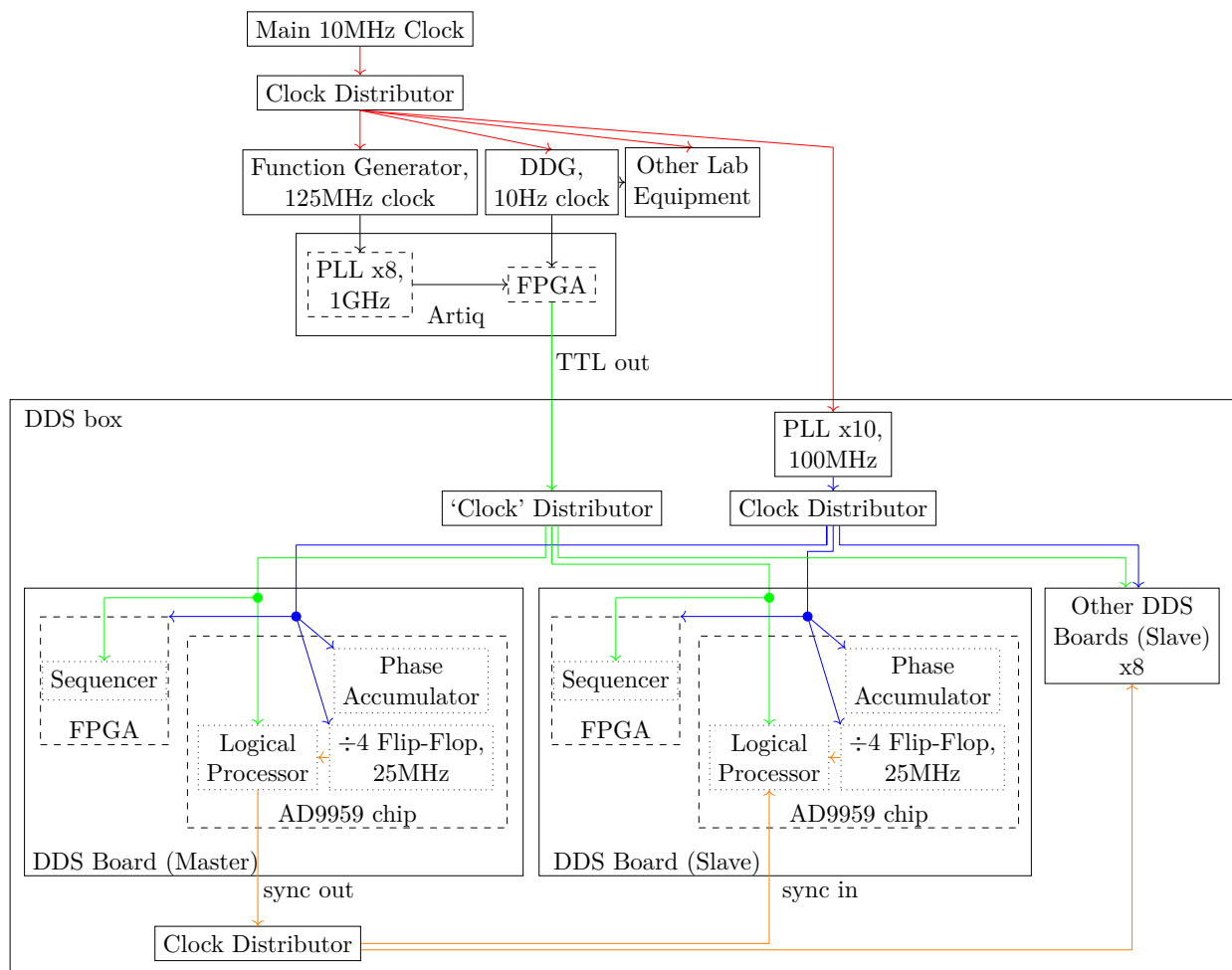


Figure 4.11: Diagram of the timing distribution system. Each solid box represents a physically distinct piece of hardware. Each arrow color represents a different clock frequency of the system. Red represents 10 MHz, blue represents 100 MHz, orange represents 25 MHz, and green represents a TTL pulse signifying the DDSs'  $t = 0$  of the experiment.

Even though the DDS’s phase accumulator runs at 100 MHz (meaning the output moves to a new discrete phase once per 10 ns), the logical processor of the DDS chip only operates at 25 MHz, meaning that the DDS only looks for the TTL rising edge once every 40 ns. The sequencer, however, has a logic clock of 100 MHz. Since they both look for the rising edge of the TTL trigger on each clock cycle, they can have a relative jitter of up to three cycles of 100 MHz. To avoid this, the TTL trigger must be sent at an integer multiple of  $(25 \text{ MHz})^{-1}$  or 40 ns. This is done by ensuring that Artiq sends the TTL trigger at an integer multiple of 40 ns from the rising edge of the 10 Hz clock signal from the DDG. Because 1/10 Hz is cleanly divided by 1/25 MHz, the 10 Hz clock rising edges are separated by an integer multiple of 40 ns (one 10Hz clock cycle is exactly  $25 \times 10^5$  cycles of the 25 MHz clock), any TTL pulse given at a 40 ns increment from a rising edge of the 10 Hz clock will be a multiple of 40 ns from the last TTL pulse, which means no timing jitter from incommensurate system clocks will occur.

Furthermore, because the rising edge of the logical clock for each DDS occurs once every four rising edges of the master clock, the logical clock for different DDS boards can be up to three master clock cycles apart. This is why the DDS boards have a synchronization function, whereby the logical clocks of nine “slave” DDS boards are aligned to the logical clock of one “master” DDS board.

Wherever timing signals are distributed to the boards, a clock distributor (Texas Instruments LMK00301 evaluation board) is used to ensure each board receives the signal at the same time without any relative phase delay.

### 4.2.3 Resonant transformers

Second harmonics of  $\mathcal{E}_{\text{rot}}$  on the rod electrodes can introduce systematic error into the experiment [51]. In addition, the amplitude of  $\mathcal{E}_{\text{rot}}$  generating voltages must be quite high ( $429 V_{\text{pk}}$  in order to reach 60 V/cm). In order to deal with both of these issues, the voltages coming out of the DDS are amplified with a PA94 high-voltage op-amp with a gain of 100, and then applied to the electrodes through a resonant transformer circuit, which provides extra gain on resonance (re-



ducing the requirement on the source voltages) and also attenuation of higher harmonics generated by nonlinearity in the voltage sources.

In addition, the rest of the voltages are introduced to the electrodes through various couplings based around the resonant transformer design. The rod driver consists of four identical circuits which each drive a set of two rod electrodes furthest from each other (e.g. rod 1 and rod 5). The rod driver electronics are designed to apply the following different voltages to each of these pairs of electrodes:

- An independent DC shim voltage for each rod
- $V_{\text{RF}}$  at 50 kHz with the same phase and amplitude.
- $V_{\text{rot}}$  at 150 kHz with the same phase and opposite sign. This must have suppressed higher harmonics to prevent systematic effects

In order to apply these voltages to the same electrodes, the following scheme is used, with the circuit diagram in Figure 4.12 and a photo in Figure 4.13:

$V_{\text{rot}}$  is applied via a transformer whose inductance paired with the capacitance on the electrode forms a resonant circuit. This allows resonant enhancement of the gain and suppression of higher harmonics due to nonlinearity in the DDS voltage or the op-amps. In addition, ground can be defined relative to the center tap of the transformer, allowing each rod to receive opposite polarity of  $V_{\text{rot}}$ .  $V_{\text{RF}}$  is then applied to the center tap of the secondary side of the transformer. This way,  $V_{\text{RF}}$  is applied with the same polarity to both rods, and the inductance on either side of the secondary partially cancels out, and with  $\omega_{\text{RF}}$  far away from the resulting resonance this portion of the circuit can be driven non-resonantly. Finally, DC shims are applied to each rod individually with a resistive coupling.

The voltages on the rods can be measured via a resistive voltage divider to ground (resistors  $R_Q$  and  $R_{\text{gain}}$ ). This resistance to ground both limits the quality factor of the resonance, and offers a point to measure the voltage. The values are chosen with  $R_{\text{gain}} \ll R_Q$  so that the voltage is divided from high voltage down to a voltage more suitable to read with a scope. In addition, this ratio

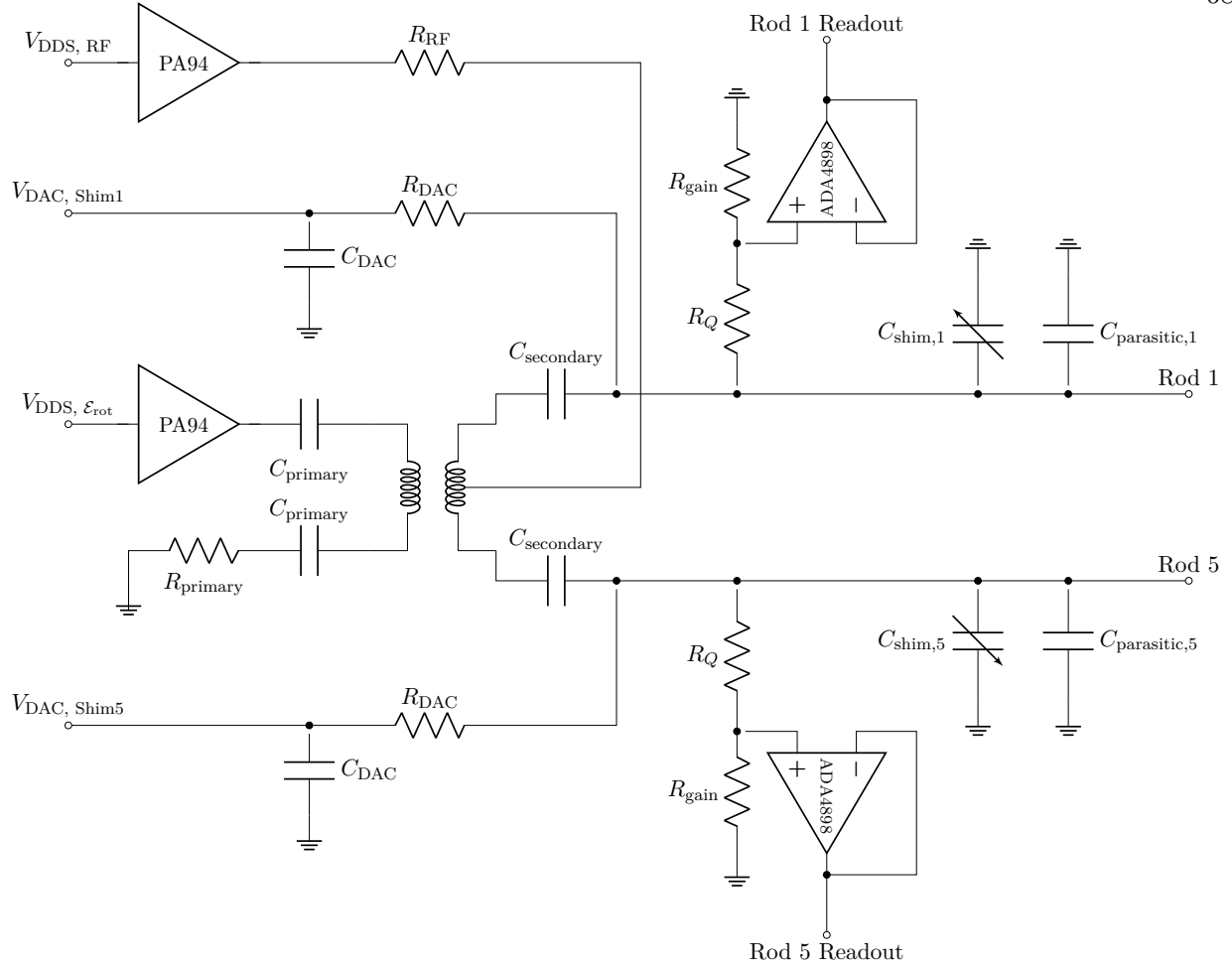


Figure 4.12: Circuit for driving the rod electrodes.

ensures that parasitics introduced by the measurement circuit do not interfere with the resonance. The readout is done with an isolation op-amp of unity gain, in a voltage follower configuration.

$C_{\text{primary}}$  and  $R_{\text{primary}}$  are designed to protect the op-amp that drives the primary. The capacitive coupling means that any DC signal on the input to the op-amp sees a high impedance, and  $R_{\text{primary}}$  limits the current sourced from the op-amp. In addition, the values are chosen such that the resonance of the primary given by

$$\omega_{\text{primary}} = \frac{1}{\sqrt{L_{\text{primary}}(\frac{1}{2}C_{\text{primary}})}} \quad (4.35)$$

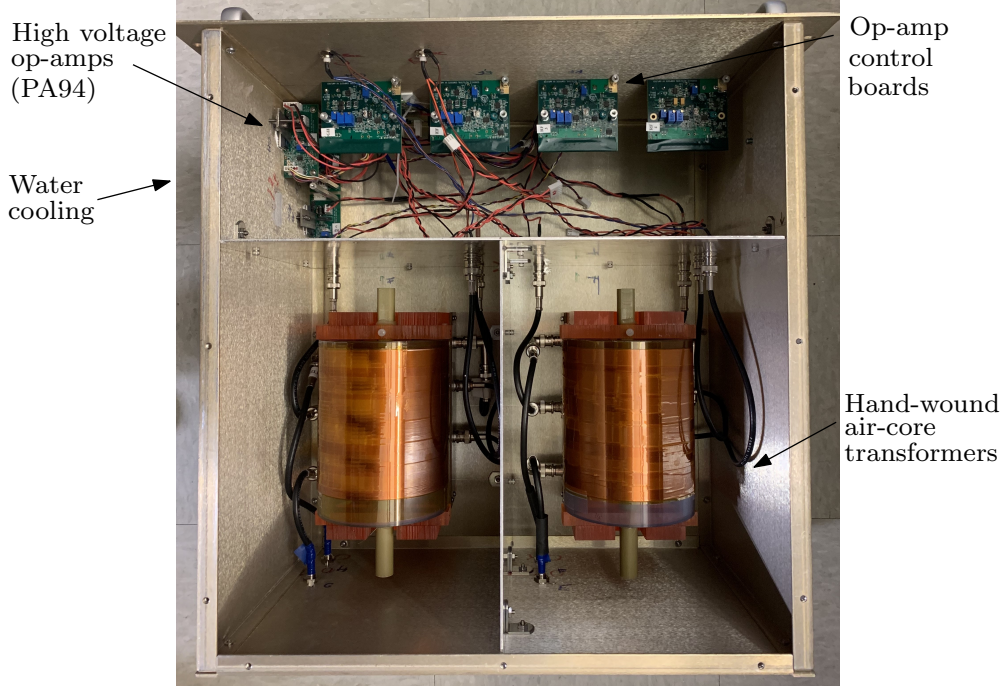


Figure 4.13: Photo of the rod-driver box. The PA94 op-amps are thermally coupled to the wall of the enclosure. On the other side of the enclosure is a thermal block containing a copper pipe flowing cold water to regulate the temperature of the op-amps. The transformers are each placed in a shielding Faraday cage to prevent coupling between channels or pickup from external sources.

is far away from the desired resonant frequency, i.e.

$$\omega_{\text{primary}} \ll \omega_0. \quad (4.36)$$

The value of  $R_{\text{primary}}$  is discussed further in Section 4.2.4.2, and the values settled on are

$$\begin{cases} R_{\text{primary}} = 100 \Omega \\ C_{\text{primary}} = 33 \text{ nF}. \end{cases} \quad (4.37)$$

$C_{\text{secondary}}$ ,  $R_{\text{DAC}}$ , and  $C_{\text{DAC}}$  are chosen to allow the shim channels to address the DC components of the rod voltages independently from the AC components. The capacitors should look like shorts in the 100 kHz regime but open to DC voltages. Furthermore,  $R_{\text{DAC}}$  should be large compared to the reactances of the circuit in this regime.  $C_{\text{DAC}}$  protects the DAC from any RF that has made it through  $R_{\text{DAC}}$  by sending it to ground. The values chosen to satisfy the above

requirements are:

$$\begin{cases} C_{secondary} = 100 \text{ nF} \\ C_{DAC} = 100 \text{ nF} \\ R_{DAC} = 1 \text{ M}\Omega. \end{cases} \quad (4.38)$$

Finally,  $C_{parasitic}$  is the parasitic capacitance both in the cabling and arising from the geometry of the rod electrodes. The capacitance is measured to be

$$C_{parasitic} = \underbrace{36 \text{ pF}}_{\text{cable transformer} \rightarrow \text{monitor}} + \underbrace{60 \text{ pF}}_{\text{cable monitor} \rightarrow \text{vacuum}} + \underbrace{63 \text{ pF}}_{\text{inside vacuum chamber}} = 158 \text{ pF}. \quad (4.39)$$

In order to correct for asymmetries in the system,  $C_{shim}$  is a variable capacitor with a range of 30 pF that can be tuned until all rods have equal capacitances to ground.

#### 4.2.4 Transformer theory

In order to treat the center tapped transformer, we treat the center tapped transformer as two separate transformers, as in Figure 4.14.

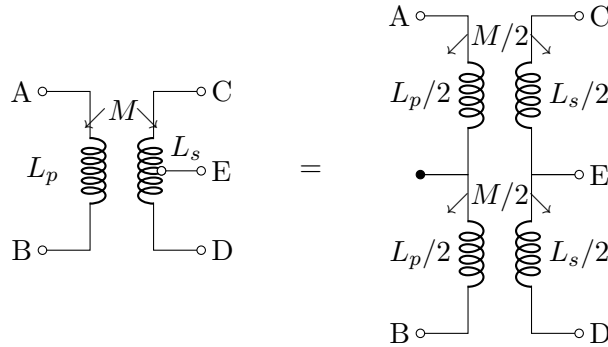


Figure 4.14: Equivalent circuit for a center tapped transformer

We can then write out the dynamics of this split transformer in terms of the induced voltages across each inductor. Let  $V_{A,B}$  be the voltage between terminals A and B and  $i_{A \rightarrow B}$  be the current

flowing from terminal A towards terminal B. The equations governing the transformer are then:

$$\begin{cases} V_{A,B} = -L_p \frac{di_{A \rightarrow B}}{dt} + \frac{M}{2} \left( \frac{di_{C \rightarrow E}}{dt} - \frac{di_{D \rightarrow E}}{dt} \right) \\ V_{C,E} = -\frac{L_s}{2} \frac{di_{C \rightarrow E}}{dt} + \frac{M}{2} \frac{di_{A \rightarrow B}}{dt} \\ V_{D,E} = -\frac{L_s}{2} \frac{di_{D \rightarrow E}}{dt} - \frac{M}{2} \frac{di_{A \rightarrow B}}{dt}. \end{cases} \quad (4.40)$$

#### 4.2.4.1 Resonance

The above equation is a fully general description of the transformer. To describe the resonance of the circuit at  $\omega_{\text{rot}}$ , we can apply this analysis to the transformer in Figure 4.12, with a few simplifying assumptions. First we can assume that the circuit is symmetric, i.e. the impedance on each rod is the same. Because the voltage at the center tap is set by  $V_{\text{RF}}$ , we can think of this voltage as ground in the  $\omega_{\text{rot}}$  frequency analysis. Finally,  $C_{\text{secondary}}$  offers a negligible reactance at  $\omega_{\text{rot}}$  (by design), so we can ignore this component. With this assumption, the voltage at the rods is exactly the voltage across the terminals of the secondary coils. In addition, the currents and voltages across the output are equal and opposite due to the symmetry of the system:

$$\begin{cases} i_{D \rightarrow E} = -i_{C \rightarrow E} \\ V_{D,E} = -V_{C,E}, \end{cases} \quad (4.41)$$

so the system given by Equation 4.40 reduces to

$$\begin{cases} V_{A,B} = -L_p \frac{di_{A \rightarrow B}}{dt} + M \frac{di_{C \rightarrow E}}{dt} \\ V_{C,E} = \frac{1}{2} \left( -L_s \frac{di_{C \rightarrow E}}{dt} + M \frac{di_{A \rightarrow B}}{dt} \right). \end{cases} \quad (4.42)$$

If the voltages and currents are periodic with frequency  $\omega$  then the time derivatives in the above equation act to simply multiply by  $j\omega$ , so the system of differential equations becomes a simple system of linear equations

$$\begin{cases} V_{A,B} = j\omega (-L_p i_{A \rightarrow B} + M i_{C \rightarrow E}) \\ V_{C,E} = \frac{1}{2} j\omega (-L_s i_{C \rightarrow E} + M i_{A \rightarrow B}). \end{cases} \quad (4.43)$$

We can then express the currents and voltages above in terms of elements of the circuit. If  $Z_{primary}$  is all impedance in series with the primary,

$$Z_{primary} = R_{primary} + \frac{2}{j\omega C_{primary}}. \quad (4.44)$$

Then the voltage across the primary is equal to the voltage  $V_{source}$  driven by the op-amp minus any voltage drop due to this series impedance:

$$V_{A,B} = V_{source} - (-i_{A \rightarrow B})Z_{primary}. \quad (4.45)$$

Next, we can write an impedance from the rod to ground

$$Z_{rod} = (R_Q + R_{gain}) \parallel \left( \frac{1}{j\omega(C_{parasitic} + C_{shim})} \right) \quad (4.46)$$

$$= \left( \frac{1}{R_Q + R_{gain}} + j\omega(C_{parasitic} + C_{shim}) \right)^{-1}, \quad (4.47)$$

so the current across the rod is given by

$$i_{C \rightarrow E} = V_{C,E} / Z_{rod}. \quad (4.48)$$

If we plug Equations 4.45 and 4.48 into Equation 4.43, we get

$$\begin{cases} V_{source} + i_{A \rightarrow B} Z_{primary} = j\omega \left( -L_p i_{A \rightarrow B} + M \frac{V_{C,E}}{Z_{rod}} \right) \\ V_{C,E} = j\omega \left( -\frac{L_s}{2} \frac{V_{C,E}}{Z_{rod}} + \frac{M}{2} i_{A \rightarrow B} \right). \end{cases} \quad (4.49)$$

We can now solve this system of equations to get the current on the source  $i_{A \rightarrow B}$  and the voltage on a rod  $V_{C,E}$ :

$$V_{C,E} = V_{source} \left( \frac{j\omega M Z_{rod}}{\omega^2 (L_p L_s - M^2) - j\omega (L_s Z_{primary} + 2L_p Z_{rod}) - 2Z_{primary} Z_{rod}} \right) \quad (4.50)$$

$$i_{A \rightarrow B} = V_{source} \left( \frac{(2Z_{rod} + j\omega L_s)}{\omega^2 (L_p L_s - M^2) - j\omega (L_s Z_{primary} + 2L_p Z_{rod}) - 2Z_{primary} Z_{rod}} \right). \quad (4.51)$$

This encapsulates the resonant behavior of the circuit. The voltage is plotted in Figure 4.15. The validity of Equation 4.50 is verified numerically in Section 4.2.4.2.

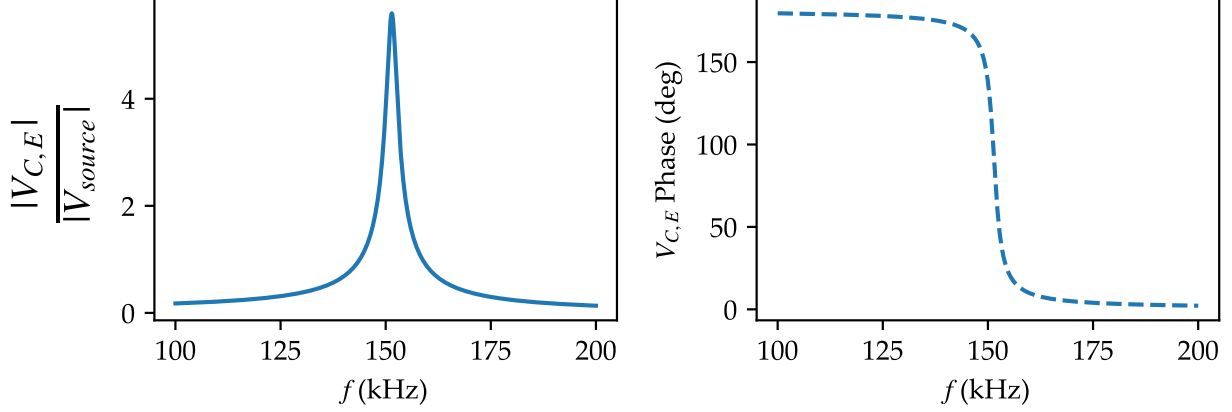


Figure 4.15: Amplitude (left) and phase (right) plots of the solution to the voltage on a rod from Equation 4.50 as a function of the driven frequency  $f$ . Standard component values are used:  $L_p = L_s = 11.5$  mH,  $M = 0.2L_p$ ,  $R_Q = 300$  k $\Omega$ ,  $R_{gain} = 1$  k $\Omega$ ,  $C_{par} = 200$  pF,  $C_{primary} = 33$  nF,  $R_{primary} = 100$   $\Omega$ .

Solving analytically for the resonant frequency and quality factor is difficult with the above equation. To do this, we must first make some approximations. The capacitance in series has a small reactance compared to other impedances in the circuit, so we can neglect its effect by taking  $C_{primary} \rightarrow \infty$ . While in reality,  $R_{primary}$  may not be negligible compared to other impedances, it is instructive to take it to zero to calculate the resonant frequency, and will discuss its effect in Section 4.2.4.2. We then take  $R_{primary} \rightarrow 0$ . Finally, since  $R_{gain} \ll R_Q$  by design, we can approximate the resistance to ground as only arising from  $R_Q$ , i.e.  $R_{gain} \rightarrow 0$ . With this, the gain  $G = |V_{C,E}/V_{source}|$  of the transformer on the rod is

$$G = \frac{\omega M R_Q}{\sqrt{R_Q^2 \omega^2 (C_{par} \omega^2 (M^2 - L_p L_s) + 2L_p)^2 + \omega^4 (M^2 - L_p L_s)^2}}. \quad (4.52)$$

The resonant frequency can be found by setting  $\frac{dG}{d\omega} = 0$  :

$$\omega_0 = \sqrt{\frac{1 - \frac{(L_p L_s - M^2)}{4L_p C_{par} R_Q^2}}{\frac{C_{par}}{2L_p} (L_p L_s - M^2)}}. \quad (4.53)$$

With the appropriate mapping of variables (and using the definition  $M = K\sqrt{L_p L_s}$ ), this result corroborates that of the analysis in Kia Boon Ng's thesis [39]. If the second term in the numerator

is small ( $\frac{L_p L_s - M^2}{4L_p C_{par} R_Q^2} \ll 1$ ), then a good approximation for the resonant frequency is given by

$$\omega_0 \approx \left( \frac{C_{par}}{2L_p} (L_p L_s - M^2) \right)^{-1/2}. \quad (4.54)$$

The quality factor can be found by solving  $G(\omega) = \frac{G(\omega_0)}{2}$  for  $\omega$  to find the half-max frequencies, and taking the difference of the two solutions. Using this method, the full width at half max  $\Delta\omega$  is

$$\Delta\omega = \frac{1}{C_{par} R_Q \sqrt{2(L_p L_s - M^2)}} \left( \sqrt{4C_{par} L_p R_Q^2 - L_p L_s + M^2 + \sqrt{3(L_p L_s - M^2)(8C_{par} L_p R_Q^2 - L_p L_s + M^2)}} - \sqrt{4C_{par} L_p R_Q^2 - L_p L_s + M^2 - \sqrt{3(L_p L_s - M^2)(8C_{par} L_p R_Q^2 - L_p L_s + M^2)}} \right). \quad (4.55)$$

Parameterizing in terms of the small variable

$$\epsilon \equiv \frac{L_p L_s - M^2}{C_{par} L_p R_Q^2} \quad (4.56)$$

(which for our values is of order  $10^{-3}$ ), we can expand the full width half max as

$$\Delta\omega = \frac{1}{R_Q C_{par}} \left( \sqrt{3} + \frac{3\sqrt{3}}{16} \epsilon + \frac{63\sqrt{3}}{512} \epsilon^2 + \mathcal{O}(\epsilon^3) \right). \quad (4.57)$$

Keeping only the first term is sufficient to reach 99.9% accuracy, giving us a quality factor of

$$Q = \frac{\omega_0}{\Delta\omega} \approx \frac{1}{\sqrt{3}} R_Q C_{par} \omega_0. \quad (4.58)$$

Finally, the gain on resonance is approximately given by

$$G(\omega_0) \approx \frac{1}{\sqrt{2}} \frac{M}{L_p} \sqrt{\frac{C_{par} L_p R_Q^2}{L_p L_s - M^2}} \approx \frac{\sqrt{3}}{2} \frac{M}{L_p} Q. \quad (4.59)$$

#### 4.2.4.2 Series resistance on primary

Including effects of  $C_{primary}$  and  $R_{primary}$  in the analysis performed in the previous section causes the analytic solution to become intractable. Qualitatively,  $C_{primary}$  has only negligible effect on the system in the range of nanofarads and above, while  $R_{primary}$  severely affects the



quality factor and thus the gain. To discuss this effect, we will move away from arguing via analytic expressions and instead demonstrate the effect using numerical solutions. In addition, we can verify our analytic expressions by comparing their numerical result with that of a circuit simulation program (LTspice<sup>®</sup>). This is done in Figure 4.16 to demonstrate the effect of  $R_{primary}$  on the gain.

When  $R_{primary}$  becomes large enough to be the same order of magnitude as the reactances characteristic of the resonant circuit's capacitors and inductors ( $\left| \frac{1}{j\omega(C_{par}/2)} \right| \sim |j\omega L_p| \sim 10 \text{ k}\Omega$ ), it starts to dampen Q and thus also reduces the gain of the circuit. The resonant frequency is also slightly shifted downwards.

The reason to include an  $R_{primary}$  is to limit current sourced by the op-amp. The effects of  $R_{primary}$  on requirements of the op-amp are explored in Figure 4.17. We can choose its value in order to satisfy the requirements of the PA94. The op-amp should be operated sufficiently far enough away from its maximum current capability (100 mA) and from the voltage of the rails ( $\pm 343 \text{ V}$ ) in order to prevent saturation and nonlinearity. In the end, a value of  $R_{primary}=100 \text{ }\Omega$  was used in the interest of maximizing gain, and the current draw is still far away from the limit of the op-amp.

#### 4.2.5 Coupling between rods

In addition to having parasitic capacitance to ground, neighboring rods also have parasitic capacitance between them. An approximation of the coupling capacitances can be made from the geometry of the rods. If the rods have a radius  $a$  and length  $L$  and are separated by a distance  $d$ , then for a rod with a charge per unit length  $q$  the electric field due to the rod is given by

$$E = \frac{q}{2\pi\epsilon_0 r}. \quad (4.60)$$

Then the voltage between the two rods is given by

$$V = \int_a^{d-a} E(r) dr = \frac{q}{2\pi\epsilon_0} \ln r \Big|_{r=a}^{r=d-a} = \frac{q}{2\pi\epsilon_0} \ln \frac{d-a}{a}. \quad (4.61)$$

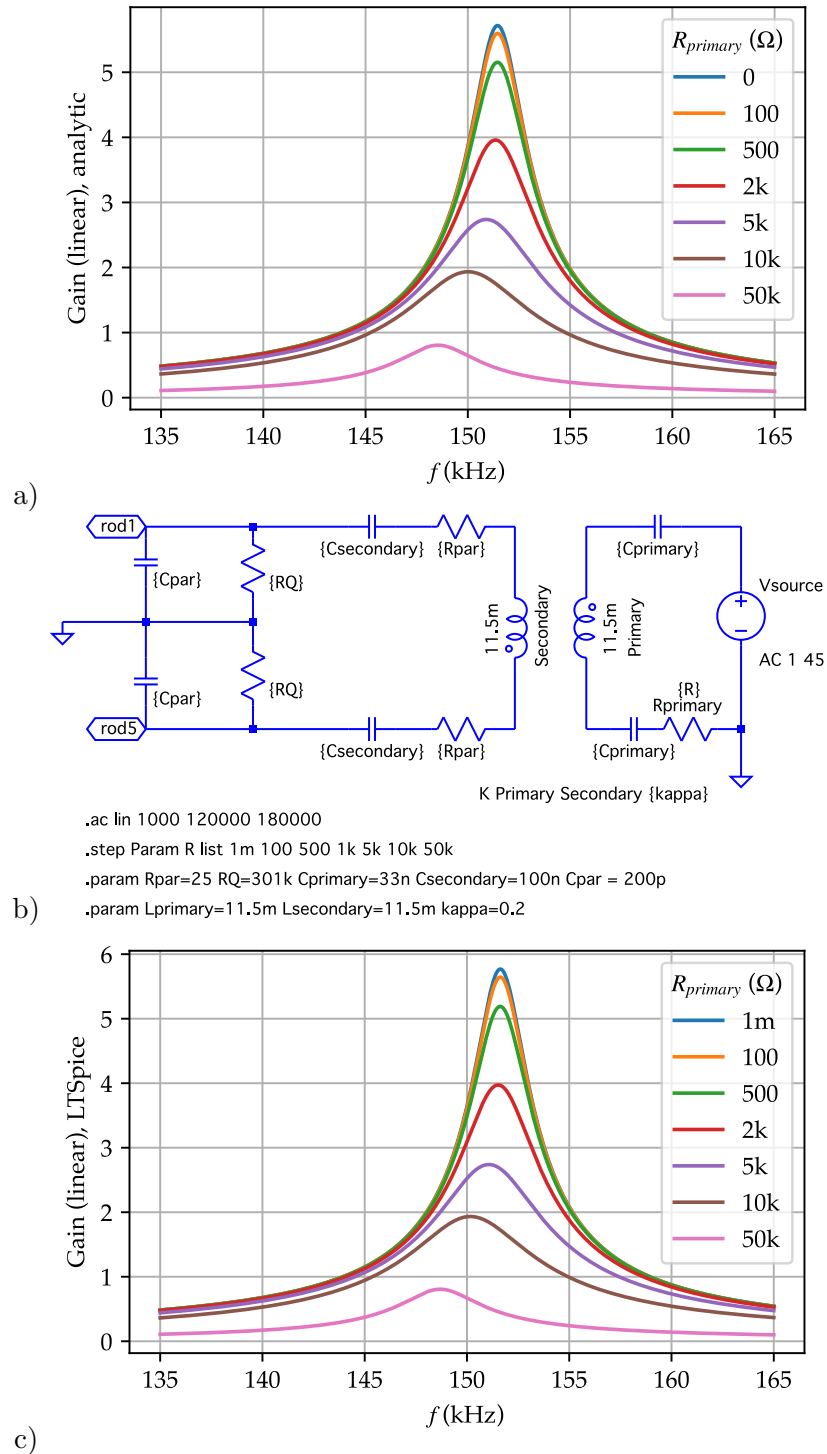


Figure 4.16: Effect of  $R_{primary}$  on the gain of the resonant circuit. a) Analytic calculation using Equation 4.50. The gain profile of the rod voltage from the source voltage is plotted for various values of  $R_{primary}$ . b) LTSpice model of the resonant circuit c) LTSpice calculation confirming the analytic result. Resistances in the software cannot go to zero, so  $R_{primary}$  is only probed down to 1 m $\Omega$ .

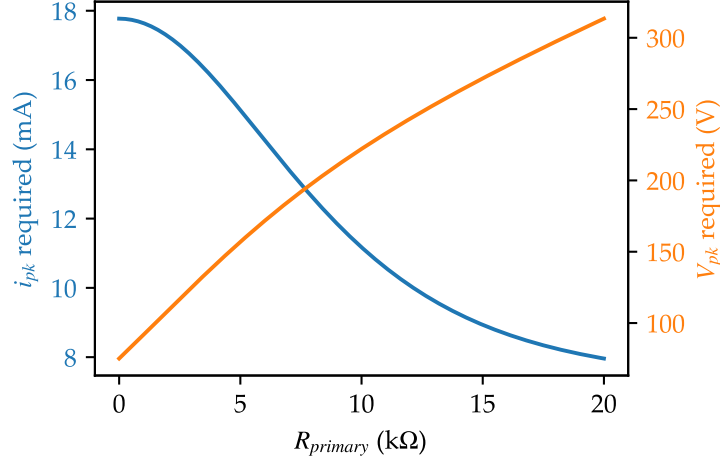


Figure 4.17: Effect of  $R_{primary}$  on current requirements for the op-amp driving  $V_{rot}$ .  $i_{pk}$  required is the current needed to drive 60 V/cm on the rods on resonance, while the primary is driven at whatever voltage is needed to produce 60 V/cm. It is calculated as  $429 V \cdot \left| \frac{i_{A \rightarrow B}}{V_{C,E}} \right|_{\omega=\omega_0}$ . Similarly,  $V_{pk}$  required is the voltage the op-amps need to put out in order to drive 60 V/cm on the rods on resonance, calculated as  $429 V \cdot \left| \frac{V_{source}}{V_{C,E}} \right|_{\omega=\omega_0}$ . These quantities are calculated using the analytic expressions in Equations 4.50 and 4.51. In reality, the required voltages and currents are higher than in this figure due to parasitics that dampen the gain, but the above plot offers a qualitative description of the function of  $R_{primary}$  in limiting current.

The rod-rod capacitance is then given by

$$C = \frac{qL}{V} = \frac{L\pi\epsilon_0}{\ln \frac{d-a}{a}}. \quad (4.62)$$

This calculation neglects edge effects, and a more accurate capacitance can be calculated using finite element software (COMSOL) with realistic geometry. If the rods are arranged at a radius  $r_{rod}$  from the origin and are spaced at an angle  $\frac{2\pi}{8}$  radians apart, then the distance between  $n$ th nearest neighbors is given by

$$d_n = \left| \left( r_{rod} \cos\left(n \frac{2\pi}{8}\right), r_{rod} \sin\left(n \frac{2\pi}{8}\right) \right) - (r_{rod}, 0) \right| \quad (4.63)$$

$$= r_{rod} \sqrt{\left(\cos\left(\frac{n\pi}{4}\right) - 1\right)^2 + \sin^2\left(\frac{n\pi}{4}\right)} \quad (4.64)$$

$$= r_{rod} \sqrt{2 - 2 \cos\left(\frac{n\pi}{4}\right)}. \quad (4.65)$$

Given that the rod electrodes have a radius  $a = 6.35$  mm, a length  $L = 123.24$  cm, and are located at  $r_{rod} = 5.85$  cm, we can calculate the rod-rod couplings, given in Table 4.1.

Coupling	$d_n$ (cm)	Analytic approximation (pF)	Finite element calculation (pF)
Nearest neighbor	4.48	19.0	18.0
2 <sup>nd</sup> nearest neighbor	8.27	13.8	13.8
3 <sup>rd</sup> nearest neighbor	10.81	12.3	12.6
4 <sup>th</sup> nearest neighbor	11.70	12.0	12.2

Table 4.1: Capacitance between pairs of rod electrodes based on their theoretical geometric coupling. The distances  $d_n$  are calculated using Equation 4.65 and the analytic approximation is calculated using Equation 4.62. The couplings may be modified by shielding from other electrodes, but this effect has not been modeled.

The capacitance leads to two overall effects. Firstly, the capacitances act to reduce the main resonant frequency of the circuit, since it adds additional capacitance pathways to ground effectively increasing  $C_{par}$ .

Secondly, when only one channel is driven and the other voltage supplies are held at zero volts a second resonance arises. To understand this, first let's look at what happens when a channel is not driven. In this case, each other voltage supply looks like a short, so each transformer just looks like an inductor (argued in Figure 4.18).

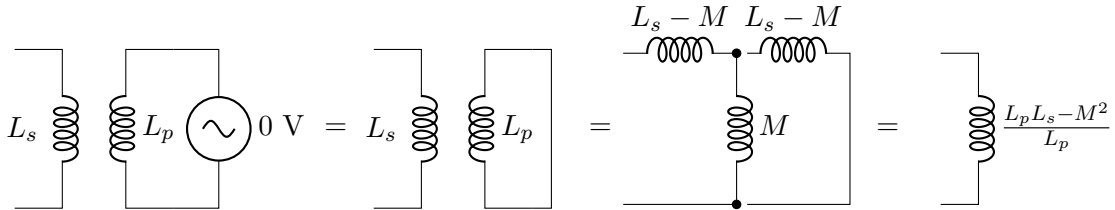


Figure 4.18: Treatment of a transformer driven at 0 V, equivalent to an inductor. The transformation of the third equivalence is given by the equivalent circuit prescribed in [56]. While this transformation makes assumptions about relative grounds, the same result arises from writing out the governing equations of the transformer (allowing for different relative grounds) and requiring the voltage across the primary to be 0 V.

We can then think of each coupling as an additional impedance network between the rods. The conceptual reduction is shown in Figure 4.19.

So each parasitic coupling to an undriven transformer can be modeled as an additional impedance between rods of

$$Z_{coup,i} = \frac{1}{j\omega C_{coup,i}} + \left( R_Q \parallel \frac{1}{j\omega C_{par}} \parallel j\omega \frac{L_p L_s - M^2}{L_p} \right) + \frac{1}{j\omega C_{coup,i}}. \quad (4.66)$$

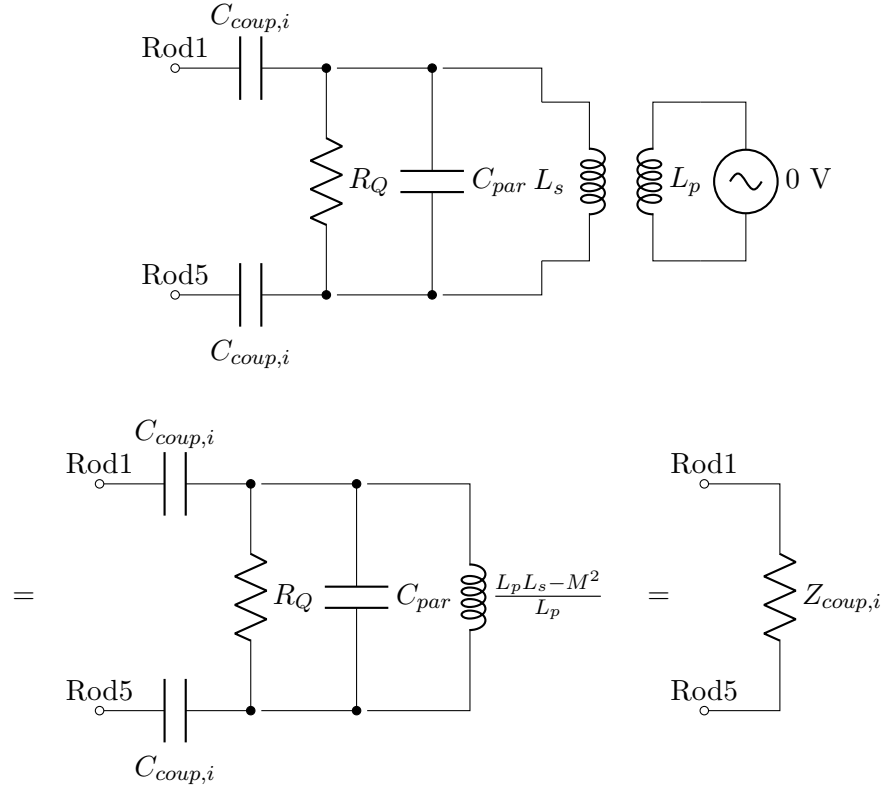


Figure 4.19: Schematic reduction of the rod electrodes to another (undriven) rod-pair into a single complex impedance  $Z_{coup,i}$

We can then include the effect of the couplings by modifying Equation 4.50 with additional impedances to ground

$$Z_{rod} \rightarrow \left( \frac{1}{Z_{rod}} + \sum_i \frac{1}{Z_{coup,i}/2} \right)^{-1}. \quad (4.67)$$

Each coupling adds an additional resonance, since each coupling has its own set of inductance and capacitance which can behave resonantly.

An expanded LTspice model, shown in Figure 4.20, contains four separately driven transformers with all the relevant rod-rod couplings. The values of the coupling capacitors are taken to be the COMSOL values from Table 4.1.

The effect of the capacitances is shown in Figure 4.21. The qualitative effect of the coupling is to create a dual resonance when only one channel is driven. However, if all channels are driven at their respective phase, the effect of the coupling cancels out and the system exhibits a symmetric

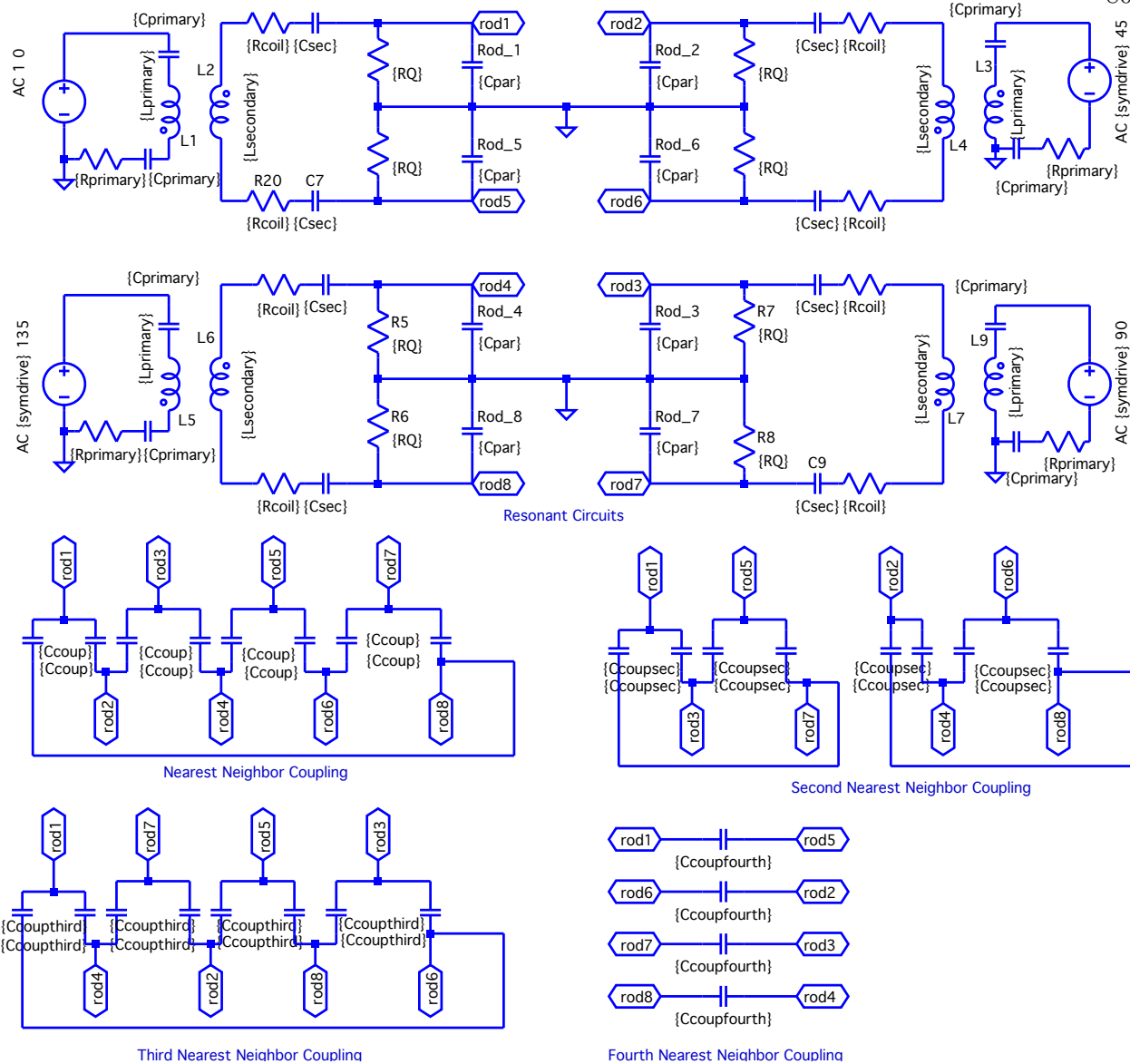


Figure 4.20: LTspice model for the four parasitically coupled resonant circuits, including all capacitive rod-rod couplings

single resonance. The figure also shows the measured response of the system, which exhibits the same qualitative behavior.

The model differs from the measured behavior in two ways. First, the resonant frequency of the actual transformer system is higher than that predicted by the model. In addition, the quality factor of the actual transformer system is lower than that of the model. This is likely due

to additional parasitic impedances in the system that are not modeled.

In addition, the difference between the resonant response of each channel is due to a combination of different inductances and couplings of each transformer, as well as asymmetry in the capacitive coupling network.

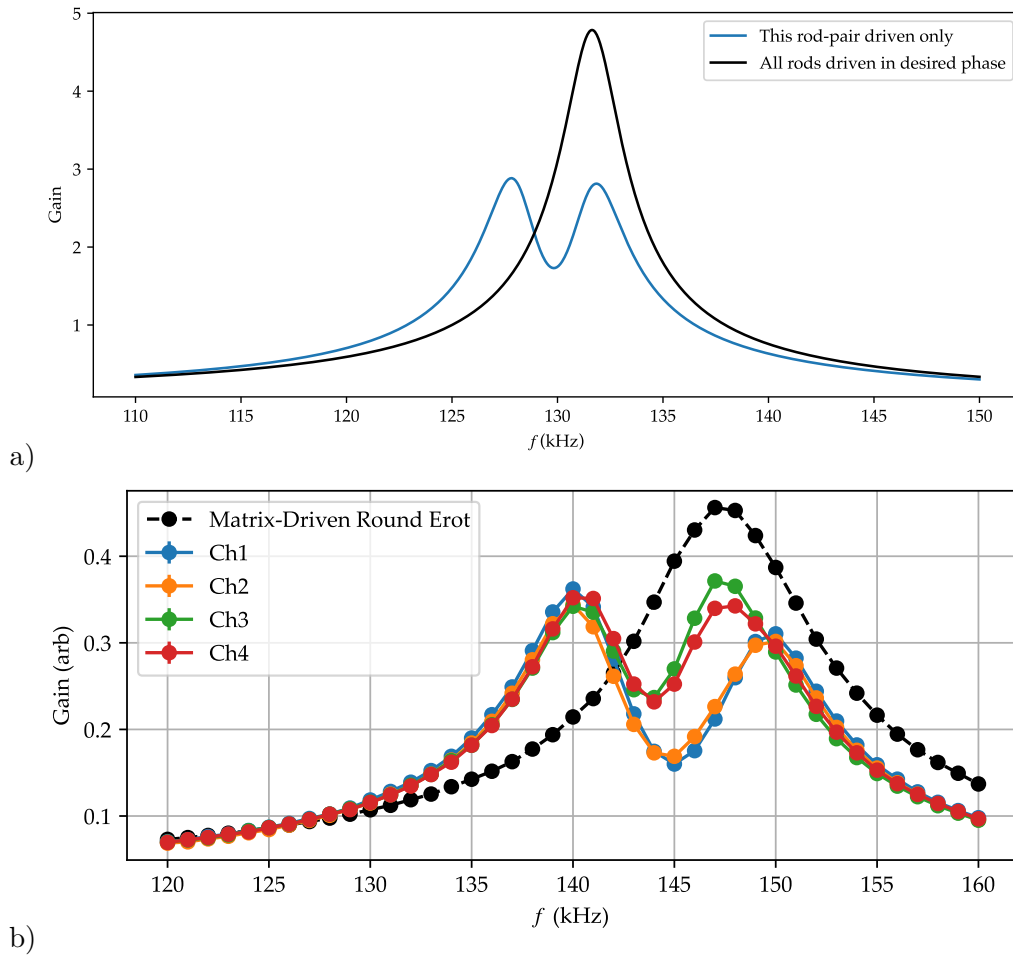


Figure 4.21: Demonstration of the dual resonance behavior arising from parasitic capacitive coupling between rods.

a) LTspice simulation of the coupled resonance.

b) Measured gain profile of the resonant circuit using the monitor box readout. The gain of each channel represents writing a fixed amplitude to a single transformer and taking the difference of the two relevant rod electrodes. For example, Ch1 represents the difference of rod 5 and rod 1, while Ch2 represents the difference between rod 6 and rod 2. The black line represents using the method described in Section 4.2.6 to produce a symmetric set of voltages on the rods at each frequency, and the value reported is the maximum symmetric amplitude that can be made.

### 4.2.6 Control matrix

Due to asymmetry the coupling between adjacent rods described in the previous section, the voltages on the rods can have significant difference in both phase and relative amplitude to the voltages applied to the sources. In order to generate the voltages we desire on the rods, some control theory must be applied in order to choose the voltages applied via the sources.

Because we are driving the system with four sources, it is convenient to only have four output voltages to keep track of. We can separate the fields produced by the rods into their common mode and differential voltages ( $V_{\text{diff},1,5} = V_{\text{rod}1} - V_{\text{rod}5}$ ,  $V_{\text{comm},1,5} = V_{\text{rod}1} + V_{\text{rod}5}$ ). If each transformer circuit is sufficiently symmetric ( $V_{\text{rod}1} \approx -V_{\text{rod}5}$ ), then we can ignore the common mode term, as its effect looks like a small oscillating quadrupole field. While this term can actually generate enough of a ponderomotive potential to lose ions if it is as large as 0.5 V/cm within the ion cloud (given by Equation 4.34), it can be compensated by applying a small amount of  $\omega_{\text{rot}}$  oscillating potential onto the RF-generating DDS until the ions are no longer kicked out of the trap. The differential term then becomes the one that contributes to  $\mathcal{E}_{\text{rot}}$ . Thus, rather than measuring all 8 rod voltages, we need only to keep track of the difference of the voltage on opposite rod pairs. We can then characterize the system with a mapping from each voltage source to the difference of the two rods connected to that source's transformer.

While applying a resonant voltage to each rod does drive all other rods with varying amplitudes and phases, the response of the system is linear in the in phase (I) and quadrature (Q) basis. Therefore, the response of the system can be represented with a matrix.

The basis for describing the  $V_{\text{rot}}$  on each rod-pair is defined to be



$$\vec{V} = \begin{pmatrix} I_1 \\ Q_1 \\ I_2 \\ Q_2 \\ I_3 \\ Q_3 \\ I_4 \\ Q_4 \end{pmatrix} \quad (4.68)$$

where each element is the in-phase and quadrature component for each channel, i.e. the voltage on channel 1 is given by

$$v_1(t) \equiv I_1 \cos(2\pi\omega_{\text{rot}}t) + Q_1 \sin(2\pi\omega_{\text{rot}}t). \quad (4.69)$$

We can then write a matrix  $M$  such that

$$\vec{V}_{\text{rods}} = M\vec{V}_{\text{dds}} \quad (4.70)$$

which fully characterizes the gain and phase shift of each channel, as well as all parasitic couplings between channels. We can then produce any arbitrary set of voltages on the rods by inverting the matrix:

$$\vec{V}_{\text{dds}} = M^{-1}\vec{V}_{\text{rods}}. \quad (4.71)$$

A symmetry requirement of the matrix is that a time shift on the input will shift the output by the same amount without changing anything else. This is equivalent to saying that global phase does not change the response of the system. This can be represented mathematically with a global phase shift operator  $R(\theta)$ . Phase shifting the input and looking at the output (represented as  $R(\theta)M$ ) should be the same as just phase shifting the output and phase shifting (represented as  $MR(\theta)$ ). In other words, our matrix must commute with the global phase operator.

Global phase is achieved by applying a phase shift to each channel, meaning applying a

rotation matrix to each pair of I,Q. This is represented in our space as a block diagonal matrix:

$$R(\theta) = \begin{pmatrix} \cos(\theta) & -\sin(\theta) & 0 & 0 & 0 & 0 & 0 & 0 \\ \sin(\theta) & \cos(\theta) & 0 & 0 & 0 & 0 & 0 & 0 \\ 0 & 0 & \cos(\theta) & -\sin(\theta) & 0 & 0 & 0 & 0 \\ 0 & 0 & \sin(\theta) & \cos(\theta) & 0 & 0 & 0 & 0 \\ 0 & 0 & 0 & 0 & \cos(\theta) & -\sin(\theta) & 0 & 0 \\ 0 & 0 & 0 & 0 & \sin(\theta) & \cos(\theta) & 0 & 0 \\ 0 & 0 & 0 & 0 & 0 & 0 & \cos(\theta) & -\sin(\theta) \\ 0 & 0 & 0 & 0 & 0 & 0 & \sin(\theta) & \cos(\theta) \end{pmatrix}. \quad (4.72)$$

For a general matrix  $M$  with elements  $m_{i,j}$ , our symmetry requirement is that the commutator

$$R(\theta)M - MR(\theta) = \begin{pmatrix} -m_{1,2} - m_{2,1} & m_{1,1} - m_{2,2} & -m_{1,4} - m_{2,3} & m_{1,3} - m_{2,4} & -m_{1,6} - m_{2,5} & m_{1,5} - m_{2,6} & -m_{1,8} - m_{2,7} & m_{1,7} - m_{2,8} \\ m_{1,1} - m_{2,2} & m_{1,2} + m_{2,1} & m_{1,3} - m_{2,4} & m_{1,4} + m_{2,3} & m_{1,5} - m_{2,6} & m_{1,6} + m_{2,5} & m_{1,7} - m_{2,8} & m_{1,8} + m_{2,7} \\ -m_{3,2} - m_{4,1} & m_{3,1} - m_{4,2} & -m_{3,4} - m_{4,3} & m_{3,3} - m_{4,4} & -m_{3,6} - m_{4,5} & m_{3,5} - m_{4,6} & -m_{3,8} - m_{4,7} & m_{3,7} - m_{4,8} \\ m_{3,1} - m_{4,2} & m_{3,2} + m_{4,1} & m_{3,3} - m_{4,4} & m_{3,4} + m_{4,3} & m_{3,5} - m_{4,6} & m_{3,6} + m_{4,5} & m_{3,7} - m_{4,8} & m_{3,8} + m_{4,7} \\ -m_{5,2} - m_{6,1} & m_{5,1} - m_{6,2} & -m_{5,4} - m_{6,3} & m_{5,3} - m_{6,4} & -m_{5,6} - m_{6,5} & m_{5,5} - m_{6,6} & -m_{5,8} - m_{6,7} & m_{5,7} - m_{6,8} \\ m_{5,1} - m_{6,2} & m_{5,2} + m_{6,1} & m_{5,3} - m_{6,4} & m_{5,4} + m_{6,3} & m_{5,5} - m_{6,6} & m_{5,6} + m_{6,5} & m_{5,7} - m_{6,8} & m_{5,8} + m_{6,7} \\ -m_{7,2} - m_{8,1} & m_{7,1} - m_{8,2} & -m_{7,4} - m_{8,3} & m_{7,3} - m_{8,4} & -m_{7,6} - m_{8,5} & m_{7,5} - m_{8,6} & -m_{7,8} - m_{8,7} & m_{7,7} - m_{8,8} \\ m_{7,1} - m_{8,2} & m_{7,2} + m_{8,1} & m_{7,3} - m_{8,4} & m_{7,4} + m_{8,3} & m_{7,5} - m_{8,6} & m_{7,6} + m_{8,5} & m_{7,7} - m_{8,8} & m_{7,8} + m_{8,7} \end{pmatrix} \quad (4.73)$$

must be identically zero for any phase  $\theta$ . This means that each element of the above array must be zero, which establishes a relationship between the elements of M. Put succinctly, if you divide up M into 2x2 blocks, the diagonal components of each block must be equal and the off-diagonal components must be opposite in sign but equal in magnitude.

One result of this symmetry is that the matrix can be measured in 4 steps by applying only an I-type signal to each input and then reading out the odd rows of the matrix. The even rows are then defined by the symmetry relationships.

Another result of the symmetry is that any feedback algorithms to fine-tune the matrix must be carefully crafted to ensure the symmetry is preserved. One such algorithm is as follows: once we have measured  $M$ , pick the desired set of outputs  $\vec{V}_d$  and use the measured matrix  $M$  to find the DDS voltages

$$\vec{v}_{\text{DDS}} = M^{-1}\vec{V}_d. \quad (4.74)$$

When  $\vec{v}_{\text{DDS}}$  is actually applied, a slightly different output is measured  $\vec{V}_m \neq \vec{V}_d$ . Then a feedback matrix can be chosen

$$N = \begin{pmatrix} \frac{V_{d1}V_{m1}+V_{d2}V_{m2}}{V_{m1}^2+V_{m2}^2} & \frac{V_{d1}V_{m2}-V_{d2}V_{m1}}{V_{m1}^2+V_{m2}^2} & 0 & 0 & 0 & 0 & 0 & 0 & 0 \\ \frac{V_{d2}V_{m1}-V_{d1}V_{m2}}{V_{m1}^2+V_{m2}^2} & \frac{V_{d1}V_{m1}+V_{d2}V_{m2}}{V_{m1}^2+V_{m2}^2} & 0 & 0 & 0 & 0 & 0 & 0 & 0 \\ 0 & 0 & \frac{V_{d3}V_{m3}+V_{d4}V_{m4}}{V_{m3}^2+V_{m4}^2} & \frac{V_{d3}V_{m4}-V_{d4}V_{m3}}{V_{m3}^2+V_{m4}^2} & 0 & 0 & 0 & 0 & 0 \\ 0 & 0 & \frac{V_{d4}V_{m3}-V_{d3}V_{m4}}{V_{m3}^2+V_{m4}^2} & \frac{V_{d3}V_{m3}+V_{d4}V_{m4}}{V_{m3}^2+V_{m4}^2} & 0 & 0 & 0 & 0 & 0 \\ 0 & 0 & 0 & 0 & \frac{V_{d5}V_{m5}+V_{d6}V_{m6}}{V_{m5}^2+V_{m6}^2} & \frac{V_{d5}V_{m6}-V_{d6}V_{m5}}{V_{m5}^2+V_{m6}^2} & 0 & 0 & 0 \\ 0 & 0 & 0 & 0 & \frac{V_{d6}V_{m5}-V_{d5}V_{m6}}{V_{m5}^2+V_{m6}^2} & \frac{V_{d5}V_{m5}+V_{d6}V_{m6}}{V_{m5}^2+V_{m6}^2} & 0 & 0 & 0 \\ 0 & 0 & 0 & 0 & 0 & 0 & \frac{V_{d7}V_{m7}+V_{d8}V_{m8}}{V_{m7}^2+V_{m8}^2} & \frac{V_{d7}V_{m8}-V_{d8}V_{m7}}{V_{m7}^2+V_{m8}^2} & 0 \\ 0 & 0 & 0 & 0 & 0 & 0 & \frac{V_{d8}V_{m7}-V_{d7}V_{m8}}{V_{m7}^2+V_{m8}^2} & \frac{V_{d7}V_{m7}+V_{d8}V_{m8}}{V_{m7}^2+V_{m8}^2} & 0 \end{pmatrix} \quad (4.75)$$

such that

$$\vec{V}_d = N\vec{V}_m. \quad (4.76)$$

Substituting this into Equation 4.74,

$$\vec{v}_{\text{DDS}} = M^{-1}N\vec{V}_m, \quad (4.77)$$

and  $M^{-1}N$  serves as a more accurate inverse transform matrix. We then update our characteristic matrix:

$$M' = (M^{-1}N)^{-1}. \quad (4.78)$$

Note that the matrix  $N$  was formulated specifically to commute with  $R(\theta)$  so that  $M'$  preserves global phase invariance. If a diagonal matrix is used instead, measurement noise can break the symmetry, causing instability when scanning trap times.

The measured matrix  $M$  of the system is displayed in Figure 4.22. Each 2x2 block represents a coupling from an input channel to an output channel. If there were no crosstalk between channels, the matrix would be block diagonal, and deviation from a block-diagonal matrix indicates strong couplings between channels. Within each 2x2 block, the diagonal components represent coupling without phase shift, while the off-diagonal components represent coupling with  $\pi/2$  phase shift.

After several iterations of feedback as in Equation 4.78, we are able to reach an  $\mathcal{E}_{\text{rot}}$  where each pair of rods has the same amplitude to within 0.1% and each phase is correct to within one tenth of a degree.

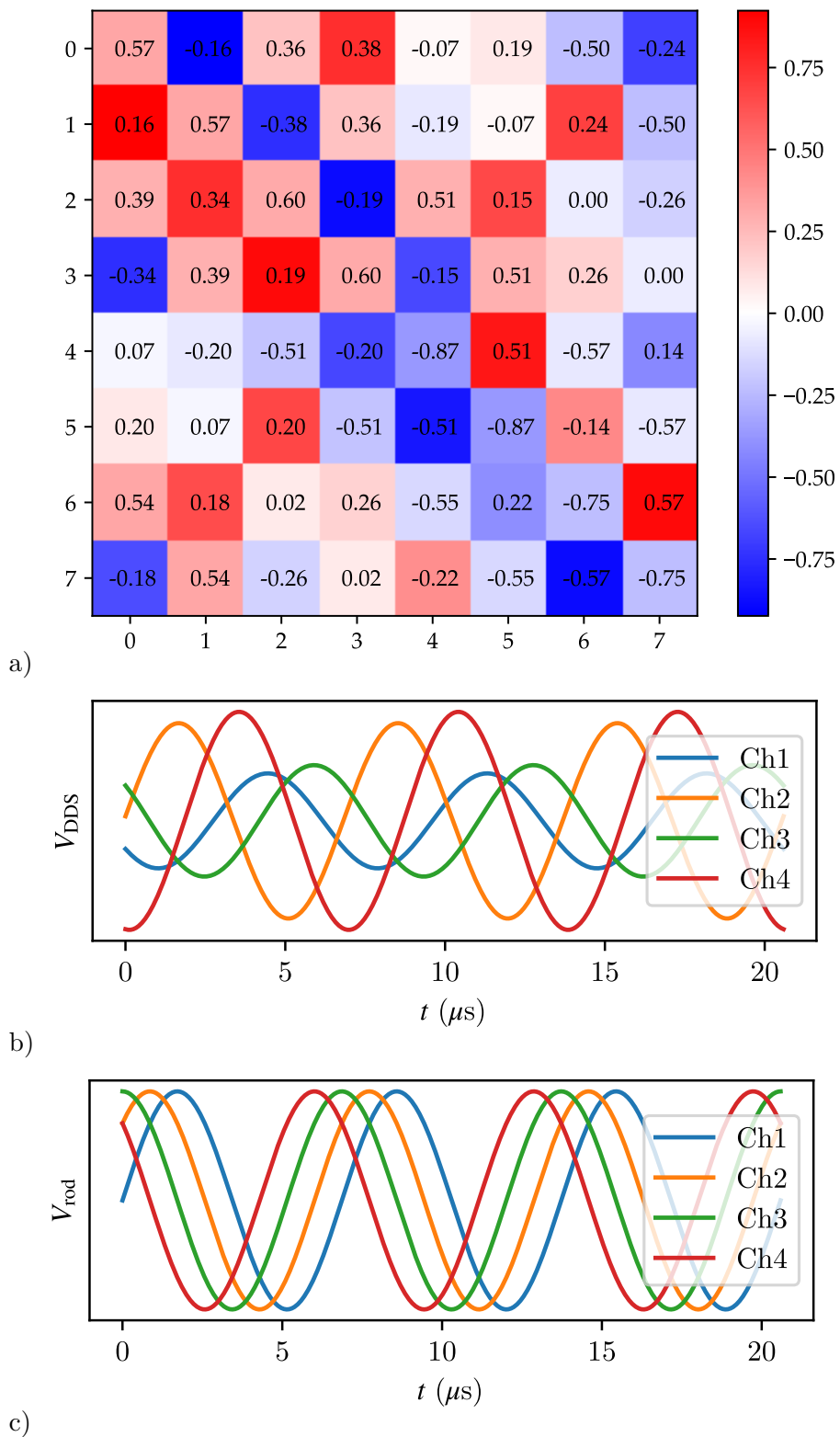


Figure 4.22: The control parameters for making a uniform  $\mathcal{E}_{\text{rot}}$  with the rod electrodes.  
 a) The measured (normalized) control matrix  $M$  relating  $V_{\text{DDS}}$  to the voltage on the rods  $V_{\text{rod}}$ .  
 b) The voltages applied to the DDSs to generate the desired  $V_{\text{rot}}$  given by inverting the matrix.  
 c) The resulting (desired) voltages applied to the rods.

## Chapter 5

### Magnetic Fields

#### 5.1 Effect of magnetic fields in the Hamiltonian

Any magnetic field that is aligned or anti-aligned with the quantization axis (defined by  $\mathcal{E}_{\text{rot}}$ ) will cause phase accumulation due to the spin of the electron. Because one rotation of the quantization axis is much faster than all other motions of the ions, phase will be accumulated if the time-average of  $\vec{B} \cdot \vec{r}_{\text{rot}}$  over one cycle of  $\mathcal{E}_{\text{rot}}$  is nonzero, and the corresponding frequency  $f^0$  is given by

$$f^0 = \frac{3g\mu_B}{h} \mathcal{B}_{\text{rot}} \quad \text{with} \quad \mathcal{B}_{\text{rot}} \equiv \langle \vec{B} \cdot \hat{r}_{\text{rot}} \rangle_t, \quad (5.1)$$

where  $g$  is the g-factor,  $\mu_B$  is the Bohr magneton,  $h$  is Planck's constant, and  $\mathcal{B}_{\text{rot}}$  is the magnetic field introduced in Section 2.1.2. The simplest field that will do this is of the form

$$\vec{B} = B_{\text{axgrad}} (x \hat{x} + y \hat{y} - 2z \hat{z}). \quad (5.2)$$

Note that as an ion traces out a circle of radius  $r_{\text{rot}}$  in the x-y plane, the time-average over once cycle is exactly

$$\mathcal{B}_{\text{rot}} = B_{\text{axgrad}} r_{\text{rot}}. \quad (5.3)$$

This is in fact the case for an ion anywhere in the x-y plane. To see this, consider an ion at location  $(x_0, y_0, z_0)$ , rotating around this point with a radius  $r_{\text{rot}}$  and period  $T$ . We can then calculate

$$\begin{aligned}
\langle \vec{B} \cdot \hat{r}_{\text{rot}} \rangle_t &= \frac{1}{T} \int_0^T \vec{B} \left[ x_0 + r_{\text{rot}} \cos\left(\frac{2\pi}{T}t\right), y_0 + r_{\text{rot}} \sin\left(\frac{2\pi}{T}t\right), z_0 \right] \cdot \left\{ \cos\left(\frac{2\pi}{T}t\right), \sin\left(\frac{2\pi}{T}t\right), 0 \right\} dt \\
&= \frac{1}{T} \int_0^T B_{\text{axgrad}} \begin{pmatrix} x_0 + r_{\text{rot}} \cos\left(\frac{2\pi}{T}t\right) \\ y_0 + r_{\text{rot}} \sin\left(\frac{2\pi}{T}t\right) \\ -2z_0 \end{pmatrix} \cdot \left\{ \cos\left(\frac{2\pi}{T}t\right), \sin\left(\frac{2\pi}{T}t\right), 0 \right\} dt \\
&= \frac{B_{\text{axgrad}}}{T} \int_0^T \left( x_0 \cos\left(\frac{2\pi}{T}t\right) + y_0 \sin\left(\frac{2\pi}{T}t\right) + r_{\text{rot}} \left( \cos\left(\frac{2\pi}{T}t\right) + \sin\left(\frac{2\pi}{T}t\right) \right) \right) dt \\
&= \frac{B_{\text{axgrad}}}{T} \left( x_0(0) + y_0(0) + r_{\text{rot}} \left( \frac{T}{2} + \frac{T}{2} \right) \right) \\
&= B_{\text{axgrad}} r_{\text{rot}}.
\end{aligned} \tag{5.4}$$

The result is independent of  $(x_0, y_0, z_0)$ . This means that all ions at all locations in the trap experience the same phase accumulation.

The ions only start to see different phase accumulations if  $B_{\text{axgrad}}$  starts to vary over the length scale of the size of the ion cloud. A first order derivative would lead to temporary phase decoherence, but would average to zero over a longer timescale as the ions slosh back and forth harmonically in the trap. A second order derivative, however, would not cancel, and would lead to decoherence.

## 5.2 $f_0$ from anti-Helmholtz coils

We can use a  $B_{\text{axgrad}}$  field configuration as the main source of frequency in our Ramsey measurement. Such a field can be created with a set of anti-Helmholtz coils. For practical reasons, a set of square coils are used. The analytical result for the field produced by a square coil is derived in Appendix A.1.

If we place two coils centered around the same axis with opposite a distance  $d$  apart and flow current in the opposite directions (as we would do for an anti-Helmholtz configuration), the

resulting fields are given by

$$\vec{B}_{\text{anti-Helmholtz}} = \vec{B}_{\text{coil}}(x, y, z + \frac{d}{2}) - \vec{B}_{\text{coil}}(x, y, z - \frac{d}{2}). \quad (5.5)$$

where  $\vec{B}_{\text{coil}}$  is given by Equation A.5. Physically, the coils must rest outside of the cryogenic insulation foam block, so the length of each side of the square coils is set to  $L = 54$  cm. To find the correct spacing  $d$  between the coils for an anti-Helmholtz configuration, we look at the on-axis equation and Taylor expand about the origin:

$$\begin{aligned} \vec{B}_{\text{anti-Helmholtz}}(0, 0, z) = & z \left( -\frac{16\mu_0 I (L^2 d (3d^2 + 5L^2))}{\pi (d^2 + L^2)^2 (d^2 + 2L^2)^{3/2}} \right) \\ & + z^3 \left( \frac{64\mu_0 I L^2 (-10d^9 - 40d^7 L^2 - 39d^5 L^4 + 26d^3 L^6 + 43dL^8)}{\pi (d^2 + L^2)^4 (d^2 + 2L^2)^{7/2}} \right) \\ & + \mathcal{O}(z^5). \end{aligned} \quad (5.6)$$

The first term leads to the linear gradient we want for the anti-Helmholtz configuration, but the second term represents an unwanted third derivative. We can then select  $d$  so that the second term goes to zero. This occurs when  $d = 51$  cm.

The expected  $B_{\text{axgrad}}$  produced by the coils is then given by the derivative

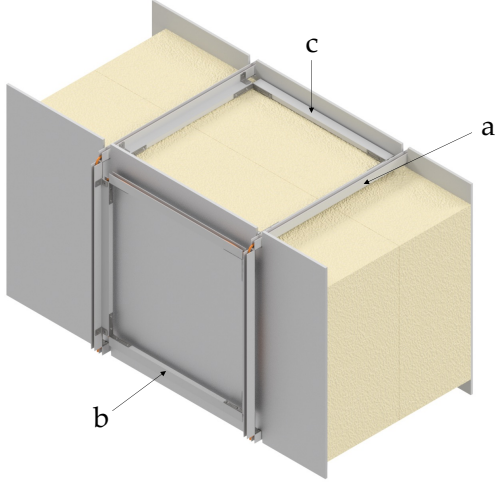
$$B_{\text{axgrad}} = \frac{1}{2} \frac{\partial \left( \hat{z} \cdot \vec{B}_{\text{anti-Helmholtz}}(0, 0, z) \right)}{\partial z} = \frac{8\mu_0 I d L^2 (3d^2 + 5L^2)}{\pi (d^2 + L^2)^2 (d^2 + 2L^2)^{3/2}}. \quad (5.7)$$

The coils are wound on aluminum u-channels to set the dimensions. Additional coil sets in all dimensions are added in Helmholtz configurations to shim away the background field, forming an aluminum cage structure that also acts to set the spacing of each coil set. Details of the setup are in Figure 5.1

### 5.3 Characterization of homogeneity

In Equation 5.2,  $B_{\text{axgrad}}$  is treated as a constant. However, one can imagine that fields of this form can have a spatially varying  $B_{\text{axgrad}}$  (or other phase-contributing forms with an effective  $B_{\text{axgrad}}$  that is spatially varying). Since the phase seen by the ions is no longer independent of





	Name	L (cm)	d (cm)
a	Anti-Helmholtz, North-South Helmholtz	54.6	50.8
b	East-West Helmholtz	46.2	52.7
c	Up-Down Helmholtz	$\left\{ \begin{array}{l} 46.2 \\ 43.3 \end{array} \right.$	52.7

Figure 5.1: The field-generating coils for both shimming away background fields and creating  $B_{\text{axgrad}}$ . The coils that lie on the North-South axis (a) serve both purposes. The dimensions of each coil's side length (L) and spacing (d) are listed in the table on the right, with allowances for a 1/2 cm offset between the current and the u-channel to account for the finite thickness of the wire assembly. Note that the Up-Down coils (c) were reduced in size along the East-West axis so that they could fit between the two pieces of aluminum used to clamp the foam assembly.

their position, this can cause the ions to decohere. Such field can be caused by inhomogeneity in the applied fields as well as any background magnetic fields. To place a bound on this effect, we aim to measure the magnetic field around the ions' resting place. Since we are interested in deviations on the order of a part in  $10^4$  of the fields over the spatial extent of the ion cloud, of order 1 cm, directly measuring the fields is impractical. Instead, we can measure the fields on a much larger surface enclosing the ion trap, with Maxwell's equations prescribing the fields inside. The proper machinery for this technique is to perform a multipole expansion of the fields about the ion location. Once we measure enough points to determine the multipole coefficients, the fields and its derivatives can be sensitively found from the analytic form of the multipole fields.

### 5.3.1 Multipole expansion

In the region where the ions are there are no current sources. In the magnetostatic regime,

$$\left\{ \begin{array}{l} \vec{\nabla} \cdot \vec{B} = 0 \\ \vec{\nabla} \times \vec{B} = 0. \end{array} \right. \quad (5.8)$$

We can then write the magnetic field as the gradient of a scalar potential  $\Phi_B$ :

$$\vec{B} = -\vec{\nabla}\Phi_B. \quad (5.9)$$

This scalar potential can be decomposed into a multipole expansion [57]

$$\Phi_B = \sum_{l=0}^{\infty} \sum_{m=-l}^l \frac{1}{2l+1} \left( a_{lm} r^l + b_{lm} \frac{1}{r^{l+1}} \right) Y_l^m(\theta, \phi), \quad (5.10)$$

where  $a_{lm}$  and  $b_{lm}$  are the multipole moments and  $Y_l^m$  are the spherical harmonics. (For convenience, we define  $r'$  as a dimensionless quantity  $r' \equiv \frac{r}{r_0}$  to absorb the spatial dimensions of the coefficients  $a_{lm}$  and  $b_{lm}$ . This is so that each coefficient has the same units. For further convenience we can define  $r_0$  as 1 meter.) Since there are no currents near the origin, it is unphysical to have terms that go to infinity at the origin. Therefore all  $b_{lm}$  terms must be zero, and we can leave them out of our expansion. Furthermore, since we are working with real magnetic fields, it is convenient to work with the “real spherical harmonics”  $Y_{lm}$ , which give rise to physical fields. These are defined as [58]

$$Y_{lm} \equiv \begin{cases} \frac{1}{\sqrt{2}} (Y_l^m + (-1)^m Y_l^{-m}) & m > 0 \\ Y_l^m & m = 0 \\ \frac{1}{i\sqrt{2}} (Y_l^m - (-1)^m Y_l^{-m}) & m < 0. \end{cases} \quad (5.11)$$

We can then define our expansion as

$$\Phi_B = \sum_{l=0}^{\infty} \sum_{m=-l}^l a_{lm} \phi_{lm} \quad \text{where} \quad \phi_{lm} \equiv \left( \frac{1}{2l+1} r^l Y_{lm}(\theta, \phi) \right). \quad (5.12)$$

In this formulation, the fields are fully described by the real scalar multipole coefficients  $a_{lm}$ . The basis scalar fields  $\phi_{lm}$  and the resulting basis vector fields  $B_{lm} \equiv -\vec{\nabla}\phi_{lm}$  (1 T·m) are tabulated in Table 5.1. Note that the  $l = 0$  term is not included since it is a constant, so it goes to zero when the gradient is taken and therefore it does not produce a magnetic field.

Note that the  $l = 2, m = 0$  term gives rise to a  $B_{\text{axgrad}}$ :

$$-\vec{\nabla}\phi_{2,0} \propto \frac{1}{2\sqrt{5}\pi} (x \hat{x} + y \hat{y} - 2z \hat{z}). \quad (5.13)$$

$l$	$m$	$\phi_{lm}$ in Cartesian Coordinates	$B_{lm}$
1	-1	$\frac{y}{2\sqrt{3\pi}}$	$\left\{0, -\frac{1}{2\sqrt{3\pi}}, 0\right\}$
	0	$\frac{z}{2\sqrt{3\pi}}$	$\left\{0, 0, -\frac{1}{2\sqrt{3\pi}}\right\}$
	1	$\frac{x}{2\sqrt{3\pi}}$	$\left\{-\frac{1}{2\sqrt{3\pi}}, 0, 0\right\}$
2	-2	$\frac{1}{2}\sqrt{\frac{3}{5\pi}}xy$	$\left\{-\frac{1}{2}\sqrt{\frac{3}{5\pi}}y, -\frac{1}{2}\sqrt{\frac{3}{5\pi}}x, 0\right\}$
	-1	$\frac{1}{2}\sqrt{\frac{3}{5\pi}}yz$	$\left\{0, -\frac{1}{2}\sqrt{\frac{3}{5\pi}}z, -\frac{1}{2}\sqrt{\frac{3}{5\pi}}y\right\}$
	0	$-\frac{x^2+y^2-2z^2}{4\sqrt{5\pi}}$	$\left\{\frac{x}{2\sqrt{5\pi}}, \frac{y}{2\sqrt{5\pi}}, -\frac{z}{\sqrt{5\pi}}\right\}$
	1	$\frac{1}{2}\sqrt{\frac{3}{5\pi}}xz$	$\left\{-\frac{1}{2}\sqrt{\frac{3}{5\pi}}z, 0, -\frac{1}{2}\sqrt{\frac{3}{5\pi}}x\right\}$
	2	$\frac{1}{4}\sqrt{\frac{3}{5\pi}}(x-y)(x+y)$	$\left\{-\frac{1}{2}\sqrt{\frac{3}{5\pi}}x, \frac{1}{2}\sqrt{\frac{3}{5\pi}}y, 0\right\}$
3	-3	$-\frac{1}{4}\sqrt{\frac{5}{14\pi}}y(y^2-3x^2)$	$\left\{-\frac{3}{4}\sqrt{\frac{5}{14\pi}}xy, \frac{3}{4}\sqrt{\frac{5}{14\pi}}(y^2-x^2), 0\right\}$
	-2	$\frac{1}{2}\sqrt{\frac{15}{7\pi}}xyz$	$\left\{-\frac{1}{2}\sqrt{\frac{15}{7\pi}}yz, -\frac{1}{2}\sqrt{\frac{15}{7\pi}}xz, -\frac{1}{2}\sqrt{\frac{15}{7\pi}}xy\right\}$
	-1	$-\frac{1}{4}\sqrt{\frac{3}{14\pi}}y(x^2+y^2-4z^2)$	$\left\{\frac{1}{2}\sqrt{\frac{3}{14\pi}}xy, \frac{1}{4}\sqrt{\frac{3}{14\pi}}(x^2+3y^2-4z^2), -\sqrt{\frac{6}{7\pi}}yz\right\}$
	0	$\frac{2z^3-3z(x^2+y^2)}{4\sqrt{7\pi}}$	$\left\{\frac{3xz}{2\sqrt{7\pi}}, \frac{3yz}{2\sqrt{7\pi}}, \frac{3(x^2+y^2-2z^2)}{4\sqrt{7\pi}}\right\}$
	1	$-\frac{1}{4}\sqrt{\frac{3}{14\pi}}x(x^2+y^2-4z^2)$	$\left\{\frac{1}{4}\sqrt{\frac{3}{14\pi}}(3x^2+y^2-4z^2), \frac{1}{2}\sqrt{\frac{3}{14\pi}}xy, -\sqrt{\frac{6}{7\pi}}xz\right\}$
	2	$\frac{1}{4}\sqrt{\frac{15}{7\pi}}z(x-y)(x+y)$	$\left\{-\frac{1}{2}\sqrt{\frac{15}{7\pi}}xz, \frac{1}{2}\sqrt{\frac{15}{7\pi}}yz, -\frac{1}{4}\sqrt{\frac{15}{7\pi}}(x-y)(x+y)\right\}$
3	$\frac{1}{4}\sqrt{\frac{5}{14\pi}}x(x^2-3y^2)$	$\left\{-\frac{3}{4}\sqrt{\frac{5}{14\pi}}(x-y)(x+y), \frac{3}{2}\sqrt{\frac{5}{14\pi}}xy, 0\right\}$	
4	-4	$\frac{1}{12}\sqrt{\frac{35}{\pi}}xy(x-y)(x+y)$	$\left\{\frac{1}{12}\sqrt{\frac{35}{\pi}}y(y^2-3x^2), -\frac{1}{12}\sqrt{\frac{35}{\pi}}x(x^2-3y^2), 0\right\}$
	-3	$-\frac{1}{12}\sqrt{\frac{35}{2\pi}}yz(y^2-3x^2)$	$\left\{-\frac{1}{2}\sqrt{\frac{35}{2\pi}}xyz, \frac{1}{4}\sqrt{\frac{35}{2\pi}}z(y^2-x^2), \frac{1}{12}\sqrt{\frac{35}{2\pi}}y(y^2-3x^2)\right\}$
	-2	$-\frac{1}{12}\sqrt{\frac{5}{\pi}}xy(x^2+y^2-6z^2)$	$\left\{\frac{1}{12}\sqrt{\frac{5}{\pi}}y(3x^2+y^2-6z^2), \frac{1}{12}\sqrt{\frac{5}{\pi}}x(x^2+3y^2-6z^2), -\sqrt{\frac{5}{\pi}}xyz\right\}$
	-1	$\frac{1}{12}\sqrt{\frac{5}{2\pi}}yz(4z^2-3(x^2+y^2))$	$\left\{\frac{1}{2}\sqrt{\frac{5}{2\pi}}xyz, \frac{1}{12}\sqrt{\frac{5}{2\pi}}z(3x^2+9y^2-4z^2), \frac{1}{4}\sqrt{\frac{5}{2\pi}}y(x^2+y^2-4z^2)\right\}$
	0	$\frac{-24z^2(x^2+y^2)+3(x^2+y^2)^2+8z^4}{48\sqrt{\pi}}$	$\left\{-\frac{x(x^2+y^2-4z^2)}{4\sqrt{\pi}}, -\frac{y(x^2+y^2-4z^2)}{4\sqrt{\pi}}, \frac{3z(x^2+y^2)-2z^3}{3\sqrt{\pi}}\right\}$
	1	$\frac{1}{12}\sqrt{\frac{5}{2\pi}}xz(4z^2-3(x^2+y^2))$	$\left\{\frac{1}{12}\sqrt{\frac{5}{2\pi}}z(9x^2+3y^2-4z^2), \frac{1}{2}\sqrt{\frac{5}{2\pi}}xyz, \frac{1}{4}\sqrt{\frac{5}{2\pi}}x(x^2+y^2-4z^2)\right\}$
	2	$-\frac{1}{24}\sqrt{\frac{5}{\pi}}(x-y)(x+y)(x^2+y^2-6z^2)$	$\left\{\frac{1}{6}\sqrt{\frac{5}{\pi}}x(x^2-3z^2), -\frac{1}{6}\sqrt{\frac{5}{\pi}}y(y^2-3z^2), -\frac{1}{2}\sqrt{\frac{5}{\pi}}z(x-y)(x+y)\right\}$
	3	$\frac{1}{12}\sqrt{\frac{35}{2\pi}}xz(x^2-3y^2)$	$\left\{\frac{1}{4}\sqrt{\frac{35}{2\pi}}z(y^2-x^2), \frac{1}{2}\sqrt{\frac{35}{2\pi}}xyz, -\frac{1}{12}\sqrt{\frac{35}{2\pi}}x(x^2-3y^2)\right\}$
4	$\frac{1}{48}\sqrt{\frac{35}{\pi}}(x^2+y^2)^2\cos(4\tan^{-1}(x,y))$	$\left\{-\frac{1}{12}\sqrt{\frac{35}{\pi}}x(x^2-3y^2), -\frac{1}{12}\sqrt{\frac{35}{\pi}}y(y^2-3x^2), 0\right\}$	

Table 5.1: Mathematical formulations of the  $\phi_{lm}$  multipole expansion functions up to  $l = 4$  and the resulting magnetic fields. Dimensional constants are dropped.

### 5.3.2 Sources of decoherence

We can repeat the integral from Equation 5.4 to find which of the basis fields contribute to phase of the ions. The fields with non-zero phase contributions are listed in Table 5.2.

$l$	$m$	$\partial_z B_z^{lm}$	$\{\partial_x^2 \partial_z, \partial_y^2 \partial_z, \partial_z^2 \partial_z\} B_z^{lm}$	$\langle \vec{B}_{lm}(\vec{r}_0 + \vec{r}_{\text{rot}}) \cdot \hat{r}_{\text{rot}} \rangle_t$
2	0	$-\frac{1}{\sqrt{5\pi}}$	$\{0, 0, 0\}$	$\frac{1}{2\sqrt{5\pi}} r_{\text{rot}}$
3	-1	$-\sqrt{\frac{6}{7\pi}} y$	$\{0, 0, 0\}$	$\sqrt{\frac{3}{14\pi}} r_{\text{rot}} y_0$
	0	$-\frac{3z}{\sqrt{7\pi}}$	$\{0, 0, 0\}$	$\frac{3}{2\sqrt{7\pi}} r_{\text{rot}} z_0$
	1	$-\sqrt{\frac{6}{7\pi}} x$	$\{0, 0, 0\}$	$\sqrt{\frac{3}{14\pi}} r_{\text{rot}} x_0$
4	-2	$-\sqrt{\frac{5}{\pi}} xy$	$\{0, 0, 0\}$	$\frac{1}{2} \sqrt{\frac{5}{\pi}} r_{\text{rot}} x_0 y_0$
	-1	$-\sqrt{\frac{10}{\pi}} yz$	$\{0, 0, 0\}$	$\sqrt{\frac{5}{2\pi}} r_{\text{rot}} y_0 z_0$
	0	$\frac{x^2 + y^2 - 2z^2}{\sqrt{\pi}}$	$\left\{ \frac{2}{\sqrt{\pi}}, \frac{2}{\sqrt{\pi}}, -\frac{4}{\sqrt{\pi}} \right\}$	$-\frac{1}{4\sqrt{\pi}} r_{\text{rot}} (r_{\text{rot}}^2 + 2(x_0^2 + y_0^2 - 2z_0^2))$
	1	$-\sqrt{\frac{10}{\pi}} xz$	$\{0, 0, 0\}$	$\sqrt{\frac{5}{2\pi}} r_{\text{rot}} x_0 z_0$
	2	$-\frac{1}{2} \sqrt{\frac{5}{\pi}} (x - y)(x + y)$	$\left\{ -\sqrt{\frac{5}{\pi}}, \sqrt{\frac{5}{\pi}}, 0 \right\}$	$\frac{1}{4} \sqrt{\frac{5}{\pi}} r_{\text{rot}} (x_0^2 - y_0^2)$

Table 5.2: The multipole expansion fields up to  $l = 4$  that lead to phase accumulation and decoherence. Dimensional constants are dropped. To recover dimensions for quoted  $\langle \vec{B}_{lm}(\vec{r}_0 + \vec{r}_{\text{rot}}) \cdot \hat{r}_{\text{rot}} \rangle_t$ , use  $r_{\text{rot}}$  and spatial initial positions in m and the result is given in T.

From this we can infer the sources of decoherence. While the  $l=3, m=\{0, \pm 1\}$  terms contribute a frequency that depends linearly on an ion's position in a single dimension during the cycle of  $\mathcal{E}_{\text{rot}}$ , the harmonic motion of the ions in the trap means that this phase contribution will average to zero over the timescale of the Ramsey fringe.

Next, consider the  $l=4, m=\{-2, -1, 1\}$  terms, which have spatial dependence on products of different dimensions. Consider the sign of such a frequency in each octant. The term  $x_0 y_0$  is positive in half the octants and negative in the other half. If the ions move in a harmonic trap with the same trapping frequency in each dimension, then assuming the ions traveled in a trajectory through the origin, the each ion will only occupy two opposite octants which contribute frequencies

of the same sign, so they will contribute an overall frequency. However, if the trapping frequencies are different in each dimension, the ions trajectories will occupy all eight octants for equal times, so the overall frequency contribution cancels out.

This means that the leading cause of decoherence in the ion cloud terms from the  $l=4$ ,  $m=\{0,2\}$  terms, which have quadratic dependence on ion location. These terms are synonymous with a  $\partial_{x_i}^2 \partial_z B_z$  since they are the only terms that have such nonzero third derivatives.

To quantify how much decoherence these terms cause, consider these derivatives as derivatives of the effective  $B_{\text{axgrad}}$ , as in  $\partial_{x_i}^2 \partial_z B_z = 2\partial_{x_i}^2 B_{\text{axgrad}}$ . Consider a hard shell of ions with radius  $r_{\text{cloud}}$ . The difference between the highest and lowest phase-contributing  $B_{\text{axgrad}}$  that the ions see due to each derivative is then

$$\Delta B_{\text{axgrad}} = -\frac{1}{2} \partial_{x_i}^2 \partial_z B_z r_{\text{cloud}}^2. \quad (5.14)$$

We want the spread in frequencies to be such that after 20s of our Ramsey fringe we want the highest deviating frequencies to have only lost or gained one tenth of a period.

The number of cycles of Ramsey fringe is given by

$$N = ft,$$

where  $t$  is the evolution time and  $f$  is the frequency. For a decohering ion, we require that the number  $N$  of cycles it undergoes is within 1/10 of the mean number of cycles  $N_0$

$$|N - N_0| < \frac{1}{10},$$

or in terms of frequencies

$$|(f_0 + \Delta f)t - f_0 t| < \frac{1}{10}.$$

From this we can derive our constraint on the frequency deviation  $\Delta f$ :

$$|\Delta f| < \frac{1}{10} \frac{1}{t}.$$

From Equations 5.1 and 5.3 we can rewrite  $\Delta f$  in terms of  $\Delta B_{\text{axgrad}}$ :

$$\left| \frac{3g\mu_B}{h} (\Delta B_{\text{axgrad}}) r_{\text{rot}} \right| < \frac{1}{10} \frac{1}{t}.$$

Then using Equation 5.14 we have

$$\left| \frac{3g\mu_B}{h} \left( \frac{1}{2} \partial_{x_i}^2 \partial_z B_z r_{\text{cloud}}^2 \right) r_{\text{rot}} \right| < \frac{1}{10} \frac{1}{t},$$

which finally gives us a limit on the third derivatives of the magnetic field:

$$|\partial_{x_i}^2 \partial_z B_z| < \frac{h}{15g\mu_B r_{\text{cloud}}^2 r_{\text{rot}} t}. \quad (5.15)$$

Given an  $r_{\text{cloud}}$  of 0.5 cm, an  $r_{\text{rot}}$  of 2.6 mm, and a Ramsey evolution time of 20 s, this gives

$$|\partial_{x_i}^2 \partial_z B_z| < 2.5 \times 10^{-3} \text{ mG/cm}^3. \quad (5.16)$$

For a  $B_{\text{axgrad}}$  of 3.07 mG/cm (corresponding to an  $f_0$  of 50 Hz), a fractional representation of this bound is given by

$$\left| \frac{\Delta B_{\text{axgrad}}}{B_{\text{axgrad}}} \right| < 10^{-4}. \quad (5.17)$$

### 5.3.3 Magnetic field measurement scheme

To determine the coefficients that describe the background magnetic field near the ions, we measure the field at grid points on the surface of a cuboid centered at the ion location with sides of length 20 cm (details in Figure 5.2). There are a few key points of this measurement grid. Firstly, each  $Y_l^m$  has a spatial dependence of order  $(\cos(\theta))^l e^{im\phi}$ , meaning some component of the fields have  $l/2$  periods over the domain of  $\theta$  (since  $\theta$  only goes from 0 to  $\pi$ ) and  $m$  periods over the domain of  $\phi$ . To accurately sample the fields, the measurement grid must contain at least  $l$  points about  $\theta$  and  $2m$  points about  $\phi$  to reach the spatial Nyquist frequency. This is demonstrated visually in Figure 5.2c.

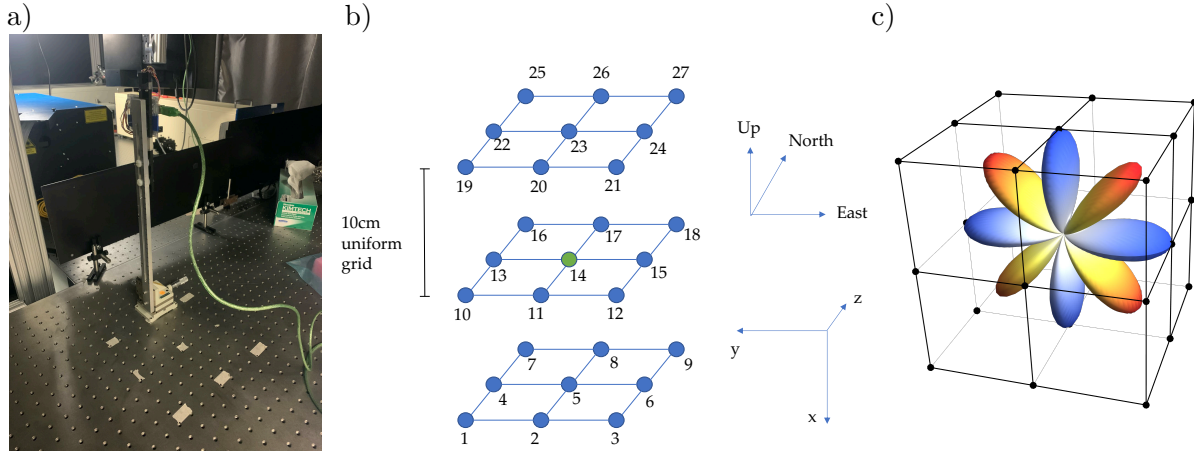


Figure 5.2: The setup for measuring the magnetic field around the ion location.

- a) an LSM303 triple-axis magnetometer, read by a microcontroller, is used to measure the fields. The magnetometer is mounted on non-magnetic plastic and aluminum components that hold it above the table. A grid of nine points spaced 10 cm apart are measured at three different heights.
- b) the resulting grid of points. The green point at the center of the grid represents the location of the ions at their resting point in the prototype experiment.
- c) The radial component of  $B_{4,\pm 4}$  in the context of the measurement grid. This view is looking down  $\hat{z}$ . Blue represents negative values and red represents positive values. Each lobe has its own measurement point, just meeting the spatial Nyquist sampling criteria.

We can then use the measured fields to fit the multipole coefficients, and then multiply each coefficient by its corresponding field's theoretical contribution to  $B_{\text{axgrad}}$  and its derivatives.

Let  $\overline{\overline{B}}_{meas}$  be a matrix where each row corresponds to a different spatial location on the measurement grid, and the columns are the  $B_x$ ,  $B_y$ , and  $B_z$  measured at each location. One can then evaluate the value of  $B_{lm}$  at each measurement point and construct the corresponding  $\overline{\overline{B}}_{lm}$  basis fields. Then the  $a_{lm}$  that fully describe the fields inside the region can be found via

$$\overline{\overline{B}}_{meas} = \sum_{l,m} a_{l,m} \overline{\overline{B}}_{lm}. \quad (5.18)$$

We truncate the expansion at  $l = 4$  since higher order terms do not occur far from field sources. If we flatten the matrices into one-dimensional row vectors ( $\overline{\overline{B}}_{meas} \rightarrow \overline{B}_{meas}$ ,  $\overline{\overline{B}}_{lm} \rightarrow \overline{B}_{lm}$ ), then this

relation can be written as

$$\bar{B}_{meas} = \begin{bmatrix} a_{(1,-1)} \\ a_{(1,0)} \\ \dots \\ a_{(4,4)} \end{bmatrix} \begin{bmatrix} \bar{B}_{(-1,1)}, \bar{B}_{(-1,0)}, \dots, \bar{B}_{(4,4)} \end{bmatrix}. \quad (5.19)$$

This can now be solved with traditional multiple linear regression techniques, with appropriate error estimation.

#### 5.4 Background fields from the optical table

Standard optical tables are made from ferromagnetic steel. Since our experiment is sensitive to magnetic fields, we need to characterize the effect of the tables on the relevant magnetic field parameters at the location of the ions. The magnetic nature of the table is demonstrated in Figure 5.3, which maps out the magnetic domains by measuring the fields on the surface of the table. The

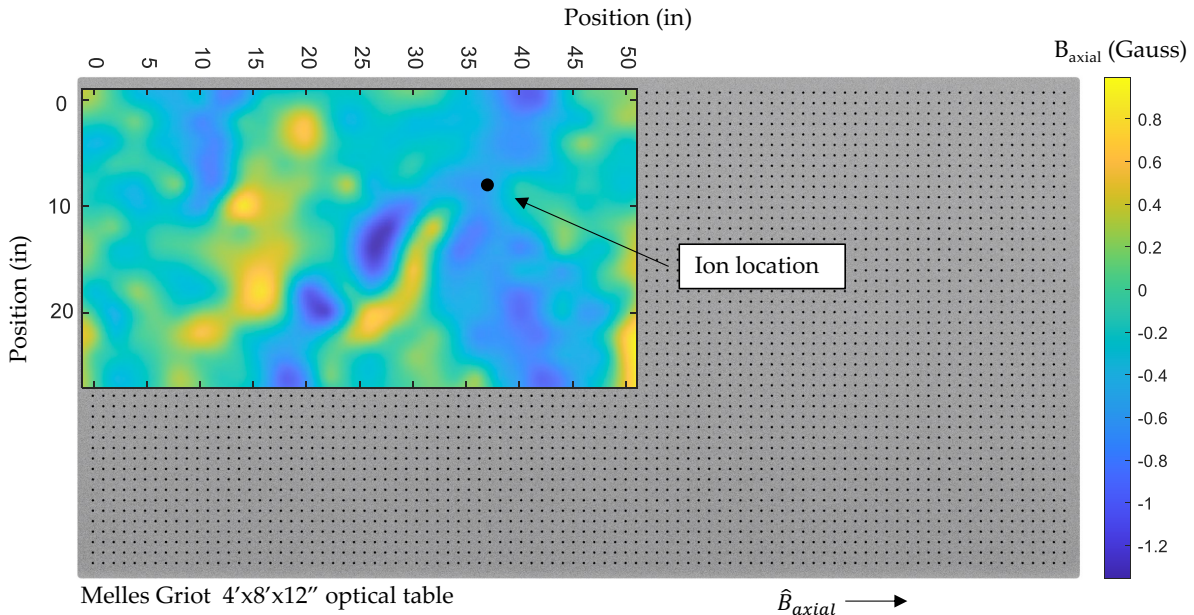


Figure 5.3: Axial magnetic field measured at the surface of the table. The fields are measured at points on a 2 inch by 2 inch grid, and the measurement is then smoothed out with a gridded interpolation.



spatial size of the domains is of order a few inches, which looks like high order multipole terms when near to the ions. We characterize the relevant fields using the technique described in Section 5.3.3 at various points in relation to the optical table. First, we measure 35 cm above the table, which represents the ideal location of the ion location for practical engineering-related concerns. Next, we measure 45 cm above the table, which represents lifting the ion trap up by (or equivalently lowering the optical table) by 10 cm to reduce the effects of the optical table. Finally, we measure 35 cm above the table and 90 cm off the end of the table, which represents the effect of the second nearest optical table if we were to remove the optical table from underneath the trap and replace it with a non-magnetic 80-20 structure. The fields at each location are listed in Table 5.3

	$B_{\text{axgrad}}$ (mG/cm)	$\partial_x^2 B_{\text{axgrad}}$ (mG/cm <sup>3</sup> )	$\partial_y^2 B_{\text{axgrad}}$ (mG/cm <sup>3</sup> )	$\partial_z^2 B_{\text{axgrad}}$ (mG/cm <sup>3</sup> )
35 cm above	$0.20 \pm 0.15$	$0.0034 \pm 0.0043$	$0.0039 \pm 0.0043$	$-0.0073 \pm 0.0055$
45 cm above	$0.01 \pm 0.06$	$-0.0004 \pm 0.0020$	$0.0015 \pm 0.0019$	$-0.0011 \pm 0.0024$
90 cm off edge	$-0.46 \pm 0.58$	$-0.0003 \pm 0.0004$	$0.0004 \pm 0.0004$	$-0.0004 \pm 0.0005$

Table 5.3: Measurements of the relevant derivatives of the background magnetic fields with 95% confidence intervals

To meet the requirement prescribed by Equation 5.16 with some margin for error, we decide to lower the table by 15 cm such that the ions sit 50 cm above the table.

## 5.5 Field-distorting effects of the optical table

The ferromagnetic properties of the table not only produce spatially inhomogeneous background magnetic fields, but can also have their spins aligned by experimental field sources, thus distorting the field lines near the surface of the table. To characterize this effect, we take a single coil from the up-down coil pair of the apparatus described in Figure 5.1 and place it so that its axis is pointing into the table. We then measure the on-axis field due to the coil both with and without the presence of the table. Each measurement is performed once with the coil turned off and once with the coil turned on, so the difference represents the background-free fields from the coils. The results are shown in Figure 5.4.

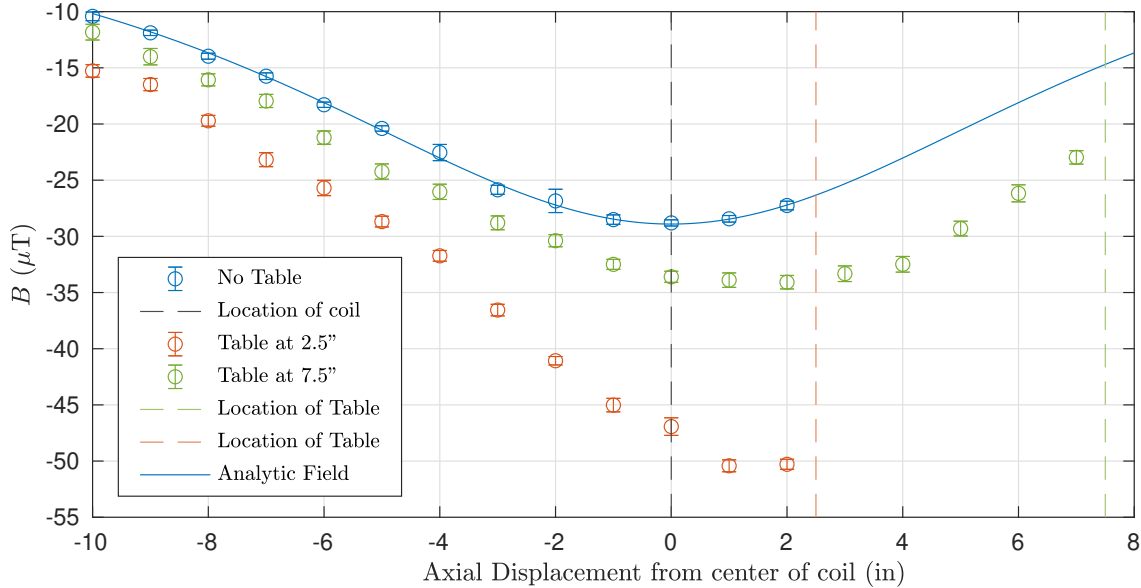


Figure 5.4: The effect of the optical table on the fields produced by a current-carrying coil with its axis perpendicular to the surface of the table

We see significant enhancement of the field produced by the coil near the surface of the table, consistent with the field from the coil magnetizing the table and aligning its spins. The experiment is performed again with the current running in the opposite direction, and the magnitude of the fields was found to be the same within errorbar.

## 5.6 Homogeneity of anti-Helmholtz fields

As you move away from the center of a pair of anti-Helmholtz coils, the higher order derivatives start to become nonzero. This could look like deviations of  $B_{axgrad}$  that lead to decoherence. To verify our coil design, we can use the full analytic fields of our anti-Helmholtz coils given by Equations 5.5, A.4, and A.3. If we evaluate take their derivative along  $z$ , we can find  $B_{axgrad}$  and then we can look for deviations of  $B_{axgrad}$  in the size of the ion cloud. The results are shown in Figure 5.5.

The saddle point behavior of  $B_{axgrad}$  is characteristic of the  $l=4, m=0$  multipole term from Table 5.2. Comparing the inhomogeneity to the benchmark prescribed by Equation 5.17, we can

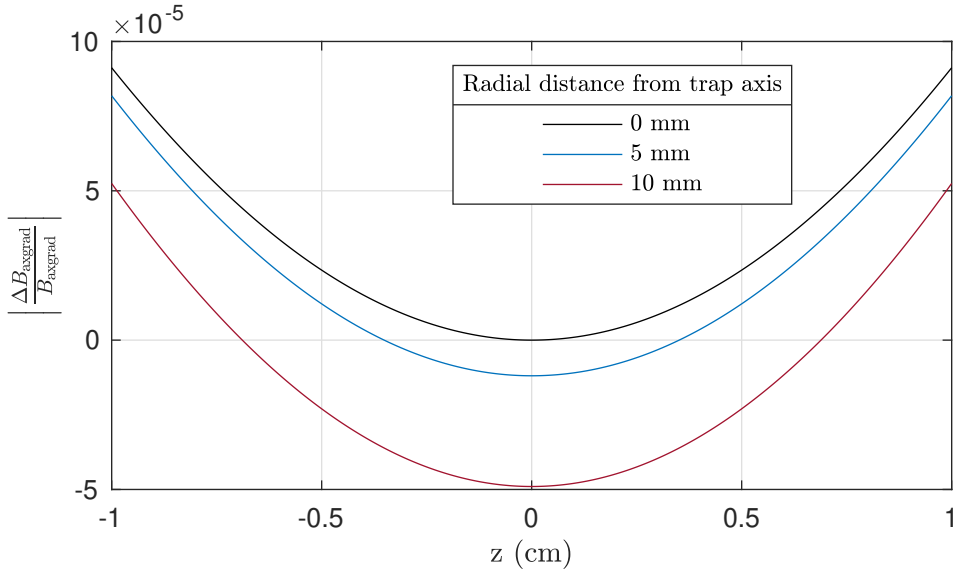


Figure 5.5: Homogeneity of the  $B_{\text{axgrad}}$  generated by the analytic fields from the designed square anti-Helmholtz coils over the spatial extent of the ion cloud. Each line represents a path along  $z$  at a different displacement along  $x$ , representing the radial distance from the trap's  $z$ -axis.

see that over the spatial extent of a 0.5cm radius cloud, the inhomogeneities are two orders of magnitude smaller than what is required.

While the theoretical fields are sufficiently homogeneous, the actual dimensions of the constructed coils will be slightly different than their theoretical counterparts. In addition, we are concerned that the ferromagnetic table underneath the coils might distort the fields in a way that causes decoherence. For these reasons, we perform the measurement described in Section 5.3.3 at the center of the anti-Helmholtz configuration both with the coils suspended on a nonmagnetic frame and above the optical table.

We pass 3.2 A of current through the coils, which are each three turns. Using Equation 5.7, the theoretical  $B_{\text{axgrad}}$  produced is 4.3 mG/cm. The measurements are listed in Figure 5.6. From these measurements we can determine that the optical table does not significantly affect the fields from the coils near the ions, and in both cases the homogeneity is sufficient to satisfy the requirement of Equation 5.16.

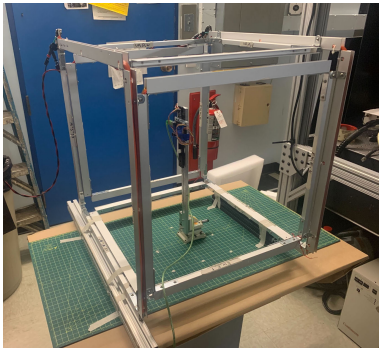
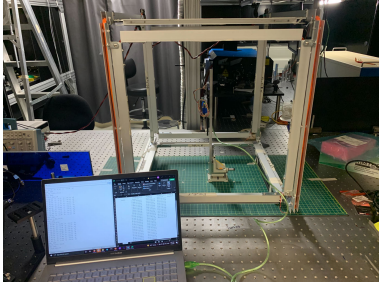
	$B_{\text{axgrad}}$ (mG/cm)	$\partial_x^2 B_{\text{axgrad}}$ (mG/cm <sup>3</sup> )	$\partial_y^2 B_{\text{axgrad}}$ (mG/cm <sup>3</sup> )	$\partial_z^2 B_{\text{axgrad}}$ (mG/cm <sup>3</sup> )
	$4.67 \pm .05$	$.0004 \pm .0014$	$.0014 \pm .0014$	$-.0017 \pm .0018$
	$4.8 \pm .05$	$.0011 \pm .0016$	$.0007 \pm .0016$	$-.0018 \pm .0021$

Figure 5.6: Measurements of the fields from the anti-Helmholtz coils. Top: measured away from the optical table on a non-magnetic aluminum surface. Bottom: measured on the surface of the optical table. Measurements at all 27 points are taken with the coils turned off, then measured again with the coils turned on. We then subtract the two to isolate the fields due to the coils, and perform the multipole expansion fits on this differential set of measurements.

## 5.7 Shim coils for $B_{4,0}$ and $B_{4,2}$

If we are unable to keep the area of interest sufficiently nonmagnetic to avoid decoherence due to magnetic field effects, we wish to be able to shim away the responsible magnetic sources of decoherence. As demonstrated in Section 5.3.2, the primary source of magnetic-field based decoherence arises from the  $l = 4, m = 0$  and  $l = 4, m = 2$  terms of the multiple expansion of the magnetic field. If we can re-create these fields using coils, we should be able to shim away these fields.

A coil array is designed to be low-profile and fit within the existing configuration, while still providing the necessary degrees of freedom required for generating the higher-order magnetic fields. The design is shown in Figure 5.7.

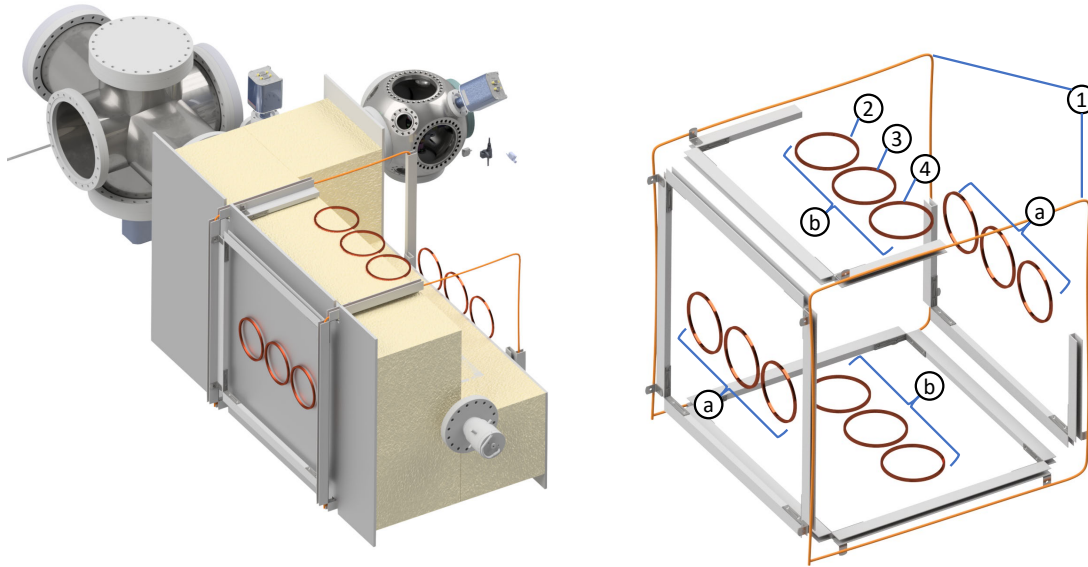


Figure 5.7: Layout of the  $B_{4,0}$  and  $B_{4,2}$  shim coils.

Each coil is placed on the surface of the foam, 25.4 cm away from the axis of the trap. Each coil has a radius of 5 cm, and adjacent coils are spaced 26 cm apart.

We will use the following notation, as labeled in Figure 5.7. coil set 1 is the existing  $B_{axgrad}$  coil set, coil set 2 are the four coils closest to the source chamber, coil set 4 is the four coils closest to the cryocooler, and coil set 3 is the last four coils. Each coil set has a subset  $a$  of two horizontal

coils and a subset  $b$  of two vertical coils.

Observing symmetries of the basis fields reduces the degrees of freedom of the relative currents through each coil. The following symmetries can be observed. For both fields coil sets 2 and 4 have the same current magnitude. For  $B_{4,0}$ , each coil set has its  $a$  subset with equal current to its  $b$  subset, and in  $B_{4,2}$  each coil has its  $a$  subset with opposite current to its  $b$  subset.

Not counting the degree of freedom of overall amp-turns, there are then two degrees of freedom for the amp-turns of the  $m = 0$  coil pair and one for the  $m = 2$  coil pair. The fields are then given by

$$\begin{cases} \vec{B}_{4,0coils} = \vec{B}_{coils1} - \alpha_{4,0}(\vec{B}_{coils2} + \vec{B}_{coils4}) + \beta_{4,0}\vec{B}_{coils3} \\ \vec{B}_{4,2coils} = (\vec{B}_{coils2a} - \vec{B}_{coils2b} + \vec{B}_{coils4a} - \vec{B}_{coils4b}) + \alpha_{4,2}(\vec{B}_{coils3b} - \vec{B}_{coils3a}). \end{cases} \quad (5.20)$$

The relevant amp-turn ratio for each coil subset can be found using the analytic form of the fields, which are given in Appendix A.2. We can then rotate and translate these fields to model the field from each coil subset and decompose these fields into the spherical harmonic basis field set described in Section 5.3.

For the  $B_{4,0}$  coils, the two degrees of freedom are constrained to set the  $B_{2,0}$  and  $B_{4,2}$  components to zero, while for the  $B_{4,2}$  coils, the single degree of freedom is constrained such that the  $B_{2,2}$  component is zero. The resulting amp-turn ratios can be found in Table 5.4.

$\alpha_{4,0}$	0.93
$\beta_{4,0}$	7.56
$\alpha_{4,2}$	6.50

Table 5.4: Solved relative amp-turn ratios for the shim coils

The fields resulting in these amp-turn ratios for this coil configuration are shown in Figure 5.8. The discrete nature of the coils results in an artifact on the generated  $B_{4,0}$  fields, which shows up as an  $l = 4$ ,  $m = 4$  contribution. Since this term does not contribute to decoherence, and in fact does not generate a  $B_{rot}$  at all, this artifact is not a problem.

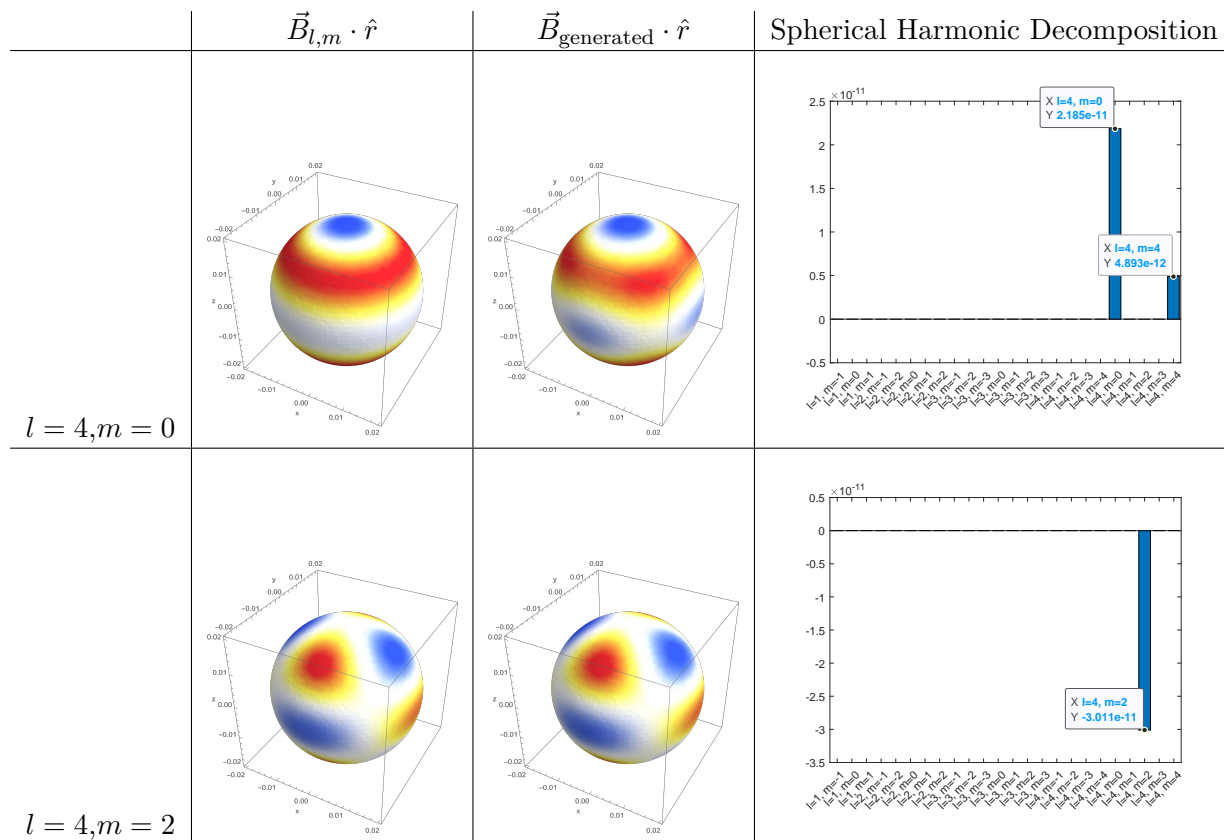


Figure 5.8: Analytic fields generated by the  $B_{4,0}$  and  $B_{4,2}$  shim coil configurations. Left: the radial component of the theoretical  $\vec{B}_{l,m}$  of the two decoherence-causing fields. Middle: The radial component generated by the coil configuration. Right: A decomposition of the resulting field into the basis fields.

## Chapter 6

### Detection

The population in the state of interest is read out by dissociating the ions state-selectively. As the molecular ions dissociate, the thorium keeps the ion's charge, leaving the fluorine atoms neutral. A high-voltage electric field is then pulsed to accelerate the thorium ions towards a detector. Because the dissociated  $\text{Th}^+$  ions are lighter than the un-dissociated  $\text{ThF}^+$  ions, they acquire more speed while traversing the same potential gradient, so they arrive at the detector sooner. This allows the two species to be differentiated, and the dissociated  $\text{Th}^+$  cloud representing the population in the state of interest (times the dissociation efficiency) can be read off separately from the un-dissociated  $\text{ThF}^+$  cloud which represents the remaining total ion number.

#### 6.1 Dissociation

Just as the neutral atoms are state-selectively ionized using a two photon process, the ions are dissociated state-selectively using a two photon process with pulsed lasers. This method is illustrated in Figure 6.1.

##### 6.1.1 Optics

The REMPD1 photon is generated using a Sirah CBST-LG-18 dye laser pumped by a Quanta-Ray PRO pulsed Nd:YAG laser. The REMPD2 photon is generated using doubled light from the same Nd:YAG laser. A diagram for generating the tunable REMPD1 photon is shown in Figure 6.2. The cavity of the laser is formed between the diffraction grating and the reflective surface of the



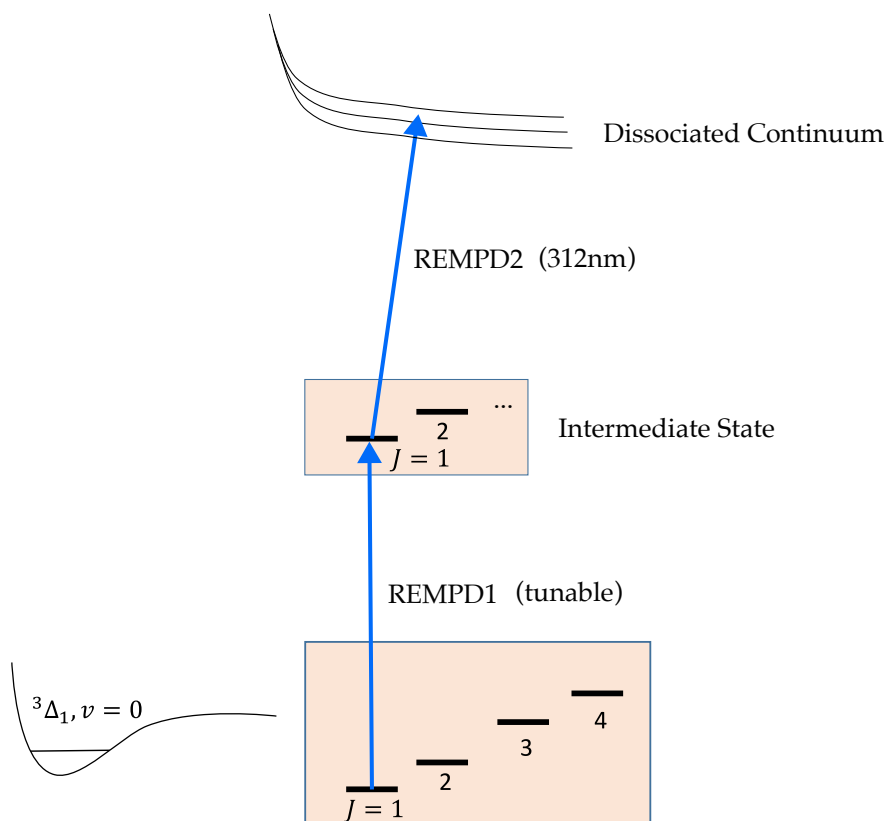


Figure 6.1: Energy level diagram for state detection using resonance-enhanced multi-photon ionization (REMPD). The first photon, denoted REMPD1, excites the ions from the state of interest to an intermediate state. The wavelength of this photon can be tuned to excite from a different initial state to the same intermediate state, thus providing state selectivity for the dissociation. Then the second photon, denoted REMPD2, excites the ions from the intermediate state to above the dissociation threshold, allowing the molecule to fly apart.

output coupler. Similarly to the ECDL configuration, the wavelength can be tuned by changing the angle of the diffraction grating with a piezoelectric crystal. The gain medium is a dye cell pumped with 532nm light from the same Nd:YAG laser that generates the REMPD2 photon. The pump light is formed into a sheet with a diverging cylindrical lens which allows the pump to spatially overlap with the profile of the lasing beam inside of the dye.

Once the light leaves the cavity, it passes through the cell again in a “preamplification” stage. It then is expanded with a set of telescoping lenses to prevent saturation of the gain medium, and is amplified in the main amplifier dye cell. Once the light leaves the laser, a small amount of power is picked off to a wavemeter and Fabry-Perot cavity to read the wavelength and image the spectrum

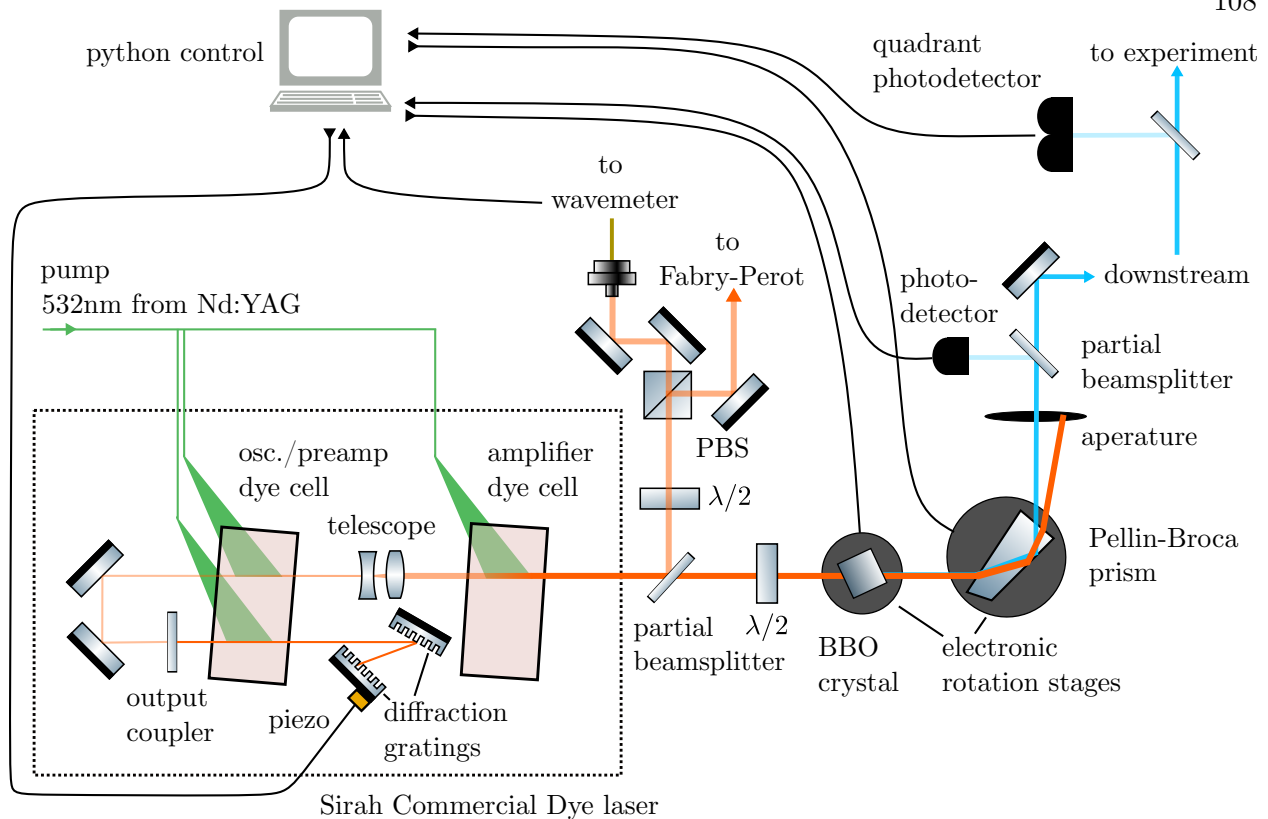


Figure 6.2: Optics layout for generating the tunable REMPDI photon.

of the light. The rest of the power goes into a beta barium borate (BBO) crystal in which second harmonic generation (SHG) produces frequency doubled light. The light then passes through a Pellin-Broca prism in which dispersion causes the two frequencies of light (fundamental and second harmonic) to become angularly resolved. The doubled light is then selected with an aperture. The doubled power is measured with a photodetector. Finally, the beam travels of order one meter to the experiment. Some of the light is sent into a quadrant photodetector, so that the downstream pointing of the beam can be measured.

The efficiency of the process of SHG in the BBO crystal is sensitive to the angle of the BBO, and the optimal angle changes with the wavelength of the light. For each wavelength, the angle of the BBO can be optimized using the intensity on the photodetector as a feedback. After performing this calibration at many different wavelengths, an optimal angle for all wavelengths can be calculated with a piecewise cubic interpolation of the optimal angle as a function of wavelength.

The downstream beam pointing can also change with the wavelength, as well as with thermal fluctuations. Since the horizontal beam pointing can be adjusted with the angle of the Pellin-Broca prism, the angle of the Pellin-Broca can be actively closed-loop controlled such that the beam points to the center of the quadrant photodetector, providing a spatially stable beam to the experiment.

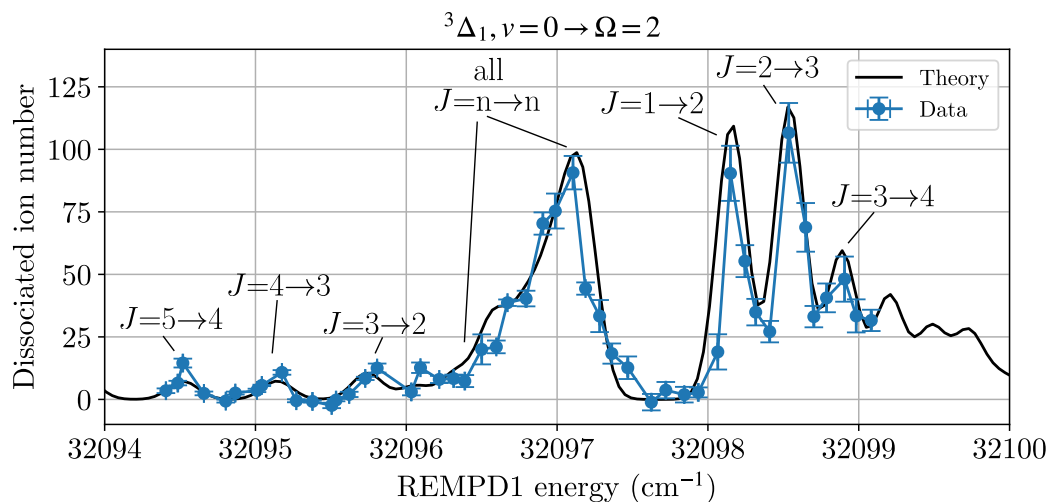
The dye used in the cell is 4-Dicyanomethylene-2-methyl-6-p-dimethylaminostyryl-4H-pyran (DCM) dye in a 0.3 g/L solution in ethanol (with a diluted solution of 0.09 g/L in the amplifier cell). This dye is chosen because it fluoresces over a broad range, offering a flat response to within 15% over the range of 600-650 nm [59], allowing the doubled photon to be tunable over a range of roughly 30800-33300  $\text{cm}^{-1}$ .

### 6.1.2 Spectroscopy

Reading the population in the different ro-vibrational states of  ${}^3\Delta_1$  is done by changing the wavelength of REMPD1. Spectroscopy of the different transitions gives us a roadmap for which REMPD1 energies we can use to measure the population in each ro-vibrational state. Spectroscopy of the  ${}^3\Delta_1, v = 0$  manifold is shown in Figure 6.3.

The population in the state of interest to the eEDM measurement ( ${}^3\Delta_1, v = 0, J = 1$ ) is measured by choosing the ( ${}^3\Delta_1, v = 0, J = 1$ )  $\rightarrow$  ( $\Omega = 0, J = 2$ ) transition.

Similarly, the populations the states of interest in the higher vibrational manifolds can be read off by tuning REMPD1 to a transition from these manifold. Transitions from  ${}^3\Delta_1, v = 1$  are shown in Figure 6.4, while transitions from  $v = 2$  are shown in Figure 6.5.

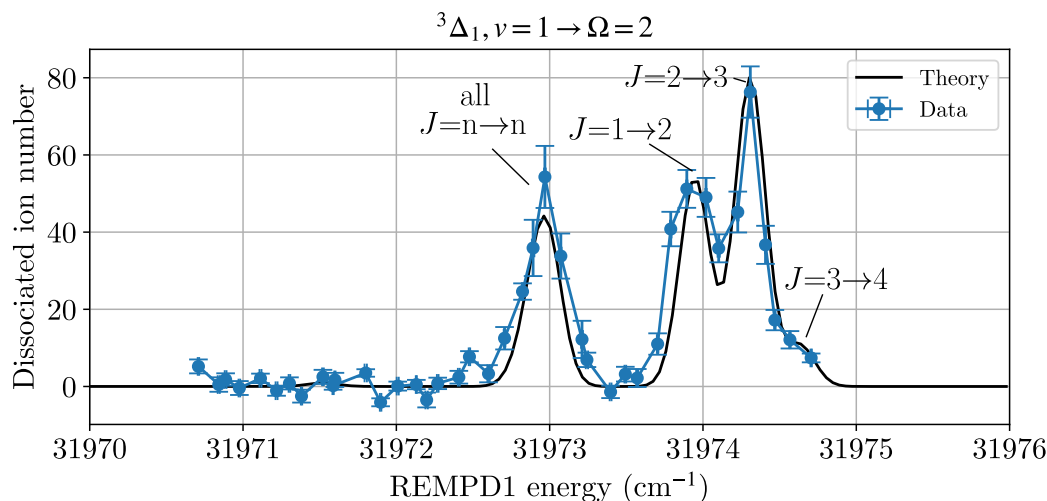


a)

Transition	Energy (cm <sup>-1</sup> )
$(^3\Delta_1, v=0, J=1) \rightarrow (\Omega=0, J=2)$	32098.16(05)
$(^3\Delta_1, v=0, J=2) \rightarrow (\Omega=0, J=3)$	32098.53(05)

b)

Figure 6.3: Dissociation spectroscopy for  $v=0$ . The electronic configuration of intermediate state is unknown. However  $\Omega$  can be inferred by the spacing and relative amplitudes of the transitions. a) Transitions to an  $\Omega=2$  intermediate state. Each peak represents a single transition, except for the central peak in which all of the transitions which preserve  $J$  overlap. b) Energies of the prominent and well-isolated transitions.

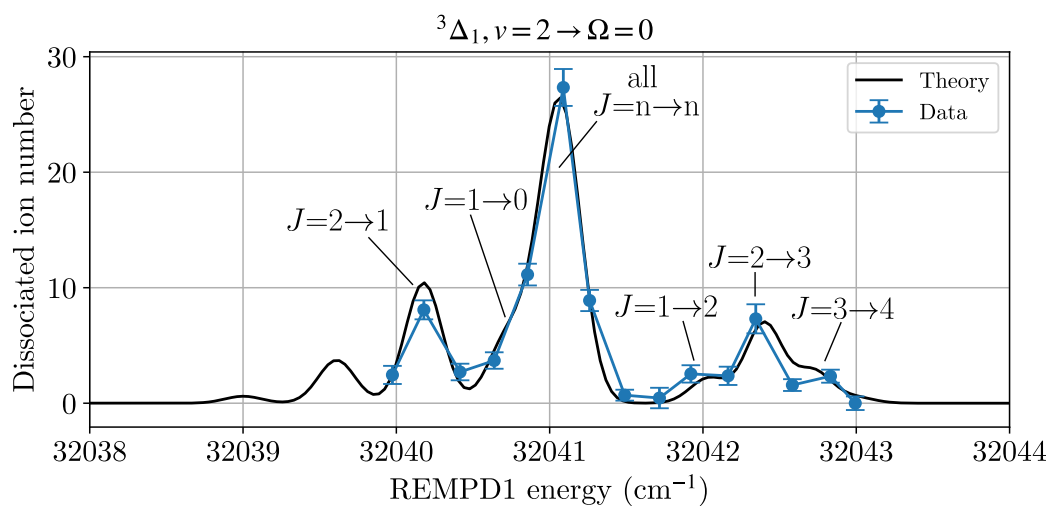


a)

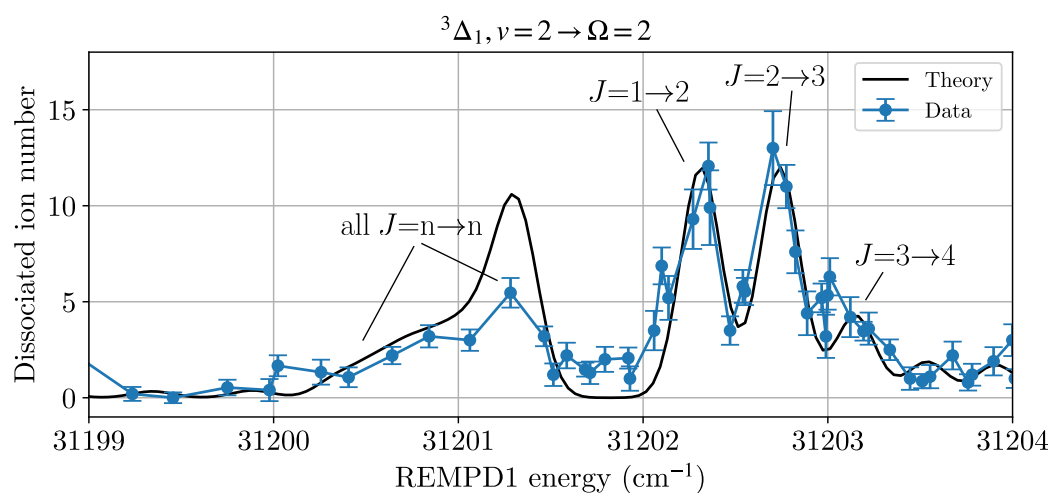
Transition	Energy (cm <sup>-1</sup> )
$(^3\Delta_1, v=1, J=1) \rightarrow (\Omega=0, J=2)$	31973.94(05)
$(^3\Delta_1, v=1, J=2) \rightarrow (\Omega=0, J=3)$	31974.31(05)

b)

Figure 6.4: Dissociation spectroscopy for  $v=1$ . a) Transitions to an  $\Omega=2$  intermediate state. b) Energies of the prominent and well-isolated transitions.



a)



b)

c)

Transition	Energy ( $\text{cm}^{-1}$ )
$({}^3\Delta_1, v=2, J=2) \rightarrow (\Omega=0, J=1)$	32040.18(05)
$({}^3\Delta_1, v=2, J=2) \rightarrow (\Omega=0, J=3)$	32042.40(05)
$({}^3\Delta_1, v=2, J=1) \rightarrow (\Omega=2, J=2)$	31202.31(05)
$({}^3\Delta_1, v=2, J=2) \rightarrow (\Omega=2, J=3)$	31202.74(05)

Figure 6.5: Dissociation spectroscopy for  $v=2$ . a) Transitions to an  $\Omega=0$  intermediate state. b) Transitions to an  $\Omega=2$  intermediate state. c) Energies of the prominent and well-isolated transitions.

### 6.1.3 Hyperfine selectivity

Because the Ramsey spectroscopy involves the hyperfine states within  ${}^3\Delta_1$ ,  $v = 0$ ,  $J = 1$ , it is not enough to read out the whole of the population in this manifold, as we can do by dissociating from the  $({}^3\Delta_1, v = 0, J = 1) \rightarrow (\Omega = 0, J = 2)$  transition from Figure 6.3. We additionally need to be able to distinguish population in  $m_F = 3/2$  and  $m_F = -3/2$ . We can do this by turning back on  $\mathcal{L}_{m_F}$  without closing any of the other vibrational and rotational levels. The effect of doing this is shown in Figure 6.6

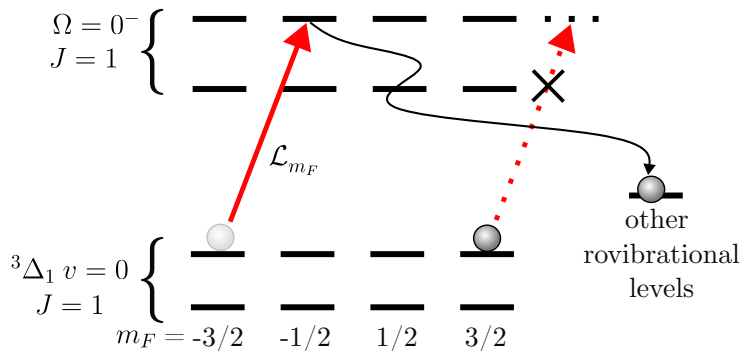


Figure 6.6: Shelving of the unwanted hyperfine states into higher ro-vibrational states with  $\mathcal{L}_{m_F}$ .

Because the excited  $\Omega = 0^-$  state does not have an  $m_F = 5/2$  state,  $\mathcal{L}_{m_F}$  does not talk to the  $m_F = 3/2$  state. Meanwhile, all other  $m_F$  levels will be excited to the  $\Omega = 0^-$  state and fall down predominantly into other ro-vibrational manifolds. If we then dissociate from  $J = 1$ , the population we dissociate will represent the population that was in  $m_F = 3/2$ .

Alternatively, we can do the exact procedure for  $m_F = -3/2$  by swapping the orientation of  $\mathcal{L}_{m_F}$  with respect to the quantization axis.

## 6.2 Ion imaging

After being state-selectively dissociated, the ions are imaged using a micro-channel plate (MCP) detector. The setup is shown in Figure 6.7. The mesh is a grid-like electrode designed to prevent electric fields from leaking out and causing lensing of the ions as they approach the detector. The MCP itself is held at a negative high voltage so that the ions accelerate towards the

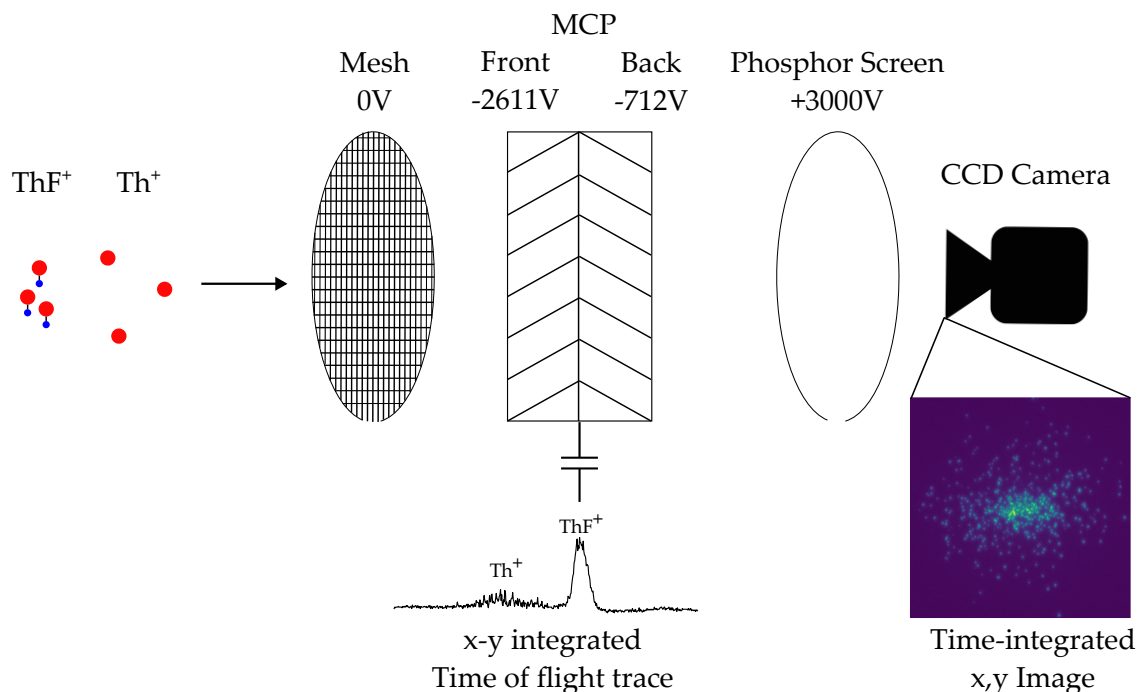


Figure 6.7: Ion imaging scheme using a micro-channel plate (MCP) detector.

detector and strike the detector with around 2700 eV of kinetic energy. This collision induces an electron avalanche along the potential gradient between the front and back plate of the MCP. The electron avalanche produces a current which can be capacitively read out from the MCP, resulting in a time-of-flight (TOF) signal of ions arriving.

The detector consists of an array many small channels. Electron avalanches happen individually in each of these small channels, keeping the detection spatially resolved. The electrons then fly out the back of the MCP and are then accelerated towards a phosphor screen a short distance away held at a high voltage. Once again, the potential gradient caused by the high voltage means the electrons hit the phosphor screen with a kinetic energy of over 3 keV, which is enough energy to cause the phosphor screen to fluoresce. Because the lifetime of the fluorescing states of the phosphor is long compared to the timescales of the ion detection (tens of  $\mu\text{s}$ ), the phosphor screen effectively integrates the 2-D projection of ions incident on the detector. A charge coupled device (CCD) camera is then used to image the fluorescing phosphor plate.

## 6.2.1 Electronics

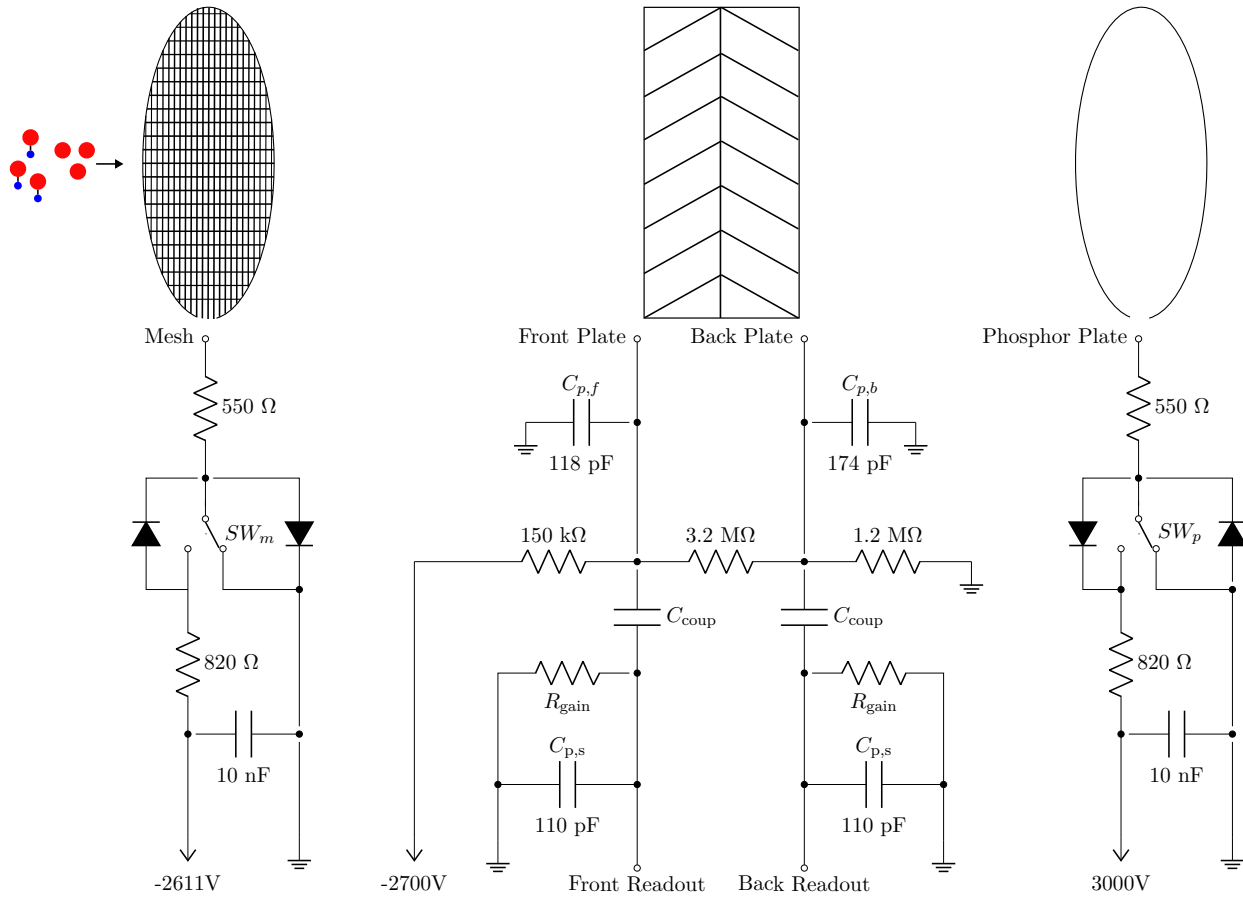


Figure 6.8: Schematic for the MCP readout circuit.  $C_{p,f}$  and  $C_{p,b}$  are the parasitic capacitance to ground of the front and back plate of the MCP respectively, while  $C_{p,s}$  is the parasitic capacitance of the oscilloscope and the cabling to the scope. The MCP is a Beam Imaging Solutions BOS-40-OPT01-MS dual matched MCP with a BOS-40-92% transmission grid mesh and a P42 phosphor screen. The switches  $SW_m$  and  $SW_p$  are Behlke HTS 31-03-HB-C fast HV transistor switches, which are controlled with an opto-isolator to protect the TTL generator from high voltage shorts. Additional protection to the power supplies on the switching circuits is provided by a set of diodes which allow high-voltage transients induced by the switching to be dumped from the output of the switch to ground.

The electronics used to drive the detector are shown in Figure 6.8. If the time domain signal is a Gaussian of width  $\sigma_t$  then the corresponding Fourier domain signal is also a Gaussian, of width  $\sigma_\omega = \frac{1}{\sigma_t}$ . To faithfully capture the signal, we want to capture frequencies up to  $2\sigma_\omega$ , which includes 97% of all frequency components in the signal. The characteristic frequency  $\omega$  that we need to be sensitive to is then  $\omega = \frac{2}{\sigma_t}$ .



This frequency informs our choice of values for the components in the readout circuit. If we want the current induced on the MCP to flow primarily through the coupling capacitor and through the gain resistor, we want the impedance of this path to be small compared to the direct path to ground through the parasitic capacitance.

$$Z_{C_{\text{coup}}} + (R_{\text{gain}} || Z_{C_{\text{p,s}}}) \ll Z_{C_{\text{p,f}}} \quad (6.1)$$

$$\frac{1}{i\omega C_{\text{coup}}} + \left( \frac{1}{R_{\text{gain}}} + i\omega C_{\text{p,s}} \right)^{-1} \ll \frac{1}{i\omega C_{\text{p,f}}} \quad (6.2)$$

$$\frac{1}{C_{\text{coup}}} \ll \frac{1}{C_{\text{p,f}}} - i\omega \left( \frac{1}{R_{\text{gain}}} + i\omega C_{\text{p,s}} \right)^{-1} \quad (6.3)$$

$$C_{\text{coup}} \gg \left( \frac{1}{C_{\text{p,f}}} - i\frac{2}{\sigma_t} \left( \frac{1}{R_{\text{gain}}} + i\frac{2}{\sigma_t} C_{\text{p,s}} \right)^{-1} \right)^{-1}, \quad (6.4)$$

where  $||$  represents impedances in parallel ( $A || B \equiv (A^{-1} + B^{-1})^{-1}$ ). We also want the RC time of the coupling capacitor and the gain resistor to be small compared to the timescale of the signal so that the voltage at the readout port can rise and fall quickly enough to faithfully reproduce the signal, i.e.

$$R_{\text{gain}} C_{\text{coup}} \ll \sigma_t. \quad (6.5)$$

The final requirement is one of signal to noise. The voltage readout on the port will be equal to the gain resistance times the current induced on the MCP plate. If we require a signal of at least  $V_{\text{min}}$  for adequate signal to noise, this means that

$$I_{\text{induced}} R_{\text{gain}} > V_{\text{min}}. \quad (6.6)$$

The parameters can then be chosen to satisfy Equations 6.4, 6.5, and 6.6. Given the measured values of the relevant parameters, as given in Table 6.1, a set of parameters that satisfy the requirements are:

$$\begin{cases} R_{\text{gain}} = 200 \, \Omega \\ C_{\text{coup}} = 235 \, \text{pF}. \end{cases} \quad (6.7)$$

$\sigma_t$	$0.5 \mu\text{s}$
$C_{p,s}$	$110 \text{ pF}$
$C_{p,f}$	$118 \text{ pF}$
$C_{p,b}$	$174 \text{ pF}$
$I_{\text{induced}}$	$0.1 \text{ mA}$
$V_{\text{min}}$	$20 \text{ mV}$

Table 6.1: Measured values relevant to the MCP readout electronics

### 6.2.2 Mesh gating

While holding the mesh at ground does minimize ion lensing effect from electric fields leaking out from the detector attracting the ions, it also leaves a "shadow" artifact on the ion cloud. This effect is shown in Figure 6.9. We leave the mesh at the same voltage as the front plate of the MCP, because the lensing can be accounted for and the grid resulting from the alternative interferes with individual ion counting.

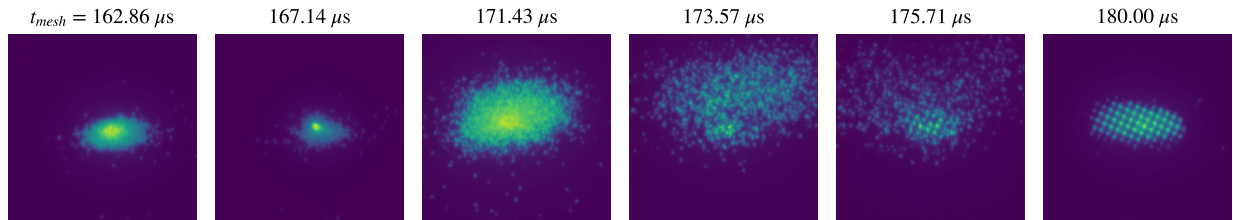


Figure 6.9: Effect of the mesh of the ion image. The mesh is held at ground until the time  $t_{\text{mesh}}$  listed above each image, at which point the voltage is switched to be the same as the front plate of the MCP. In the time scale of the ion arrivals, the left image is equivalent to leaving the mesh at the same voltage as the front plate the whole time, while the right image is equivalent to leaving the mesh at ground the whole time. The images in between represent switching the voltage during the ion arrival, resulting in extreme lensing. When the mesh is grounded, lensing is suppressed, but the mesh leaves an artifact on the image. When the mesh is held at the same voltage as the front plate of the MCP, lensing focuses the image of the cloud and the grid artifact is removed. The images are taken using  $\text{ThF}^+$  without dissociation.

The image of the mesh projected on the ion cloud can be used to calibrate the distance scale on the image to the distance scale on the plane of arrival of the ions onto the MCP. This calibration is done in Figure 6.10.

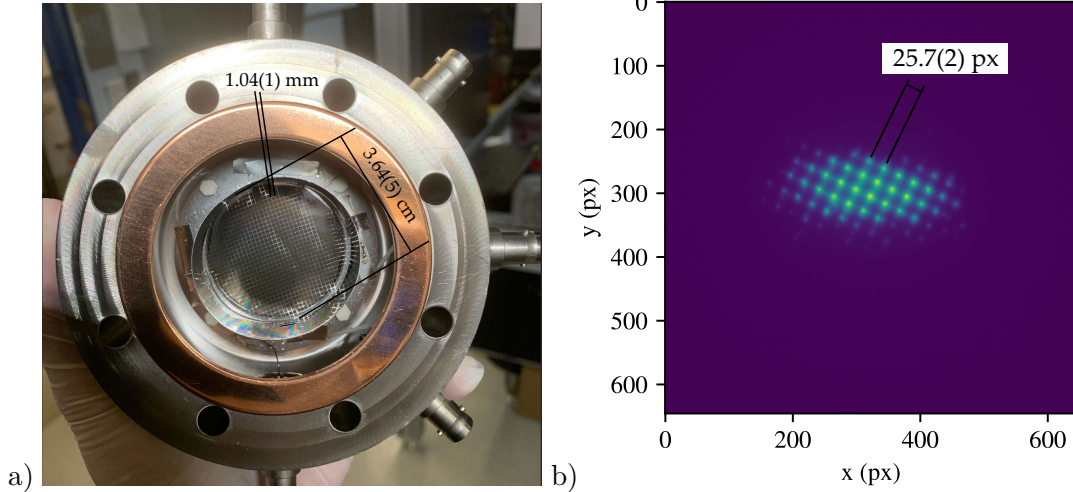


Figure 6.10: Comparison of the MCP mesh geometry and image artifact. a) An image of the MCP detector. b) An image of a  $\text{ThF}^+$  cloud with the mesh grounded. From these the pixel size can be calibrated to a size of the ion cloud when it hits the detector. 1 pixel represents a size of  $40.5(5) \mu\text{m}$ .

### 6.2.3 Phosphor screen gating

The dissociated  $\text{Th}^+$  ion number constitutes the signal of interest. In general in our system, there are no more than 200 dissociated ions, meaning we can image them in 2-D on our detector and can count individual ions based on their location without significant overlap. However, the non-dissociated  $\text{ThF}^+$  ions will also arrive at the detector. The slight difference in mass between the two species means that the  $\text{Th}^+$  ions will arrive at the detector slightly before the  $\text{ThF}^+$  ions. We can then selectively image the  $\text{Th}^+$  ions by turning off the phosphor screen in the time between the arrival of the two species. This is demonstrated in Figure 6.11.

High temperature ions on the tail of the  $\text{ThF}^+$  cloud can still be captured by the phosphor screen and show up as background on the signal. To prevent this, the time at which the phosphor screen is turned off is tuned to maximally capture the  $\text{Th}^+$  cloud without any pollution of  $\text{ThF}^+$  ions. Because this timing changes with arrival time, it must be scanned every time the trap is shimmed. Figure 6.12 shows an example of such a scan.

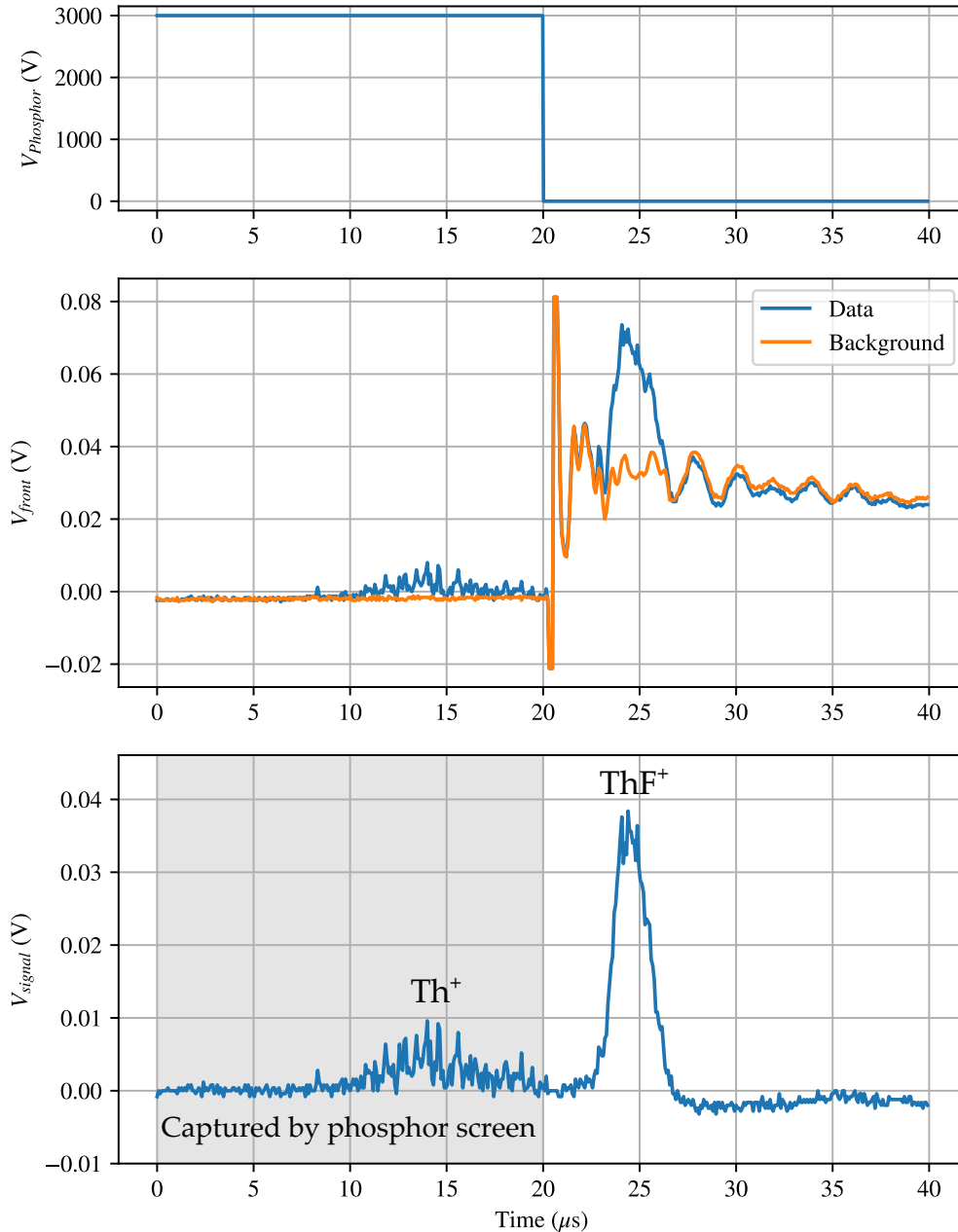


Figure 6.11: MCP capacitive readout signal with phosphor gating. Top: the set voltage on the phosphor plate as a function of time. The potential is turned off between the  $\text{Th}^+$  and  $\text{ThF}^+$  arrival times so that only the  $\text{Th}^+$  is imaged. Middle: the resulting scope trace of the capacitive readout of the front. Switching the phosphor voltage to ground creates a pickup on the signal via parasitic capacitance between the mesh and the MCP (orange). However, this pickup is repeatable, so the difference between the scope trace and a background trace with no ions gives the ion signal, shown in the bottom. The data shown is a single shot, with a single shot background. This data was taken with high REMPD power and optically pumping all ions into the dissociated state, so the  $\text{Th}^+$  count in this trace is higher than in normal operation.

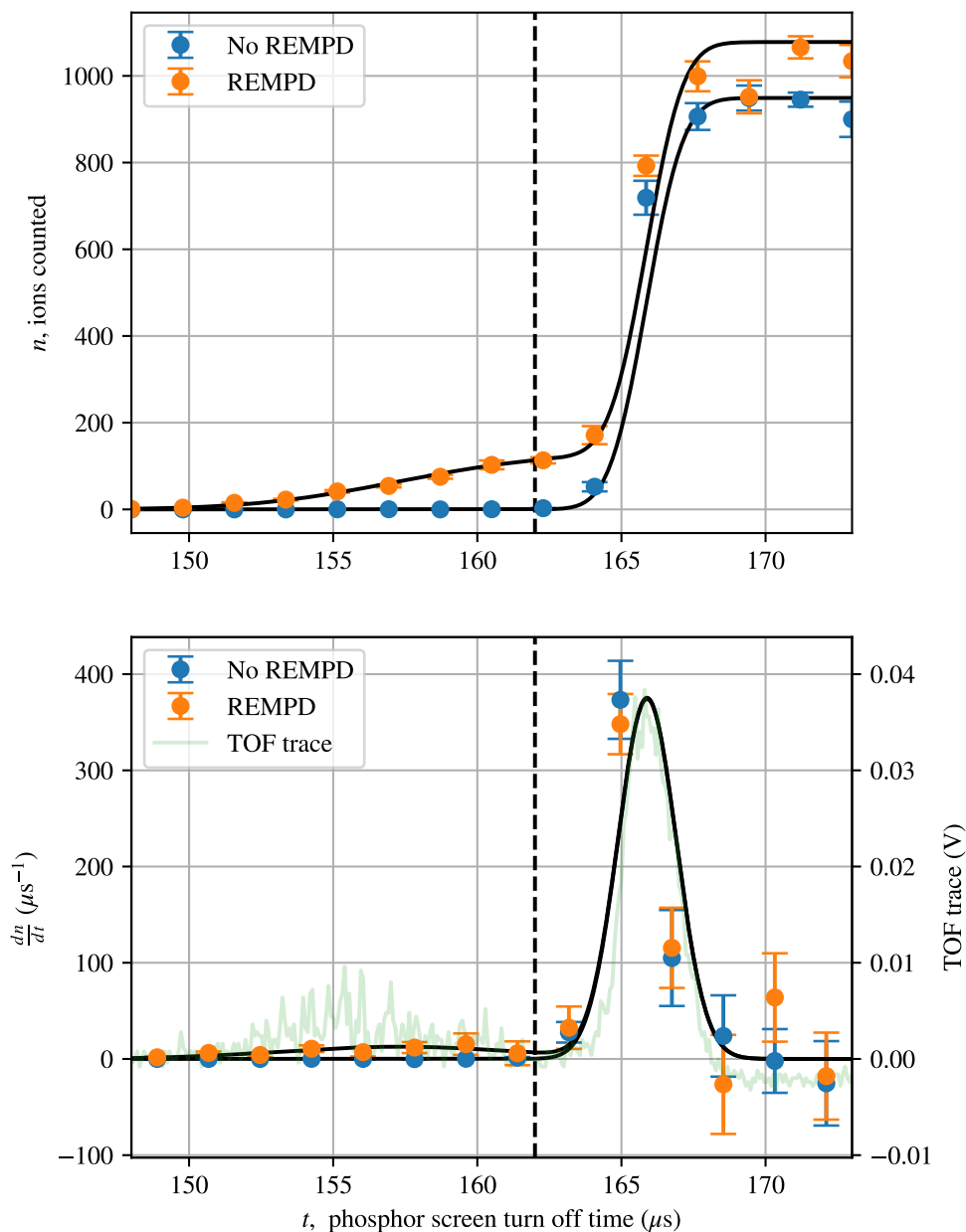


Figure 6.12: Scan of phosphor gate turn off time. Top: ions counted on the phosphor image. The data without REMPd is fitted to a single erf function representing the integral of the  $\text{ThF}^+$  cloud, while the data with REMPd is fitted to a sum of two erf functions representing the integral of both the  $\text{Th}^+$  and  $\text{ThF}^+$  clouds. Bottom: the derivative of the above curves, corresponding to the actual ion intensity profile. Overlaid in green is a time of flight trace from another experiment. The dashed vertical line represents the time in which no  $\text{ThF}^+$  ions pollute the phosphor signal, i.e. the blue signal on the top plot is negligible.

## 6.2.4 Capacitive readout interpretation

### 6.2.4.1 Theory

The MCP plate is held at  $-2700$  V, so the kinetic energy at the time of impact is  $2700$  eV. For ThF ions, this equates to  $45$  km/s, meaning the ions spend only  $0.2 \mu\text{s}$  within  $1$  cm of the detector. The electrons knocked loose then undergo an acceleration in an electric field of order kV/cm, so the timescale of the electron avalanche effect is similarly short. Since this is small compared to RC times of the detector, the shape of a single ion's response is dominated by the RC response of the system rather than the shape of the individual ion's interaction. If the detector has a rise time of  $\tau_{\text{rise}}$  and a fall time of  $\tau_{\text{fall}}$ , then the voltage response of an individual ion on the detector is given by

$$R_V(t) = \frac{e^{1-\frac{t}{\tau_{\text{rise}}}} (e^{t/\tau_{\text{rise}}} - 1) \theta(\tau_{\text{rise}} - t, t)}{e - 1} + \theta(t - \tau_{\text{rise}}) e^{-\frac{\tau_{\text{rise}} - t}{\tau_{\text{fall}}}}, \quad (6.8)$$

where  $\theta$  is the Heaviside step function. Since we are reading out the current via a capacitive coupling, the current response is given by

$$R_I(t) = C \frac{dR_V}{dt} \propto \frac{e^{1-\frac{t}{\tau_{\text{rise}}}} \theta(\tau_{\text{rise}} - t, t)}{(e - 1)\tau_{\text{rise}}} - \frac{e^{-\frac{\tau_{\text{rise}} - t}{\tau_{\text{fall}}}} \theta(t - \tau_{\text{rise}})}{\tau_{\text{fall}}}. \quad (6.9)$$

If  $N_{\text{ions}}$  fall on the detector in the form of a Gaussian with width  $\sigma_{\text{ion}}$ , then the signal read on the detector look like a convolution of this with the current response function:

$$I_{\text{readout}}(t) \propto \left( \frac{N_{\text{ions}}}{\sigma_{\text{ion}} \sqrt{2\pi}} e^{-\frac{t^2}{2\sigma_{\text{ion}}^2}} \right) * R_I(t) \\ = N_{\text{ions}} \left( \frac{e^{\frac{\sigma_{\text{ion}}^2 - 2\tau_{\text{rise}} t}{2\tau_{\text{rise}}^2} + 1} \left( \text{erf} \left( \frac{\sigma_{\text{ion}}^2 + \tau_{\text{rise}}(\tau_{\text{rise}} - t)}{\sqrt{2}\sigma_{\text{ion}}\tau_{\text{rise}}} \right) - \text{erf} \left( \frac{\sigma_{\text{ion}}^2 - \tau_{\text{rise}} t}{\sqrt{2}\sigma_{\text{ion}}\tau_{\text{rise}}} \right) \right)}{2(e-1)\tau_{\text{rise}}} - \frac{e^{\frac{\sigma_{\text{ion}}^2 + 2\tau_{\text{fall}}\tau_{\text{rise}} - 2\tau_{\text{fall}} t}{2\tau_{\text{fall}}^2}} \text{erfc} \left( \frac{\sigma_{\text{ion}}^2 + \tau_{\text{fall}}(\tau_{\text{rise}} - t)}{\sqrt{2}\sigma_{\text{ion}}\tau_{\text{fall}}} \right)}{2\tau_{\text{fall}}} \right). \quad (6.10)$$

This current is converted to a voltage ready by the scope by the gain-setting resistor  $R_{\text{gain}}$ . The impulse response functions (Equation 6.8 and 6.9) and the resulting readout signal (Equation 6.10)

are shown in Figure 6.13, wherein a fit to the TOF signal yields time constants:

$$\begin{cases} \tau_{\text{rise}} = 2.50 \pm .04 \mu\text{s} \\ \tau_{\text{fall}} = 44 \pm 3 \mu\text{s}. \end{cases} \quad (6.11)$$

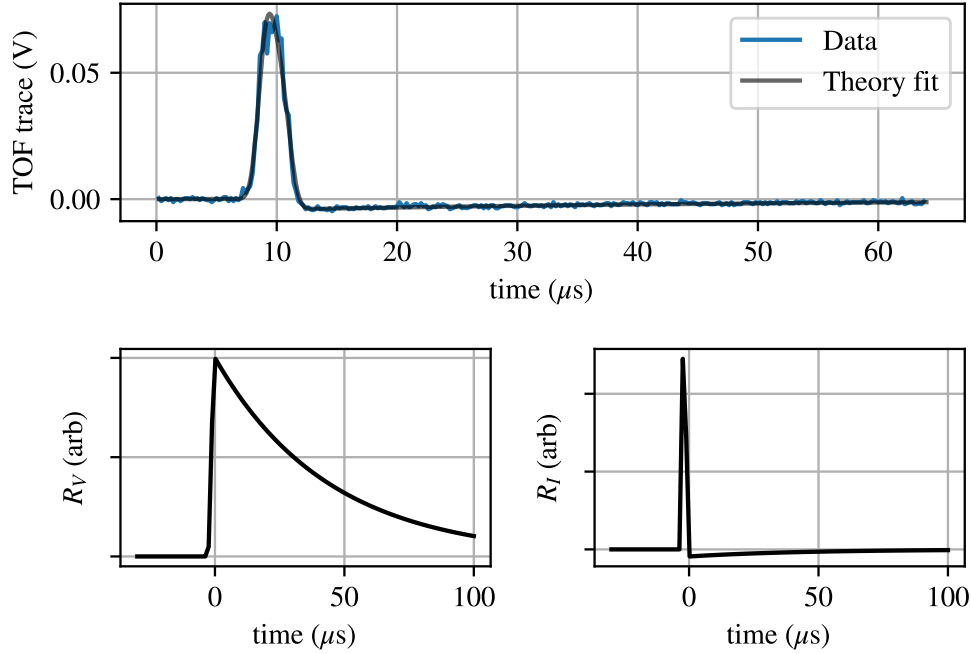


Figure 6.13: The impulse response functions of the MPC capacitive readout. Top: The TOF trace of a  $\text{ThF}^+$  cloud, and a fit of the theoretical form given by Equation 6.10. Bottom: The voltage and current impulse response given by Equations 6.8 and 6.9, where the time constants are given by the above fit.

The fall time can be understood to as the  $RC$  time for the power supply to recharge the front plate through the  $150 \text{ k}\Omega$  current-limiting resistor, with the relevant capacitance being all capacitances from the front plate to ground:

$$\tau_{\text{fall}} \sim (150 \text{ k}\Omega)(C_{\text{p,f}} + (C_{\text{coup}}^{-1} + C_{\text{p,s}}^{-1})^{-1}) = 30 \mu\text{s}. \quad (6.12)$$

One thing to note is that integrating the whole waveform is not a measure of Ion number since it evaluates identically to zero:

$$\int_{-\infty}^{\infty} I_{\text{readout}}(t) dt = 0. \quad (6.13)$$

Instead, one can first take the indefinite integral of the measured waveform and then integrate this signal over all time. Using first the relation of convolution to indefinite integrals and then the relation of convolution to integrals over all space, we can see how this is proportional to the number of ions:

$$\int_{-\infty}^{\infty} \int_{-\infty}^{t'} I_{\text{readout}}(t) dt dt' \propto \int_{-\infty}^{\infty} \int_{-\infty}^{t'} \left( \frac{N_{\text{ions}}}{\sigma_{\text{ion}} \sqrt{2\pi}} e^{-\frac{t^2}{2\sigma_{\text{ion}}^2}} \right) * R_I(t) dt dt' \quad (6.14)$$

$$= \int_{-\infty}^{\infty} \left( \frac{N_{\text{ions}}}{\sigma_{\text{ion}} \sqrt{2\pi}} e^{-\frac{t^2}{2\sigma_{\text{ion}}^2}} \right) * \left( \int_{-\infty}^{t'} R_I(t) dt \right) dt' \quad (6.15)$$

$$\propto \int_{-\infty}^{\infty} \left( \frac{N_{\text{ions}}}{\sigma_{\text{ion}} \sqrt{2\pi}} e^{-\frac{t^2}{2\sigma_{\text{ion}}^2}} \right) * R_V(t) dt \quad (6.16)$$

$$= N_{\text{ions}} \left( \int_{-\infty}^{\infty} \left( \frac{1}{\sigma_{\text{ion}} \sqrt{2\pi}} e^{-\frac{t^2}{2\sigma_{\text{ion}}^2}} \right) dt \right) \left( \int_{-\infty}^{\infty} R_V(t) dt \right) \quad (6.17)$$

$$\propto N_{\text{ions}}. \quad (6.18)$$

since the first integral evaluates to 1 and  $R_V$  does not depend on any ion-dependent features. In practice, this method for ion counting is impractical because a) any low-pass filtering from parasitic capacitance interferes with this measure, b) this requires that multiple ion clouds arriving on the detector be much farther apart than the length of the MCP recharge, and c) this method is more susceptible to noise and offsets on the signal.

Alternatively, we can recover the signal representing the time density of ions hitting the detector. If we know the impulse response function  $R_I$  using the time constants fit in Figure 6.17, we can simply deconvolve the measured signal with this impulse response to recover the time-domain ion density.

Generally, deconvolution is sensitive to noise, particularly high frequency noise. This is because deconvolution of A and B is mathematically equivalent to dividing A by B in Fourier space. The regions of frequency space where the Fourier transform of B,  $\mathcal{F}\{B\}$ , goes to zero are divided by a small number, so any noise in  $\mathcal{F}\{A\}$  in these regions is greatly enhanced.

To treat this, we can apply a low-pass bidirectional Butterworth filter with cutoff frequency at  $\omega_c = 2\pi \frac{2}{\tau_{\text{rise}}}$ . Because frequencies above this are naturally filtered away by the  $RC$  response



of the MCP, we do not lose any signal information by applying this filter, and we only remove detection noise. With this treatment, we are able to successfully deconvolve the impulse response  $R_I$  from the detector to remove the negative tail corresponding to MCP recharging. The result is shown in Figure 6.14.

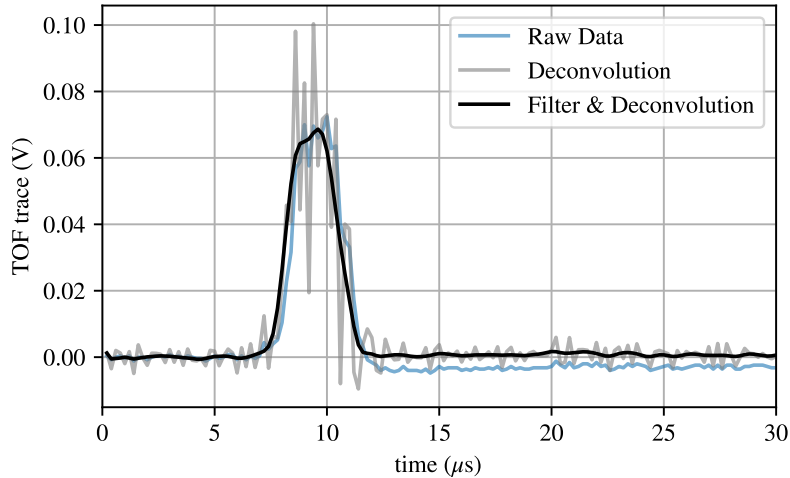


Figure 6.14: Recovery of the ion signal of a  $\text{ThF}^+$  cloud via deconvolution with the current impulse response function, given by Equation 6.9 with values from Equation 6.11. The deconvolution removes the negative tail of the signal, allowing the signal to be directly integrated to recover the ion number corresponding to the peak.

The deconvolution algorithm still requires sufficient signal to noise ratio, since some frequencies below  $\omega_c$  are still enhanced. For lower ion numbers with insufficient signal to noise, directly integrating the positive part of the signal is a good approximation of the area, and a much more robust algorithm.

#### 6.2.4.2 Area algorithm and uncertainty

To count the number of  $\text{ThF}^+$  ions in the TOF trace, we must integrate the area under the TOF signal. There is some nuance in the way this is done in order to allow for noise and offsets, as well as to characterize the uncertainty in the measurement. The algorithm used to extract the area is as follows:

- (1) Use timings to predict rough arrival time of ion cloud

- (2) Fit the ion signal to a Gaussian using the prediction of arrival time as the initial fit condition. From the fit extract the arrival time and the Gaussian width
- (3) Take the mean of the portion of the signal that is  $3.5\sigma$  or more away from the fit location in order to find the background on the signal. Subtract this background away
- (4) Numerically integrate the background-subtracted signal to  $3.5\sigma$  on either side of the arrival time to extract the area under the curve.

In order to place an uncertainty prediction on this measurement, we must consider the following:

- (a) Statistical uncertainty in the background of the signal. This uncertainty is given by the product  $\sigma_{\text{background}} \cdot (\text{width of area integrated})$ , where  $\sigma_{\text{background}}$  is standard deviation of the points used to determine the background divided by the square root of the number of points.
- (b) Algorithmic uncertainty from the arbitrary assignment of  $3.5\sigma$  as the region of interest. To probe this, we can vary the width integrated over and look at the standard deviation of the results.
- (c) Statistical uncertainty from the noise on the signal. Since this cannot be directly measured, we can approximate it by assuming that the noise profile in the background is the same as the noise profile on the signal. This is mathematically equivalent to the value calculated in the uncertainty of the background.

The total uncertainty can be estimated by adding these three uncertainties in quadrature. To verify the validity of this error characterization method, a Monte Carlo simulation is done with a Gaussian signal in the presence of white noise. The results are displayed in Figure 6.15.

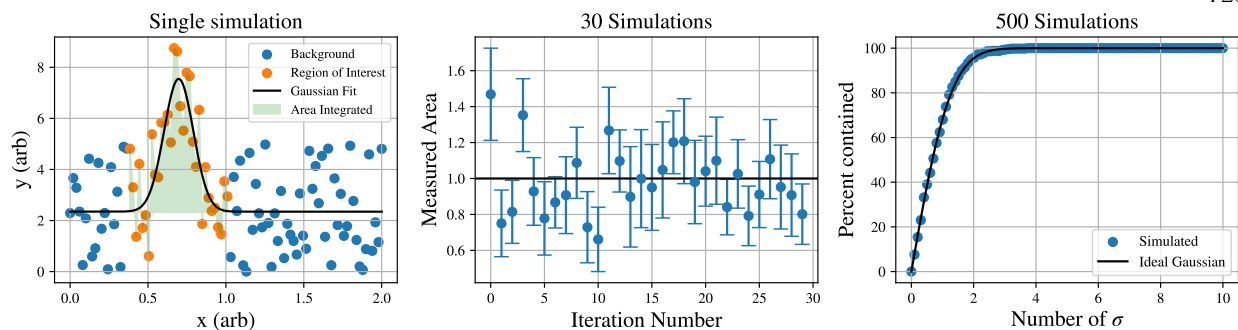


Figure 6.15: Monte Carlo simulation of the area counting algorithm for a small Gaussian signal in the presence of significant noise. Left: A single simulated signal. Middle: The area counted by the algorithm for 30 simulations, with error bars representing the uncertainty calculated according to the method proposed. The actual area of the simulated Gaussian is 1. Right: statistics on 500 simulations. The percent of simulations in which the area measured by the algorithm is  $N\sigma$  away from the true value is shown for varying  $N$ . The black line represents the ideal behavior of a Gaussian distribution. Agreement with this line indicates that the  $\sigma$  calculated by the algorithm is correct.

### 6.2.5 Ion counting

Ions imaged on the phosphor screen are counted individually using the python package `skimage`. The code is listed in Figure 6.16. First, a smoothing filter is applied with a width of two pixels, so that pixel-to-pixel CCD noise is removed. Then, an erosion filter is applied such that nearby, partially overlapping ions have the bridging region between them carved away. This helps in uniquely identifying the two neighboring ions. Next, the peaks are found using a threshold of three pixel brightness units and a minimum ion-ion distance of five pixels.

```
import skimage as sk
import scipy.ndimage as sn

def get_img_info_count(img, IMG_threshold = 3, IMG_min_distance = 5):
    # Smooth image
    img = sn.median_filter(img, size=2)
    # Erode between ions
    img = sk.morphology.erosion(img)
    # Find peaks
    peaks = sk.feature.peak_local_max(img, threshold_abs=IMG_threshold, min_distance=
                                     IMG_min_distance)
    return peaks
```

Figure 6.16: Python code to count individual ions on the phosphor screen image

Using ions identified with this algorithm, a point spread function for an ion incident on the detector can be measured. This is done in Figure 6.17.

If the ion density is high enough that the distance between adjacent ions is smaller than the width of the point spread function, the ions become indiscernible in the image, and cannot be counted separately. This means that the algorithm that counts the number of ions in the image will begin to saturate. This is demonstrated in Figure 6.18 using a Monte Carlo method.

### 6.3 Simultaneous doublet readout

Reading the dissociated  $\text{Th}^+$  ions in a spatially resolved way allows additional information to be extracted from the readout. In a single image, populations in the two different doublets can be differentiated by making use of the fact that the two doublet states have opposite orientation relative to  $E_{rot}$ . During photodissociation, the excess energy of the absorbed photons relative to the dissociation threshold translates into kinetic energy of the dissociated atoms, which then fly apart from each other along their inter-nuclear axis. As the neutral fluorine atom flies away from the heavier thorium ion, the direction of the kinetic energy imparted to the thorium is determined by the molecule orientation. The result of this process is that we see two spatially separated clouds of Thorium ions on our detector, each cloud corresponding to different orientation and thus a different doublet state. This is demonstrated in Figure 6.19.

We can then count individual ions in each cloud, thereby directly reading out the number of ions in each state. This dissociation-based state readout technique is further detailed in [60], as well as in Ng's thesis [39].

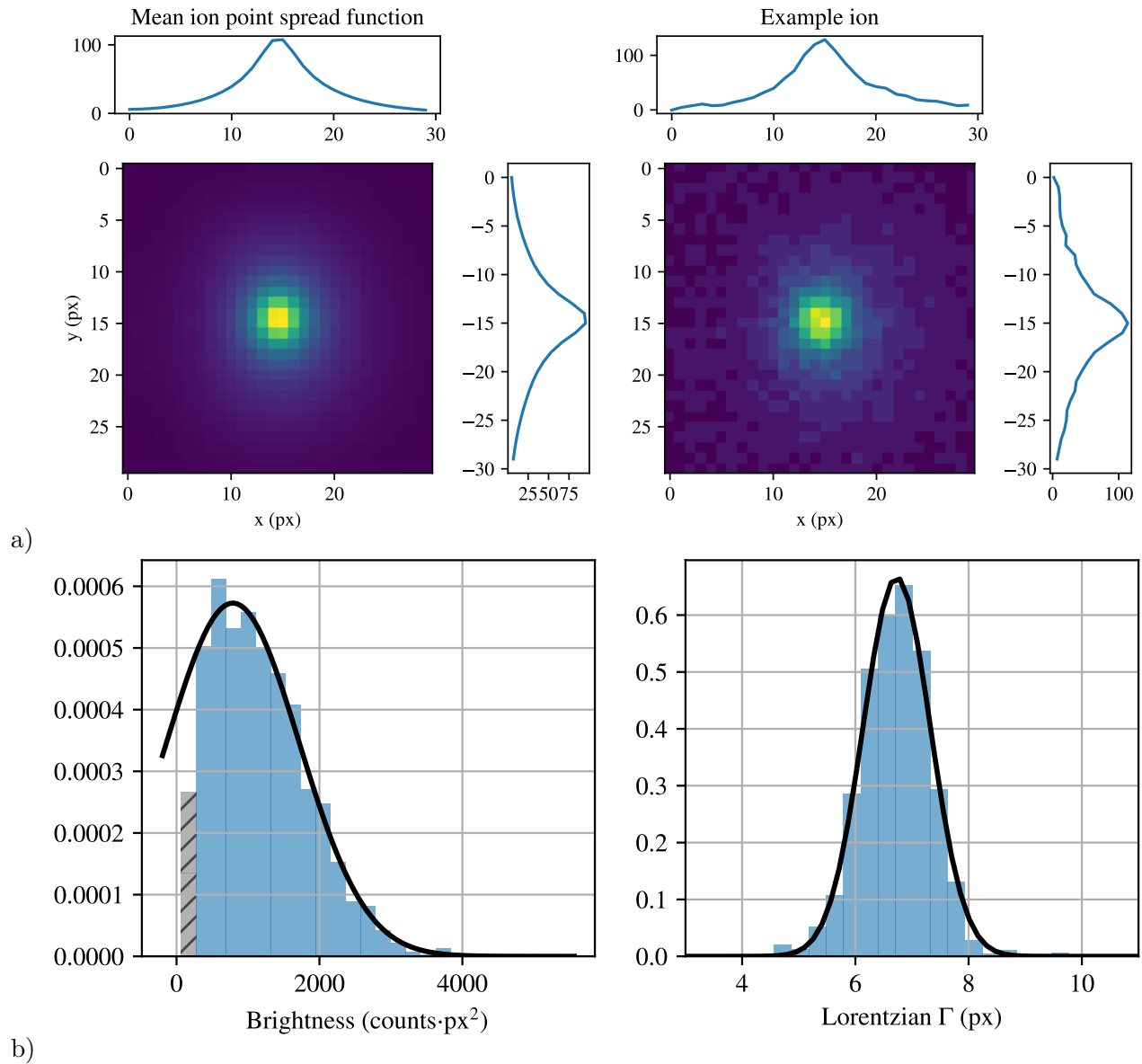


Figure 6.17: Phosphor image of  $\text{Th}^+$  ions. 2153 captured images of individual ions are analyzed. a) The point spread function of each ion on the detector. On the left is the mean image of all ions counted, and on the right is an image of a single ion. Each dimension is integrated along both axes. The spatial distribution fits nicely to a Lorentzian as a function of radius. b) Statistics on the ion pictures. On the left is the integrated brightness on the detector due to the ion. The greyed histogram bar indicated where the algorithm used to count the ions is undercounting due to low signal to noise ratio. This bin is excluded from the fit of the distribution. On the right is the distribution of widths of a Lorentzian fit to each ion image. Both distributions fit nicely to normal distributions.

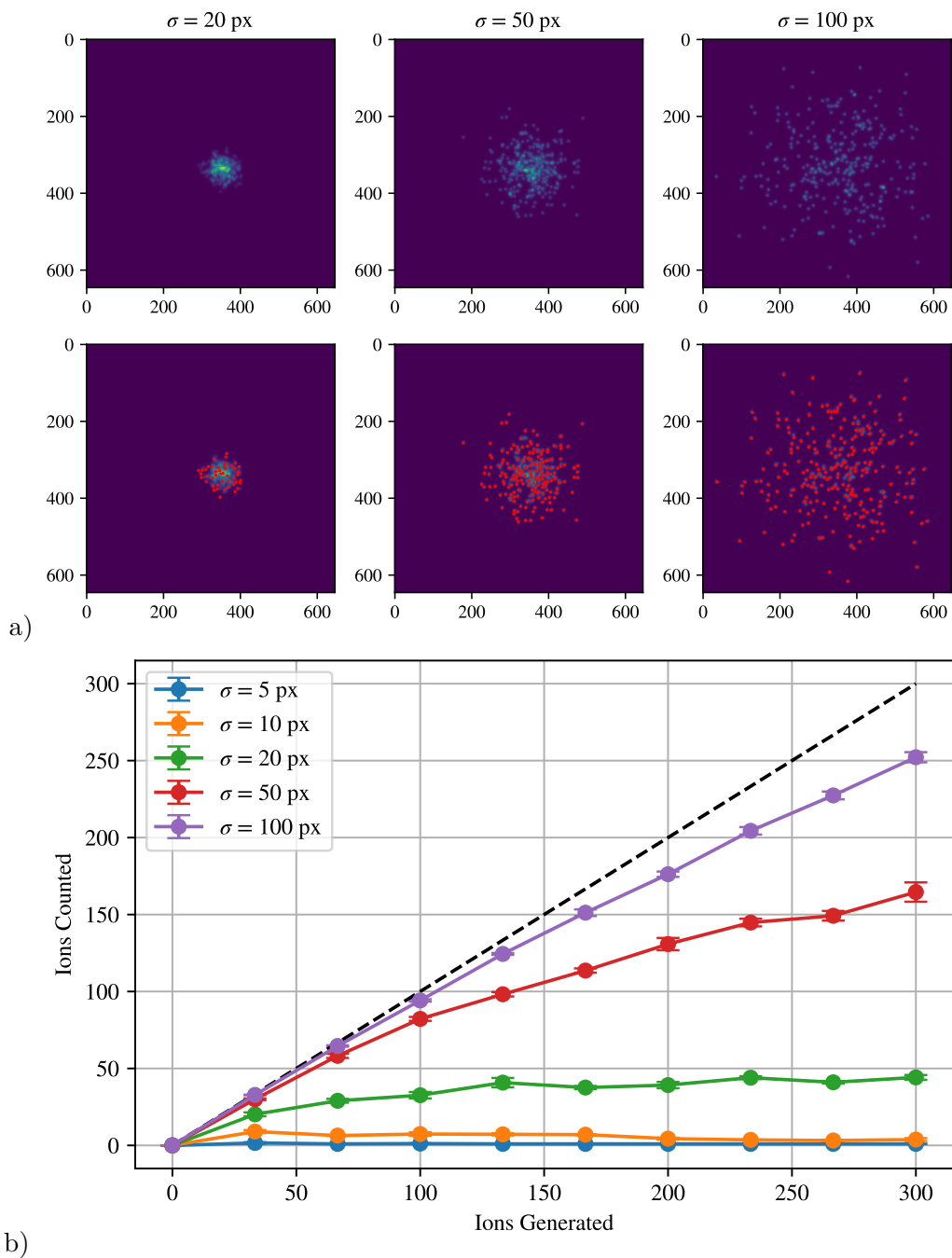


Figure 6.18: Demonstration of ion counting algorithm and its saturation via a Monte Carlo simulation. a) Top: simulated images of ion clouds using the point spread function from Figure 6.17 for each of 300 ions in a normal spatial distribution of varying widths. Bottom: The same images, with the ions detected by the counting algorithm overlaid in red. Significant under-counting of the ions can be observed in the image with distribution width 20 px. b) Resulting saturation of the counting algorithm at different cloud widths. Each point represents five simulations.

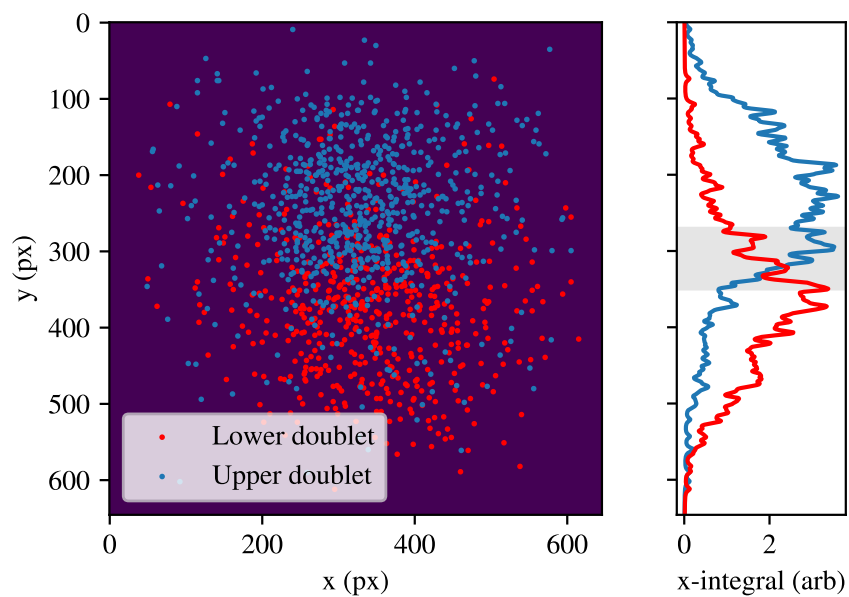


Figure 6.19: Spatially resolved images of the two doublets. For each image, the one doublet is depleted using the appropriate microwave transition, leaving only population in the remaining doublet. Each image represents the ion locations cumulatively counted from 3 images. Plotted to the right is the integral of each cloud across the horizontal axis. The shaded gray region indicates the region where the doublets overlap, beyond which the signal predominantly represents a single doublet.

## Chapter 7

### Preliminary Results and Conclusion

#### 7.1 Rabi oscillations

With the trapping, state preparation, and readout techniques previously described we are able to perform quantum operations in the eEDM sensitive states. A demonstration of Rabi flopping is shown in Figure 7.1.

The Rabi flopping is done by reducing the magnitude of the polarizing field until the hyperfine states are near-degenerate leading to population mixing. An  $\mathcal{E}_{\text{rot}}$  of 13.7 V/cm is chosen such that the Rabi rate is equal for both doublets. More information on this can be found in Ng’s thesis [39].

Each of the ion number data points corresponds to either preparing one hyperfine level<sup>1</sup>  $m_F = \pm 3/2$  and reading out the population<sup>2</sup> in the same state  $m_F = \pm 3/2$  (labeled as “In”) or preparing in the other hyperfine level  $m_F = \mp 3/2$  and reading out from  $m_F = \pm 3/2$  (labeled as “Anti”). We vary the prepared state instead of the final state because the polarization of the dissociation laser changes the efficiency of dissociating from different final states. From the population in each of the two states we can extract the “asymmetry.” The asymmetry between the ion numbers  $N_{\text{In}}$  and  $N_{\text{Anti}}$  measured in this way is defined as

$$\text{Asymmetry} \equiv \frac{N_{\text{In}} - N_{\text{Anti}}}{N_{\text{In}} + N_{\text{Anti}}}. \quad (7.1)$$

This quantity is normalized and is therefore immune certain types of common mode noise, such as slow drift in ion creation or dissociation efficiency.

---

<sup>1</sup> Here we denote a the  $m_F$  level with  $\pm$  because of the ambiguity as to which state is prepared.

<sup>2</sup> The method for reading out population in a specific hyperfine state is described in Section 6.1.3.



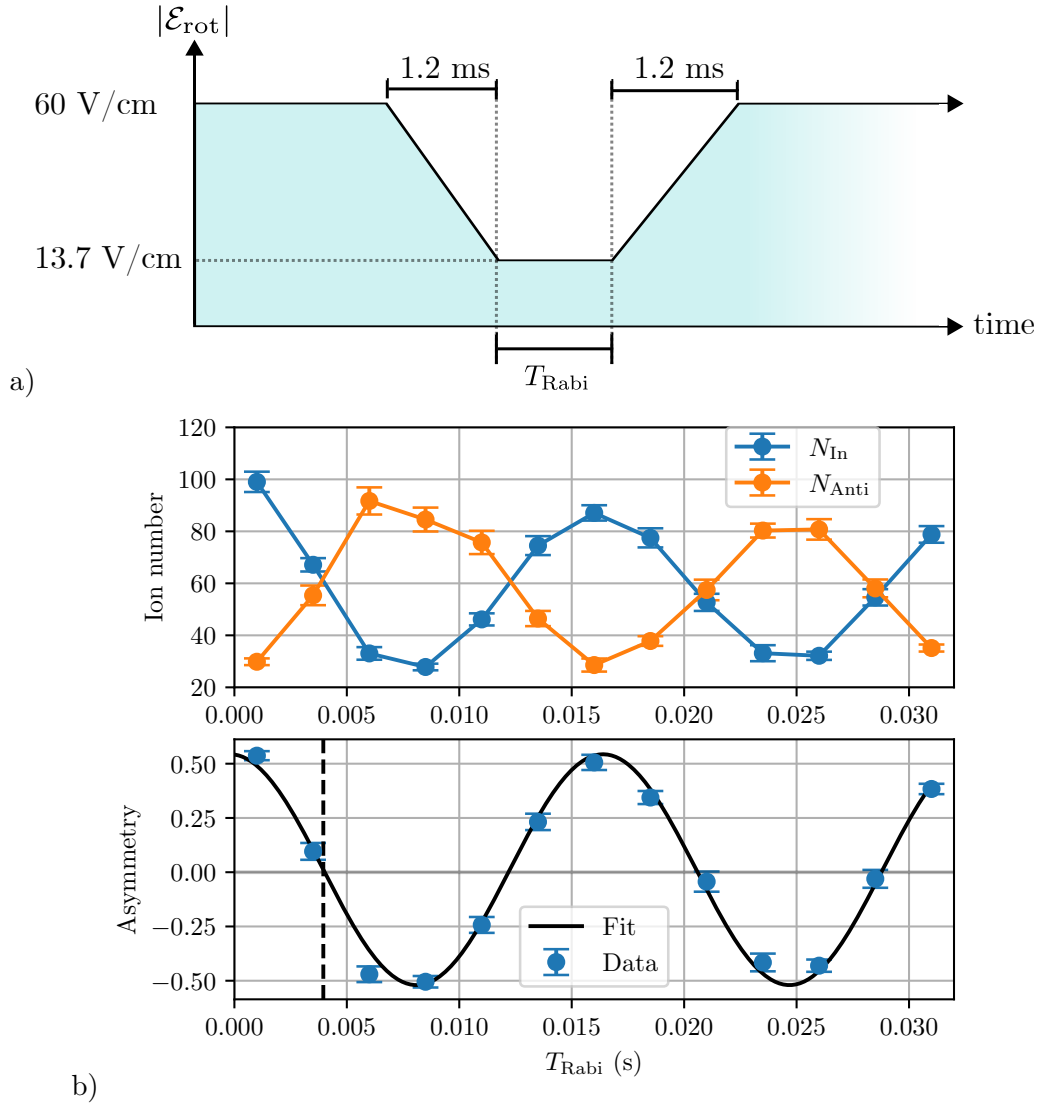


Figure 7.1: Rabi flopping of the eEDM-sensitive states.

a) Modulation of the magnitude of  $\mathcal{E}_{\text{rot}}$  that gives rise to the Rabi oscillations. The magnitude is ramped in 1.2 ms, the maximum speed at which the resonant circuit can ramp linearly based on its response time (which is different for each channel).

b) Oscillations in the population in each state. First the ions are optically pumped to one side of the hyperfine manifold, then the Rabi sequence is performed. Finally, the population on one side of the hyperfine manifold is read out by turning on  $\mathcal{L}_{m_F}$  and dissociating. The asymmetry of the two curves (defined in Equation 7.1) is calculated and the results fit to a sinusoid. The Rabi frequency  $\Omega_{\text{Rabi}}$  is fit to 60.30(49) Hz. From this we can determine the time at which the phase of the sinusoid is  $\pi/2$  (marked with a dashed black line). The time for an effective  $\pi/2$  pulse can then be extracted from this phase, yielding  $T_{\pi/2} = 3.95(6)$  ms.

We can then fit this quantity to extract the Rabi frequency and the phase. The phase of the asymmetry does not quite go to zero for zero  $T_{\text{Rabi}}$  since the ramps have finite duration, so a small amount of phase accrues during each ramp. An effective  $\pi/2$  pulse can then be chosen by finding where the asymmetry first crosses zero.

## 7.2 Ramsey oscillations

With a  $\pi/2$  pulse demonstrated in the Rabi oscillation, we then have the tools to perform the Ramsey scheme discussed in Section 2.1.3. Since our state preparation sequence populates both orientation states of the  $m_F = \pm 3/2$  hyperfine state and the  $\pi/2$  pulse is designed to be effective for both doublets, the Ramsey experiment will work on both doublets simultaneously. If we then use the spatially selective readout technique discussed in Section 6.3 to measure the population in each doublet independently, we can measure the frequencies of both doublets simultaneously in a single Ramsey experiment. This is done in Figure 7.2

We apply a magnetic field with coils described in Section 5.2 to generate an  $f_0$  of  $\sim 110$  Hz. At early times the doublets are in phase, but after some time the doublets go out of phase due to their different g-factors (as in Equation 2.5). At around 1 s, the doublets are maximally out of phase.

With this, we have demonstrated simultaneous measurement of the eEDM sensitive frequency channels  $f_u$  and  $f_l$  from Equation 2.6.

## 7.3 Concluding remarks

This thesis has documented the building of an experiment to measure the eEDM from conceptual design of the experiment to the sensitive measurement of eEDM sensitive states. Along the way, we have provided many engineering and technological solutions to the unique problems of an experiment as complicated as this one.

Now that Ramsey fringes have been demonstrated, the next steps towards realizing an eEDM measurement in this system are:

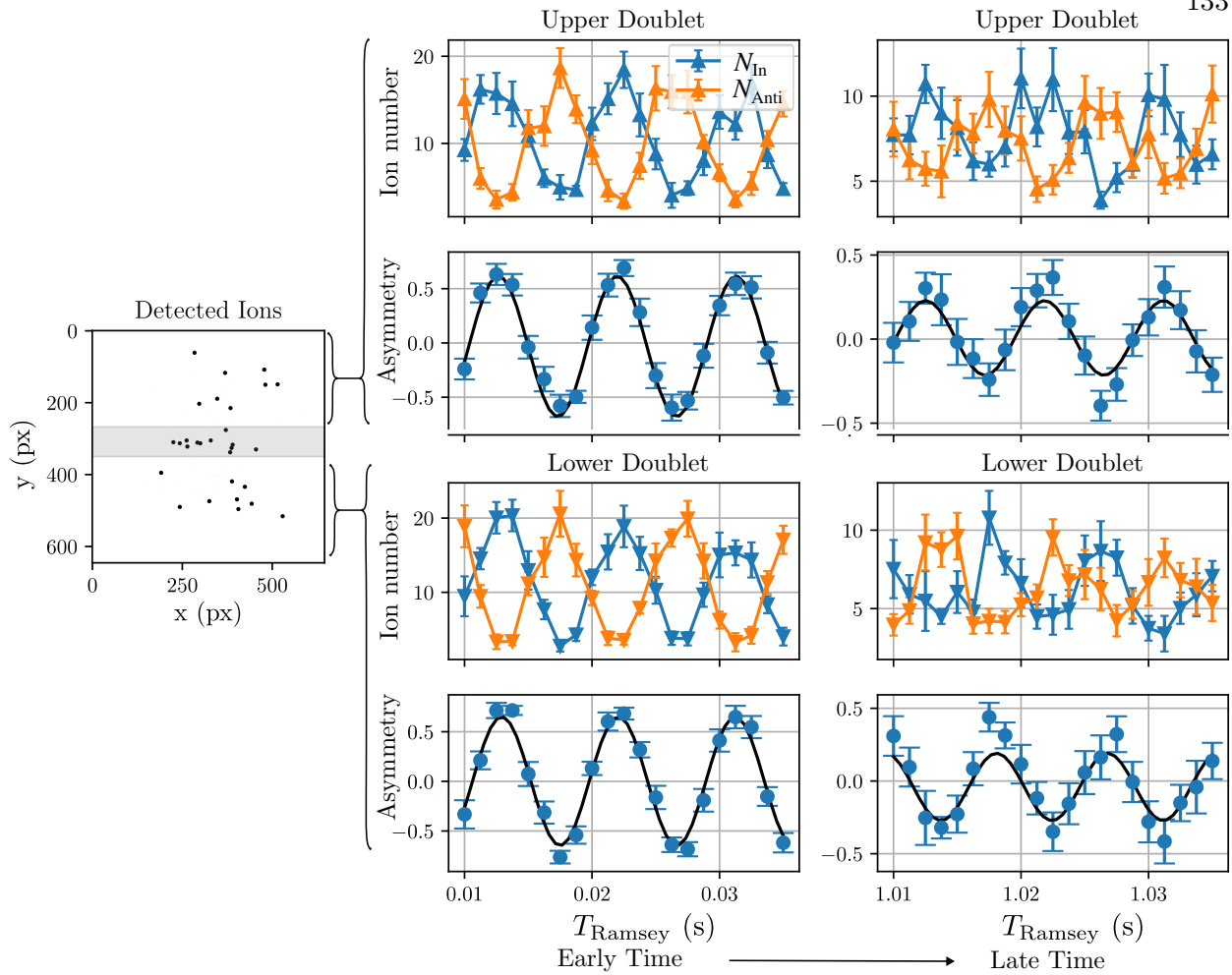


Figure 7.2: Ramsey fringes for the two doublets measured simultaneously via angular resolved photo-dissociation.

- Demonstrate blackbody-limited coherence time ( $\sim 20$  s).
- Multiplex the experiment to allow for continuous loading and readout using the demonstrated ion shuttling electrode design.
- Characterize sources of systematic error in the experiment (as was done in [51]).
- Collect blinded eEDM-sensitive measurements until the statistical uncertainty is similar in magnitude to the characterized systematic uncertainty.

Just as several graduate student years had been spent on production techniques and spectroscopy of  $\text{ThF}^+$  before I joined, many graduate student years will be spent after I leave completing these four steps, and I am confident that they are left in capable hands.

## Bibliography

- [1] A. D. Sakharov, “Violation of CP invariance, C asymmetry, and baryon asymmetry of the universe,” Soviet Physics Uspekhi, vol. 34, p. 392, may 1991.
- [2] M. Dine and A. Kusenko, “Origin of the matter-antimatter asymmetry,” Rev. Mod. Phys., vol. 76, pp. 1–30, Dec 2003.
- [3] S. Sarkar, “Big bang nucleosynthesis and physics beyond the standard model,” Reports on Progress in Physics, vol. 59, no. 12, p. 1493, 1996.
- [4] J. Ellis, “Beyond the standard model with the LHC,” Nature, vol. 448, no. 7151, p. 297, 2007.
- [5] J. H. Smith, E. M. Purcell, and N. F. Ramsey, “Experimental limit to the electric dipole moment of the neutron,” Phys. Rev., vol. 108, pp. 120–122, Oct 1957.
- [6] C. G. Shull and R. Nathans, “Search for a neutron electric dipole moment by a scattering experiment,” Phys. Rev. Lett., vol. 19, pp. 384–386, Aug 1967.
- [7] W. B. Dress, J. K. Baird, P. D. Miller, and N. F. Ramsey, “Upper limit for the electric dipole moment of the neutron,” Phys. Rev., vol. 170, pp. 1200–1206, Jun 1968.
- [8] J. K. Baird, P. D. Miller, W. B. Dress, and N. F. Ramsey, “Improved upper limit to the electric dipole moment of the neutron,” Phys. Rev., vol. 179, pp. 1285–1291, Mar 1969.
- [9] W. B. Dress, P. D. Miller, and N. F. Ramsey, “Improved upper limit for the electric dipole moment of the neutron,” Phys. Rev. D, vol. 7, pp. 3147–3149, Jun 1973.
- [10] W. B. Dress, P. D. Miller, J. M. Pendlebury, P. Perrin, and N. F. Ramsey, “Search for an electric dipole moment of the neutron,” Phys. Rev. D, vol. 15, pp. 9–21, Jan 1977.
- [11] I. Altarev, Y. Borisov, A. Brandin, A. Egorov, V. Ezhov, S. Ivanov, V. Lobashov, V. Nazarenko, G. Porsev, V. Ryabov, A. Serebrov, and R. Taldaev, “A search for the electric dipole moment of the neutron using ultracold neutrons,” Nuclear Physics A, vol. 341, no. 2, pp. 269–283, 1980.
- [12] J. Pendlebury, K. Smith, R. Golub, J. Byrne, T. McComb, T. Sumner, S. Burnett, A. Taylor, B. Heckel, N. Ramsey, K. Green, J. Morse, A. Kilvington, C. Baker, S. Clark, W. Mampe, P. Ageron, and P. Miranda, “Search for a neutron electric dipole moment,” Physics Letters B, vol. 136, no. 5, pp. 327–330, 1984.

- [13] K. Smith, N. Crampin, J. Pendlebury, D. Richardson, D. Shiers, K. Green, A. Kilvington, J. Moir, H. Prosper, D. Thompson, N. Ramsey, B. Heckel, S. Lamoreaux, P. Ageron, W. Mampe, and A. Steyerl, “A search for the electric dipole moment of the neutron,” Physics Letters B, vol. 234, no. 1, pp. 191–196, 1990.
- [14] I. Altarev, Y. Borisov, N. Borovikova, S. Ivanov, E. Kolomensky, M. Lasakov, V. Lobashev, V. Nazarenko, A. Pirozhkov, A. Serebrov, Y. Sobolev, E. Shulgina, and A. Yegorov, “New measurement of the electric dipole moment of the neutron,” Physics Letters B, vol. 276, no. 1, pp. 242–246, 1992.
- [15] E. Kolomensky, M. Lasakov, V. Lobashev<sup>o</sup>, and V. Nazarenko, “Search for the neutron electric dipole moment,” Physics of Atomic Nuclei, vol. 59, no. 7, pp. 1152–1170, 1996.
- [16] P. G. Harris, C. A. Baker, K. Green, P. Iaydjiev, S. Ivanov, D. J. R. May, J. M. Pendlebury, D. Shiers, K. F. Smith, M. van der Grinten, and P. Geltenbort, “New experimental limit on the electric dipole moment of the neutron,” Phys. Rev. Lett., vol. 82, pp. 904–907, Feb 1999.
- [17] C. A. Baker, D. D. Doyle, P. Geltenbort, K. Green, M. G. D. van der Grinten, P. G. Harris, P. Iaydjiev, S. N. Ivanov, D. J. R. May, J. M. Pendlebury, J. D. Richardson, D. Shiers, and K. F. Smith, “Improved experimental limit on the electric dipole moment of the neutron,” Phys. Rev. Lett., vol. 97, p. 131801, Sep 2006.
- [18] A. P. Serebrov, E. A. Kolomenskiy, A. N. Pirozhkov, I. A. Krasnoschekova, A. V. Vassiljev, A. O. Polyushkin, M. S. Lasakov, A. N. Murashkin, V. A. Solovey, A. K. Fomin, I. V. Shoka, O. M. Zhrebtsov, P. Geltenbort, S. N. Ivanov, O. Zimmer, E. B. Alexandrov, S. P. Dmitriev, and N. A. Dovator, “New search for the neutron electric dipole moment with ultracold neutrons at ILL,” Phys. Rev. C, vol. 92, p. 055501, Nov 2015.
- [19] C. Abel, S. Afach, N. J. Ayres, C. A. Baker, G. Ban, G. Bison, K. Bodek, V. Bondar, M. Burghoff, E. Chanel, Z. Chowdhuri, P.-J. Chiu, B. Clement, C. B. Crawford, M. Daum, S. Emmenegger, L. Ferraris-Bouchez, M. Fertl, P. Flaux, B. Franke, A. Fratangelo, P. Geltenbort, K. Green, W. C. Griffith, M. van der Grinten, Z. D. Grujić, P. G. Harris, L. Hayen, W. Heil, R. Henneck, V. H elaine, N. Hild, Z. Hodge, M. Horras, P. Iaydjiev, S. N. Ivanov, M. Kasprzak, Y. Kermaidic, K. Kirch, A. Knecht, P. Knowles, H.-C. Koch, P. A. Koss, S. Komposch, A. Kozela, A. Kraft, J. Krempel, M. Kuźniak, B. Lauss, T. Lefort, Y. Lemi ere, A. Leredde, P. Mohanmurthy, A. Mchedlishvili, M. Musgrave, O. Naviliat-Cuncic, D. Pais, F. M. Piegsa, E. Pierre, G. Pignol, C. Plonka-Spehr, P. N. Prashanth, G. Qu em ener, M. Rawlik, D. Rebreyend, I. Rien acker, D. Ries, S. Roccia, G. Rogel, D. Rozpedzik, A. Schnabel, P. Schmidt-Wellenburg, N. Severijns, D. Shiers, R. Tavakoli Dinani, J. A. Thorne, R. Viot, J. Voigt, A. Weis, E. Wursten, G. Wyszynski, J. Zejma, J. Zenner, and G. Zsigmond, “Measurement of the permanent electric dipole moment of the neutron,” Phys. Rev. Lett., vol. 124, p. 081803, Feb 2020.
- [20] I. Khriplovich and A. Zhitnitsky, “What is the value of the neutron electric dipole moment in the kobayashi-maskawa model?,” Physics Letters B, vol. 109, no. 6, pp. 490–492, 1982.
- [21] E. E. Salpeter, “Some atomic effects of an electronic electric dipole moment,” Phys. Rev., vol. 112, pp. 1642–1648, Dec 1958.
- [22] D. F. Nelson, A. A. Schupp, R. W. Pidd, and H. R. Crane, “Search for an electric dipole moment of the electron,” Phys. Rev. Lett., vol. 2, pp. 492–495, Jun 1959.

- [23] J. Goldemberg and Y. Torizuka, “Upper limit of the electric dipole moment of the electron,” Phys. Rev., vol. 129, pp. 2580–2581, Mar 1963.
- [24] E. S. Ensberg, “Experimental upper limit for the permanent electric dipole moment of  $\text{Rb}^{85}$  by optical-pumping techniques,” Phys. Rev., vol. 153, pp. 36–43, Jan 1967.
- [25] J. Angel, P. Sandars, and M. Tinker, “Observation of a  $v \times E$  effect in an electric dipole moment experiment using a reversible atomic beam machine,” Physics Letters A, vol. 25, no. 2, pp. 160–161, 1967.
- [26] M. C. Weisskopf, J. P. Carrico, H. Gould, E. Lipworth, and T. S. Stein, “Electric dipole moment of the cesium atom. a new upper limit to the electric dipole moment of the electron,” Phys. Rev. Lett., vol. 21, pp. 1645–1648, Dec 1968.
- [27] M. A. Player and P. G. H. Sandars, “An experiment to search for an electric dipole moment in the  $^3P_2$  metastable state of xenon,” Journal of Physics B: Atomic and Molecular Physics, vol. 3, p. 1620, dec 1970.
- [28] T. G. Vold, F. J. Raab, B. Heckel, and E. N. Fortson, “Search for a permanent electric dipole moment on the  $^{129}\text{Xe}$  atom,” Phys. Rev. Lett., vol. 52, pp. 2229–2232, Jun 1984.
- [29] D. Cho, K. Sangster, and E. A. Hinds, “Tenfold improvement of limits on t violation in thallium fluoride,” Phys. Rev. Lett., vol. 63, pp. 2559–2562, Dec 1989.
- [30] K. Abdullah, C. Carlberg, E. D. Commins, H. Gould, and S. B. Ross, “New experimental limit on the electron electric dipole moment,” Phys. Rev. Lett., vol. 65, pp. 2347–2350, Nov 1990.
- [31] E. D. Commins, S. B. Ross, D. DeMille, and B. C. Regan, “Improved experimental limit on the electric dipole moment of the electron,” Phys. Rev. A, vol. 50, pp. 2960–2977, Oct 1994.
- [32] B. C. Regan, E. D. Commins, C. J. Schmidt, and D. DeMille, “New limit on the electron electric dipole moment,” Phys. Rev. Lett., vol. 88, p. 071805, Feb 2002.
- [33] J. J. Hudson, D. M. Kara, I. J. Smallman, B. E. Sauer, M. R. Tarbutt, and E. A. Hinds, “Improved measurement of the shape of the electron,” Nature, vol. 473, pp. 493–496, May 2011.
- [34] T. A. Collaboration, J. Baron, W. C. Campbell, D. DeMille, J. M. Doyle, G. Gabrielse, Y. V. Gurevich, P. W. Hess, N. R. Hutzler, E. Kirilov, I. Kozyryev, B. R. O’Leary, C. D. Panda, M. F. Parsons, E. S. Petrik, B. Spaun, A. C. Vutha, and A. D. West, “Order of magnitude smaller limit on the electric dipole moment of the electron,” Science, vol. 343, no. 6168, pp. 269–272, 2014.
- [35] W. B. Cairncross, D. N. Gresh, M. Grau, K. C. Cossel, T. S. Roussy, Y. Ni, Y. Zhou, J. Ye, and E. A. Cornell, “Precision measurement of the electron’s electric dipole moment using trapped molecular ions,” Phys. Rev. Lett., vol. 119, p. 153001, Oct 2017.
- [36] V. Andreev, D. G. Ang, D. DeMille, J. M. Doyle, G. Gabrielse, J. Haefner, N. R. Hutzler, Z. Lasner, C. Meisenhelder, B. R. O’Leary, C. D. Panda, A. D. West, E. P. West, X. Wu, and A. C. M. E. Collaboration, “Improved limit on the electric dipole moment of the electron,” Nature, vol. 562, pp. 355–360, Oct 2018.

- [37] Y. Ema, T. Gao, and M. Pospelov, “Standard model prediction for paramagnetic electric dipole moments,” Phys. Rev. Lett., vol. 129, p. 231801, Nov 2022.
- [38] T. S. Roussy, L. Caldwell, T. Wright, W. B. Cairncross, Y. Shagam, K. B. Ng, N. Schlossberger, S. Y. Park, A. Wang, J. Ye, and E. A. Cornell, “A new bound on the electron’s electric dipole moment,” 2022.
- [39] K. B. Ng, The ThF<sup>+</sup> eEDM experiment: concept, design, and characterization. PhD thesis, University of Colorado Boulder, 2023.
- [40] M. Denis and T. Fleig, “In search of discrete symmetry violations beyond the standard model: Thorium monoxide reloaded,” The Journal of Chemical Physics, vol. 145, Dec. 2016.
- [41] L. V. Skripnikov, “Combined 4-component and relativistic pseudopotential study of ThO for the electron electric dipole moment search,” The Journal of Chemical Physics, vol. 145, Dec. 2016.
- [42] V. Andreev, D. G. Ang, D. DeMille, J. M. Doyle, G. Gabrielse, J. Haefner, N. R. Hutzler, Z. Lasner, C. Meisenhelder, B. R. O’Leary, C. D. Panda, A. D. West, E. P. West, X. Wu, and A. C. M. E. Collaboration, “Improved limit on the electric dipole moment of the electron,” Nature, vol. 562, pp. 355–360, Oct 2018.
- [43] E. R. Meyer, J. L. Bohn, and M. P. Deskevich, “Candidate molecular ions for an electron electric dipole moment experiment,” Phys. Rev. A, vol. 73, p. 062108, Jun 2006.
- [44] A. N. Petrov, N. S. Mosyagin, T. A. Isaev, and A. V. Titov, “Theoretical study of Hff<sup>+</sup> in search of the electron electric dipole moment,” Phys. Rev. A, vol. 76, p. 030501, Sep 2007.
- [45] T. Fleig, “ $\mathcal{P}$ ,  $\mathcal{T}$ -odd and magnetic hyperfine-interaction constants and excited-state lifetime for hff<sup>+</sup>,” Phys. Rev. A, vol. 96, p. 040502, Oct 2017.
- [46] W. B. Cairncross, D. N. Gresh, M. Grau, K. C. Cossel, T. S. Roussy, Y. Ni, Y. Zhou, J. Ye, and E. A. Cornell, “Precision measurement of the electron’s electric dipole moment using trapped molecular ions,” Phys. Rev. Lett., vol. 119, p. 153001, Oct 2017.
- [47] M. Denis, M. S. Nørby, H. J. A. Jensen, A. S. P. Gomes, M. K. Nayak, S. Knecht, and T. Fleig, “Theoretical study on ThF<sup>+</sup>, a prospective system in search of time-reversal violation,” New Journal of Physics, vol. 17, p. 043005, apr 2015.
- [48] L. V. Skripnikov and A. V. Titov, “Theoretical study of ThF<sup>+</sup> in the search for  $T$ ,  $P$ -violation effects: Effective state of a Th atom in ThF<sup>+</sup> and ThO compounds,” Phys. Rev. A, vol. 91, p. 042504, Apr 2015.
- [49] R. D. Freeman, “Quantities, units, and symbols in physical chemistry (mills, ian; cvitas, tomislav; homann, klaus; kallay, nikola; kuchitsu, kozo),” Journal of Chemical Education, vol. 66, p. A188, Jul 1989.
- [50] K. B. Ng, Y. Zhou, L. Cheng, N. Schlossberger, S. Y. Park, T. S. Roussy, L. Caldwell, Y. Shagam, A. J. Vigil, E. A. Cornell, and J. Ye, “Spectroscopy on the electron-electric-dipole-moment-sensitive states of thf<sup>+</sup>,” Phys. Rev. A, vol. 105, p. 022823, Feb 2022.



- [51] L. Caldwell, T. S. Roussy, T. Wright, W. B. Cairncross, Y. Shagam, K. B. Ng, N. Schlossberger, S. Y. Park, A. Wang, J. Ye, and E. A. Cornell, “Systematic and statistical uncertainty evaluation of the  $\text{HfF}^+$  electron electric dipole moment experiment,” Phys. Rev. A, vol. 108, p. 012804, Jul 2023.
- [52] J. Ye, S. Swartz, P. Jungner, and J. L. Hall, “Hyperfine structure and absolute frequency of the  $^{87}\text{Rb}$   $5\text{P}_{3/2}$  state,” Opt. Lett., vol. 21, pp. 1280–1282, Aug 1996.
- [53] J. R. Rubbmark, M. M. Kash, M. G. Littman, and D. Kleppner, “Dynamical effects at avoided level crossings: A study of the landau-zener effect using Rydberg atoms,” Phys. Rev. A, vol. 23, pp. 3107–3117, Jun 1981.
- [54] D. M. Pozar, Microwave engineering; 3rd ed. Hoboken, NJ: Wiley, 2005.
- [55] P. Sarafis and A. G. Nassiopoulou, “Dielectric properties of porous silicon for use as a substrate for the on-chip integration of millimeter-wave devices in the frequency range 140 to 210 GHz,” Nanoscale Research Letters, vol. 9, p. 418, Aug 2014.
- [56] J. W. Nilsson, Electric circuits / James W. Nilsson, Susan A. Riedel. Upper Saddle River, N.J: Prentice Hall, 6th ed. [rev. print.] ed., 2001.
- [57] J. D. Jackson, Classical electrodynamics; 2nd ed. New York, NY: Wiley, 1975.
- [58] C. D. H. Christholm, Group theoretical techniques in quantum chemistry. 1976.
- [59] P. Hammond, “Laser dye DCM, its spectral properties, synthesis and comparison with other dyes in the red,” Optics Communications, vol. 29, no. 3, pp. 331–333, 1979.
- [60] Y. Zhou, Y. Shagam, W. B. Cairncross, K. B. Ng, T. S. Roussy, T. Grogan, K. Boyce, A. Vigil, M. Pettine, T. Zelevinsky, J. Ye, and E. A. Cornell, “Second-scale coherence measured at the quantum projection noise limit with hundreds of molecular ions,” Phys. Rev. Lett., vol. 124, p. 053201, Feb 2020.

## Appendix A

### Biot-Savart Integrals

In order to design coil geometries for generating desired magnetic fields, it is useful to have analytic expressions for the general building blocks for these coils. While the resulting expressions are complicated, they can be evaluated numerically in order to simulate the fields of a superposition of these coils without the need for approximation. The square coil expression is used in Sections 5.2 and 5.6, while the circular coil expression is used in Section 5.7.

#### A.1 Square current loop

Here we derive the analytic expression for the fields from a square loop of wire. Begin with a single square current loop with sides of length  $L$ . The relevant geometry is depicted in Figure A.1. The Biot-Savart law [57] tells us that the magnetic field from a length of current is given by

$$\vec{B}(\vec{r}) = \frac{\mu_0 I}{4\pi} \int \frac{d\vec{r}' \times \vec{R}'}{|\vec{R}'|^3}. \quad (\text{A.1})$$

Considering each segment separately we can write this as

$$\begin{aligned} \vec{B}_{\text{coil}}(\vec{r}) &= \vec{B}_{12} + \vec{B}_{23} + \vec{B}_{34} + \vec{B}_{41} \\ &= \frac{\mu_0 I}{4\pi} \left( \int_{-\frac{L}{2}}^{\frac{L}{2}} \frac{\{0, -dy', 0\} \times \{x + \frac{L}{2}, y - y', z\}}{|\{x + \frac{L}{2}, y - y', z\}|^3} + \int_{-\frac{L}{2}}^{\frac{L}{2}} \frac{\{dx', 0, 0\} \times \{x - x', y + \frac{L}{2}, z\}}{|\{x - x', y + \frac{L}{2}, z\}|^3} \right. \\ &\quad \left. + \int_{-\frac{L}{2}}^{\frac{L}{2}} \frac{\{0, dy', 0\} \times \{x - \frac{L}{2}, y - y', z\}}{|\{x - \frac{L}{2}, y - y', z\}|^3} + \int_{-\frac{L}{2}}^{\frac{L}{2}} \frac{\{-dx', 0, 0\} \times \{x - x', y - \frac{L}{2}, z\}}{|\{x - x', y - \frac{L}{2}, z\}|^3} \right). \end{aligned} \quad (\text{A.2})$$

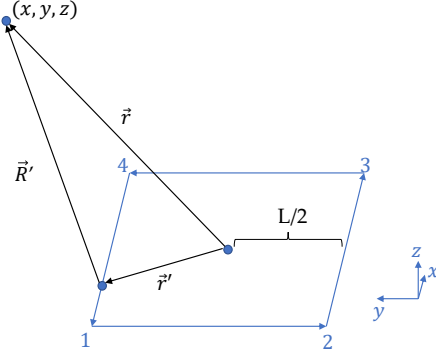


Figure A.1: The geometry of a square loop of current. The origin is taken to be the center of the loop. The current is taken to run anticlockwise in the order of nodes 1, 2, 3, and 4.  $\vec{r}$  is defined as the vector to an arbitrary point in space  $(x, y, z)$  at which we wish to know the field,  $\vec{r}'$  is defined as the vector to the differential part of the current loop which we are integrating over, and  $\vec{R}'$  is defined as the distance from this differential wire length to  $(x, y, z)$ . Note that  $\vec{R}' = \vec{r} - \vec{r}'$ .

If we define a function that looks like the solution to an integral of this form,

$$H(a, b, i, j, k) \equiv \frac{\mu_0 I}{4\pi} \left( \frac{a - \frac{L}{2}}{\left( -\left( b + \frac{L}{2}(-1)^i \right)^2 - z^2 \right) \sqrt{\left( \frac{L}{2}(-1)^{(k+1)\delta_{j,0+i}} + x \right)^2 + \left( \frac{L}{2}(-1)^{k\delta_{j,0+i}} + y \right)^2 + z^2}} - \frac{a + \frac{L}{2}}{\left( -\left( b + \frac{L}{2}(-1)^i \right)^2 - z^2 \right) \sqrt{\left( \frac{L}{2}(-1)^{(k+1)\delta_{j,1+i}} + x \right)^2 + \left( \frac{L}{2}(-1)^{k\delta_{j,1+i}} + y \right)^2 + z^2}} \right), \quad (\text{A.3})$$

where  $\delta_{i,j}$  is the Kronecker delta, then the solution to the integral from Equation A.2 can be written as

$$\vec{B}_{\text{coil}}(\vec{r}) = \left\{ \begin{array}{c} zH(y, x, 1, 1, 1) - zH(y, x, 0, 0, 1) \\ zH(x, y, 1, 1, 0) - zH(x, y, 0, 0, 0) \\ \left( \frac{L}{2} + y \right) H(x, y, 0, 0, 0) + \left( \frac{L}{2} - y \right) H(x, y, 1, 1, 0) + \left( \frac{L}{2} + x \right) H(y, x, 0, 0, 1) + \left( \frac{L}{2} - x \right) H(y, x, 1, 1, 1) \end{array} \right\}. \quad (\text{A.4})$$

If we evaluate this expression at  $x = y = 0$ , this turns into the familiar expression for the on-axis field from a square loop of wire:

$$\vec{B}_{\text{coil}}(0, 0, z) = \left\{ 0, 0, \frac{\mu_0 I L^2}{2\pi \left( \frac{L^2}{4} + z^2 \right) \sqrt{\frac{L^2}{2} + z^2}} \right\}. \quad (\text{A.5})$$

## A.2 Circular current loop

Direct integration of the Biot-Savart equation (Equation A.1) tells us the magnetic field from a circular loop of current centered at the origin with its axis aligned in  $\hat{z}$  with a radius or  $R$  passing current  $I$ :

$$\vec{B} = \frac{\mu_0 I}{4\pi} \frac{\varrho^2 \left( \zeta (r^2 + R^2) E \left( -\frac{4R\rho}{\varrho^2} \right) - \zeta^2 \left( \varrho K \left( \frac{4R\rho}{\zeta^2} \right) + \zeta K \left( -\frac{4R\rho}{\varrho^2} \right) \right) \right) + \zeta^2 \varrho (r^2 + R^2) E \left( \frac{4R\rho}{\zeta^2} \right)}{\rho^2 \left( (r^2 + R^2)^2 - 4\rho^2 R^2 \right)^{3/2}} \cdot \left[ \begin{array}{c} xz \\ yz \\ \frac{\rho^2 \left( \zeta^2 \varrho^2 \left( \varrho K \left( \frac{4R\rho}{\zeta^2} \right) + \zeta K \left( -\frac{4R\rho}{\varrho^2} \right) \right) + 2R^2 \sqrt{(r^2 + R^2)^2 - 4\rho^2 R^2} \left( \zeta E \left( \frac{4R\rho}{\zeta^2} \right) + \varrho E \left( -\frac{4R\rho}{\varrho^2} \right) \right) - \zeta^2 \varrho (r^2 + R^2) E \left( \frac{4R\rho}{\zeta^2} \right) - \zeta \varrho^2 (r^2 + R^2) E \left( -\frac{4R\rho}{\varrho^2} \right) \right)}{\zeta \varrho \left( -\zeta \varrho \left( \varrho K \left( \frac{4R\rho}{\zeta^2} \right) + \zeta K \left( -\frac{4R\rho}{\varrho^2} \right) \right) + \zeta (r^2 + R^2) E \left( \frac{4R\rho}{\zeta^2} \right) + \varrho (r^2 + R^2) E \left( -\frac{4R\rho}{\varrho^2} \right) \right)} \end{array} \right], \quad (\text{A.6})$$

where

$$\left\{ \begin{array}{l} \rho = x^2 + y^2 \\ r = x^2 + y^2 + z^2 \\ \varrho = \sqrt{(R - \rho)^2 + z^2} \\ \zeta = \sqrt{(\rho + R)^2 + z^2} \end{array} \right.$$

and  $E$  and  $K$  are the elliptic E and K integrals, respectively.

## Appendix B

### A modified chain rule for vector fields

In the derivation for the ponderomotive potential in Section 4.1.2, in order to expand the electric field about the secular position, we had to introduce an operator for the gradient of a vector field:

$$\vec{\nabla} \vec{E} \equiv \begin{bmatrix} \frac{\partial}{\partial x} \vec{E} \\ \frac{\partial}{\partial y} \vec{E} \\ \frac{\partial}{\partial z} \vec{E} \end{bmatrix}. \quad (\text{B.1})$$

We then later used a modified version of the chain rule in this higher-dimensional space to arrive at our result:

$$(\vec{\nabla} \vec{E}) \cdot \vec{E} = \frac{1}{2} \vec{\nabla} |E|^2 - \vec{E} \times (\vec{\nabla} \times \vec{E}). \quad (\text{B.2})$$

We will prove this relation here. Begin with the left hand side:

$$(\vec{\nabla} \vec{E}) \cdot \vec{E} = \begin{bmatrix} \frac{\partial}{\partial x} \vec{E} \\ \frac{\partial}{\partial y} \vec{E} \\ \frac{\partial}{\partial z} \vec{E} \end{bmatrix} \cdot \begin{bmatrix} E_x \\ E_y \\ E_z \end{bmatrix} = \sum_i E_i \left( \frac{\partial}{\partial r_i} \vec{E} \right), \quad (\text{B.3})$$

where the sum over  $i$  is a sum over the dimensions  $r_i = \{x, y, z\}$  and  $E_i = \{E_x, E_y, E_z\}$ . We can write this in vector form and distribute the factor of  $E_i$ , giving

$$(\vec{\nabla} \vec{E}) \cdot \vec{E} = \sum_i E_i \begin{bmatrix} \frac{\partial}{\partial r_i} E_x \\ \frac{\partial}{\partial r_i} E_y \\ \frac{\partial}{\partial r_i} E_z \end{bmatrix} = \sum_i \begin{bmatrix} E_i (\frac{\partial}{\partial r_i} E_x) \\ E_i (\frac{\partial}{\partial r_i} E_y) \\ E_i (\frac{\partial}{\partial r_i} E_z) \end{bmatrix}. \quad (\text{B.4})$$

We can add a clever zero to this equation of the form

$$(\vec{\nabla} \vec{E}) \cdot \vec{E} = \sum_i \begin{bmatrix} E_i(\frac{\partial}{\partial r_i} E_x) \\ E_i(\frac{\partial}{\partial r_i} E_y) \\ E_i(\frac{\partial}{\partial r_i} E_z) \end{bmatrix} - \underbrace{\sum_i \begin{bmatrix} E_i(\frac{\partial}{\partial x} E_i) \\ E_i(\frac{\partial}{\partial y} E_i) \\ E_i(\frac{\partial}{\partial z} E_i) \end{bmatrix}}_{=0} + \sum_i \begin{bmatrix} E_i(\frac{\partial}{\partial x} E_i) \\ E_i(\frac{\partial}{\partial y} E_i) \\ E_i(\frac{\partial}{\partial z} E_i) \end{bmatrix}, \quad (\text{B.5})$$

then combine the first two sums to get

$$(\vec{\nabla} \vec{E}) \cdot \vec{E} = \sum_i \begin{bmatrix} E_i(\frac{\partial}{\partial r_i} E_x - \frac{\partial}{\partial x} E_i) \\ E_i(\frac{\partial}{\partial r_i} E_y - \frac{\partial}{\partial y} E_i) \\ E_i(\frac{\partial}{\partial r_i} E_z - \frac{\partial}{\partial z} E_i) \end{bmatrix} + \sum_i \begin{bmatrix} E_i(\frac{\partial}{\partial x} E_i) \\ E_i(\frac{\partial}{\partial y} E_i) \\ E_i(\frac{\partial}{\partial z} E_i) \end{bmatrix}. \quad (\text{B.6})$$

We can then move the sum inside the vector:

$$(\vec{\nabla} \vec{E}) \cdot \vec{E} = \begin{bmatrix} \sum_i E_i(\frac{\partial}{\partial r_i} E_x - \frac{\partial}{\partial x} E_i) \\ \sum_i E_i(\frac{\partial}{\partial r_i} E_y - \frac{\partial}{\partial y} E_i) \\ \sum_i E_i(\frac{\partial}{\partial r_i} E_z - \frac{\partial}{\partial z} E_i) \end{bmatrix} + \sum_i \begin{bmatrix} E_i(\frac{\partial}{\partial x} E_i) \\ E_i(\frac{\partial}{\partial y} E_i) \\ E_i(\frac{\partial}{\partial z} E_i) \end{bmatrix}. \quad (\text{B.7})$$

Note that the term in parenthesis goes to zero if  $i = x$  in the first row,  $i = y$  in the second row, or  $i = z$  in the third row, so we can exclude his from the sum, giving

$$(\vec{\nabla} \vec{E}) \cdot \vec{E} = \begin{bmatrix} \sum_{i \neq x} E_i(\frac{\partial}{\partial r_i} E_x - \frac{\partial}{\partial x} E_i) \\ \sum_{i \neq y} E_i(\frac{\partial}{\partial r_i} E_y - \frac{\partial}{\partial y} E_i) \\ \sum_{i \neq z} E_i(\frac{\partial}{\partial r_i} E_z - \frac{\partial}{\partial z} E_i) \end{bmatrix} + \sum_i \begin{bmatrix} E_i(\frac{\partial}{\partial x} E_i) \\ E_i(\frac{\partial}{\partial y} E_i) \\ E_i(\frac{\partial}{\partial z} E_i) \end{bmatrix}, \quad (\text{B.8})$$

or explicitly

$$(\vec{\nabla} \vec{E}) \cdot \vec{E} = \begin{bmatrix} E_z(\frac{\partial}{\partial z} E_x - \frac{\partial}{\partial x} E_z) + E_y(\frac{\partial}{\partial y} E_x - \frac{\partial}{\partial x} E_y) \\ E_x(\frac{\partial}{\partial x} E_y - \frac{\partial}{\partial y} E_x) + E_z(\frac{\partial}{\partial z} E_y - \frac{\partial}{\partial y} E_z) \\ E_y(\frac{\partial}{\partial y} E_z - \frac{\partial}{\partial z} E_y) + E_x(\frac{\partial}{\partial x} E_z - \frac{\partial}{\partial z} E_x) \end{bmatrix} + \sum_i \begin{bmatrix} E_i(\frac{\partial}{\partial x} E_i) \\ E_i(\frac{\partial}{\partial y} E_i) \\ E_i(\frac{\partial}{\partial z} E_i) \end{bmatrix}. \quad (\text{B.9})$$

We can then recognize each term in parentheses as a component of the curl of  $\vec{E}$ :

$$(\vec{\nabla} \vec{E}) \cdot \vec{E} = \begin{bmatrix} E_z(\vec{\nabla} \times \vec{E})_y - E_y(\vec{\nabla} \times \vec{E})_z \\ E_x(\vec{\nabla} \times \vec{E})_z - E_z(\vec{\nabla} \times \vec{E})_x \\ E_y(\vec{\nabla} \times \vec{E})_x - E_x(\vec{\nabla} \times \vec{E})_y \end{bmatrix} + \sum_i \begin{bmatrix} E_i(\frac{\partial}{\partial x} E_i) \\ E_i(\frac{\partial}{\partial y} E_i) \\ E_i(\frac{\partial}{\partial z} E_i) \end{bmatrix}, \quad (\text{B.10})$$

and then recognize this vector as (negative) the cross product of  $\vec{E}$  with its curl:

$$(\vec{\nabla}\vec{E}) \cdot \vec{E} = -\vec{E} \times (\vec{\nabla} \times \vec{E}) + \sum_i \begin{bmatrix} E_i(\frac{\partial}{\partial x} E_i) \\ E_i(\frac{\partial}{\partial y} E_i) \\ E_i(\frac{\partial}{\partial z} E_i) \end{bmatrix}. \quad (\text{B.11})$$

With the remaining vector, we can then use the one dimensional chain rule  $\frac{\partial}{\partial x}(f(x)^2) = 2f\frac{\partial f}{\partial x}$  to arrive at

$$(\vec{\nabla}\vec{E}) \cdot \vec{E} = -\vec{E} \times (\vec{\nabla} \times \vec{E}) + \sum_i \begin{bmatrix} \frac{1}{2}(\frac{\partial}{\partial x} E_i^2) \\ \frac{1}{2}(\frac{\partial}{\partial y} E_i^2) \\ \frac{1}{2}(\frac{\partial}{\partial z} E_i^2) \end{bmatrix}. \quad (\text{B.12})$$

We can pull out the factor of 1/2 from the vector and move the sum inside the derivatives:

$$(\vec{\nabla}\vec{E}) \cdot \vec{E} = -\vec{E} \times (\vec{\nabla} \times \vec{E}) + \frac{1}{2} \begin{bmatrix} \frac{\partial}{\partial x} (\sum_i E_i^2) \\ \frac{\partial}{\partial y} (\sum_i E_i^2) \\ \frac{\partial}{\partial z} (\sum_i E_i^2) \end{bmatrix}, \quad (\text{B.13})$$

and finally, recognizing that  $\sum_i E_i^2$  is exactly the magnitude  $|E|^2$ , we arrive at the result:

$$(\vec{\nabla}\vec{E}) \cdot \vec{E} = -\vec{E} \times (\vec{\nabla} \times \vec{E}) + \frac{1}{2}\vec{\nabla}|E|^2. \quad (\text{B.14})$$

ProQuest Number: 30639284

INFORMATION TO ALL USERS

The quality and completeness of this reproduction is dependent on the quality and completeness of the copy made available to ProQuest.



Distributed by ProQuest LLC (2023).

Copyright of the Dissertation is held by the Author unless otherwise noted.

This work may be used in accordance with the terms of the Creative Commons license or other rights statement, as indicated in the copyright statement or in the metadata associated with this work. Unless otherwise specified in the copyright statement or the metadata, all rights are reserved by the copyright holder.

This work is protected against unauthorized copying under Title 17, United States Code and other applicable copyright laws.

Microform Edition where available © ProQuest LLC. No reproduction or digitization of the Microform Edition is authorized without permission of ProQuest LLC.

ProQuest LLC  
789 East Eisenhower Parkway  
P.O. Box 1346  
Ann Arbor, MI 48106 - 1346 USA